THE UNIVERSITY
of EDINBURGH

Investigation of the Nanomechanical Properties of Soft Biomaterials Using Atomic Force Microscopy (AFM)

Ibrahim Ahmed Albaijan

THE UNIVERSITY *of* EDINBURGH

Doctor of Philosophy

The University of Edinburgh
2017

Declaration

I declare that this thesis has been composed solely by myself and that it has not been submitted, in whole or in part, in any previous application for a degree. Except where stated otherwise by reference or acknowledgment, the work presented is entirely my own.

(Ibrahim Albaijan)

March 2017

Acknowledgements

In the beginning, I want to thank my God for his blessing and helping to enable me to finish my thesis. Without his supporting guidance and providence this project would not have been completed.

It is a fact, without the guidance and orientations of several people this dream could not have been achieved, and I would like to express my thanks and my gratitude to all of them.

First and foremost, I would like to thank my supervisor Professor Vasileios Koutsos at the School of Engineering in The University of Edinburgh for his valuable guidance, explanations, comments, patience and encouragement. He was always next to me, whenever I needed his support and he did not hesitate to share with me his useful and beneficial experience. This work was a genuine challenge; however, his guidance and suggestions surmounted the difficulties. His advice was the mainstay of this project and was very active so, I appreciate him now and forever.

Secondly, I want to express my great thanks to my wonderful (first) colleagues Dr. Apostolos Evangelopoulos, Dr. Julia Morris and Dr. Michail Kalloudis. Those who shared the same office and who brought to our working environment the level of harmony, comfort, kindness, friendliness and respect where we could share our experiences and exchange advice, not only on the academic issues but also on life issues, in unforgettable chats and debates if the tiny amount of free time allowed. I would like to thank Dr. Julia Morris for her help in learning how to use the atomic

force microscope (AFM) and to practise using it under her supervision at the beginning of the PhD study. Dr. Michail Kalloudis was the closest friend to me and we shared many things even out of the collage. Unfortunately, Dr. Apostolos Evangelopoulos' last steps were my first steps in the PhD journey, however we were able to enjoy the rest of the time. I wish to express my thanks to all my other colleagues and friends. Special thanks go to Dr. Alexander McVey in School of Physics and Astronomy for his collaboration and preparation of the hydrogel specimens which were investigated in Chapter 6. Also, I would like to thank Mrs Jenifer Spencer for her proof-reading of an unfamiliar subject to her, on which, nevertheless, she provided me with valuable comments and feedback.

I want to thank my government, represented by the Ministry of Higher Education who supported and funded this work during my study.

Last but not least, I would like to express my deepest thanks and gratitude to my lovely precious wife, who supported me and stayed beside me to achieve this dream. There is no doubt that without her support and her effort this work would not have been completed. She did not spare any effort to make my life and our home environment able to support me in achieving such a big dream. She is a superwoman who could control and manage the house needs, the children, her volunteer work and her personal activities. She is a partner in this success: therefore, I dedicate to her this achievement.

Lay summary

I have used a specialised technique called atomic force microscopy (AFM) to investigate two types of soft biomaterials: soft-shelled microbubbles (MBs) made from phospholipids (major component of cell membranes) and soft gels (hydrogels) composed of water and agarose (biomolecule extracted from seaweed). The MBs are commonly used in medical applications either in diagnostic applications as ultrasound contrast agents (UCAs) or in therapeutic applications as drug/gene delivery carriers. The hydrogels are used in medical applications to treat cartilages defects. The atomic force microscope has been used widely in the recent years for the study of structural and mechanical properties of soft materials because of its high resolution and ease of use directly on biomedical materials in buffer solutions resembling physiological conditions. The aim of this study was to investigate the mechanical properties of the phospholipid MBs and agarose hydrogels. Their mechanical response to deformation was indeed probed systematically and comprehensively by microscopic and nanoscopic probes and the measurements revealed their complex and in many cases unexpected behaviour.

Abstract

This study presents a systematic investigation of two types of soft biomaterials: phospholipid-based microbubbles (MBs) and agarose hydrogels, using atomic force microscopy (AFM) force-distance curves. Microbubbles are used widely in several applications, especially in medical applications, where they are used as ultrasound contrast agents (UCAs) and as vehicles for transporting the drugs and genes to their targets, which is commonly known as drug/gene delivery. Although plenty of attention has been paid to these materials by medical researchers there is a shortage of engineering research on the properties of these materials. The present study tries to address this gap by studying these materials from the engineering perspective; therefore, the aim of this study is to investigate the mechanical properties of MBs and hydrogels.

In this research, phospholipid-based microbubbles (MBs), commercially called SonoVue® microbubbles and used as UCAs, were investigated to measure their mechanical properties using an AFM mode of operation called force-distance curves (or force spectroscopy mode); this mode allows for direct mechanical tests to acquire the force-deformation (F-Δ) behaviour of the MBs. The compression tool was a flat (tipless) cantilever moved at constant speed, whereas the variable was MB size. The MBs behaviour was assessed by calculating several mechanical properties, which were the stiffness, Young's modulus (three different models were applied), hysteresis, plasticity, adhesion forces, nonlinearity and instability. The stiffness and the Young's modulus values were measured to be in the same range as found in similar studies. A phenomenon was observed that the local stiffness of the MB increases after each unstable step provided that the MB stays within the linear elastic region. The Young's

modulus was calculated applying three models, two for estimating the elastic modulus of the shell and the third for modulus of elasticity of the whole MB. The stretching component of the membrane theory was found to provide the best prediction of the Young's modulus value.

To investigate the effect of the tip geometry on the mechanical properties of the MBs, the MBs were studied with different cantilever/tips, including a conical-tipped cantilever. The study concluded that there is no impact of the contact geometry on the mechanical properties of the MBs if the applied forces and the spring constant of the cantilever are the same. The same phenomenon, increasing the local stiffness of the MB after each unstable step, was found however with a higher rate.

Hydrogels were also studied in this research using AFM and adopting a nanoindentation technique. The indenter was a conical tip moving toward the sample surface with constant speed and applying similar forces on all samples, where the variable was the gel concentration. In addition to the previous mechanical properties, other properties were investigated, such as hardness, universal hardness and pressure. An effect of the gel concentration on the mechanical properties of the gels was observed. There is a difference in the results compared to those reported in the literature review, where some of the results are in the same range as those found here, while others were either higher or lower, due to the influence of factors such as the indenter geometry, the applied force and the load rate; moreover, it was found that the viscoelastic behaviour of the gels played a significant role.

Table of Contents

List of Symbols and Abbreviations:

Abbreviations:

Atomic Force Microscopy	AFM
Dipalmitoylphosphatidylglycerol	DPPG
Distearoylphosphatidylcholine	DSCP
Distilled and deionised water	d. d. H_2O
Extracellular Matrix	ECM
Intermittent-contact	IC
International Business Machines	IBM
Linear Variable Differential Transformer	LVDT
Microbubble	MB
Microbubbles	MBs
Molecular Force Probe	MFP
Non-contact	NC
Phospholipids	PLs
Poly Ethylene Glycol	PEG
Polyacrylic acid	PAA
Polyvinyl alcohol	PVA
Scanning Electron Microscope	SEM
Scanning Probe Microscopy	SPM
Scanning Tunnelling Microscope	STM
Transmission Electron Microscope	TEM
Ultrasound	US
Ultrasound Contrast Agents	UCAs

Symbols:

Area between the two curves	A_b
Area under the loading curve	A_l
Area under the unloading curve	A_u
Cantilever deflection	X
Cantilever spring constant	k_c
Cone base radius	r
Cone height	h
Cone slant length	l
Contact depth	h_c
Contact radius	a
Contact stiffness	S
Displacement rate	$\dot{h}$
Elastic displacement depth	h_s
Final depth	h_f
Force	F
Force-deformation	F-Δ
Force-indentation	F-δ
Force-relative deformation	F-ε
Geometry constants	λ, β
Half angle of the cone	ϕ
Hardness	H
Indentation	δ
Infinity	∞
Initial diameter	D_0
Initial inner radius	r_i
Initial radius	R_0
Maximum indentation depth	h_{max}
Microbubble stiffness	k_b

Piezo displacement	Z
Plasticity index	η
Poisson's ratio	υ
Pressure	P
Projected contact area	A
Reduced elastic modulus	E_r
Registered sign	®
Relative deformation	ε
Sample deformation	Δ
Slope	s
Stiffnesses of the sample	k_s
Stiffnesses of the whole system	k_t
Strain	ξ
Strain rate	$\acute{\varepsilon}$
Stress	σ
Thickness	t
Tip radius	R_{Tip}
Universal hardness	UH
Young's modulus	E

CHAPTER 1
INTRODUCTION

CHAPTER 1: INTRODUCTION

1.1 Introduction

In recent years, soft biomaterials have attracted a good deal of attention, due tothe possibility of their applications in many fields. [1] Examples of such biomaterials are biomedical materials, such as microbubbles (MBs). Microbubbles are particles that encapsulate an inert gas by means of a very thin shell suspended in the surrounding medium. The shell consists of lipid (as in the present study), protein, polymers or a mix of these materials. [2] Microbubbles are used in several applications, commercially and medically. [3] However, their medical applications have a significant importance , where they are used in both diagnostic applications, as ultrasound contrast agents (UCAs), [4] and in therapeutic applications, as drug/gene delivery vehicles. [5] Another type of biomaterials are the tissue engineering materials, for instance the hydrogels. A hydrogel is defined as a water-swollen material, produced by the simple reaction of one or more monomers, containing cross-linked polymeric networks. [6] The hydrogels are used in different applications such as artificial snow, sealing and food additives [7-9] and in medical applications, for instance as scaffolds for tissue engineering [10] which helps cover the gap between the supply and demand of organs and tissues for transplantation. [11] The hydrogels can be classified, based on their source, into natural and synthetic. [12] There is a great number of studies from the biological and medical perspectives concerning biomaterials; however, there is a lack of studies of those materials from the engineering side. ***The Aim of this study is to investigate and measure the nanomechanical properties of soft biomaterials namely phospholipid microbubbles (MBs) and***

agarose hydrogels, using the atomic force microscopy (AFM) technique at force spectroscopy mode. Investigating such materials involves complexity and challenges, because of their viscoelastic behaviour. However, the atomic force microscopy (AFM) technique has enhanced the study of such materials and made it possible, even for live cells. The AFM is a type of scanning probe microscope (SPM), [13] which has been widely used in recent decades to probe and determine the topography of the samples' surfaces using the imaging mode [14] and to measure the local mechanical properties of the materials using the force spectroscopy mode. [15] AFM is commonly used, especially with soft materials, due to its high resolution, reaching to less than a nanometre (nm) [16] and high force sensitivity reaching to a piconewton (pN). [17] This technique was adopted in the present study to calculate the micro/nanomechanical properties of the MBs and gels.

This study is divided into seven chapters and appendices as follows:

Chapter 1: is a general introduction providing the incentive and overall organization of the thesis (which you are reading now).

Chapter 2: provides a general background regarding the investigated materials, which are the MBs and the gels, concentrating on their definition, structure, types, production and applications. In addition, the chapter describes the operational principles of an atomic force microscope (AFM) as weel as its history.

Chapter 3: explains the theoretical background and the analytical equations that are used to investigate the mechanical properties of the materials, including the concepts and the basic relations of stiffness, Young's modulus (with different models), hysteresis, plasticity and hardness.

Chapter 4: investigates the mechanical properties of microbubbles, commercially called SonoVue®, and includes the results for stiffness, Young's modulus using different models, hysteresis, plasticity, adhesion forces, nonlinearity and instability. The compression tool is a rectangular flat cantilever (tipless cantilever).

Chapter 5: is similar to Chapter 4; however, the compression tool is a tipped cantilever where the tip is a cone, to investigate the impact of the tip geometry on the mechanical properties of the MBs.

Chapter 6: reports the study of the mechanical properties of the agarose hydrogels including hardness, the universal hardness and the applied pressure.

Chapter 7: includes a general conclusion and the intended future work.

Appendices: more details are provided for the results of Chapter 4 (Appendix A), Chapter 5 (Appendix B) and Chapter 6 (Appendix C) and related publications are presented in Appendix D.

1.2 References

1. Agarwal, A., W.J. Ng, and Y. Liu, *Principle and applications of microbubble and nanobubble technology for water treatment.* Chemosphere, 2011. **84**(9): p. 1175-1180.

2. Sirsi, S. and M. Borden, *Microbubble compositions, properties and biomedical applications.* Bubble Science, Engineering & Technology, 2009. **1**(1-2): p. 3-17.

3. Arakawa, T., T. Yamamoto, and S. Shoji, *Micro-bubble formation with organic membrane in a multiphase microfluidic system.* Sensors and Actuators A: Physical, 2008. **143**(1): p. 58-63.

4. Blomley, M. J., Cooke, J. C., Unger, E. C., Monaghan, M. J. and D. O. Cosgrove, *Microbubble contrast agents: a new era in ultrasound.* British Medical Journal, 2001. **322**(7296): p. 1222-1225.

5. Swanson, E. J., Mohan, V., Kheir, J. and M. A. Borden, *Phospholipid-stabilized microbubble foam for injectable oxygen delivery.* Langmuir, 2010. **26**(20): p. 15726-15729.

6. Ahmed, E. M., *Hydrogel: Preparation, characterization, and applications: A review.* Journal of Advanced Research, 2015. **6**(2): p. 105-121.

7. Iza, M., Stoianovici, G., Viora, L., Grossiord, J. and G, *Hydrogels of poly (ethylene glycol): mechanical characterization and release of a model drug.* Journal of Controlled Release, 1998. **52**(1): p. 41-51.

8. Jang, H., Chung, Y. and S. Kim, *Preparation and characterization of silicone hydrogel lens containing poly (ethylene glycol).* Polymer Korea, 2009. **33**(2): p. 169-174.

9. Peyton, S.R., Raub, C. B., Keschrumrus, V. P. and A. J. Putnam, *The use of poly (ethylene glycol) hydrogels to investigate the impact of ECM chemistry and mechanics on smooth muscle cells.* Biomaterials, 2006. **27**(28): p. 4881-4893.

10. Jeong, B., S.W. Kim, and Y.H. Bae, *Thermosensitive sol–gel reversible hydrogels.* Advanced drug delivery reviews, 2012. **64**: p. 154-162.

11. Drury, J. L. and D.J. Mooney, *Hydrogels for tissue engineering: scaffold design variables and applications.* Biomaterials, 2003. **24**(24): p. 4337-4351.

12. Ahmed, E.M., Aggor, F. S., Awad, A. M. and A. T. El-Aref, *An innovative method for preparation of nanometal hydroxide superabsorbent hydrogel.* Carbohydrate polymers, 2013. **91**(2): p. 693-698.

13. Allison, D. P., Mortensen, N. P.,Sullivan, C. J. and M. J. Doktycz, *Atomic force microscopy of biological samples.* Wiley Interdisciplinary Reviews: Nanomedicine and Nanobiotechnology, 2010. **2**(6): p. 618-634.

14. Bottomley, L. A., J.E. Coury, and P.N. First, *Scanning probe microscopy.* Analytical Chemistry, 1996. **68**(12): p. 185-230.

15. Ellul, M. D., A.H. Tsou, and W. Hu, *Crosslink densities and phase morphologies in thermoplastic vulcanizates.* Polymer, 2004. **45**(10): p. 3351-3358.

16. Aikawa, M., *Studies on falciparum malaria with atomic-force and surface-potential microscopes.* Annals of Tropical Medicine & Parasitology, 1997. **91**(7): p. 689-692.

17. Butt, H., Cappella, B. and M. Kappl, *Force measurements with the atomic force microscope: Technique, interpretation and applications.* Surface science reports, 2005. **59**(1): p. 1-152.

CHAPTER 2
GENERAL BACKGROUND

CHAPTER 2: GENERAL BACKGROUND

2.1 Introduction

Since the beginning of the 1980s the investigation of soft nonconductive materials, such as biological and biomedical materials, has become a competitive and interesting field. The investigations can be conducted by using an AFM, which is an instrument that can scan the topography of the surface and provide the mechanical properties of the material. Thus, it is appropriate to first describe and discuss the type of biomedical materials adopted in this investigation, which are phospholipidic microbubbles (MBs) and agarose hydrogels. The instrument used to investigate these materials, which employs one of the atomic force microscopy (AFM) techniques, is the molecular force probe (MFP-1D).

2.2 Atomic Force Microscopy (AFM)

Atomic force microscopy (AFM) belongs to the scanning probe microscopy (SPM) family [1, 2] providing high resolution in space with field of view in the range of 10 nm-100 μm and resolution ~0.1 nm and ~10 nm [3-7] for vertical and lateral resolution, respectively and measures forces which help us to see the topography of the samples' surfaces and their structure [8-10] and measure the local mechanical properties of the materials [11-13]. Most types of samples can be imaged using AFM, whether they are hard materials such as ceramics and metals or soft such as microbubbles (MBs) and hydrogels. In contrast with other microscopy techniques,

AFM does not produce the images by focusing light or electrons onto the surface of the sample, as optical or electron microscopes do. Instead, the AFM physically feels and tries to read the sample surface topography by means of a sharp probe. [7] AFM is currently the most common type of scanning probe microscopy (SPM) and is used in most fields of science. [14]

2.2.1 History of AFM

It is accepted that without the optical microscope, which was invented in the 17th century, [15, 16] some fields such as biological, natural and medical sciences would not have been developed as they are today. In the 1930s, a second major development occurred in morphostructural surface analysis, which was the introduction of the scanning electron microscope (SEM). [17] An electron microscope with a high resolution obtained by scanning a very small raster, the pattern of image capture and reconstruction used in television

, with a focused electron beam was invented by Manfred von Ardenne in 1937. [18] SEM uses electrons and electromagnetic lenses (magnetic coils) instead of light (photons) and glass lenses. Because of the long distance between the sample and the probe, the optical and scanning electron microscopes are called “far-field microscopes”. [19] At the beginning of the 1980s, Binnig and Rohrer were able to see the first image of an individual silicon atom on a surface without using lenses, photons, or electrons, but only by exploring the sample surface by genuine direct mechanical scanning. Working for IBM [13], they published a paper in 1982 [20] unveiling their new invention, which was the scanning tunnelling microscope (STM). Before the invention of the STM, such a high resolution needed a huge transmission electron

microscope (TEM), weighing thousands of kilograms and requiring a large room size, to accommodate it. In 1986 Binnig and Rohrer shared the Nobel Prize for physics for the invention of the STM. [21] Although the STM was a fascinating development in scientific research, it has a disadvantage in that it is appropriate only for electrically conductive samples. Nevertheless, STM is still used widely in certain applications and remains a useful instrument, even with this limitation. This limitation immediately encouraged the researchers to think about a new technique which would be able to work with nonconductive materials. Binnig, Quate and Gerber published a further paper in 1986 [22] entitled the "Atomic Force Microscope". In this paper, they introduced the atomic force microscope (AFM) as a new type of microscope that can investigate an insulated material on an atomic scale using a combination of the STM technique and the stylus profilometer technique. The first AFM instrument, which was built by Binnig et al., remains in the Science Museum in London, and attracts interested visitors. Figure 2-1 is the first AFM instrument; while the instruments used today are somewhat different in shape and construction, the underlying concept remains the same.

Because of the interest in using the AFM, it was produced commercially and rapidly became available on the market, where it was launched in 1988. [13, 23, 24] Scanning probe microscopy (SPM) is a technique that uses a local probe to investigate the sample surface. Therefore, both STM and AFM are considered as SPM instruments. STM and AFM share several features in their concept and design; however, they differ in that the STM maps the sample surface by means of a conductive probe while the AFM investigates the surface by means of a sharp tip mounted on the end of a flexible cantilever. Figure 2-2 shows the differences between STM and AFM techniques. [2]

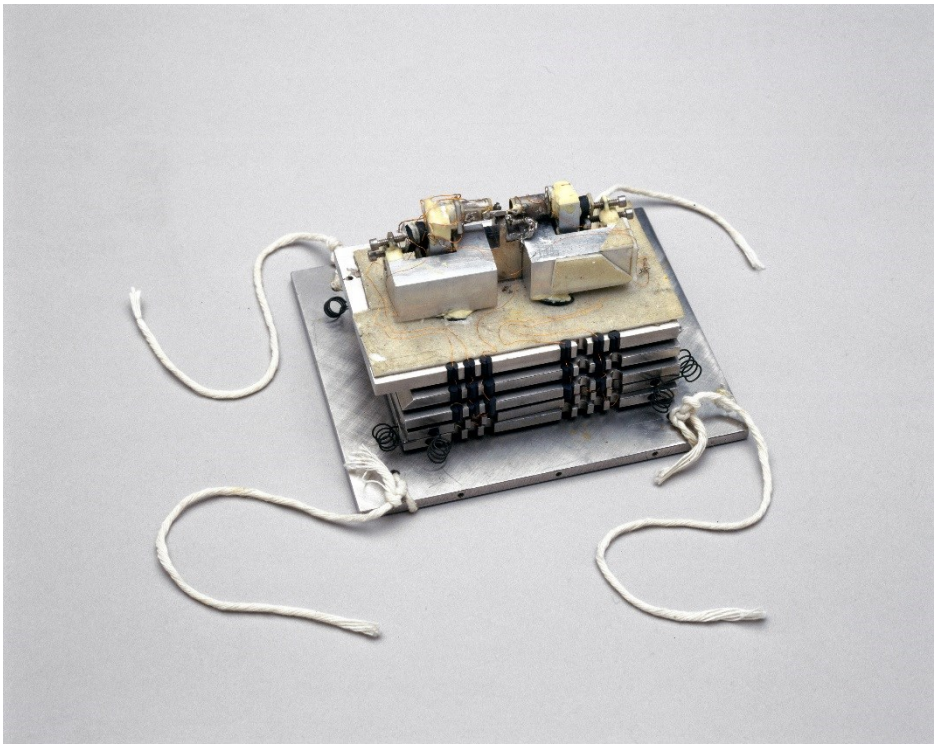

Figure 2-1: The first AFM instrument, which was invented by Binnig, Quate and Gerber, is preserved in the Science Museum in London. Obtained from the Science Museum (London) with permission.

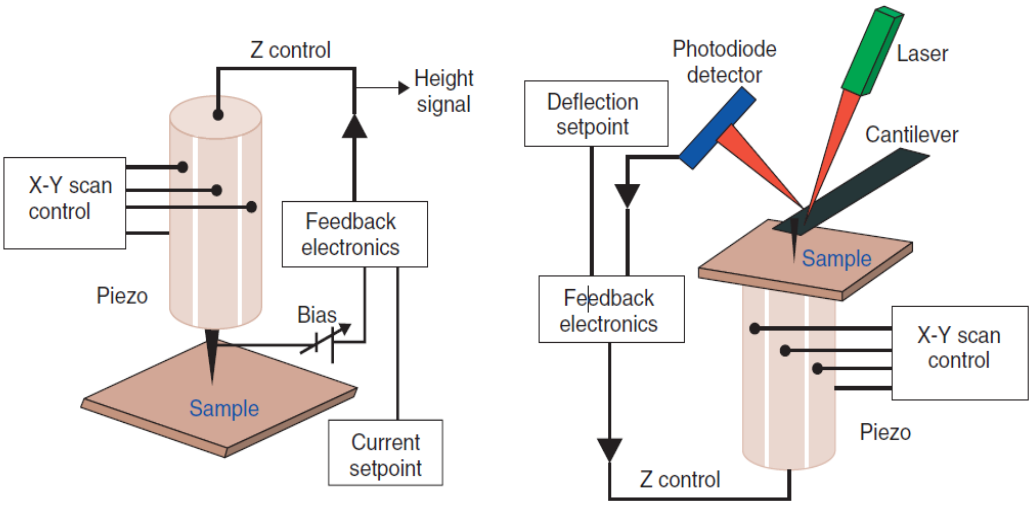

Scanning Tunnelling Microscope, (STM)

Atomic Force Microscope, (AFM)

Figure 2-2: Illustrating the difference between STM and AFM instruments, where the STM feels the changes in the surface topography by monitoring a tunnelling current electronically between a conductive sample and a conductive tip, while the AFM feels the surface topography by touch or near to touch the surface with a sharp tip on the end of the cantilever and monitors the change by a reflected laser beam. [2]

Since AFM instruments can work with most types of samples and in most environments, they are used widely at the present time especially with biological and biomedical materials.

2.2.2 How Does AFM Work?

AFM sensing can be described as depicted by Engel et al., [25] as being similar to a stick held in a blind person's hand to scan the environment to explore the path ahead. The topography of the sample surface image can be acquired in 3D by using the AFM technique on a nanoscale, measuring the forces between a sharp probe (tip) (radius at the tip apex < 10 nm) and the sample surface. The AFM tip touches the sample surface gently, or nearly touches it depending upon the mode used. The forces between the sample and the probe (tip) produce a deflection of the cantilever depending on Hooke's law. The tip could consist of a sharp tip, a large sphere, e.g. a colloid particle, or be without a tip (tipless), depending on the application for which it is intended to be used. It is usually a sharp tip for the topography surface imaging applications and could be a relatively large (or without) tip in the force spectroscopy experiments. [26-28] This type of instrument was used to implement all the experiments in this study. Figure 2-3-(a) shows an AFM while Figure 2-3-(b) illustrates a schematic of the internal parts of the AFM instrument, adapted from the manual of the manufacturing company (Asylum Research, Santa Barbra, CA) which has provided with the instrument. [29] The cantilever can approach or retract from the sample surface in the vertical direction, where this could be achieved either by moving the cantilever holder or by moving the sample stage, depending on the instrument configuration. The piezoelectric actuator produces this movement while a Linear Variable Differential Transformer (LVDT)

controls it. [29] The cantilever deflects when the sample surface is in contact with the tip. The laser beam focused on the backside of the cantilever is reflected onto a photodetector. The angle of the reflecting laser beam changes and the position of the reflecting laser spot accordingly changes on the photodetector. As a result, the displacement of the laser spot on the photodetector can be measured and translated to a cantilever deflection. [26, 30]

The AFM is used widely to investigate the topography of a sample surface. The surface area is scanned by the cantilever movement in a raster pattern of up to hundreds of square microns with very high resolution, reaching to few angstroms (Å), to produce a topographic image of the surface. [31] While the tip moves over the sample surface, the voltage of the z-axis piezo crystal is changed continuously by a feedback system to control the tip sample distance to avoid damaging the sample and the tip. [30, 32]

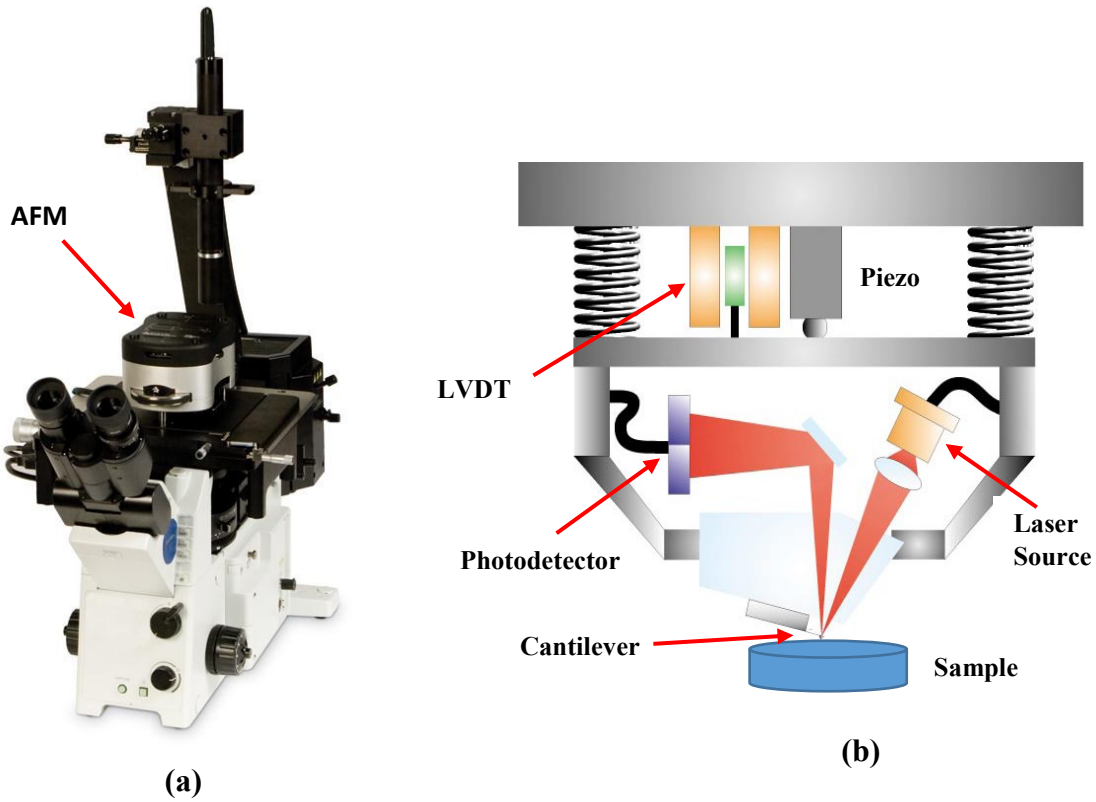

Figure 2-3: (a) The atomic force microscope (AFM) instrument used in this study, mounted on the inverted optical microscope. (b) Schematic drawing of internal equipment of the atomic force microscope (AFM) (obtained from the manufacturing company manual provided with the instrument), with some modifications.

2.2.3 AFM Modes

Since the AFM is used widely with very high resolution in most science fields, there are several modes that can be used when operating the AFM. [33, 34] However this study will talk about the most three common used modes, which are contact, non-contact and intermittent-contact (tapping) modes.

- **Contact Mode**

In the contact mode the cantilever moves towards the sample to be in direct contact with the sample surface (see contact region in Figure 2-4-a) and experience the strong short-range electrostatic repulsions in addition to van der Waals, capillary (in a wet environment) and other (long-range) electrostatic forces which could influence the overall force. In the contact mode the dominant force is repulsive (see Figure 2-4-a). The cantilever bends according to the forces acting between the tip and the sample surface; the cantilever's spring constant is usually lower than the effective stiffness of the sample which causes bending of the cantilever. The topographic image of the surface can be produced by maintaining the separation between the tip and the sample constant, at a set-point in the operating system, using the constant force mode which is controlled by the feedback loop to keep the tip at the desired set-point while it scans across the sample surface. A constant height mode can be employed for atomically smooth surfaces. Compared to other modes, this is relatively fast with high resolution. However, it is inappropriate for soft materials which might be damaged. [35, 36]

- **Non-contact Mode**

In the non-contact (NC) mode, also called dynamic mode, the separation between the tip and the sample surface is in the order of hundreds of angstroms (Å), with no contact. The dominant forces in the non-contact (NC) mode are attractive (see Figure 2-4-a) and low (around 10^{-12} N) which makes it suitable for soft materials to avoid damaging the sample. The cantilever in NC mode is stiffer than in contact mode, to avoid pulling the cantilever onto the sample surface and coming into contact with the sample. In this mode the cantilever vibrates near its resonant frequency, depending on its spring constant, with amplitude around hundreds of angstroms (Å). The separation between the tip and the sample surface is monitored by the feedback loop, either using a constant frequency or a constant amplitude technique. However, this mode provides less resolution and the scanning is relatively slower than the contact mode. [35, 36]

- **Intermittent-contact (Tapping) Mode**

Intermittent-contact (IC) works like NC mode where the cantilever is near the sample surface and vibrates at its resonant frequency however at the bottom of the vibration the cantilever touches or hits (taps) the sample surface which does not happen in NC mode. The separation between the tip and the sample is controlled in the same way as in the NC mode. This mode has many advantages; it is suitable for larger scan sizes than the NC mode, it is faster than NC mode and less damaging to the sample than the contact mode therefore it is widely used. Lateral resolution is better compared with both contact and NC modes. [35, 36] Figure 2-4 shows (a) the three modes'

regions on the Van der Waals curve (obtained from [35]) and (b) a schematic of the three modes.

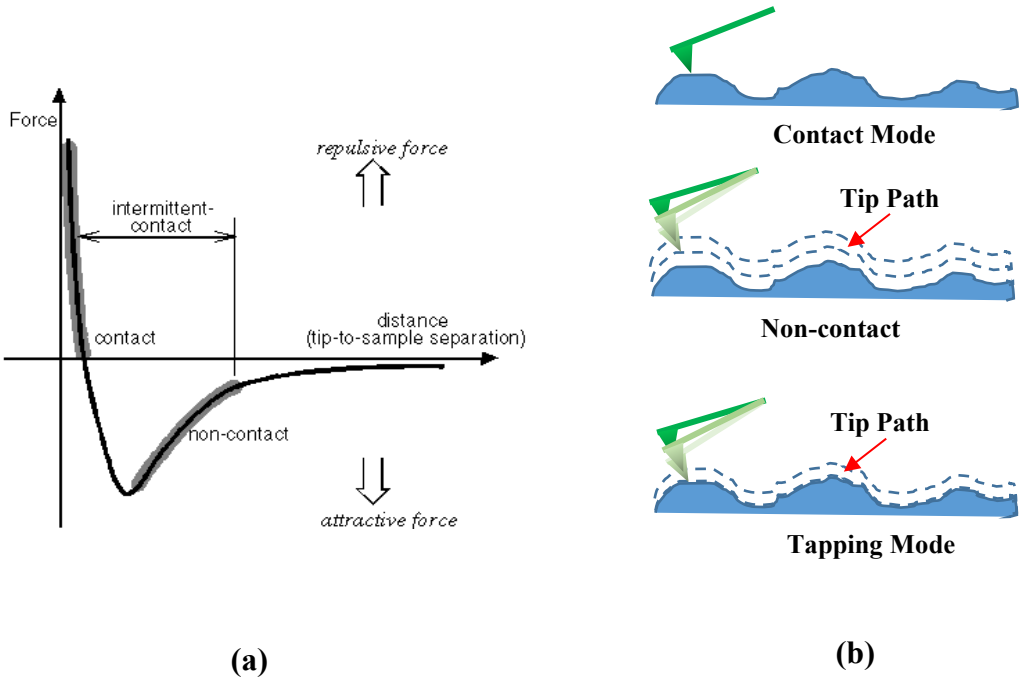

Figure 2-4: (a) Representing the three modes regions on the force-distance curve (obtained from [35]) and (b) schematic of the contact, non-contact and tapping modes.

2.2.4 Force Spectroscopy

Force spectroscopy is a basic technique in AFM used to measure the interaction forces between the tip of the cantilever and the sample surface. [30, 37] This technique of analysis was used in all the experimental work of this study. The AFM not only has a high resolution in the topographic imaging analysis but also has a high sensitivity to very small forces, down to 10 pico-Newtons (10^{-11} N), in the force mode. [38] The soft cantilever responds and deflects according to the exerted forces, which may reach the scale of few pico-Newtons (pN). Such an order of magnitude of forces can break a

hydrogen bond. [30] The ability to control and measure a force of very small order of magnitude is helpful to test very soft materials, either in compression, such as phospholipid microbubbles (MBs), or indentation, e.g. hydrogels, which are examined in this study. The force is measured as a function of the tip position in the z-direction with no change of the lateral position. [36]. Subsequently the data can be converted to force-distance curves using Hooke's law where the spring constant of the cantilever is known.

Figure 2-5-(a) illustrates a typical force-distance curve from the experiments in this study, consisting of the approach line, load curve (dashed blue line) and the retrace line, unload curve (solid red line) and focuses on the main regions of importance in the curve. In Figure 2-5-(b) shows a schematic of cantilever movement in the AFM experiment using the force spectroscopy technique. In region (A), the cantilever moves towards the sample surface from a setting point away from contact, where no interaction forces between the sample surface and the tip exist and no deflection appears on the cantilever. The gap between the tip and the sample surface decreases with movement of the cantilever down towards the sample. The attractive forces between the tip and the sample increase in region (B), because of the van der Waals forces and the cantilever begins to bend toward the sample slightly, then jumps suddenly to contact with the sample (called snap-in). [39] In region (C), the cantilever bends more and more in the opposite direction of its movement after the contact point between the tip and the sample, producing a straight line in the force-distance curve. The material under the tip in this region is compressed and either deformed, as in the microbubble (MB) experiments, or indented as in the hydrogel experiments where the piezo movement (piezo displacement) in this region converts into two displacements

the deflection of cantilever and the deformation of the sample (see equation 4 in Chapter 3). The cantilever withdraws at the maximum approach and changes its direction of movement in region (D), where a small hysteresis may appear between the approach (load) and retract (unload) curves [40, 41] (due to certain factors such as the adhesion forces between the tip and the surface). As the cantilever retreats from the sample, it passes the zero point (distance-axes, F=0) while the tip is in contact with the sample and the force becomes negative in the force-distance curve because the adhesion force pulls the tip down toward the sample. At a certain point the cantilever overcomes the adhesion forces and the tip becomes free with no contact with the sample surface and returns sharply to the initial position (F=0), as shown in region (E). The adhesion forces appear due to several interaction forces such as the van der Waals, electrostatic and capillary, in humid environment, forces. [42] Finally, in region (F),

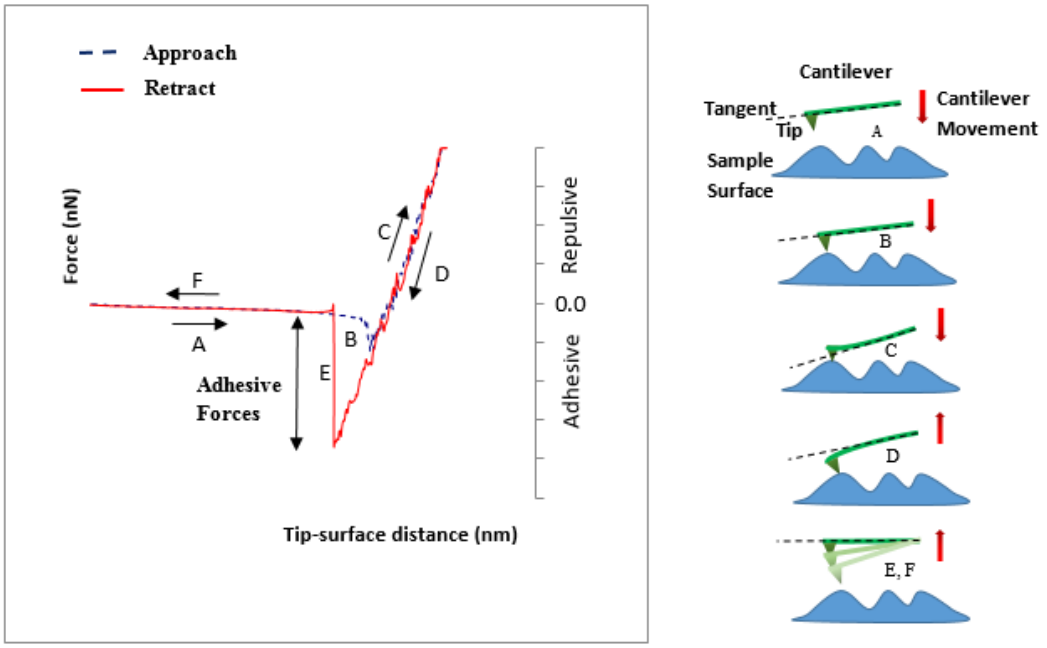

Figure 2-5: A typical force-distance curve highlighting regions of importance. (A) Non-contact and approach. (B) Snap-in to contact. (C) Approach in contact with increasing cantilever deflection. (D) Retract in contact with decreasing cantilever deflection. (E) The cantilever passes the original contact point due to adhesion forces. (F) Retract out of contact with change the movement direction.

the cantilever continues retracting away from the sample to its original position; however, the movement is now in the opposite direction.

2.2.5 Cantilevers

The main tool in the AFM technique is the cantilever, where its sensitivity and the sharpness of its tip play a signficant role and affect the resolution of the AFM, combined with other factors such as step size and the number of scanning lines. The cantilever/tip assembly is the most common probe used with scanning probe microscopy (SPM) and is appropriate for imaging the topography of the sample. There are several cantilevers differing in shape and in the material used for various applications. The body of the cantilever is usually manufactured from silicon or silicon nitride and the back of the cantilever is coated with different materials such as aluminium or gold to enhance the reflectance of the laser beam to the detector area. Cantilevers are produced in different shapes, either rectangular or V-shaped, and integrated by a tip microfabricated at the free end, while in some applications there is no need for a tip at all. They are provided on a chip that sometimes has more than one cantilever on both sides. Typically, the length of the cantilever ranges from 100 μm to 200 μm and the width from 10 μm to 40 μm, while the thickness is in the range from 0.3 μm to 2 μm. [35] Figure 2-6 shows a schematic of both shapes of the cantilever, the rectangular shape and the V-shape (triangle), obtained from the MikroMasch® web page [43] and the Bruker AFM Probes web page [44]. The shape of the cantilever and its dimensions, together with the manufacturing material, determine its spring constant, where the shorter and the thicker the cantilever is, the higher its resonant

frequencies and spring constant. Typically, cantilevers are manufactured to have a spring constant in the range from 0.01 N/m to 100 N/m depending on the desired application. In the present study, the cantilevers were chosen according to the stiffness of the tested materials where it was preferable for the spring constant of the cantilever to be in the same range as the tested material stiffness so that it would not be too hard or too soft compared to the material stiffness.

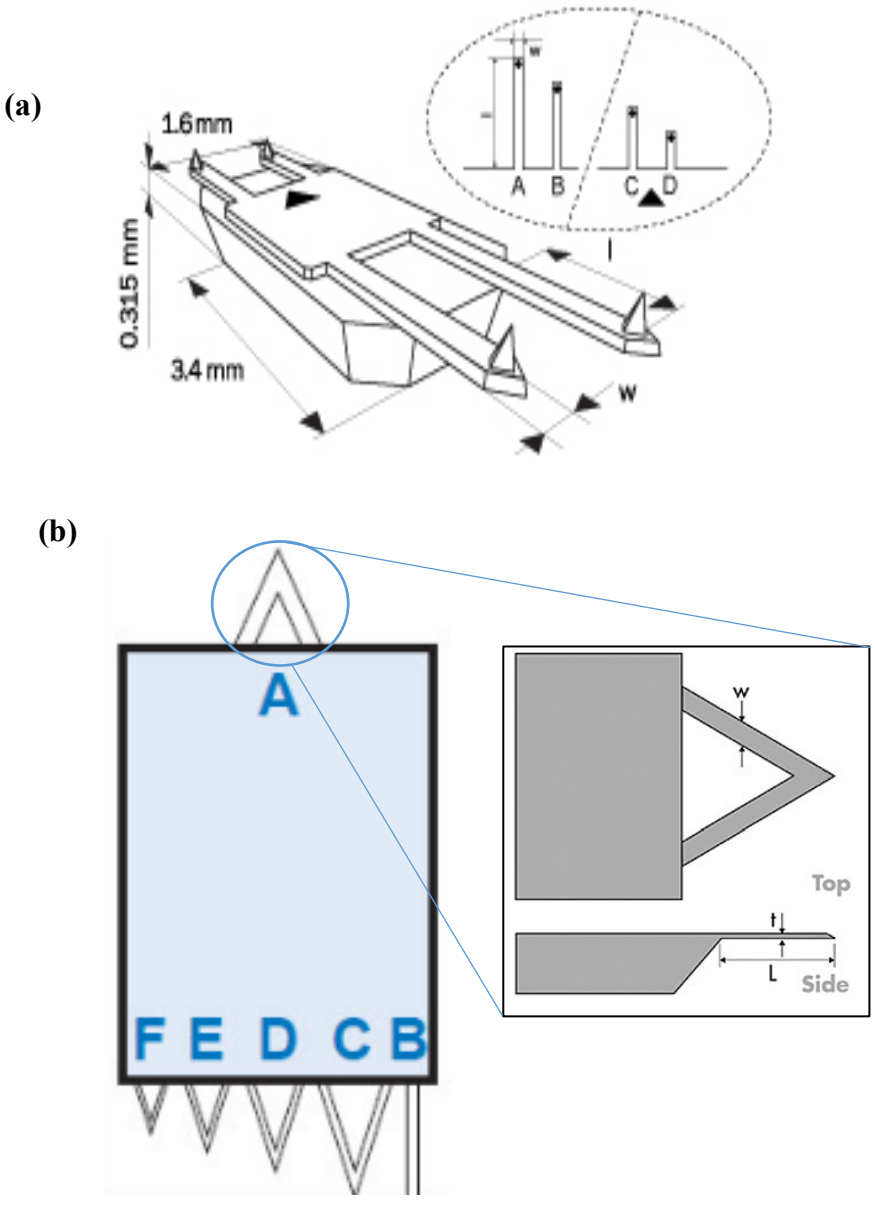

Figure 2-6 : Drawings of two types of cantilever shapes (a) schematic of four rectangular cantilevers on a chip with lengths 500, 210, 150 and 90 µm for A, B, C and D respectively and width 30 µm and thickness 2.7 µm. [43] (b) A chip has five triangular cantilevers and one rectangular cantilever with lengths 170, 200, 300, 215, 130 and 75 µm and widths 22, 20, 20, 20, 18, and 18 µm for A, B, C, D, E and F respectively and thickness 0.515 µm. [44]

In addition, the reflection of the laser beam from the back of the cantilever to the detector was taken in the account for the choice of the cantilevers;cantilevers with adequate reflection properties were chosen.

There are two factors determining the lateral resolution of the AFM image, the scanning step size and the radius of the tip. The appropriate shape and sharpness of the tip depend on the desired application, where sharpness of the tip might reach down to a few Å radius. The sharpest tips produce highest resolution, but they exert high contact pressures and thus have less durability. There are several tips available commercially to meet most of the applications needs; Figure 2-7 shows typical tips. [43-45]

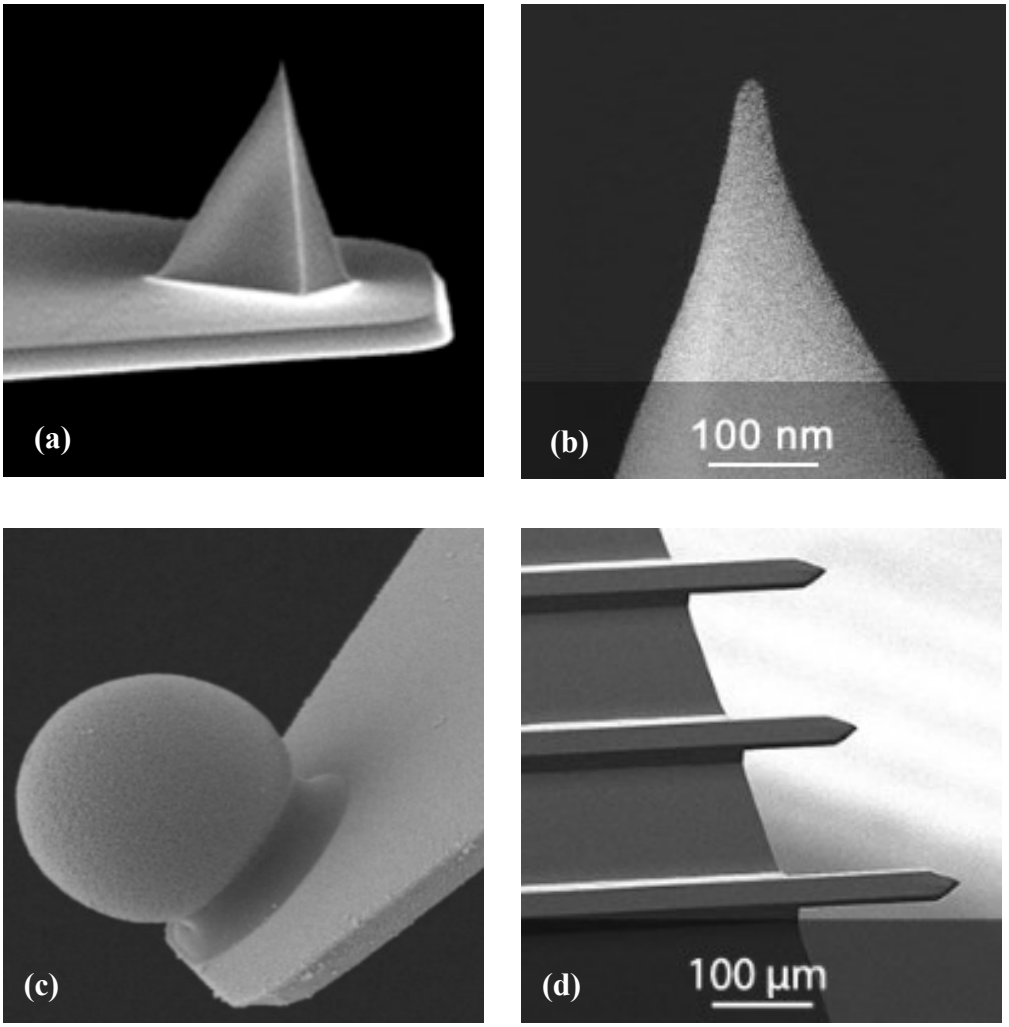

Figure 2-7: Different types of tips: (a) pyramidal tip with radius 12 nm, [44] (b) conical tip with radius 8 nm, [43] (c) colloidal probe with spherical tip (2-15 µm diameter) [45] and (d) flat cantilevers without tip (tipless). [43]

2.2.6 Limitations of AFM

The AFM technique has gained a wide attention, especially in scientific research, and it is used in many applications and to investigate most types of materials whether they are hard or soft and conductive or non-conductive. In addition, the technique is applicable in most environments, including vacuum, air or aqueous medium. However, the AFM is not a solution for all scientific problems: just as it has advantages, it sometimes has disadvantages, and other techniques are more appropriate than AFM for particular applications. Some of the advantages and disadvantages of AFM are presented briefly as follows:

- **Advantages**

  High resolution reaching to few angstroms (Å).

  High resolution force sensing reaching to few pico-Newtons (pN).

  The samples do not need special preparation.

  Measures both conductive and nonconductive materials.

  Possibility to investigate biological macromolecules and living cells.

  Investigates both hard and soft materials.

  Ability to produce the topography of the surface in three dimensions.

  Appropriate for most media.

  Reasonable price compared to other instruments or techniques.

  Small size which makes it easy to move or attach to other equipment such as an inverted optical microscope. [30, 36-38, 46-50]

- **Disadvantages**

Not appropriate to measure a large area (greater than 150x150 $(\mu m)^2$ and height 10-20 μm).

Scanning speed is relatively low compared to other techniques.

Hysteresis and creep could affect the images due to non-linearity.

The real sample topography is not exactly reflected in the image as the sharpness of the tip is not perfect; it has finite dimensions and there is convolution between the tip's shape and the surface features.

Steep or overhanging walls cannot be measured due to the nature of the AFM probes' motion. [30, 36-38, 46-50]

2.3 Microbubbles (MBs)

There has been a great deal of attention paid and great efforts in research studies toward understanding the physical and medical aspects of microbubbles (MBs). However, there appears to be a lack of research from the mechanical engineering perspective, and especially in studying their mechanical properties and understanding their response to applied loads. [51] This study will try to cover some of this gap and concentrate on studying the mechanical properties of the phospholipid microbubbles (MBs). Before investigating them, it is appropriate to give the reader a brief overview regarding MBs, including their structure, manufacture and applications.

2.3.1 Ultrasound Contrast Agents

The sound waves that have frequency above the threshold of the human ear, around 20 kHz, are called ultrasound waves. Ultrasound waves are used widely in different fields. [52] In 1968 Gramiak & Shah [53] were the first to report that small gas bubbles can enhance the ultrasound contrast. In the late 1960s, while Dr Claude Joyner, [54] was studying the cardiac results of a patient during a routine diagnosis, he coincidently realized that the ultrasound signal increased directly after the injection of a dye into the ventricle. This phenomenon was interpreted, as Gramiak and Shah suggested, [55, 56] as being due to the effect of gas bubbles which were forming at the tip of the needle at the moment of injection. Since that accidental discovery, MBs have been widely used as ultrasound contrast agents (UCAs). However, the life of an air bubble is very short if it is introduced without a stabilizing shell. Therefore, the researchers developed methods of stabilizing the gas-liquid interface. At the same time, they introduced gases with low diffusivity, such as a perfluorocarbon or sulphur hexafluoride, to increase the microbubble's circulation time. [57] Reflecting or scattering of the ultrasound wave helps improve ultrasound imaging. The improvement comes from the difference between the density of the gas inside the MBs and the densities of the surrounding tissues and blood. This means the ultrasound waves move through the gas much more slowly than through the other media because of their low density, which makes the images clearer and creates more contrast, resulting from the acoustic impedance mismatch between the MBs and the surrounding materials. [51, 58] New generations of MBs were developed with more effective MB stabilisers, such

as a phospholipid shell, which is more flexible and more resistant to rupture than other coatings, such as albumin. [59, 60]

2.3.2 Structure of Phospholipid MBs

The material of the nanoparticle shell is commonly composed of surfactants, proteins, polymers, lipids, metals, a virus-based nanoparticle or a combination of these materials. [58, 61] The most desirable nanomedicine systems are the liposome particles. These are colloidal and self-assembling structures containing a mono- or bilayer lipids. SonoVue microbubbles, which were investigated in this study, are monolayer lipid microbubbles (MBs). [52, 62, 63] Phospholipids are typically found in biological components such as the cell membranes. A phospholipid molecule consists of the head group, which is hydrophilic, and two long tails, which are hydrophobic, connected to the head. The components of the hydrophilic head are the glycerol molecule and the phosphate group, while hydrophobic (tail) component consists of a long chain of fatty acids, for example hydro or fluorocarbon chains. The phospholipids can organize themselves so that the hydrophobic tails face the gas region while the hydrophilic heads face toward the water. Figure 2-8 shows a schematic of phospholipid microbubbles (MBs) in both monolayer and bilayer forms, and the phospholipid molecule components. [64]

The hydrophobic tails play a significant role in the MBs' properties, where altering of hydrocarbon chain length affects properties such as surface viscosity, surface tension, gas permeation resistance and buckling stability of the shell. The presence of poly ethylene glycol (PEG) groups, which are long chains of molecules, on the phospholipid MB shells is common. These long chains point out of the MB shell surface either in

the form of a brush or a mushroom layer, which creates an extra zone of several Angstroms (Å) thickness on the MB shell. [65]

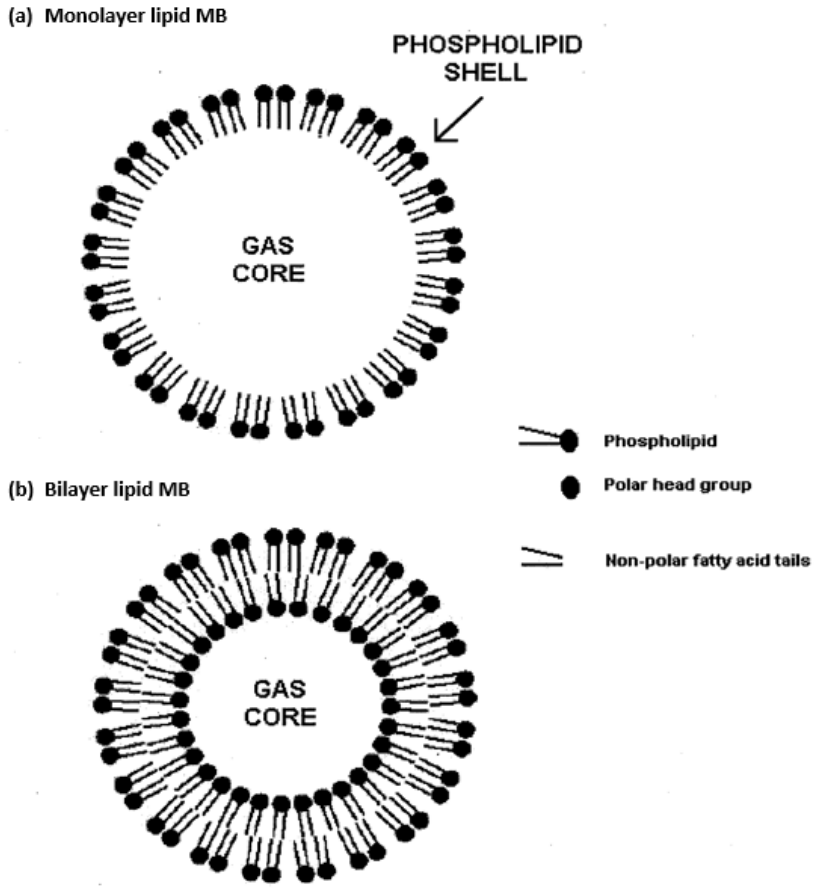

Figure 2-8: Representing both types of lipid MBs, the monolayer and the bilayer MBs and the phospholipid molecule components which are the hydrophilic (head) and hydrophobic (tail) where the diameter is at the micrometre scale and the shell thickness at nanometre scale. Adopted from [64]

2.3.3 Microbubble Production

There are several methods to generate and produce microbubbles (MBs); however, the most commonly used methods are sonication or microfluidic processing. The sonication method is used widely in the manufacture of commercial phospholipid MBs as ultrasound contrast agents (UCA). This method uses ultrasound waves with high intensity to encourage the formation of gas MBs in the suspension material which is intended to be a coating of the MBs, in the present case phospholipids. [66-68] The phospholipids arrange themselves as a coating (self-assemble), once the gas MBs appear. The excess phospholipids are washed off to clean the coated MBs. Subsequently, the MBs are re-suspended in another liquid, typically in saline solution, to be ready for use. This technique produces MBs of various sizes which depend on the applied ultrasound pulse. The patient might suffer an embolism due to large diameter MBs, therefore these must be filtered out. [69]

The second method, known as the microfluidic technique, was proposed by Thorsen et al. [70] in 2001. This method produces a very narrow size distribution of MBs. The technique includes a T-junction where the gas flow meets the liquid flow at a certain pressure and flow rate, where the gas produces a jet surrounded by the liquid. When the gas jet passes the meeting point by a certain distance, the gas-liquid interface becomes unstable, which forms MBs by a “pinch-off” process. [71] Another mechanism for this technique, similar to the T-junction, is called the flow-focusing junction which first appeared in 2001. [72, 73] While the discrete phase is injected perpendicular to the continuous phase in the T-junction, it is injected into a co-flowing

continuous phase in the flow-focusing junction. Figure 2-9 shows the set-up equipment of the T-junction method in (a), adopted from [74] , and the two mechanisms of the microfluidic technique which are the T-junction, in (b), and the flow-focusing junction, in (c), obtained from [75]. There are different regimes of T-junction and flow-focusing junction techniques, such as dripping, squeezing and jetting regimes, depending on the desired MB sizes, where they are larger with the dripping regime and smaller with the jetting regime. Figure 2-10 represents the dripping and jetting regimes for T-junction and flow-focusing junction techniques which are obtained from Elveflow® web page. [76]

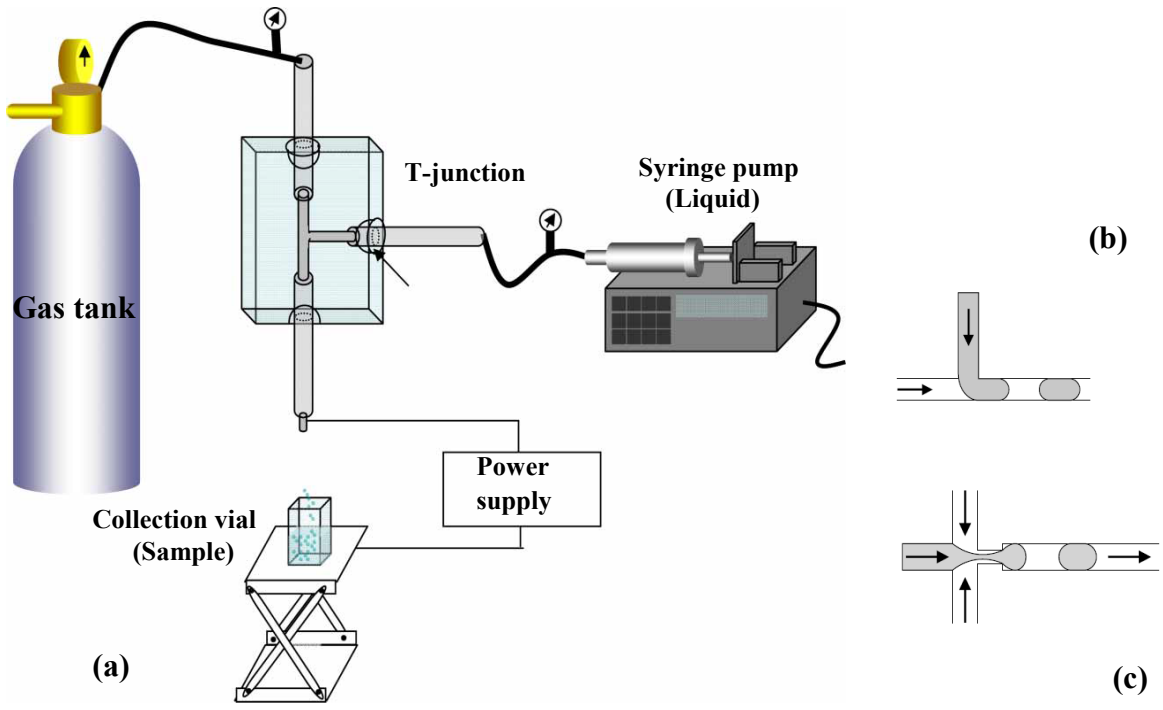

Figure 2-9: (a) Schematic representation of the equipment set-up for the generation of microbubbles by the specially designed T-junction. (b) Schematic of a T-junction. The discrete phase is injected perpendicular to the continuous phase and is sheared off to produce droplets where the width of the input and output channels is 100 µm. (c) Schematic of a flow-focusing junction. The discrete phase is injected into a co-flowing continuous phase. At the flow-focusing junction, there can be a narrow constriction to focus the flow (the width at the flow-focusing constriction ranges from 25 to 50 µm). Images obtained from [74] and [75].

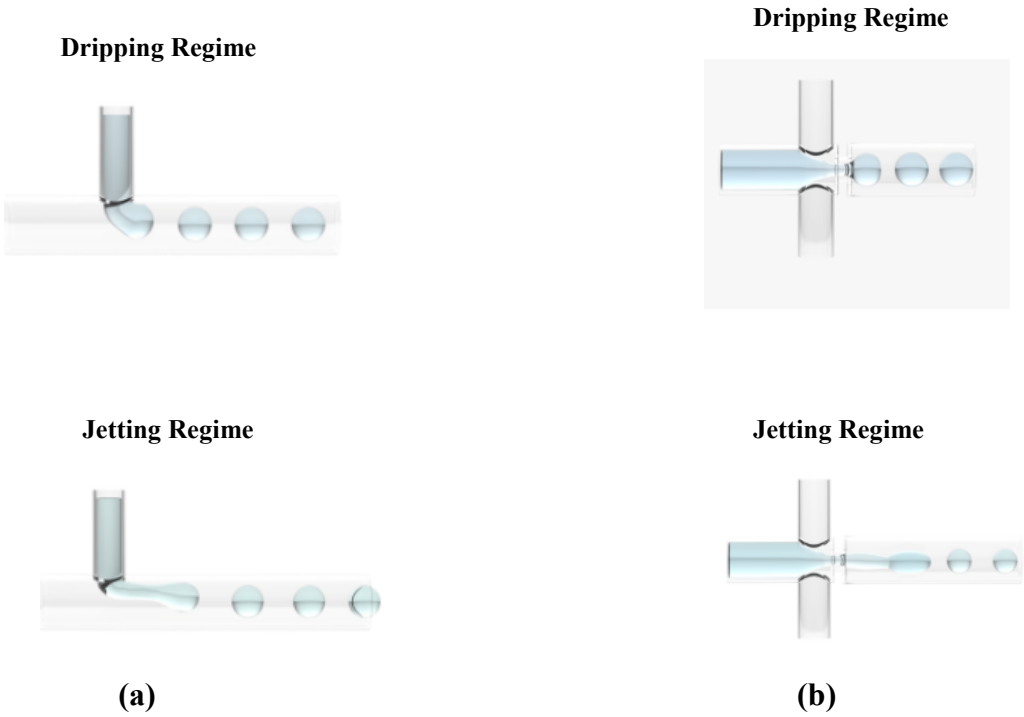

Figure 2-10: (a) Showing the dripping and the jetting regimes in the T-junction technique where dimensions of the input and output are 30 µm and 60 µm, respectively and (b) flow-focusing junction technique where dimension of input and output is 200 µm. [76]

2.3.4 Microbubble Applications

In the last decades, microbubble technologies have gained a great attention because of their wide applications in several science and technology fields. [77] A variety of research disciplines have focused on microbubbles, since they have different applications such as encapsulation of fragrances and flavours in food products, the fabrication of lightweight materials, water treatment and cosmetics. [77-83] However, the most important application of the microbubbles is in the medical field. They are widely used in both diagnostic and therapeutic medical applications.

- **Diagnostic Applications**

The most common imaging method in medical applications is ultrasound imaging. Sound moves faster in liquids or solids than in gas. Thus the slow speed of sound through microbubbles (gas) produces an acoustic impedance mismatch between blood and the tissue surrounding the microbubble. [58] The difference in the speed comes from the difference in the density, which is lower in gas than in a liquid or solid. This property of low density of MBs has helped to develop a number of potential medical applications, and microbubbles are now commonly used as ultrasound contrast agents (UCAs) to improve the diagnostic ultrasound imaging, where the images using UCAs are more visible and clearer than the images without them. They are used in cardiology and radiology, where they are used for visualizing tumours, giving a good ultrasound imaging of areas of tissue which have defects, and are used in imaging certain human organs, such as the liver and the heart. [84]

- **Therapeutic Applications**

An even more important use of the microbubbles than the diagnostic uses is their use in treatment. [85] After administering the drug orally or by systemic injection, it is expected to travel through the bloodstream and cross the capillary walls to its target. [63] Therefore, when the drug is free, the healthy tissues could be damaged, during the treatment process, due to side effects, such as the high level of toxicity of the drug. [63, 86, 87] In addition, the medicine will need to be given in a high dose, to ensure that the drug reaches the target tissues, because some of the amount of the drug administered will be received by the healthy tissues, where it is unneeded. To

overcome these problems which accompany the therapeutic process when using free drugs, researchers have developed methods to deliver the drugs to the target cells to reduce the side effects of the medicine and to give the correct and the accurate dose of the drug. The method involves encapsulating the medicine in a drug carrier (drug delivery) such as lipid MBs to perform this task and to reduce the side effects compared to those from the free drug treatment. [88, 89]

- **Drug/gene delivery**

Because both hydrophilic and lipophilic drug molecules can be carried by liposome MBs, the lipid MBs are used widely in the medical applications for drug/gene delivery. Lipid-based microbubbles are easy to break and highly favourable to design as carriers, because of their response when they are exposed to ultrasonic waves. However, their capacity to act as a carrier of the drugs is low and this limitation can be dramatically improved using layer-by-layer assembly or chemically linking to the microbubble surface lipid carriers. The microbubble has a diameter less than 10 μm, which is similar to the size of a red blood cell. This allows the MBs to be displayed as red blood cells in the micro vessels and capillaries throughout the body in the blood stream. [61, 90] Most of the particle's volume is the gas core, which provides the mechanism for drug/gene delivery and the ultrasound backscatter. Drugs and genes can be delivered by ultrasound microbubbles which work as a "cavitation nuclei" to drive the drugs or genes to their targets. [58, 61, 84, 85, 91, 92], as shown in Figure 2-11, adopted from Unger et al. [58]. The loading strategies of the drugs can be into or onto the MBs. [58, 61] The activity of the microbubbles when exposed to ultrasonic waves is a key to their success as drug delivery vehicles, where the core gas contracts

during the compression phase and expands during the rarefaction phase of the pressure wave. [93]

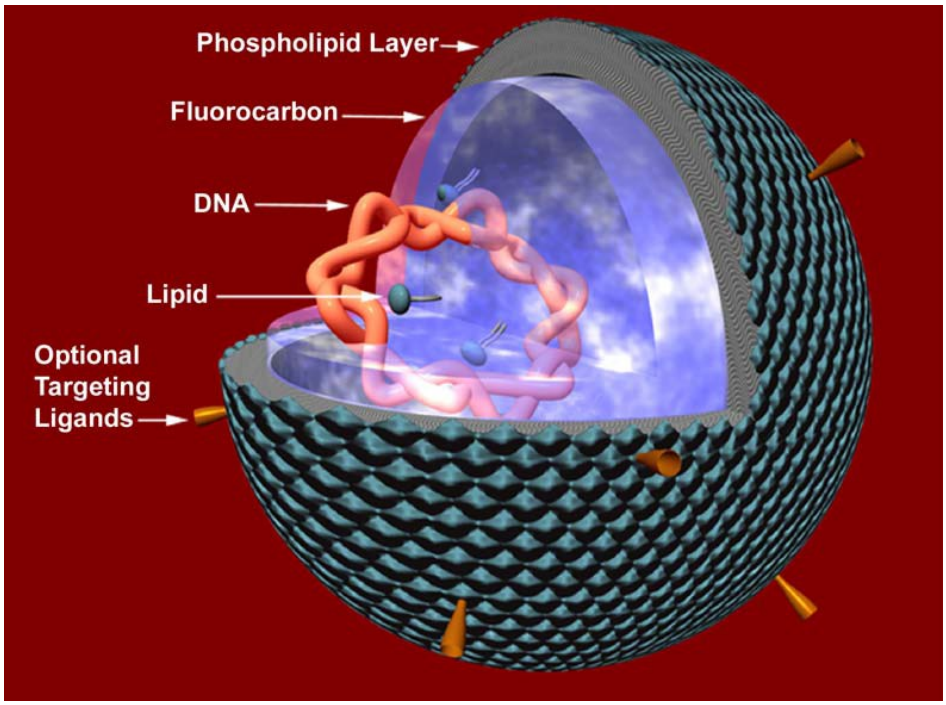

Figure 2-11: Illustrating Liquid perfluorocarbon gene carrier with diameter about 100-200 nm. [58]

- **Advantages of Using PEG on MBs**

Poly (ethylene glycol) (PEG) is widely used on the outside of the MB shell to improve their dispersion properties and also to impart stealth properties so that they can be used as biomedical delivery vehicles. The MB lifetime and the whole MB mechanical response can be improved by the use of PEG as the outer layer. According to Abou-saleh et al., the maximum MB concentration (abundance) and stability (lifetime) can be optimized by the use of a PEG-lipid at low concentration. [94] Moreover, for tissue targeting applications, lipid-shelled MBs can be functionalized on the outer surface by various targeting ligands linked to active terminal groups

incorporated in the PEG molecules. PEG can improve the drug bioavailability, prolong the circulation time and reduce undesirable side effects. Furthermore, by introducing specific ligands they can provide targeting capacity to MBs to a specific cell or tissue and the intracellular localization in organelles. [95] A large variety of biomolecules are separated using PEG components in aqueous two-phase partition systems (ATPS). [96]

2.4 Hydrogels

Hydrogels are polymer networks which are exceedingly swollen with water. Hydrogels which are referred to as hydrophilic gels are those which have networks of polymeric chains. Hydrogels can be also based on colloidal systems (colloidal gels) where water is the dispersion medium. [97, 98] There are different definitions of hydrogels. The most common one defines the hydrogels as water-swollen, produced by the simple reaction of one or more monomers, and with cross-linked polymeric networks. Another definition says that the hydrogels are polymeric materials that have the ability to swell and retain a large amount of water inside their structure; however they do not dissolve in water.[98] In recent years, synthetic hydrogels have progressively superseded natural hydrogels, as synthetic hydrogels have a high water absorption capacity, long service life and high gel strength. Furthermore, they remain stable with strong or sharp fluctuations of temperature.

Hydrogels are capable of absorbing large quantities of water because of their hydrophilic crosslinked polymeric network structure. [99] They are multifunctional materials which are used in different applications, e.g. vehicles for drug delivery,

scaffolds for tissue engineering, contact lenses, biosensors and cosmetic products.[100-104] Because of their high nontoxicity, hydrophilicity and biocompatibility, hydrogels are widely used in the biomedical and biological areas. [105-107] When they are fully hydrated, hydrogels can acquire the physical characteristics similar to those of soft tissues, [108], and they accelerate the healing process of wounds, when they are partially hydrated. [109] The formation of three-dimensional scaffolds consisting of extracellular matrix (ECM) molecules can be obtained by hydrogel engineering. These engineered hydrogels are capable of providing the cells with structural support, adhesion and biomechanical properties. [99] The wide mismatch between the supply and demand of organs and tissues for transplantation illustrates the necessity of tissue engineering. [110] To meet the massive need for organs and tissues, the tissue engineering field was developed to fabricate living replacement parts for the human body. [110-112]

2.4.1 Classification of the Hydrogels

The hydrogels are classified on various bases such as source, polymeric composition, configuration, type of cross-linking, physical appearance and network electrical charge. The classifications can be summarized as follow:

Based on the source

Natural hydrogels.

Synthetic hydrogels**.**

Based on their polymeric composition

Homopolymeric hydrogels (single species of monomer).

Copolymeric hydrogels (two or more different monomer species).

Interpenetrating polymeric hydrogel (IPN) (two independent cross-linked synthetic and/or natural polymer component).

Based on their configuration

Amorphous (non-crystalline).

Semi-crystalline.

Crystalline.

Based on the type of cross-linking

Chemical cross-linked networks.

Physical cross-linked networks.

Based on their physical appearance

Matrix.

Film.

Microsphere.

Based on the network's electrical charge

Nonionic (neutral).

Ionic.

Amphoteric electrolyte.

Zwitterionic. [98, 113-117]

2.4.2 Applications of Hydrogels

Once articular cartilage is damaged, it is difficult to heal naturally and not easy to repair. However, tissue engineering with scaffolds of hydrogels is being developed

to overcome this challenge. Because hydrogels mimic the collagen networks of the cartilage by containment of highly hydrated crosslinked networks, they are employed to treat the cartilage defects and to support the neocartilage regeneration and the chondrocyte proliferation. [113] In addition to the applications mentioned previously, there are many more applications for which hydrogels can be used. Since the first synthetic hydrogels were produced in 1954 by Wichterle and Lim, [118] they have become widely used in several fields. They are applicable in scientific and technical areas such as agriculture, hygienic products, drug delivery systems, coal dewatering, sealing, food additives, artificial snow, biomedical applications, pharmaceuticals, diagnostics, tissue engineering, separation of biomolecules or cells, wound dressing, biological adhesions and as biosensors. [98, 119-131]

2.4.4 Preparation of the Hydrogels

As defined earlier, a hydrogel is a polymer network with hydrophilic properties; thus, the hydrogels are prepared based on hydrophilic monomers which can also be used to control the properties of the hydrogels to make them suitable for certain applications. Either synthetic polymers or natural polymers can be used to prepare the hydrogels. The synthetic polymers are chemically stronger than natural polymers and they are hydrophobic in nature. They have a slow degradation rate, due to their mechanical strength; however, the mechanical strength leads to high durability. By using the optimal design, these two opposite properties, when they are used in some applications, can be balanced to produce an appropriate hydrogel. [132] Hydrogels might also be prepared based on the natural polymers, where suitable functional groups are added to these natural polymers. [133] Put simply, to produce an elastic structure

we need to use a hydrophilic polymeric network that is cross-linked in some way. Thus, any technique that can produce a cross-linked polymer can help to produce a hydrogel. By reacting hydrophilic monomers with multifunctional cross-linkers, hydrogels can be produced using copolymerization/cross-linking free-radical polymerizations.

Hydrogels of natural or synthetic origin may be formed using a number of methods:

- Linking polymer chains by chemical reactions.
- The main-chain free radicals can be generated using ionizing radiation.
- By physical interactions e.g. electrostatics, entanglements and crystallite formation.

Any technique for polymerization might be used to produce the hydrogels, including solution, bulk and suspension polymerization.

2.5 References

1. Hansma, H.G. and L. Pietrasanta, *Atomic force microscopy and other scanning probe microscopies.* Current opinion in chemical biology, 1998. **2**(5): p. 579-584.

2. Allison, D.P., Mortensen, N. P., Sullivan, C. J. and M. J. Doktycz, *Atomic force microscopy of biological samples.* Wiley Interdisciplinary Reviews: Nanomedicine and Nanobiotechnology, 2010. **2**(6): p. 618-634.

3. Aikawa, M., *Studies on falciparum malaria with atomic-force and surface-potential microscopes.* Annals of Tropical Medicine & Parasitology, 1997. **91**(7): p. 689-692.

4. McLean, R.S., M. Doyle, and B.B. Sauer, *High-resolution imaging of ionic domains and crystal morphology in ionomers using AFM techniques.* Macromolecules, 2000. **33**(17): p. 6541-6550.

5. Mou, J., Czajkowsky, D. M., Zhang, Y. and Z. Shao, *High-resolution atomic-force microscopy of DNA: the pitch of the double helix.* FEBS Letters, 1995. **371**(3): p. 279-282.

6. Wadu-Mesthrige, K., Amro, N. A., Garno, J. C., Cruchon-Dupeyrat, S. and G. Liu, *Contact resonance imaging — a simple approach to improve the resolution of AFM for biological and polymeric materials.* Applied Surface Science, 2001. **175–176**: p. 391-398.

7. Alton, P., *Atomic Force Microscopy*. 2010, New York, USA: Oxford University Press.

8. Bottomley, L.A., J.E. Coury, and P.N. First, *Scanning probe microscopy.* Analytical Chemistry, 1996. **68**(12): p. 185-230.

9. Ikai, A., *STM and AFM of bio/organic molecules and structures.* Surface Science Reports, 1996. **26**(8): p. 261-332.

10. Frommer, J., *Scanning tunneling microscopy and atomic force microscopy in organic chemistry.* Angewandte Chemie International Edition in English, 1992. **31**(10): p. 1298-1328.

11. Ellul, M.D., A.H. Tsou, and W. Hu, *Crosslink densities and phase morphologies in thermoplastic vulcanizates.* Polymer, 2004. **45**(10): p. 3351-3358.

12. Vinckier, A. and G. Semenza, *Measuring elasticity of biological materials by atomic force microscopy.* FEBS letters, 1998. **430**(1-2): p. 12-16.

13. Burnham, N.A. and R.J. Colton, *Measuring the nanomechanical properties and surface forces of materials using an atomic force microscope.* Journal of Vacuum Science & Technology A: Vacuum, Surfaces, and Films, 1989. **7**(4): p. 2906-2913.

14. Han, Y., S. Schmitt, and K. Friedrich, *Nanoscale indentation and scratch of short carbon fiber reinforced PEEK/PTFE composite blend by atomic force microscope lithography.* Applied Composite Materials, 1999. **6**(1): p. 1-18.

15. Wilson, C., *The invisible world: early modern philosophy and the invention of the microscope*. Vol. 228. 1995: Princeton.

16. Shmaefsky, B., *Biotechnology 101*. 2006: Greenwood Publishing Group.

17. Braga, P.C. and D. Ricci, *Atomic Force Microscopy: Biomedical Methods and Applications*. 2004, USA: Humana Press Inc.

18. Von Ardenne, M., *Improvements in electron microscopes.* British patent, 1937(511204).

19. Thoss, A. and M. Pfeffer, *New microscopes push the limits of far field microscopy.* Advanced Optical Technologies, 2013. **2**(3): p. 209-210.

20. Binnig, G., Rohrer, H., Gerber,Ch. and E. Weibel, *Surface studies by scanning tunneling microscopy.* Physical review letters, 1982. **49**(1): p. 57-61.

21. Binnig, G. and H. Rohrer, *Scanning Tunneling Microscopy—from Birth to Adolescence (Nobel Lecture.* Angewandte Chemie International Edition in English, 1987. **26**(7): p. 606-614.

22. Binnig, G., Quate, C.F. and Gerber, Ch., *Atomic Force Microscope.* Physical review letters, 1986. **56**(9): p. 930-934.

23. Bennig, G.K., *Atomic force microscope and method for imaging surfaces with atomic resolution*. 1988, International Businas Machines Corporation, Armonk, N.Y., USA, United States Patent. p. 1-8.

24. Binnig, G.K., *Atomic force microscope and method for imaging surfaces with atomic resolution*. 1990, International Businas Machines Corporation, Armonk, N.Y., USA, United States Patent. p. 1-8.

25. Engel, A., Lyubchenko, Y. and D. Müller, *Atomic force microscopy: a powerful tool to observe biomolecules at work.* Trends in cell biology, 1999. **9**(2): p. 77-80.

26. Morris, J.K., *Mechanical properties of phospholipid coated microbubbles*. 2014, The University of Edinburgh: UK, PhD thesis. p. 157.

27. Baclayon, M., Wuite, G. and W. Roos, *Imaging and manipulation of single viruses by atomic force microscopy.* Soft Matter, 2010. **6**(21): p. 5273-5285.

28. Kuznetsov, Y.G. and A. McPherson, *Atomic force microscopy in imaging of viruses and virus-infected cells.* Microbiology and molecular biology reviews, 2011. **75**(2): p. 268-285.

29. DeGraw, Y., *Molecular Force Probe (MFP) Installation and Startup Guide*. 2000, Asylum Research, Inc.

30. Butt, H.-J., Cappella, B. and M. Kappl, *Force measurements with the atomic force microscope: Technique, interpretation and applications.* Surface science reports, 2005. **59**(1): p. 1-152.

31. Ahmad, A., Schuh, A. and I.W. Rangelow, *Adaptive AFM scan speed control for high aspect ratio fast structure tracking.* Review of Scientific Instruments, 2014. **85**(10): p. 103706-103711.

32. Alessandrini, A. and P. Facci, *AFM: a versatile tool in biophysics.* Measurement science and technology, 2005. **16**(6): p. R65-R92.

33. Dokukin, M.E. and I. Sokolov, *Quantitative mapping of the elastic modulus of soft materials with HarmoniX and PeakForce QNM AFM modes.* Langmuir, 2012. **28**(46): p. 16060-16071.

34. Tello, M. and R. García, *Nano-oxidation of silicon surfaces: Comparison of noncontact and contact atomic-force microscopy methods.* Applied Physics Letters, 2001. **79**(3): p. 424-426.

35. Howland, R., Benatar, L. and P.S. Instruments, *A practical guide to scanning probe microscopy*. 1997: Park Scientific Instruments.

36. Meyer, E., *Atomic force microscopy.* Progress in surface science, 1992. **41**(1): p. 3-49.

37. Donno, R., *Nanomechanical characterisation of cells and biocompatible substrates*. 2014, University of Manchester: UK, PhD thesis. P. 258

38. Kalloudis, M., *Thin polymer films of block copolymers and blend/nanoparticle composites.* 2013, The University of Edinburgh: UK, PhD thesis. p. 198.

39. Burnham, N.A., Colton, R.J. and H.M. Pollock, *Interpretation issues in force microscopy.* Journal of Vacuum Science & Technology A: Vacuum, Surfaces, and Films, 1991. **9**(4): p. 2548-2556.

40. Vinogradova, O.I., Butt, H., Yakubov, G. E. and F. Feuillebois, *Dynamic effects on force measurements. I. Viscous drag on the atomic force microscope cantilever.* Review of scientific instruments, 2001. **72**(5): p. 2330-2339.

41. Hoh, J.H. and A. Engel, *Friction effects on force measurements with an atomic force microscope.* Langmuir, 1993. **9**(11): p. 3310-3312.

42. Müller, D.J. and A. Engel, *Conformations, flexibility, and interactions observed on individual membrane proteins by atomic force microscopy.* Methods Cell Biol, 2002. **68**: p. 257-299.

43. Mikromasch. *Mikromasch* https://www.spmtips.com/afm-tip-hq-xsc11-no-al]. February, 2017.

44. Bruker AFM Probes. *Bruker AFM Probes*. http://www.brukerafmprobes.com/p-3719-mlct-o10.aspx]. February, 2017

45. NanoAndMore GmbH. *NanoAndMore GmbH*. https://www.nanoandmore.com/AFM-Probe-CP-PNP-SiO.html]. February, 2017

46. *Machinemakers*. [http://machinemakers.typepad.com/machine-makers/advantages-and-disadvantages-of-atomic-force-microscopy.html]. February, 2017

47. Christina, P. *Atomic Force Microscopy*. [http://www.e21.ph.tum.de/uploads/media/Atomic_Force_Psylla.pdf]. February, 2017

48. Eaton, P., Fernandes, J.C., Pereira, E., Pintado, M.E. and F.X. Malcata, *Atomic force microscopy study of the antibacterial effects of chitosans on Escherichia coli and Staphylococcus aureus.* Ultramicroscopy, 2008. **108**(10): p. 1128-1134.

49. Kuznetsov, Y.G., Malkin, A. J., Lucas, R. W., Plomp, M. and A. McPherson, *Imaging of viruses by atomic force microscopy.* Journal of General Virology, 2001. **82**(9): p. 2025-2034.

50. Czajkowsky, D.M., H. Iwamoto, and Z. Shao, *Atomic force microscopy in structural biology: from the subcellular to the submolecular.* Journal of electron microscopy, 2000. **49**(3): p. 395-406.

51. Sboros, V., *Response of contrast agents to ultrasound.* Advanced drug delivery reviews, 2008. **60**(10): p. 1117-1136.

52. Finnøy, A., *Acoustic and Mechanical Properties of Microbubbles Stabilized by Polymeric Nanoparticles*. 2013, Norwegian University of Science and Technology. p. 94.

53. Gramiak, R. and P.M. Shah, *Echocardiography of the aortic root.* Investigative radiology, 1968. **3**(5): p. 356-366.

54. Feigenbaum, H., Stone, J. M., Lee, D. A., Nasser, W. K. And S. Chang, *Identification of Ultrasound Echoes from the Left Ventricle by Use of Intracardiac Injections of Indocyanine Green.* Circulation, 1970. **41**(4): p. 615-621.

55. Kremkau, F., Gramiak, R., Carstensen, E., Shah, P. and D. Kramer, *Ultrasonic Detection of Cavitation at Catheter Tips.* Investigative Radiology, 1971. **6**(4): p. 293-293.

56. Kremkau, F.W., Gramiak, R., Carstensen, E. L., Shah, P.M. and D. H. Kramer, *Ultrasonic detection of cavitation at catheter tips.* The Journal of the Acoustical Society of America, 1969. **45**(1): p. 340-340.

57. Ferrara, K., R. Pollard, and M. Borden, *Ultrasound microbubble contrast agents: fundamentals and application to gene and drug delivery.* Annu. Rev. Biomed. Eng., 2007. **9**: p. 415-447.

58. Unger, E.C., Porter, T., Culp, W., Labell, R., Matsunaga, T. and R. Zutshi, *Therapeutic applications of lipid-coated microbubbles.* Advanced drug delivery reviews, 2004. **56**(9): p. 1291-1314.

59. Stride, E. and N. Saffari, *On the destruction of microbubble ultrasound contrast agents.* Ultrasound in medicine & biology, 2003. **29**(4): p. 563-573.

60. Borden, M.A., Kruse, *D. E.,* Caskey, C. F., Zhao, S., Dayton, P. A. and K. W. Ferrara, *Influence of lipid shell physicochemical properties on ultrasound-induced microbubble destruction.* IEEE transactions on ultrasonics, ferroelectrics, and frequency control, 2005. **52**(11): p. 1992-2002.

61. Sirsi, S. and M. Borden, *Microbubble compositions, properties and biomedical applications.* Bubble Science, Engineering & Technology, 2009. **1**(1-2): p. 3-17.

62. Steichen, S.D., M. Caldorera-Moore, and N.A. Peppas, *A review of current nanoparticle and targeting moieties for the delivery of cancer therapeutics.* European Journal of Pharmaceutical Sciences, 2013. **48**(3): p. 416-427.

63. Afadzi, M., *Delivery of Encapsulated Drugs to Cancer Cells and Tissue: The Impact of Ultrasound*. 2013, PhD thesis, Norwegian University of Science and Technology. p. 141

64. Wu, H., *Custom-formulated phospholipid microbubbles and methods and uses thereof*. 2011, Patent Application Publication: USA. p. 10.

65. Needham, D. and D.H. Kim, *PEG-covered lipid surfaces: bilayers and monolayers.* Colloids and Surfaces B: Biointerfaces, 2000. **18**(3): p. 183-195.

66. Zhao, Y., Liang, H., Mei, X. And M. Halliwell, *Preparation, characterization and in vivo observation of phospholipid-based gas-filled microbubbles containing hirudin.* Ultrasound in Medicine & Biology, 2005. **31**(9): p. 1237-1243.

67. Christiansen, C., Kryvi, H., Sontum, P. and T. Skotland, Physical and biochemical characterization of Albunex, a new ultrasound contrast agent

consisting of air-filled albumin microspheres suspended in a solution of human albumin. Biotechnology and applied biochemistry, 1994. **19**(3): p. 307-320.

68. Unger, E.C., Mccreery, T. P., Sweitzer, R. H., Caldwell, V. E. And Y. Wu, Acoustically active lipospheres containing paclitaxel: a new therapeutic ultrasound contrast agent. Investigative radiology, 1998. **33**(12): p. 886-892.

69. Stride, E. and M. Edirisinghe, Novel microbubble preparation technologies. Soft matter, 2008. **4**(12): p. 2350-2359.

70. Thorsen, T., Roberts, R. W., Arnold, F. H., and S. R. Quake, Dynamic pattern f ormation in a vesicle-generating microfluidic device. Physical review letters, 2001. **86**(18): p. 4163-4166.

71. Pancholi, K., E. Stride, and M. Edirisinghe, *Dynamics of bubble formation in highly viscous liquids.* Langmuir, 2008. **24**(8): p. 4388-4393.

72. Gañán-Calvo, A.M. and J.M. Gordillo, *Perfectly monodisperse microbubbling by capillary flow focusing.* Physical review letters, 2001. **87**(27): p. 274501-274504.

73. Ganán-Calvo, A.M., *Perfectly monodisperse microbubbling by capillary flow focusing: An alternate physical description and universal scaling.* Physical Review E, 2004. **69**(2): p. 027301-027303.

74. Pancholi, K., E. Stride, and M. Edirisinghe, *Generation of microbubbles for diagnostic and therapeutic applications using a novel device.* Journal of drug targeting, 2008. **16**(6): p. 494-501.

75. Sullivan, M.T. and H.A. Stone, *The role of feedback in microfluidic flow-focusing devices.* Philosophical Transactions of the Royal Society of London A: Mathematical, Physical and Engineering Sciences, 2008. **366**(1873): p. 2131-2143.

76. Elveflow. *Microfluidic*. http://www.elveflow.com/microfluidic-tutorials/microfluidic-reviews-and-tutorials/digital-microfluidics-microfluidic-droplet-emulsion-science/]. February, 2017

77. Agarwal, A., W.J. Ng, and Y. Liu, *Principle and applications of microbubble and nanobubble technology for water treatment.* Chemosphere, 2011. **84**(9): p. 1175-1180.

78. Arakawa, T., Yamamoto, T. and S. Shoji, *Micro-bubble formation with organic membrane in a multiphase microfluidic system.* Sensors and Actuators A: Physical, 2008. **143**(1): p. 58-63.

79. Böhmer, M.R., Klibanov, A. L., Tiemann, K., Hall, C. S., Gruell, H. and O. C. Steinbach, *Ultrasound triggered image-guided drug delivery.* European Journal of Radiology, 2009. **70**(2): p. 242-253.

80. Chapuis, J., Schmaltz, R.M., Tsosie, K. S., Belohlavek, M. and S. M. Hecht, *Carbohydrate Dependent Targeting of Cancer Cells by Bleomycin−Microbubble Conjugates.* Journal of the American Chemical Society, 2009. **131**(7): p. 2438-2439.

81. De Jong, N., A. Bouakaz, and P. Frinking, *Basic acoustic properties of microbubbles.* Echocardiography, 2002. **19**(3): p. 229-240.

82. Klibanov, A., *Ultrasound Contrast Agents: Development of the Field and Current Status*, in *Contrast Agents II*, W. Krause, Editor. 2002, Springer Berlin Heidelberg. p. 73-106.

83. Lum, A.F.H., Borden, M. A., Dayton, P. A., Kruse, D. E., Simon, S. I. and K. W. Ferrara, *Ultrasound radiation force enables targeted deposition of model drug carriers loaded on microbubbles.* Journal of Controlled Release, 2006. **111**(1–2): p. 128-134.

84. Blomley, M.J., Cooke, J. C., Unger, E. C., Monaghan, M. J. and D. O. Cosgrove, *Microbubble contrast agents: a new era in ultrasound.* British Medical Journal, 2001. **322**(7296): p. 1222-1225.

85. Wu, Y., Unger, E. C., McCREERY, T. P., Sweitzer, R. H., Shen, D., Wu, G. and M. D. Vielhauer, *Binding and lysing of blood clots using MRX-408.* Investigative radiology, 1998. **33**(12): p. 880-885.

86. Drummond, D.C., Meyer, O., Hong, K., Kirpotin, D. B. and D. Papahadjopoulos, *Optimizing liposomes for delivery of chemotherapeutic agents to solid tumors.* Pharmacological reviews, 1999. **51**(4): p. 691-744.

87. Speth, P., Q. Van Hoesel, and C. Haanen, *Clinical pharmacokinetics of doxorubicin.* Clinical pharmacokinetics, 1988. **15**(1): p. 15-31.

88. Gabizon, A. and F. Martin, *Polyethylene glycol-coated (pegylated) liposomal doxorubicin.* Drugs, 1997. **54**(4): p. 15-21.

89. Mayer, L.D., Tai, L. C., Ko, D. S., Masin, D., Ginsberg, R. S., Cullis, P. R. and M. B. Bally, *Influence of vesicle size, lipid composition, and drug-to-lipid ratio on the biological activity of liposomal doxorubicin in mice.* Cancer Research, 1989. **49**(21): p. 5922-5930.

90. Lindner, J.R., Song, J., Jayaweera, A. R., Sklenar, J. and S. Kaul, *Microvascular rheology of Definity microbubbles after intra-arterial and intravenous administration.* Journal of the American Society of Echocardiography, 2002. **15**(5): p. 396-403.

91. Unger, E.C., Hersh, E., Vannan, M., Matsunaga, T. O. and T. McCreery, *Local drug and gene delivery through microbubbles.* Progress in cardiovascular diseases, 2001. **44**(1): p. 45-54.

92. Swanson, E.J., Mohan, V., Kheir, J. and M. A. Borden, *Phospholipid-stabilized microbubble foam for injectable oxygen delivery.* Langmuir, 2010. **26**(20): p. 15726-15729.

93. Epstein, P.S. and M.S. Plesset, *On the stability of gas bubbles in liquid-gas solutions.* The Journal of Chemical Physics, 1950. **18**(11): p. 1505-1509.

94. Abou-Saleh, R.H., Swain, M., Evans, S.D. and N.H. Thomson, *Poly (ethylene glycol) lipid-shelled microbubbles: abundance, stability, and mechanical properties.* Langmuir, 2014. **30**(19): p. 5557-5563.

95. Wang, R., Xiao, R., Zeng, Z., Xu, L. and J. Wang, *Application of poly (ethylene glycol)–distearoylphosphatidylethanolamine (PEG-DSPE) block copolymers and their derivatives as nanomaterials in drug delivery.* International journal of nanomedicine, 2012. **7**: p. 4185-4198.

96. Platis, D. and N.E. Labrou, *Application of a PEG/salt aqueous two-phase partition system for the recovery of monoclonal antibodies from unclarified transgenic tobacco extract.* Biotechnology journal, 2009. **4**(9): p. 1320-1327.

97. Ahmed, E.M., Aggor, F. S., Awad, A. M. and A. T. El-Aref, *An innovative method for preparation of nanometal hydroxide superabsorbent hydrogel.* Carbohydrate polymers, 2013. **91**(2): p. 693-698.

98. Ahmed, E.M., *Hydrogel: Preparation, characterization, and applications: A review.* Journal of Advanced Research, 2015. **6**(2): p. 105-121.

99. Drira, Z. and V.K. Yadavalli, *Nanomechanical measurements of polyethylene glycol hydrogels using atomic force microscopy.* Journal of the mechanical behavior of biomedical materials, 2013. **18**: p. 20-28.

100. Jeong, B., S.W. Kim, and Y.H. Bae, *Thermosensitive sol–gel reversible hydrogels.* Advanced drug delivery reviews, 2012. **64**: p. 154-162.

101. Khademhosseini, A. and R. Langer, *Microengineered hydrogels for tissue engineering.* Biomaterials, 2007. **28**(34): p. 5087-5092.

102. Miyata, T., N. Asami, and T. Uragami, *A reversibly antigen-responsive hydrogel.* Nature, 1999. **399**(6738): p. 766-769.

103. Nicolson, P.C. and J. Vogt, *Soft contact lens polymers: an evolution.* Biomaterials, 2001. **22**(24): p. 3273-3283.

104. Van Tomme, S.R., G. Storm, and W.E. Hennink, *In situ gelling hydrogels for pharmaceutical and biomedical applications.* International journal of pharmaceutics, 2008. **355**(1): p. 1-18.

105. Iza, M., Stoianovici, G., Viora, L., Grossiord, J. and G. Couarraze, *Hydrogels of poly (ethylene glycol): mechanical characterization and release of a model drug.* Journal of Controlled Release, 1998. **52**(1): p. 41-51.

106. Jang, H.-N., Y.-B. Chung, and S.-S. Kim, *Preparation and characterization of silicone hydrogel lens containing poly (ethylene glycol).* Polymer Korea, 2009. **33**(2): p. 169-174.

107. Peyton, S.R., Raub, C. B., Keschrumrus, V. P. and A. J. Putnam, *The use of poly (ethylene glycol) hydrogels to investigate the impact of ECM chemistry and mechanics on smooth muscle cells.* Biomaterials, 2006. **27**(28): p. 4881-4893.

108. Ahearne, M., Yang, Y., El Haj, A. J., Then, K. Y. and K. Liu, *Characterizing the viscoelastic properties of thin hydrogel-based constructs for tissue engineering applications.* Journal of The Royal Society Interface, 2005. **2**(5): p. 455-463.

109. Yoshii, F., Zhanshan, Y., Isobe, K., Shinozaki, K. and K. Makuuchi, *Electron beam crosslinked PEO and PEO/PVA hydrogels for wound dressing.* Radiation Physics and Chemistry, 1999. **55**(2): p. 133-138.

110. Drury, J.L. and D.J. Mooney, *Hydrogels for tissue engineering: scaffold design variables and applications.* Biomaterials, 2003. **24**(24): p. 4337-4351.

111. Vacanti, J.P. and R. Langer, *Tissue engineering: the design and fabrication of living replacement devices for surgical reconstruction and transplantation.* The lancet, 1999. **354**: p. S32-S34.

112. Vacanti, J.P. and C.A. Vacanti, *The history and scope of tissue engineering.* Principles of tissue engineering, 2000. **3**: p. 3-6.

113. Zhao, W., Jin, X., Cong, Y., Liu, Y. and J. Fu, *Degradable natural polymer hydrogels for articular cartilage tissue engineering.* Journal of Chemical Technology and Biotechnology, 2013. **88**(3): p. 327-339.

114. Iizawa, T., Taketa, H., Maruta, M., Ishido, T., Gotoh, T. and S. Sakohara, *Synthesis of porous poly (N-isopropylacrylamide) gel beads by sedimentation polymerization and their morphology.* Journal of applied polymer science, 2007. **104**(2): p. 842-850.

115. Yang, L., J.S. Chu, and J.A. Fix, *Colon-specific drug delivery: new approaches and in vitro/in vivo evaluation.* International Journal of Pharmaceutics, 2002. **235**(1): p. 1-15.

116. Maolin, Z., Jun, L., Min, Y. and H. Hongfei, *The swelling behavior of radiation prepared semi-interpenetrating polymer networks composed of polyNIPAAm and hydrophilic polymers.* Radiation Physics and Chemistry, 2000. **58**(4): p. 397-400.

117. Hacker, M. and A. Mikos, *Synthetic polymers, principles of regenerative medicine*. 2011, Academic press, San Diego.

118. Wichterle, O. and D. Lim, *Hydrophilic gels for biological use.* Nature, 1960. **185**(4706): p. 117-118.

119. Saxena, A.K., *Synthetic biodegradable hydrogel (PleuraSeal) sealant for sealing of lung tissue after thoracoscopic resection.* The Journal of thoracic and cardiovascular surgery, 2010. **139**(2): p. 496-497.

120. Hamidi, M., A. Azadi, and P. Rafiei, *Hydrogel nanoparticles in drug delivery.* Advanced drug delivery reviews, 2008. **60**(15): p. 1638-1649.

121. Sun, X., Zhang, G., Shi, Q., Tang, B. and Z. Wu, *Preparation and characterization of water-swellable natural rubbers.* J Appl Polym Sci, 2002. **86**: p. 3212-717.

122. Chen, X., Martin, B. D., Neubauer, T. K., Linhardt, R. J., Dordick, J. S. and D. G. Rethwisch, *Enzymatic and chemoenzymatic approaches to synthesis of sugar-based polymer and hydrogels.* Carbohydrate Polymers, 1995. **28**(1): p. 15-21.

123. Kashyap, N., N. Kumar, and M.N.V.R. Kumar, *Hydrogels for pharmaceutical and biomedical applications.* Critical Reviews in Therapeutic Drug Carrier Systems, 2005. **22**(2): p. 107-149.

124. Kaihara, S., S. Matsumura, and J.P. Fisher, *Synthesis and characterization of cyclic acetal based degradable hydrogels.* European Journal of Pharmaceutics and Biopharmaceutics, 2008. **68**(1): p. 67-73.

125. Stamatialis, D.F., Papenburg, B. J., Gironés, M., Saiful, S., Bettahalli, S. N. M., Schmitmeier, S. and M. Wessling, *Medical applications of membranes: Drug delivery, artificial organs and tissue engineering.* Journal of Membrane Science, 2008. **308**(1–2): p. 1-34.

126. Zhang, L., Li, K., Xiao, W., Zheng, L., Xiao, Y., Fan, H. and X. Zhang, *Preparation of collagen–chondroitin sulfate–hyaluronic acid hybrid hydrogel scaffolds and cell compatibility in vitro.* Carbohydrate Polymers, 2011. **84**(1): p. 118-125.

127. Van der Linden, H.J., Herber, S., Olthuis, W. and P. Bergveld, *Stimulus-sensitive hydrogels and their applications in chemical (micro) analysis.* Analyst, 2003. **128**(4): p. 325-331.

128. Sikareepaisan, P., U. Ruktanonchai, and P. Supaphol, *Preparation and characterization of asiaticoside-loaded alginate films and their potential for use as effectual wound dressings.* Carbohydrate Polymers, 2011. **83**(4): p. 1457-1469.

129. Wang, F., Li, Z., Khan, M., Tamama, K., Kuppusamy, P., Wagner, W. R., Sen, C. K. and J. Guan, *Injectable, rapid gelling and highly flexible hydrogel composites as growth factor and cell carriers.* Acta Biomaterialia, 2010. **6**(6): p. 1978-1991.

130. Roy, D., J.N. Cambre, and B.S. Sumerlin, *Future perspectives and recent advances in stimuli-responsive materials.* Progress in Polymer Science, 2010. **35**(1–2): p. 278-301.

131. Krsko, P., McCann, T. E., Thach, T. T., Laabs, T. L., Geller, H. M. and M. R. Libera, *Length-scale mediated adhesion and directed growth of neural cells by surface-patterned poly(ethylene glycol) hydrogels.* Biomaterials, 2009. **30**(5): p. 721-729.

132. Tabata, Y., *Biomaterial technology for tissue engineering applications.* Journal of the Royal Society Interface, 2009. **6**(Suppl 3): p. S311-S324.

133. Shantha, K. and D. Harding, *Synthesis and evaluation of sucrose-containing polymeric hydrogels for oral drug delivery.* Journal of applied polymer science, 2002. **84**(14): p. 2597-2604.

CHAPTER 3
THEORETICAL BACKGROUND

CHAPTER 3: THEORETICAL BACKGROUND

3.1 Introduction

This study investigates the mechanical properties of the soft biomaterials such as phospholipid microbubbles (MBs) and tissue engineering materials e.g. hydrogels. This chapter will concentrate on the theoretical background of the mechanical properties studied in the present research, including Young's Modulus, stiffness, hysteresis, plasticity and hardness. This chapter will provide the theoretical base of the present study. The models and related equations are introduced here in some detail and will not be explained further in the results and chapters; however, I will refer to them where necessary.

3.2 Stiffness

As mentioned previously (see section 2.2.4 Force Spectroscopy), the raw data in the AFM force-distance curves are the deflection of the cantilever and the vertical extension of the piezo (the piezo position). Hooke's law is applicable here as shown in equation (1), where the deflection and the force are both known.

$$F = k_c \times X \qquad (1)$$

where F, k_c, X are the force, cantilever spring constant and cantilever deflection, respectively. By using equation (1) the deflection in the raw data, will be converted to force which helps to convert the deflection-position curve to a force-position curve. At the contact point, the piezo displacement (the vertical position displacement) is

translated to deflection on the cantilever and deformation on the sample, which means that the whole system works as two springs connected in a series order and the inverse of the stiffness of the whole system is equal to the sum of inverse stiffnesses of both the cantilever and the sample (thought of as two springs), as shown in Figure 3-1.

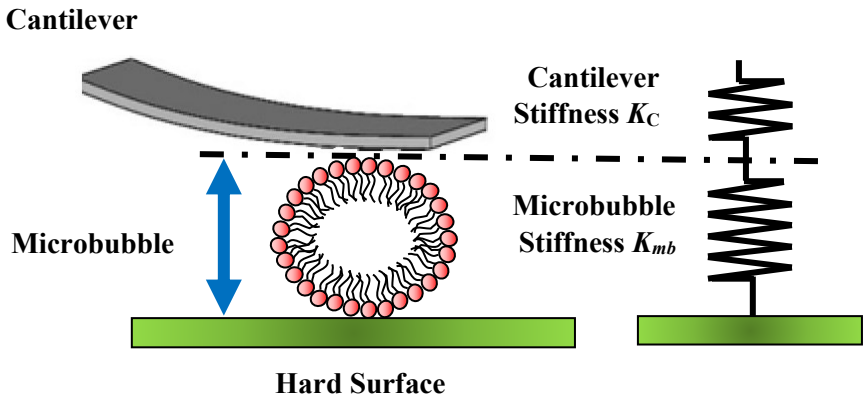

Figure 3-1: Schematic drawing showing a microbubble (MB) compressed under a cantilever (left). Right: schematic drawing explaining that the stiffness of the whole system involves the cantilever and MB stiffnesses in series.

Figure 3-1 shows that the system (the cantilever and the sample together) works as two springs which are connected in series. [1] [2] SThe stiffness of the whole system is related to both the cantilever and sample stiffnesses by equation 2:

$$\frac{1}{k_t} = \frac{1}{k_c} + \frac{1}{k_s} \qquad (2)$$

where: k_t, k_c and k_s are the stiffnesses of the whole system, the cantilever and the sample respectively. Multiplying equation (2) by force, F, will give the following equation:

$$\frac{F}{k_t} = \frac{F}{k_c} + \frac{F}{k_s} \qquad (3)$$

Referring to equation (1), and substituting it into equation (3) the resulting equation, equation (4), will represent the displacements, as follows:

$$Z = X + \Delta \quad (4)$$

Where Z, X and Δ are the piezo displacement, the cantilever deflection and the sample deformation respectively. Thus, the sample deformation is given by

$$\Delta = Z - X \quad (5)$$

Note that equation (5) is applicable for both the microbubble experiments, as deformation (Δ), and the hydrogel experiments, as indentation (δ); this equation excludes the response of the cantilever and retains the response of the sample whether it is a deformation or an indentation. [3] Therefore, the use of equation (5) is helping to convert the force-distance (piezo position) curve to a force-deformation (F-Δ) curve in the MB experiments, and the force-indentation (F-δ) curve in the gel experiments. This happens by subtracting the deflection of the cantilever from the piezo displacement (position) to acquire the deformation of the sample. [2, 4-6] Eventually, the force-deformation (F-Δ) curves will be obtained and these curves are used in the analytical calculations to investigate the stiffness of the sample, where the stiffness is the gradient of this curve in the linear region. The conversion from raw data to the force-deformation (F-Δ) curve passes through several stages, which are summarized in Figure 3-2. The raw data obtained from the AFM instrument is the deflection-LVDT curve, where LVDT is the Linear Variable Differential Transformer, as shown in Figure 3-2-(a). The deflection-LVDT curve is shifted to the zero point (origin point) to be the deflection-position curve, as shown in Figure 3-2-(b) [7], then the data pass through the procedures which were explained previously.

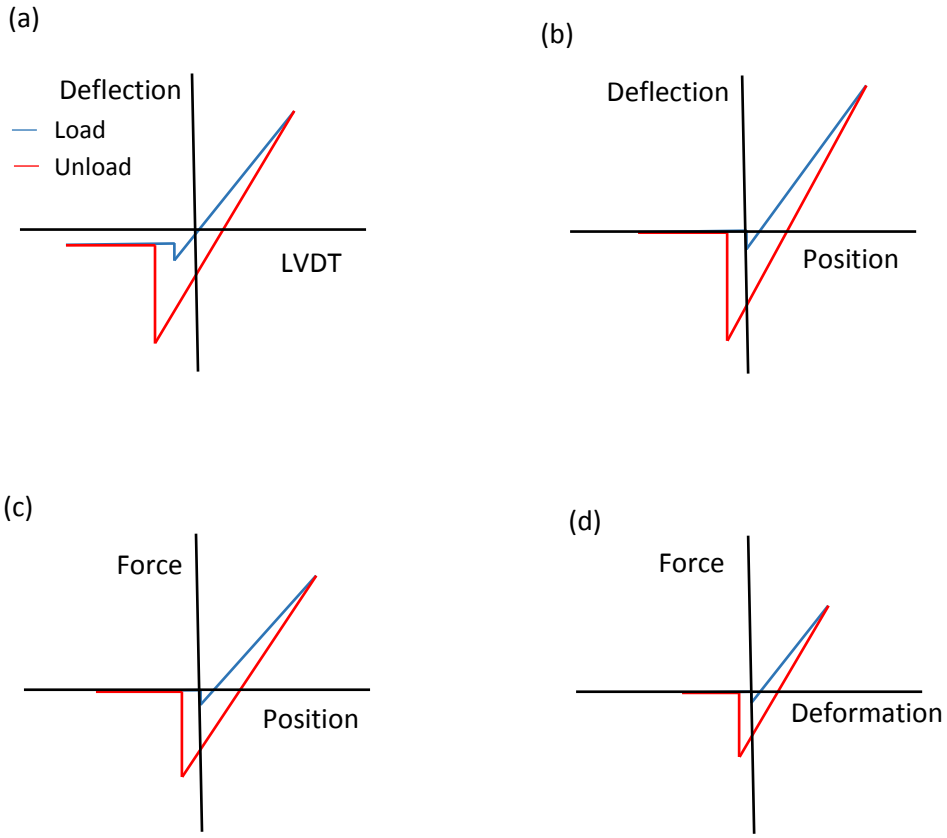

Figure 3-2: Schematic drawing illustrating the stages of conversion from the raw data to the final data that are used in the analytical calculations, where (a) shows the raw data, (b) the data shifted to the zero point, (c) conversion of the deflection to the force and (d) conversion of the position to deformation.

3.3 Young's Modulus

The modulus of elasticity (Young's modulus) was calculated in the present study using four different models which are Reissner's theory, elastic membrane theory, Hertz theory and the Sneddon model which is modified from Hertz theory. Three models were applied to evaluate the Young's modulus of the microbubbles (MBs) reported in Chapter 4 and Chapter 5, where the first two models calculate the modulus of elasticity of the MB shell, while the third model estimates the modulus of elasticity

of the whole MB as a homogenous spherical body. The fourth model was applied to investigate the Young's modulus of the hydrogels which were reported in Chapter 6. In general, Young's modulus, E, can be calculated from the gradient of a stress-strain (σ- ξ) curve, while the curve is in the linear region.

$$E = \frac{\sigma}{\xi} \tag{6}$$

where: E is Young's modulus, σ is stress and ξ is strain. However, this is not straightforward with nonlinear models, since it involves some complexity due to the system geometry and the nonlinearity. The following sections will discuss each model briefly and describe how they are applied in this study.

3.3.1 Reissner's Theory

After obtaining the force-deformation (F-Δ), it is appropriate that we normalize the deformation with the MB diameter, to create the relative deformation (ε), and thus reduce the effect of the variation of the MBs' sizes. The relative deformation (ε) is the deformation of the MB (Δ) divided by the initial diameter of the MB (D_0). [7, 8]

$$\varepsilon = \frac{\Delta}{D_0} \tag{7}$$

Reissner's theory [9-11] was the first model applied in this investigation. The Reissner model was a good solution when used to predict the polymer MB properties [4], where the results are associated with the bulk polymer, which stimulated me to use this model. This theory is the basis of the analytical solution of the thin shell deformation. The model is a solution for the shallow [9] spherical caps, which are isotropic elastic thin shells with small deformation. This structure is applicable to the MBs investigated

in this study, as they are spherical hollow thin-shelled particles. Therefore, it is appropriate for estimating the mechanical properties of the MBs using this model. The Young's Modulus of a MB with initial radius R_0 and shell thickness t can be calculate using Reissner's theory as follows:

$$E = \frac{\sqrt{3(1-v^2)}}{4}\frac{R_0}{t^2}s \qquad (8)$$

where E is the Young's modulus, υ is Poisson's ratio and s is the slope of the linear part of the force-deformation (F-Δ) curve. It is clear that Young's modulus can be calculated straightforwardly from the force-deformation (F-Δ) curve using the Reissner model, where it has a linear relationship with slope, s, of the curve as appears in the previous equation, equation (8). This equation can be rewritten and re-arranged, by substituting s with F/ Δ and Δ with $\Delta = D_0\varepsilon$ from equation (7), to be as follows:

$$E = \frac{\sqrt{3(1-v^2)}}{8t^2}\left[\frac{F}{\varepsilon}\right] \qquad (9)$$

Taking into account the fact that the deformation happens at both poles of the MB and the original Reissner equation is considering only one pole, the strain has to be halved which leads to the following equation:

$$E = \frac{\sqrt{3(1-v^2)}}{4t^2}\left[\frac{F}{\varepsilon}\right] \qquad (10)$$

Since the Poisson's ratio (υ) and the thickness (t) are constants for each MB, the Young's modulus is equal to a factor multiplied by the gradient of the linear part of the force-relative deformation (F-ε) curve (this model is used in the analysis in Chapter 4).

$$E = Factor \times \left[\frac{F}{\varepsilon} \right] \quad (11)$$

The Reissner model is applicable with certain assumptions, such as that the thickness/radius ratio should be very small ($t/R_0 < 1/20$), [12]; the load must be concentrated on a very small area as a point and the load must be on the MB poles. The first condition is valid in the experiments in the present study where the thickness assumed to be approx. 5 nm and the smallest MB radius is 1400 nm and the second condition is valid with tipped cantilever experiments; however, with the tipless cantilever experiments, the contact area is much greater than in those with a tipped cantilever. The third condition, which is that the load should be exerted symmetrically on the poles is applicable with approximation at best, where the tip is on the top of the MB and the cantilever is parallel to the hard substrate surface. [4] According to Elsner et al. [13], the Reissner model is applicable with non-point-like loads and also with a large contact area. The Reissner model is a useful solution for the hollow, thin-walled spherical structures under a small deformation. Therefore, it has been used for several applications. [4, 5, 14-16]

3.3.2 Elastic Membrane Theory

This model, like the previous one, estimates modulus of elasticity of the MB shell. Elastic membrane theory is a good model to understand the MBs' behaviour as encapsulated structures. [14, 17] The model depends on membrane theory, which translates the bending and stretching energy due to the deformation of the shell. For this model to be applicable, the MB can be assumed to have an impermeable membrane, where the MB becomes like an incompressible fluid filling a balloon. [18]

The volume of the balloon remains constant during the compression because of the impermeable membrane. The compression pressure is exerted homogeneously in all directions due to the inner fluid. The pressure is balanced by stretching the balloon membrane (which is the shell in the MB). At the contact area, bending of the membrane might occur and can be considered, if the deformation is small. [18]

In the beginning, the bending of the membrane will be a local response to the applied load. The membrane is deformed at the contact area while the free surface of the membrane remains un-deformed, keeping its shape as a uniform circle. The deformation increases globally in the free membrane with an increasing load and the surface stretches due to increased internal pressure. Figure 3-3 [7] shows the bending and stretching deformation during the low and high load.

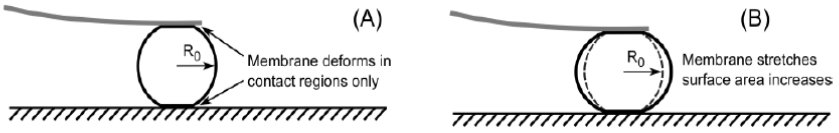

Figure 3-3: Schematic representing a bending deformation with low load in (A) and stretching deformation with high load in (B).

The correlation between the force and deformation using the membrane model can be explained as follows: [8, 17, 18]

$$F_m = F_{Stretching} + F_{Bending} \tag{12}$$

$$F_m = 2\pi \frac{E_m}{1-\upsilon_m} t R_0 \varepsilon^3 + \pi \frac{E_m}{2\sqrt{2}} t^2 \varepsilon^{1/2} \tag{13}$$

where F_m is the exerted force and E_m and υ_m represent the Young's modulus and Poisson's ratio of the membrane respectively. It is necessary to estimate the bending-stretching force ratio to distinguish the effective parameters in this ratio.

$$\frac{F_{Bending}}{F_{Stretching}} = \frac{t}{R_0}\frac{1-\upsilon}{4\sqrt{2}}\frac{1}{\varepsilon^{5/2}} \tag{14}$$

If the ratio of the shell thickness (t) to the initial MB radius (R_0) is very small, which is the case in the MBs investigated in the present study, the bending component can be ignored, especially with relatively high deformation, where the stretching force is the dominant. [8, 18] In this study the force ratio was very small ($F_{Bending}/F_{Stretching} \leq 0.08$), therefore the bending component was neglected and equation (12) can be written as:

$$F = 2\pi\frac{E}{1-\upsilon}tR_0\varepsilon^3 \tag{15}$$

Rearranging equation (15) leads to the following equation:

$$E = \frac{1-\upsilon}{2\pi R_0 t}\left[\frac{F}{\varepsilon^3}\right] \tag{16}$$

Since the Poisson's ratio (υ), the initial radius (R_0) and the thickness (t) are constants for each MB, equation (16) becomes:

$$E = Factor \times \left[\frac{F}{\varepsilon^3}\right] \tag{17}$$

Therefore, the Young's modulus of the MB shell is the gradient of the linear part of the ($F-\varepsilon^3$) curve multiplied by a factor (this model was used in the analysis in Chapter 4).

3.3.3 Hertz Theory

In contrast with the previous models, which estimate the modulus of elasticity of the MB shell, this model calculates the modulus of elasticity of the whole MB body. If two curved bodies come into contact, in the beginning they make contact at a single point, e.g. for spheres, or along a line, for forms such as cylinders, then the contact area increases with an increasing load. The first solution to determining the size of the contact area was introduced in 1881 by Heinrich Hertz. [19-21] This solution is a general solution for two semi-infinite spheres in contact which are deformed elastically.[22] Hertz described his solution with some assumptions: [23-25]

(i) The curved bodies' sizes are much bigger than the contact area size ($a << R$), where R is the probe curvature radius and a is the contact radius.

(ii) The surfaces of the contacting bodies are smooth and frictionless.

(iii) Each body can be treated as an elastic half space (a flat surface on an infinite elastic solid, known as an elastic half space).

Hertz theory can be modified and extended to be applicable for other models and geometries such as sphere-plate contact. [18] The model has been used in several similar studies [26-30], which indicates that this solution is an appropriate model to calculate Young's modulus in such a form of contact. The model does not consider the adhesion forces and assumes them to be much smaller than the applied force and that they are not effective on the deformed area, so the present experiments were implemented in an aqueous environment to reduce the adhesion forces. Hertz theory can be used with different types of applications. Either the probe is much greater than the sample [18] or the probe much smaller than the sample. [26] The model can be

used with sphere-plate geometry, which is suitable for a tipless cantilever with a MB, where the cantilever is assumed as a very big sphere (R= ∞) and the sample (MB) has a specific radius. This structure of this model is used in Chapter 4. The relation between the applied force and the deformation of the MB can be presented in the following equation. [8, 18]

$$F = \frac{\sqrt{2}E}{3(1-\upsilon^2)} R_0{}^2 \varepsilon^{3/2} \qquad (18)$$

Rearranging equation (18) leads to the next equation:

$$E = \frac{3(1-\upsilon^2)}{\sqrt{2}R_0{}^2}\left[\frac{F}{\varepsilon^{3/2}}\right] \qquad (19)$$

Because the Poisson's ratio (υ) and the initial radius (R_0) are constants for each MB, equation (19) becomes:

$$E = Factor \times \left[\frac{F}{\varepsilon^{3/2}}\right] \qquad (20)$$

Therefore, the effective Young's modulus of the whole MB using a tipless cantilever is the gradient of the linear part of the ($F-\varepsilon^{3/2}$) curve multiplied by a factor (this model is used in Chapter 4 Analysis).

The Hertz model can be also used with a conical tipped cantilever and a MB in compression test where the tip is much smaller than the MB; in this case the tip apex can be considered as a small (hemi) sphere while the MB is a very huge ball (compared to the tip); the radius of curvature of the tip is 10 nm while the smallest MB radius is 1400 nm; then, comparatively it can be considered as flat (R= ∞). However, the situation is now the opposite where the deformation will be defined by the tip geometry, which requires us to adopt a modified Hertzian model. [23, 26]

$$F = \frac{4ER_{Tip}^{1/2}}{3(1-\upsilon^2)}\delta^{3/2} \quad (21)$$

where R_{Tip} is radius of the curvature of the tip and δ is the indentation.

In similar manner, equation (21) needs to be rearranged to obtain the relationship between the Young's modulus and the applied force in the following equation:

$$E = \frac{3(1-\upsilon^2)}{4R_{Tip}^{1/2}}\left[\frac{F}{\delta^{3/2}}\right] \quad (22)$$

Assuming that the indentation (δ) is the deformation of the MB (Δ), substituting equation (7) into equation (22) leads to the following equation:

$$E = \frac{3(1-\upsilon^2)}{2^{7/2}R_{Tip}^{1/2}R_0^{3/2}}\left[\frac{F}{\varepsilon^{3/2}}\right] \quad (23)$$

Again, the Poisson's ratio (υ), radius of the tip curvature (R_{Tip}) and the initial radius of the MB (R_0) are constants for each tip and MB; therefore, equation (23) becomes:

$$E = Factor \times \left[\frac{F}{\varepsilon^{3/2}}\right] \quad (24)$$

It is notable, that the effective Young's modulus of the whole MB using a tipless or tipped cantilever is the gradient of the linear part of the ($F-\varepsilon^{3/2}$) curve multiplied by a factor, where the factor depends on the geometries of the tip and the MB (this model was used in the analysis in Chapter 5).

3.3.4 The Sneddon Model

Because the Hertz solution is specifically applicable for bodies with curvature, there were attempts to expand the model to be valid for other geometries. Sneddon succeeded in modifying and expanding the Hertz model to be applicable and

appropriate for other axisymmetric geometries, such as a flat cylindrical punch, or a paraboloid or cone. [31-33] In 1965, Sneddon [34] introduced his solution which helps to use Hertz model with other geometries and to make it more appropriate for other applications. By generalizing the force-indentation (F-δ) relation, as shown in equation (25), [23, 35] several specific solutions can be represented by choosing the desired geometry parameters, which are shown in table 3-1.

$$F = \lambda \delta^{\beta} \tag{25}$$

where λ and β are constants depending on the geometry and material of the contacting body (the punch). Table 3-1 [23] displays values of λ, β and the radius of the contact area (R_{cont}), according to the geometry of the punch.

Sneddon's approach was adopted in this study to investigate the modulus of elasticity of the gel where this model is applicable for indentation experiments with a conical tipped cantilever. By substituting the values of λ, β from Table 3-1 into equation (25), Sneddon's solution becomes as in the following equation for the conical indenter:

$$F = \frac{2E \tan\phi}{\pi(1-\upsilon^2)} \delta^2 \tag{26}$$

where ϕ is the half angle of the conical tip and δ is the indentation depth. After arranging and rewriting equation (26), it becomes as follows:

$$E = \frac{\pi(1-\upsilon^2)}{2\tan\phi}\left[\frac{F}{\delta^2}\right] \tag{27}$$

Table 3-1: Showing values of the constants in the general Hertz model. Note that the parabolic geometry is the first model described by Hertz.

	Geometry	λ	β	R_{Cont}
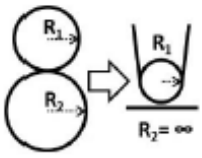	Parabolic tip with a sphere of radius R at its end	$\frac{4ER^{1/2}}{3(1-\nu^2)}$	3/2	$(R\delta)^{1/2}$
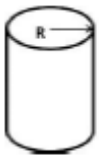	Cylinder	$\frac{2ER}{(1-\nu^2)}$	1	R
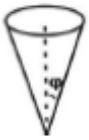	Sharp cone (Sneddon solution)	$\frac{2Etan\phi}{\pi(1-\nu^2)}$	2	$\frac{2\delta tan\phi}{\pi}$
	Sharp pyramid (Bilodeau solution)	$\frac{1.4906Etan\phi}{2(1-\nu^2)}$	2	$\frac{1.579^{1/2}\ \delta\ \tan\phi}{2}$
	Blunted pyramid (Rico solution)	$\frac{Etan\phi}{2^{1/2}(1-\nu^2)}$	2	$\frac{\delta tan\phi}{2^{1/2}}$

Since Poisson's ratio (υ) and the half-angle of the conical tip (ϕ) are constants, the relation becomes:

$$E = Factor \times \left[\frac{F}{\delta^2}\right] \qquad (28)$$

Therefore, the Young's modulus of the gels corresponding to Sneddon's model using a conical tipped cantilever, is the gradient of the linear part of the ($F-\delta^2$) curve

multiplied by a factor, where the factor depends on the geometries of the tip and the gel material (the Poisson's ratio);this model is used in the analysis in Chapter 6.

3.4 Hysteresis and Plasticity

The study investigated both the hysteresis and the plasticity behaviours for the microbubbles (MBs), as reported in Chapters 4 and 5, and also for gels, as reported in Chapter 6.

3.4.1 Hysteresis

Elastic hysteresis is an important phenomenon that needs to be determined because of the energy loss during the compression cycle: the load (trace) and unload (retrace) cycle. [36, 37] It happens when the two curves, load (trace) and unload (retrace), diverge and confine an area between them. If the hysteresis area exists, the force on the load (trace) curve is higher than the force on the unload (retrace) curve at the same deformation, which means that energy was lost during the cycle between the load (trace) and unload (retrace) curves. This area can be calculated using different methods and techniques; however; the trapezoidal rule [38, 39] was adopted in this study to determine the hysteresis area. The trapezoidal method is presented in the following equations associated with Figure 3-4. To calculate the area under the curve we can take the integration of the function $f(x)$ from (a) to (b) or, instead, we can approximate the area by dividing it into numbers of trapezoids and estimating the area for each trapezoid individually then taking the summation. Note that width of the trapezoid (Δx) equals the length of the function $f(x)$ on the x-axis divided by the number of trapezoids (n) where:

$$\Delta x = \frac{b-a}{n} \tag{29}$$

The approximation of the area is shown in equation (30).

$$Area \approx \frac{1}{2}(y_0 + y_1)\Delta x + \frac{1}{2}(y_1 + y_2)\Delta x + \frac{1}{2}(y_2 + y_3)\Delta x + \ldots \tag{30}$$

Equation (30) can be simplified for (n) numbers of trapezoids to be:

$$Area \approx \Delta x(\frac{y_0}{2} + y_1 + y_2 + y_3 + \ldots + \frac{y_n}{2}) \tag{31}$$

$$Area = \int_a^b f(x)dx \approx \Delta x(\frac{y_0}{2} + y_1 + y_2 + y_3 + \ldots + \frac{y_n}{2}) \tag{32}$$

(This method, the trapezoid rule, is used in Chapters 4, 5 and 6).

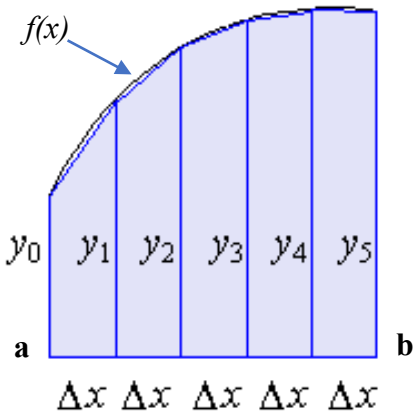

Figure 3-4: The area under the curve is divided into numbers of trapezoids.

To eliminate the effect of the size differences of the samples on the energy loss per cycle, the unit volume is considered, where the energy loss per unit volume equals the

energy loss per cycle divided by the volume of the sample. [40] Assuming the MB is a homogenous hollow sphere, with a homogenous diameter and thickness, the MB volume becomes as shown in the following equation.

$$\mathrm{MB\,volume} = \frac{4}{3} \times \pi (R_0{}^3 - r_i{}^3) \qquad (33)$$

where R_0 and r_i are the initial outer and inner radii of the MB respectively.

Note that, $\mathrm{r_i} = R_0 - t$, where t is the MB thickness. (This equation is applied in Chapters 4 and 5).

For the gels, we assume that the tip is a completely sharp conical tip to be consistent with the model used, and also that the difference in the volume is very small and can be neglected as it does not affect the result. In addition, it was assumed that the volume of the deformed material is equal to the volume of the immersed part of the tip, where the material is in contact with the surface tip to the maximum indentation depth (h_{max}). According to these assumptions, the volume of the deformed gel is shown in the following equation:

$$\mathrm{The\,cone\,volume} = \frac{1}{3} \pi r^2 h \qquad (34)$$

where r and h are the radius of base of the cone and the height of the cone respectively. Note that the height is the maximum indentation depth (h_{max}) and the radius of the base of the cone is the radius of the projected contact area (a) as shown in Figure 3-5. (This formula is used in Chapter 6).

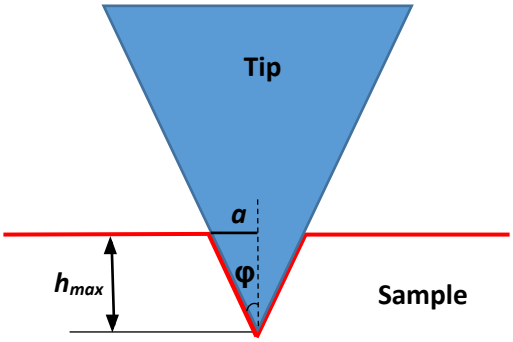

Figure 3-5: Schematic representing a conical tip indented in the gel sample, where h_{max} and a are the maximum indentation and the radius of the projected contact area respectively.

3.4.2 Plasticity

When a soft material is exposed to a compression test, it is important to take into account the viscoelastic behaviour. [41] The retracing or unloading curve may give predictions about the elastic, viscoelastic and plastic behaviour of the soft material. [42] The plasticity index (η) can be used to indicate the viscoelastic behaviour of the material. The plasticity index (η) is equal to the ratio of the area under the unloading curve to the area under the loading curve. Therefore, the correlation between the plasticity index (η) and these areas may be represented in the following equation: [35]

$$\text{Plasticity index } (\eta) = 1 - \frac{A_u}{A_l} \qquad (35)$$

where A_u and A_l are the area under the unloading curve and the area under the loading curve respectively. By modifying equation (35) we obtain the following equation:

$$\Rightarrow \eta = \frac{A_l - A_u}{A_l} \qquad (36)$$

However, the area under the loading curve includes the area between the two curves (load and unload) and the area under the unloading curve where:

$$A_l = A_b + A_u \tag{37}$$

Note that A_b is the area between the two curves and above the deformation axis (axis F=0). Subsuming equation (37) into equation (36) leads to:

$$\eta = \frac{A_b}{A_b + A_u} \tag{38}$$

Referring to Figure 3-6, adopted from Butt et al. [35] with some modifications, it can be seen that, for a totally elastic material $A_u = A_l$ and the unloading curve is identical to the loading curve, therefore, the plasticity index is zero (η=0). However, for purely plastic materials $A_u = 0$, which means that the unloading curve is perpendicular to the x-axis (deformation axis) and the plasticity index is equal to one (η=1). [35, 41-43] The viscoelastic-plastic behaviour is found in the intermediate values between the two extreme limits, where ($0 < \eta < 1$). (The plasticity index (η) is calculated in Chapters 4, 5 and 6).

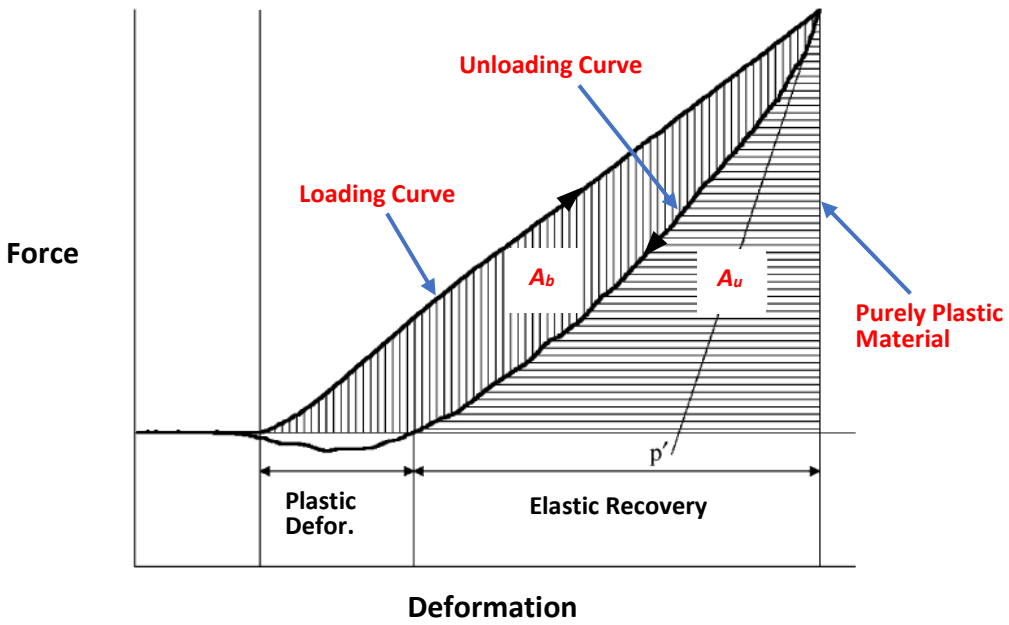

Figure 3-6: Schematic showing the elastic and plastic deformation regions where A_u, A_b are the areas under the unloading curve and between the two curves respectively above the deformation axis (the axis of F=0).

3.5 Hardnesses

- **Hardness**

When an indentation technique is adopted the most two important mechanical properties are the elastic modulus (Young's modulus) (E) and the hardness (H). [44, 45] These two properties were investigated in this study, where the Young's modulus was calculated for both the MBs and gels (Chapters 4, 5, and 6) while the hardness was estimated for the gels (Chapter 6), where the test was an indentation method (which is not applicable with the MB experiments). This section will cover the theoretical base of the concept of hardness and discuss the definition of hardness and its formulae.

The elastic contact theory plays an important role in the analysis of hardness. Returning to the origin of the elastic contact theory, we find that the theory was founded in the 19th century by Hertz [19] and Boussinesq. [46] Hertz described a solution for the elastic contact of two spheres with different radii, while Boussinesq introduced a method to compute the stress and the displacements on an elastic body loaded by a rigid indenter. Later, Sneddon [34] added another major contribution by expanding and developing Hertz's theory to his general solution, which is that the relationship between the load, displacement and the contact area for any indenter can be considered as a solid of revolution of a smooth function. [44] After obtaining the force-indentation (F-δ) curve, the unloading curve is analysed according to the model for the deformation of the elastic half-space by a rigid axisymmetric indenter [45, 47, 48], which is a conical tip indenter in this study. The nanoindentation technique is widely used for small-scale measurements of mechanical properties, due to its high

resolution and the simplicity of the analysis depending on the elastic and elastic/plastic contact theory. [49-52]

A formula which is commonly applied in the indentation analyses, with different forms, connects the elastic modulus, Poisson's ratio and the projected contact area to the indentation contact stiffness, in the following relationship: [44, 45, 53, 54]

$$S = \frac{2}{\sqrt{\pi}} E_r \sqrt{A} \qquad (39)$$

where S, E_r and A are the contact stiffness, the reduced elastic modulus and the projected contact area, respectively. The contact stiffness (S) can be measured experimentally from the gradient of the force-indentation (F-δ) curve of the upper part of the unloading curve; in this study, one third of the upper part of the unloading curve was adopted. [44, 51]

$$S = \frac{dF}{d\delta} \qquad (40)$$

The reduced elastic modulus, E_r can be estimated from the elastic deformation of both the sample and the indenter and given by the following equation: [53]

$$\frac{1}{E_r} = \frac{(1-\nu_i^2)}{E_i} + \frac{(1-\nu^2)}{E} \qquad (41)$$

where E_i, υ_i and E, υ are the modulus and Poisson's ratio of the indenter and the sample, respectively. However if the indenter is very hard compared to the sample, which is the case in this study, where the indenter material is either a silicon nitride or a silicon and the Young's modulus (E) for silicon nitride is 160-290 GPa, while for silicon it is 130-185 GPa, [23], the deformation will occur to the sample alone. Therefore, the first term might be neglected and the equation becomes:

$$\frac{1}{\mathrm{E_r}} = \frac{(1-\nu^2)}{E} \tag{42}$$

Substituting relation (42) into equation (39) gives the following equation:

$$\mathrm{S} = \frac{2E}{\sqrt{\pi}(1-\nu^2)}\sqrt{A} \tag{43}$$

The basic definition of hardness is the maximum load divided by the contact area (the area of indentation). However, there is a significant debate about the definition of hardness, where, after Meyer [47, 55, 56], it came to be defined as the maximum load divided by the projected contact area.

$$\mathrm{H} = \frac{F_{\max}}{A} \tag{44}$$

where H and A are the hardness and the projected contact area respectively. Investigating the properties of soft materials involves complexity, due to their elastic/plastic or viscoelastic behaviour. Thus, to calculate the hardness, it is necessary to calculate the projected contact area accurately.

When a soft material is exposed to a maximum load, the material deforms, responding to the exerted load. However, the deformation does not overlap with the indenter surface completely, but the sample deforms as a curvature, where some of the material at a certain indentation depth is in contact with the indenter surface while the rest is not in contact. The maximum indentation, maximum depth, h_{max}, equals the contact depth, h_c, plus the elastic displacement depth, h_s. During unloading, the elastic displacement recovers, when the indenter retreats from the sample, with the final depth, h_f, of the residual hardness impression remaining. Figure 3-7 helps to visualize the parameters that are used to estimate the projected contact area, where Figure 3-7-(a) shows those parameters physically during the loading and unloading test, while

Figure 3-7-(b) illustrates the parameters on the force-indentation (F−δ) curve. Since the load is known, the mean point is determining the projected contact area accurately to calculate the hardness. In contrast with the conventional methods to estimate the projected contact area, which depend on the imaging of the indentation after the retreat of the tip and removing the load by measuring the diagonal lengths, which involves some errors after removing the load, Doerner and Nix [51] developed a method to calculate the projected contact area more easily, quickly and accurately, based on the fitting of the upper portion of the unloading curve of the force-indentation (F−δ) data. They state that the area does not change in the initial unloading curve. By intersecting the fitting of the upper part of the unloading curve (1/3 of the curve) with the x-axis (indentation axis), the elastic displacement depth, h_s is specified, as shown in Figure 3-7-(b), and from the previous note, the contact depth, h_c can be determined, since the maximum depth, h_{max} is known by the following equation:

$$h_c = h_{max} - h_s \tag{45}$$

The relation between the contact depth, h_c and the contact radius, a, is illustrated in the next equation.

$$a = \tan(\varphi) \times h_c \tag{46}$$

Where, φ is half of the cone angle. Because the indenter used was a conical tip, the projected contact area, is a circle and can be written as:

$$A = \pi a^2 \tag{47}$$

This area, the projected contact area, can be used to calculate the hardness of the material.

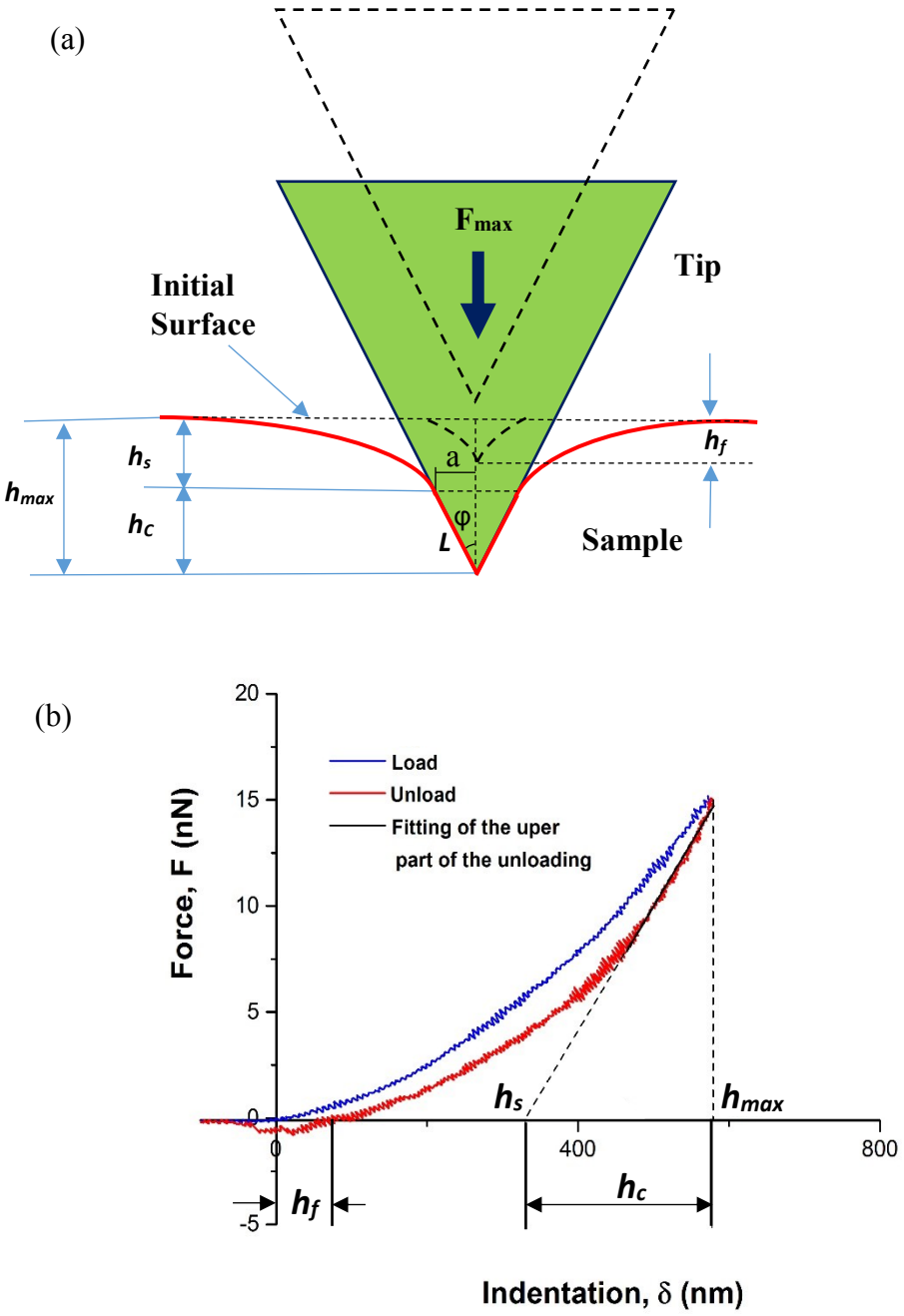

Figure 3-7: (a) Schematic drawing showing indentation form of the conical tip during and after the loading. (b) A typical force-indentation (F-δ) curve for a gel sample, where h_f , h_s, h_{max} and h_c are shown on the indentation axis.

- **Universal Hardness**

Because of the debate regarding the definition of the contact area, as mentioned in the previous section, real contact versus projected contact area, [57] there is another quantity to determine hardness, which takes into account the whole deformation of the material and is not limited only to the plastic deformation. This quantity is called the universal hardness, UH, which is different from the previous hardness in its definition of the projected contact area, where the material is considered to be in full contact with the indenter surface to the maximum depth, h_{max}. Based on this definition, the universal hardness can be written as:

$$\mathrm{UH} = \frac{F_{\max}}{A} \tag{48}$$

where A is the projected contact area at the maximum depth and might be defined similarly to equation (47); however, the contact radius, a, is equal to:

$$\mathrm{a} = \tan(\varphi) \times h_{\max} \tag{49}$$

- **Pressure**

Through the definition of pressure, which is the normal force exerted on the unit area, we can see that the pressure in these experiments is equal to the normal force on the contact surface between the tip and the sample, which represents the lateral surface of the cone to the contact depth.

$$\mathrm{P} = \frac{F}{A} \tag{50}$$

$$\mathrm{F} = \sin(\varphi) \times F_{\max} \tag{51}$$

The lateral surface of the cone to the contact is written in the following equation.

$$A = \pi a L \tag{52}$$

Where L is length of the cone slant to the contact depth, see Figure 3-7-(a).

$$L = \sqrt{a^2 + h_c^{\,2}} \tag{53}$$

3.5 References

1. McKendry, J., Grant, C., Johnson, B., Coletta, P., Evans, J. and S. Evans, *Force spectroscopy of streptavidin conjugated lipid coated microbubbles.* Bubble Science, Engineering & Technology, 2010. **2**(2): p. 48-54.

2. Sboros, V., Glynos, E., Pye, S., Moran, C., Butler, M., Ross, J., Short, R., McDicken, W. and V. Koutsos, *Nanointerrogation of ultrasonic contrast agent microbubbles using atomic force microscopy.* Ultrasound in medicine & biology, 2006. **32**(4): p. 579-585.

3. Domke, J. and M. Radmacher, *Measuring the elastic properties of thin polymer films with the atomic force microscope.* Langmuir, 1998. **14**(12): p. 3320-3325.

4. Glynos, E., V. Sboros, and V. Koutsos, *Polymeric thin shells: Measurement of elastic properties at the nanometer scale using atomic force microscopy.* Materials Science and Engineering: B, 2009. **165**(3): p. 231-234.

5. Glynos, E., Koutsos, V., McDicken, W.N., Moran, C.M., Pye, S.D., Ross, J.A. and V. Sboros, *Nanomechanics of biocompatible hollow thin-shell polymer microspheres.* Langmuir, 2009. **25**(13): p. 7514-7522.

6. Sboros, V., Glynos, E., Pye, S., Moran, C., Butler, M., Ross, J., McDicken, W. and V. Koutsos, *Nanomechanical probing of microbubbles using the atomic force microscope.* Ultrasonics, 2007. **46**(4): p. 349-354.

7. Morris, J.K., *Mechanical properties of phospholipid coated microbubbles*. 2014, The University of Edinburgh: Edinburgh, UK. PhD thesis. p. 157

8. Buchner Santos, E., Morris, J.K., Glynos, E., Sboros, V. and V. Koutsos, *Nanomechanical properties of phospholipid microbubbles.* Langmuir, 2012. **28**(13): p. 5753-5760.

9. Reissner, E., *Stresses and Small Displacements of Shallow Spherical Shells. I.* Journal of Mathematics and Physics, 1946. **25**(1-4): p. 80-85.

10. Reissner, E., *Stresses and Small Displacements of Shallow Spherical Shells. II.* Journal of Mathematics and Physics, 1946. **25**(1-4): p. 279-300.

11. Reissner, E., *Corrections to the paper "Stresses and Small Displacements of Shallow Spherical Shells II".* Journal of Mathematics and Physics, 1948. **27**(1-4): p. 240-240.

12. Wan, F.Y., R.D. Gregory, and T.I. Milac, *A thick hollow sphere compressed by equal and opposite concentrated axial loads: An asymptotic solution.* SIAM Journal on Applied Mathematics, 1998. **59**(3): p. 1080-1097.

13. Elsner, N., Dubreuil, F., Weinkamer, R., Wasicek, M., Fischer, F. and A. Fery, *Mechanical properties of freestanding polyelectrolyte capsules: a quantitative*

approach based on shell theory, in *Characterization of Polymer Surfaces and Thin Films*. 2006, Springer. p. 117-123.

14. Fery, A. and R. Weinkamer, *Mechanical properties of micro-and nanocapsules: Single-capsule measurements.* Polymer, 2007. **48**(25): p. 7221-7235.

15. Dieluweit, S., Csiszár, A., Rubner, W., Fleischhauer, J., Houben, S. and R. Merkel, *Mechanical properties of bare and protein-coated giant unilamellar phospholipid vesicles. A comparative study of micropipet aspiration and atomic force microscopy.* Langmuir, 2010. **26**(13): p. 11041-11049.

16. Leonenko, Z., Cramb, D., Amrein, M. and E. Finot, *Atomic force microscopy: interaction forces measured in phospholipid monolayers, bilayers and cell membranes*, in *Applied scanning probe methods IX*. 2008, Springer. p. 207-234.

17. Lulevich, V.V., D. Andrienko, and O.I. Vinogradova, *Elasticity of polyelectrolyte multilayer microcapsules.* The Journal of chemical physics, 2004. **120**(8): p. 3822-3826.

18. Lulevich, V., Zink, T., Chen, H., Liu, F. and G. Liu, *Cell mechanics using atomic force microscopy-based single-cell compression.* Langmuir, 2006. **22**(19): p. 8151-8155.

19. Hertz, H., *On the contact of elastic solids.* J. reine angew. Math, 1881. **92**(1): p. 156-171.

20. Hertz, H.R., *Über die Berührung fester elastischer Körper und über die Härte.* 2006.

21. Johnson, K., K. Kendall, and A. Roberts. *Surface energy and the contact of elastic solids*. in *Proceedings of the Royal Society of London A: Mathematical, Physical and Engineering Sciences*. The Royal Society, 1971.**324**(1558): p. 301-313.

22. Weisenhorn, A.L., Khorsandi, M., Kasas, S., Gotzos, V. and H. Butt, *Deformation and height anomaly of soft surfaces studied with an AFM.* Nanotechnology, 1993. **4**(2): p. 106-113.

23. Donno, R., *Nanomechanical characterisation of cells and biocompatible substrates*. 2014, University of Manchester:UK, PhD thesis. P. 258

24. Dwyer-Joyce, R., *Tribological Design Data Part 3: Contact Mechanics.* University of Sheffield, 1997.

25. Lin, D.C. and F. Horkay, *Nanomechanics of polymer gels and biological tissues: a critical review of analytical approaches in the Hertzian regime and beyond.* Soft matter, 2008. **4**(4): p. 669-682.

26. Hu, M., Wang, J., Zhao, H., Dong, S. and J. Cai, *Nanostructure and nanomechanics analysis of lymphocyte using AFM: from resting, activated to apoptosis.* Journal of biomechanics, 2009. **42**(10): p. 1513-1519.

27. Radmacher, M., Fritz, M., Kacher, C.M., Cleveland, J.P. and P.K. Hansma, *Measuring the viscoelastic properties of human platelets with the atomic force microscope.* Biophysical journal, 1996. **70**(1): p. 556-567.

28. Laney, D.E., Garcia, R.A., Parsons, S.M. and H.G. Hansma, *Changes in the elastic properties of cholinergic synaptic vesicles as measured by atomic force microscopy.* Biophysical journal, 1997. **72**(2): p. 806-813.

29. Liang, X., G. Mao, and K.S. Ng, *Mechanical properties and stability measurement of cholesterol-containing liposome on mica by atomic force microscopy.* Journal of colloid and interface science, 2004. **278**(1): p. 53-62.

30. Lulevich, V., Shih, Y., Lo, S. and G. Liu, *Cell tracing dyes significantly change single cell mechanics.* The Journal of Physical Chemistry B, 2009. **113**(18): p. 6511-6519.

31. Costa, K. and F. Yin, *Analysis of indentation: implications for measuring mechanical properties with atomic force microscopy.* Transactions-American Society of Mechanical Engineers Journal of Biomechanical Engineering, 1999. **121**: p. 462-471.

32. Rico, F., Roca-Cusachs, P., Gavara, N., Farré, R., Rotger, M. and D. Navajas, *Probing mechanical properties of living cells by atomic force microscopy with blunted pyramidal cantilever tips.* Physical Review E, 2005. **72**(2): p. 021914-021923.

33. Sneddon, I.N. *Boussinesq's problem for a rigid cone*. in *Mathematical Proceedings of the Cambridge Philosophical Society*.. Cambridge University Press, 1948. **44**(4): p. 492-507.

34. Sneddon, I.N., *The relation between load and penetration in the axisymmetric Boussinesq problem for a punch of arbitrary profile.* International journal of engineering science, 1965. **3**(1): p. 47-57.

35. Butt, H.-J., B. Cappella, and M. Kappl, *Force measurements with the atomic force microscope: Technique, interpretation and applications.* Surface science reports, 2005. **59**(1): p. 1-152.

36. Love, A.E.H., *A treatise on the mathematical theory of elasticity*. 2013: Cambridge university press.

37. Dharan, C.K. and T. Tan, *A hysteresis-based damage parameter for notched composite laminates subjected to cyclic loading.* Journal of materials science, 2007. **42**(6): p. 2204-2207.

38. Atkinson, K.E., *An introduction to numerical analysis*. 2008: John Wiley & Sons.

39. Stewart, J., *Single variable calculus: Early transcendentals*. 2015: Cengage Learning.

40. Parthasaradhy, P. and S. Ranganayakulu, *Hysteresis and eddy current losses of magnetic material by Epstein frame method-novel approach.* Int. J. Eng. Sci.(IJES), 2014: p. 85-93.

41. Abou-Saleh, R.H., Peyman, S.A., Critchley, K., Evans, S.D. and N. Thomso, *Nanomechanics of lipid encapsulated microbubbles with functional coatings.* Langmuir, 2013. **29**(12): p. 4096-4103.

42. Briscoe, B., L. Fiori, and E. Pelillo, *Nano-indentation of polymeric surfaces.* Journal of Physics D: Applied Physics, 1998. **31**(19): p. 2395-2405.

43. Klymenko, O., Wiltowska-Zuber, J., Lekka, M. and W. Kwiatek, *Energy dissipation in the AFM elasticity measurements.* Acta Physica Polonica-Series A General Physics, 2009. **115**(2): p. 548-551.

44. Oliver, W.C. and G.M. Pharr, *An improved technique for determining hardness and elastic modulus using load and displacement sensing indentation experiments.* Journal of materials research, 1992. **7**(06): p. 1564-1583.

45. Hay, J.C., A. Bolshakov, and G. Pharr, *A critical examination of the fundamental relations used in the analysis of nanoindentation data.* Journal of materials Research, 1999. **14**(06): p. 2296-2305.

46. Boussinesq, J., *Application des potentiels à l'étude de l'équilibre et du mouvement des solides élastiques*. 1885: Gauthier-Villars.

47. Borodich, F.M. and L.M. Keer, *Contact problems and depth-sensing nanoindentation for frictionless and frictional boundary conditions.* International Journal of Solids and Structures, 2004. **41**(9): p. 2479-2499.

48. Costa, K.D., M.M. Ho, and C.T. Hung. *Multi-scale measurement of mechanical properties of soft samples with atomic force microscopy*. in *Summer bioengineering conference*. 2003. Sonesta Beach Resort in Key Biscayne, Florida, USA.

49. Pethicai, J., R. Hutchings, and W.C. Oliver, *Hardness measurement at penetration depths as small as 20 nm.* Philosophical Magazine A, 1983. **48**(4): p. 593-606.

50. Stone, D., LaFontaine, W., Alexopoulos, P., Wu, T. and C. Li, *An investigation of hardness and adhesion of sputter-deposited aluminum on silicon by utilizing a continuous indentation test.* Journal of Materials Research, 1988. **3**(01): p. 141-147.

51. Doerner, M.F. and W.D. Nix, *A method for interpreting the data from depth-sensing indentation instruments.* Journal of Materials research, 1986. **1**(04): p. 601-609.

52. Field, J. and M. Swain, *A simple predictive model for spherical indentation.* Journal of Materials Research, 1993. **8**(02): p. 297-306.

53. VanLandingham, M.R., *Review of instrumented indentation.* Journal of Research of the National Institute of Standards and Technology, 2003. **108**(4): p. 249-265.

54. Balooch, M., Wu-Magidi, I., Balazs, A., Lundkvist,A.S., Marshall, S.J., Marshall, G.W., Siekhaus, W.J. and J. H. Kinney, *Viscoelastic properties of demineralized human dentin measured in water with atomic force microscope (AFM)-based indentation.* Journal of biomedical materials research, 1998. **40**(4): p. 539-544.

55. Tabor, D., *The Hardness of Metals, Clarendon*. 1951, Oxford, UK: Oxford University Press.

56. Sakai, M., *The Meyer hardness: a measure for plasticity?* Journal of Materials Research, 1999. **14**(09): p. 3630-3639.

57. Turnbull, A. and D. White, *Nanoindentation and microindentation of weathered unplasticised poly-vinyl chloride (UPVC).* Journal of materials science, 1996. **31**(16): p. 4189-4198.

CHAPTER 4

EVALUATION OF THE NANOMECHANICAL PROPERTIES OF SONOVUE® USING TIPLESS CANTILEVER

CHAPTER 4: EVALUATION OF THE NANOMECHANICAL PROPERTIES OF SONOVUE® USING TIPLESS CANTILEVERS

4.1 Introduction

Microbubble-based contrast agents were introduced some years ago for the ultrasound imaging field, and their use is now widely established in routine clinical practice. [1] In the past years, a large number of studies have described and discussed the effectiveness of microbubble-based agents in many clinical and medical applications. [2-5] It is recognised that microbubble-based agents have received a high level of attention in the ultrasound (US) field. Moreover, there are many other applications for microbubbles, such as gene/drug therapy, where they can be used as delivery vehicles. [6,7] Although they have gained a wide adoption on the medical side, there is a lack of studies from the engineering perspective, especially in assessing their mechanical properties.

One of the types of microbubbles is the lipidic shell microbubble. This chapter will focus on certain factors and mechanical properties that may impact or control the behaviour of the lipid microbubbles, commercially called SonoVue® microbubbles, which will be shortened to MBs henceforth. The properties intended to be studied are those related to mechanical behaviour, or in other words, those that can measured by a direct mechanical test in addition to the other methods, for example, the effective stiffness of the shell and whole MB body, Young's Modulus, using different models, the hysteresis, plasticity and adhesion forces. The compression tool here is a

rectangular, flat, tipless cantilever. The chapter is divided into several sections. The first sections describe the material and its characteristics and the sample preparation methods. The sections describing the experimental test describe the machine (AFM) and its specifications in addition to describing the compression tool (cantilevers). The final part presents the results and their details.

4.2 Materials and Methods

4.2.1 Materials

In this research, Phospholipid-stabilized Microbubbles (MBs) of the type SonoVue® (Bracco UK Ltd., Ireland, United Kingdom) were used to evaluate their nanomechanical properties. One vial containing 25 mg lyophilized powder was reconstituted with 5ml sodium chloride 0.9% w/v for injection. [8] The lyophilisate is a combination of macrogol 4000, phospholipids (PLs) and palmitic acid. SonoVue® MBs are composed of a monolayer, as shown in Figure 4-1, [9] of two PLs, which are distearoylphosphatidylcholine (DSCP) and dipalmitoylphosphatidylglycerol sodium (DPPG.Na). SonoVue® is a second-generation [10, 11] contrast agent with a diameter of less than 8-10 μm (mean, 2.5 μm) [11-13] and smaller than a red blood cell. [8] SonoVue® MBs are small enough to overcome trapping in the capillary vasculature. Figure 4-2 [1] compares MB size to red blood cell size, where it can be seen that most of the MBs are smaller. These MBs encapsulate sulphur hexafluoride (SF_6) [8, 10] inert gas in a very thin shell, where the assumed thickness was around 5 nm, according to similar studies. [14, 15] As a highly elastic material, the Poisson's ratio was assumed to be 0.5, which is consistent with previous studies. [16-19]

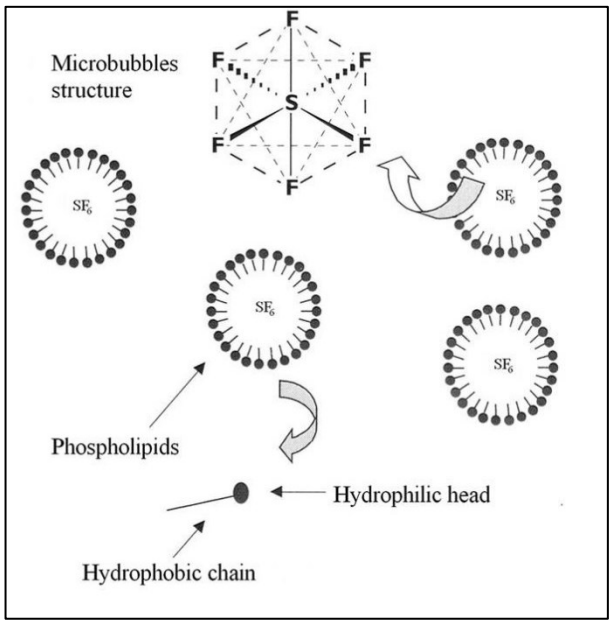

Figure 4-1: Schematic representation of SonoVue microbubble structure. Where the diameter of the majority of the MBs is less than 10 µm and the mean 2.5 µm. [9]

Sulphur hexafluoride is an inorganic, colourless, odourless, inert and non-flammable gas. [20] A molecule of this gas consists of six fluorine atoms attached to a central sulphur atom. It is safe and innocuous to use in medical applications. [12] Compared to air, the (SF_6) gas provides the bubbles with a higher resistance to pressure increases.[21, 22]

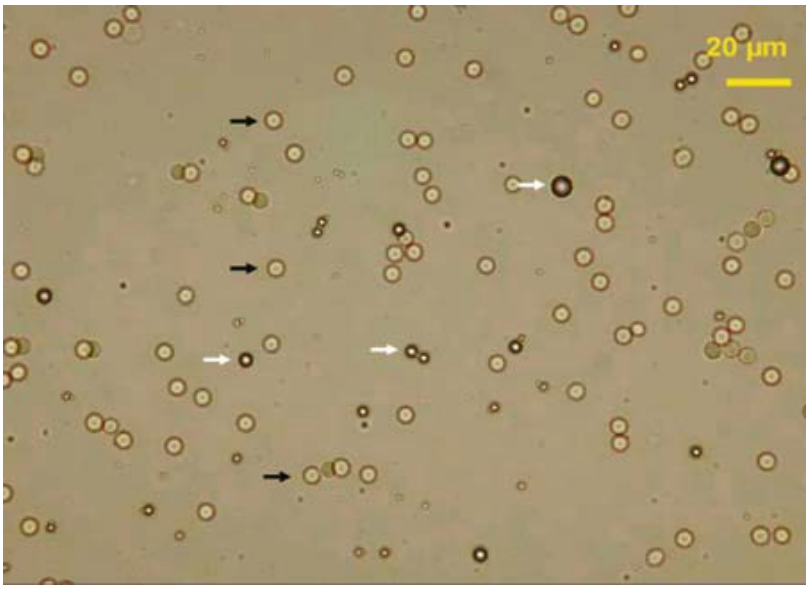

Figure 4-2: Microscopic photo of red blood cells (black arrows) (20× magnification; optical microscope) compared to SonoVue (white arrows) microbubbles. [1]

4.2.2 Sample Preparation

A package of commercial SonoVue microbubbles contains a glass vial with 25 mg lyophilized powder, holding a plastic vial, piston of the syringe and syringe filled with 5 ml sterile saline solution (see figure 4-3). Figure 4-4 illustrates vial preparation. To prepare the SonoVue microbubble vial, the piston of the syringe is turned clockwise to connect it to the plastic supporter. The lid of the syringe is then removed, and the syringe is turned clockwise to connect it to the plastic vial. After removing the blue lid of the glass vial, the operator holds the plastic supporter, with the index and middle fingers and pushes the lyophilized powder vial into the plastic vial, using his or her thumb, until a click is heard. The syringe piston is pushed to discharge the sterile saline solution into the lyophilized powder glass vial and the mixture has to be shaken gently for about 10s. A milky suspension of microbubbles is obtained, which has to stay at rest for about 1 min to help the microbubbles to break up. [1] Then the piston is pulled upwards to obtain the desired amount of microbubble mixture for the experiment.

In order to acquire accurate compression experiments on MBs, it is important to fix them on a hard surface to prevent them from slipping. Adhesion of the MBs to the surface can be obtained either physically, [14] as adopted in this study, or chemically. [23] Firstly, the internal surface of an appropriate cell culture dish (60X15mm, Greiner Bio-OneGmbH, Frickenhausen, Germany) needs to be coated with very thin layer of a 1:10 solution of poly-L-lysine (v/v) (Sigma-Aldrich Co., St. Louis, MO, USA). The internal dish surface specifications play an important role, therefore treated Greiner Cellstar® dishes are used. The excess amount of poly-L-lysine on the surface is sucked

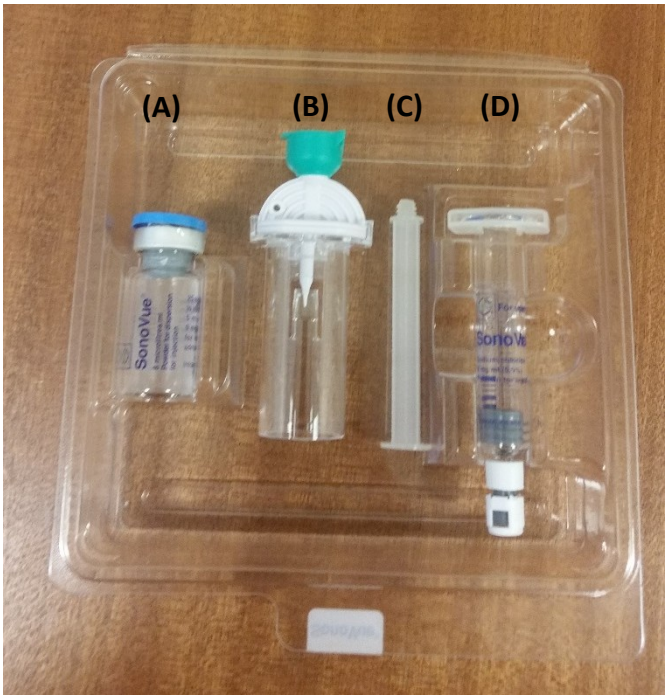

Figure 4-3: Package of the commercial SonoVue microbubbles consists of (A) glass vial with lyophilized powder, (B) plastic vial with supportive shoulders, (C) piston of the syringe and (D) syringe filled with sterile saline solution.

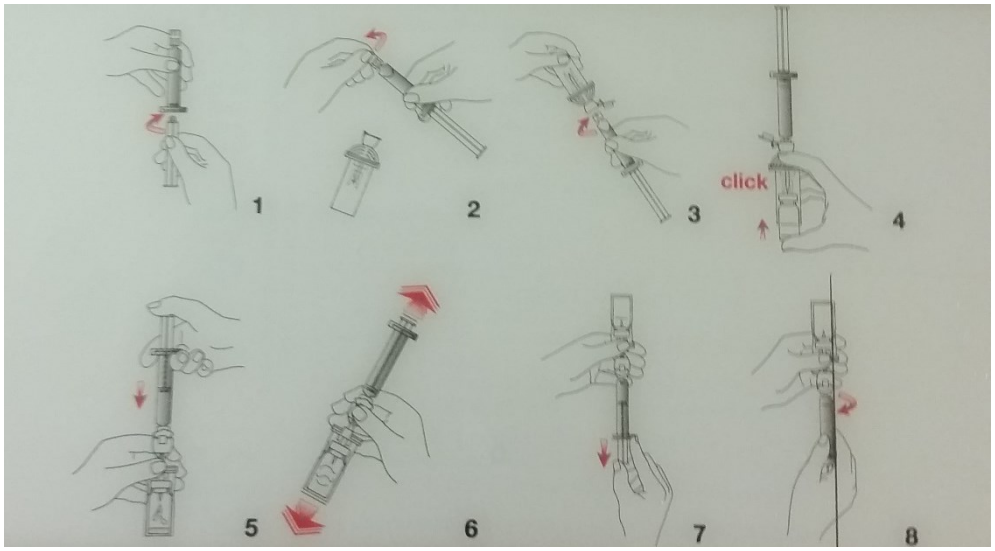

Figure 4-4: Schematic drawing showing SonoVue microbubble vial preparation steps, obtained from the packaging of the sample.

up by the syringe and washed lightly with deionised water. After coating the petri dish, it is left for around 3-5 minutes to acquire a sticky surface. Secondly, because the MBs are filled by an inert gas, each bubble floats like a ball in a swimming pool: this advantage gives us the ability to connect the MBs to a coated petri dish surface. A glass bowl larger than the cell culture dish is filled with distilled and deionised water with resistivity 18 MΩ cm, obtained from Ultra-Pure Water System (SG water system) (Evoqua Water Technologies, Warrendale, PA, USA). Then, using the syringe, around 0.3 ml of milky suspension MBs is added to the water bowl. Gently, the cell culture dish is placed upside down on the top of the water where the MBs are floating. When MBs come in contact with the dish surface, they stick onto it, because of the poly-L-lysine. The petri dish is turned every few minutes by 90^0, to ensure MBs distribution over the entire cell culture dish surface. This mechanism can be seen in schematic (A) and image (B) in figure 4-5. [14]

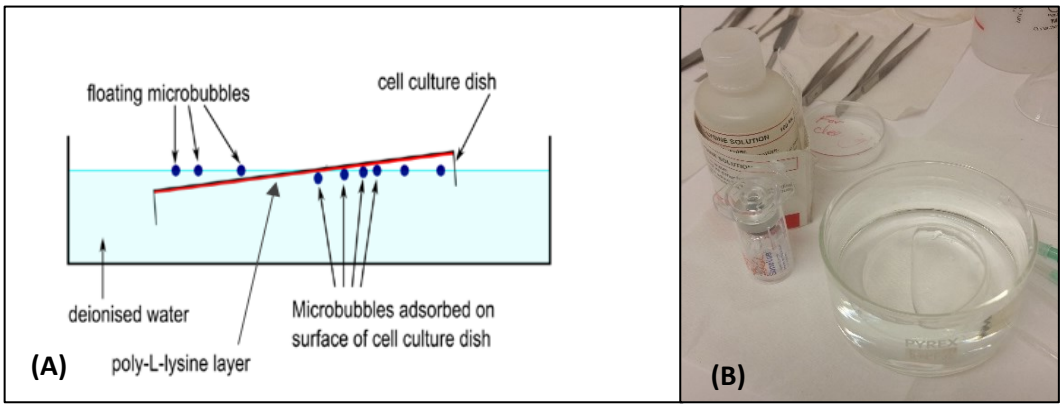

Figure 4-5: (A) Schematic illustrating the method of attaching MBs to a coated surface, with some modifications. (B) A photograph showing a petri dish inverted in a big bowl filled with distilled water and floating MBs, poly-L-lysine bottle and SonoVue MBs vial. [14]

A resting time of around ten to fifteen minutes is sufficient to produce a testable area of MBs on the petri dish surface. Gentle washing with deionised water is recommended

to remove undesired particles or any freestanding MBs. A sufficient amount of saline solution (0.9% Sodium Chloride), (Baxter, Compton, Newbury, UK) is added to immerse the MBs and the AFM tip. The samples are ready now for the real compression test.

4.2.3 Experimental Approach

A large number of experiments, involving more than 300 curves, were carried out, with some limitations, such as duration after opening the vial, where all the experiments had to be performed within 36 hours of opening the vial to obviate deterioration, decay or non-persistence of the MBs. [14] Thirty-nine MBs were tested over two days using different vials. The results where MBs behaved atypically (the force-deformation curve was messy and unusual) were excluded from the analysis. This could originate from a variety of causes and phenomena: for instance slipping or movement during the test, sticking to the cantilever, premature shell destruction or simply displaying an odd curve shape. Eventually, consistent measurements in 18 MBs were acquired for further analysis. In order to capture MB deformation and forces the AFM force-distance curve mode was adopted. NSC 12 tipless cantilevers were used as a compression tool to perform at least 50 force curves for each MB with constant speed (3μm/s). The spring constants of the cantilevers were estimated by calibration procedures, which are explained elsewhere in this study, prior to the experiment. All three cantilevers on one side of the chip were calibrated at once, in anticipation of any breaking or other circumstances. Cantilever with 350μm length and 35μm width was used. Using a 60x immersion objective of an inverted optical microscope, four MB images were acquired and their diameters were measured; the mean was used in the

calculations. The last 5 curves, out of 8 curves, were considered to investigate the MB behaviour. All experiments were implemented in an aqueous environment to minimize adhesion and interference forces at room temperature. During the specimen test all vibration or heat sources, i.e. light, AC and camera, were turned off. The acquired raw data passed through several stages to convert them from deflection-distance to force-deformation curves, which will be explained in more detail elsewhere in this study. Before each MB compression, the cantilever was tested against a hard surface to make sure its sensitivity was still in the same range. The initial linear part of the force-deformation curve was taken into consideration to evaluate a MB's stiffness or effective spring constant.

4.2.4 Apparatus and Tools

The main instrument used in this study was one of the atomic force microscope (AFM) family, which is the molecular force probe (MFP 1-D) (Asylum Research, Santa Barbra, CA), which was mounted on a Nikon TE2000U (Nikon UK Limited, Surrey, UK) inverted optical microscope, in order to allow the placement of the microbubble below the cantilever before the force measurements and the determination of the measured microbubble size. Figure 4-6 shows a MB positioned exactly under tip of the cantilever before the test, taken using a digital camera connected to the inverted optical microscope. Figure 4-7 illustrates the laboratory where the experiments were performed, with some other equipment. The MFP 1-D was mounted on the inverted optical microscope and both were mounted on a pneumatic table to reduce the effect of vibrations and reaction forces

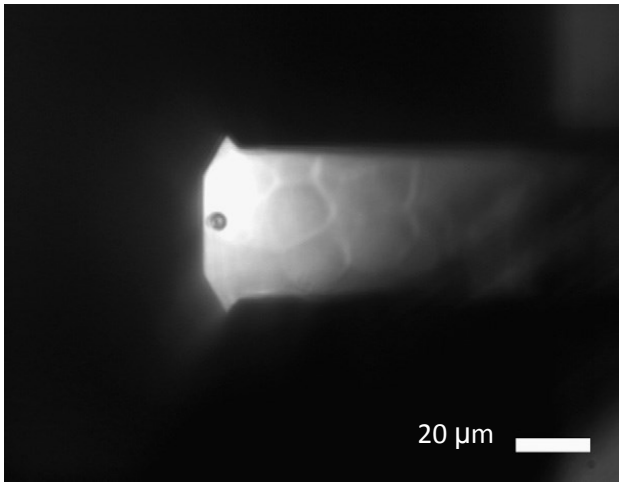

Figure 4-6: Optical microscopy image of a tipless cantilever with 35 µm width placed on the top of a microbubble in preparation for compression test.

. The system was connected to two computers, one for a digital camera (Orca-ER C4742-80, Hamamatsu Photonics, Hamamatsu, Japan) software IPLab v3.7 (BD Bioscience Bioimaging, Rockville, MD) and the other for the MFP-1D analyses program (IGOR Pro v.4.0), providing the ability to manipulate and control the experimental parameters and observe the images simultaneously.

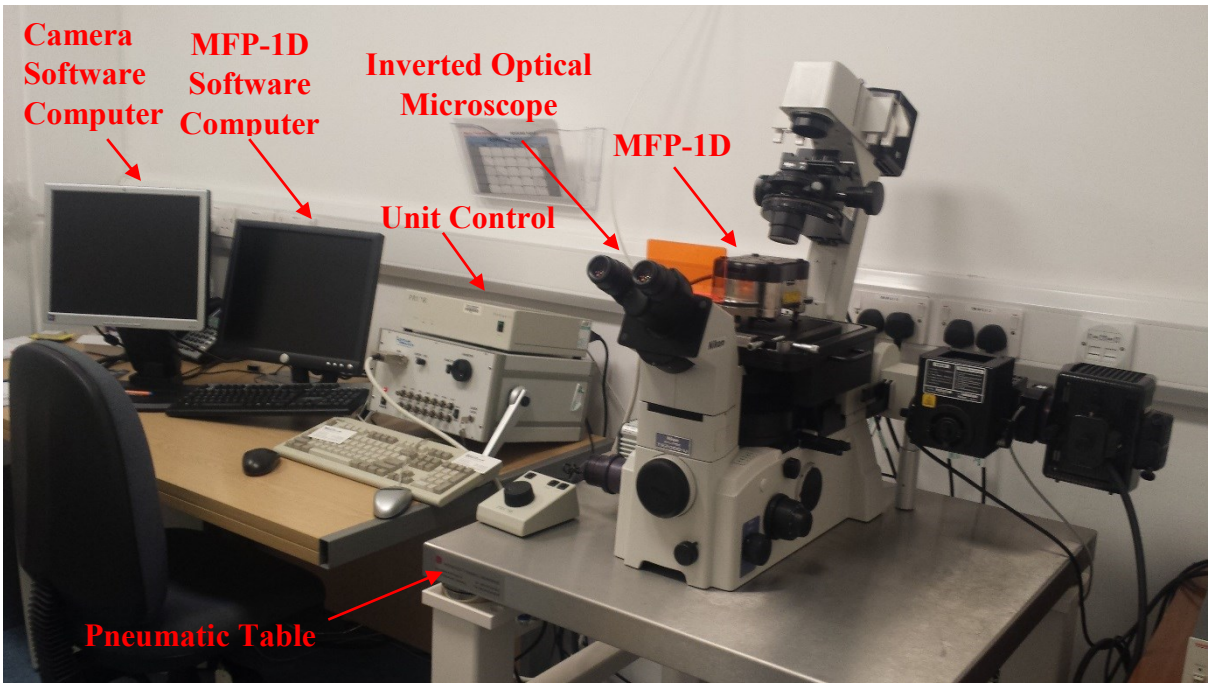

Figure 4-7: Showing the lab where experiments were performed and MFP-1D was placed on an inverted optical microscope connected to two computers by unit control.

AFM measurements were obtained using NSC 12/ tipless/ Al BS cantilevers (MikroMasch, Tallinn, Estonia) with aluminium backside coating Al (30 nm) and a silicon lever [24] with a calibrated spring constant in the range of 0.26±0.003 – 0.34±0.008 N/m, where the typical value in the data sheet was 0.3 N/m and the range 0.1-0.4 N/m. The cantilevers were moved with constant velocity (3 μm/s) and same distance, 3 μm, where this distance includes the contact and noncontact region.

The acquired raw position-deflection data were converted to force-distance (F-d) using Hook's law then transformed to force-deformation (F-Δ) by subtracting deflection of the cantilever from the piezo position and finally to force-relative deformation (F-ε) by dividing the initial diameter by the deformation of the MB. The stiffness of the MB was calculated from the gradient of force-deformation (F-Δ) curves, which depicts only the deformation of the MB excluding the cantilever behaviour, while the Young's modulus is estimated from the gradient of the force-relative deformation (F-ε) curves with different powers, according to the adopted model.

4.3 Results

4.3.1 Introduction

Among the most important and the least understood physical properties of the MBs are the mechanical properties, and there is significant challenge to incorporate these parameters in modelling of and experiments with MBs. There are various experimental techniques used in this field, e.g. acoustical, optical, [25] micropipette aspiration [26] [27], osmotic swelling, [28] and flow cytometry [29]; however, these

techniques cannot provide us with a real direct mechanical test to evaluate the MB's mechanical properties. It is worth saying that the measurement of individual microbubble properties is important to boost the progress of microbubble science and can guide and drive both modelling and applications. Specifically, the measurement of the mechanical properties of the microbubbles can predict behaviour of the shell and the whole MB. The AFM was used to present a systematic study to assess the mechanical properties of individual microbubbles by acquiring position-deflection curves. This microscope is not just a tool to image the topography of solid objects at high resolution but can be used to provide data about local material properties, such as elasticity, the Hamaker constant, hardness, plasticity index, adhesion and surface charge densities. [25]

4.3.2 Tipless Cantilever

In this stage, the speed of the cantilever movement (load rate) was fixed during approach and retraction at 3μm/s, and cantilever deflection at 150 nm (force~ 45nN), while the diameters of MBs were varied to investigate the effect of the MB's size on the mechanical properties. The cantilevers were calibrated according to measurement of the intensity of thermal noise method, as proposed by Hutter and Bechhofer [30], to record the raw position-deflection data, which were subsequently converted to force-deformation (F-Δ), as explained previously. 18 MBs were acquired with different sizes, ranging in diameter from 2.80 μm to 16.16 μm and mean 8.17 μm where their curves are appropriate for further analyses to investigate the MBs mechanical properties. All experiments were performed in an aqueous environment.

Figure 4-8 shows a typical force-deformation (F-Δ) curve on a microbubble with diameter 8.28 μm and stiffness k_b= 0.158 N/m, using a cantilever with spring constant k_c= 0.2839 N/m. During approach and before the contact point between the cantilever and the microbubble surface the deflection is zero, as there are no long range forces. After the cantilever contacts the microbubble at 0 nm deformation the force is recorded as positive and the curve start to go up (blue line) with a nonlinear part at the beginning, followed by a linear region. At maximum force, in this curve 50 nN, the direction of the cantilever movement changes and the cantilever begins to retract (red line). When the cantilever reaches 0 nN force again, the microbubble attempts to attract the cantilever, pulling it down and producing an adhesion force, here -4.03 nN, in the negative direction of the force-axis. At a certain point after the adhesion force becomes weak, the microbubble suddenly releases the cantilever to be free of contact, reaching zero deformation and the cantilever moves away from the microbubble surface. In addition, the figure illustrates a divergence between the approach (load or trace, blue dashed line) and retraction (unload or retrace, red solid line) curves, producing a hysteresis area. It is worth mentioning that the adhesion force and hysteresis area do not exist or are not clearly visible in all curves; however, they depend on the type of cantilever and the specimen.

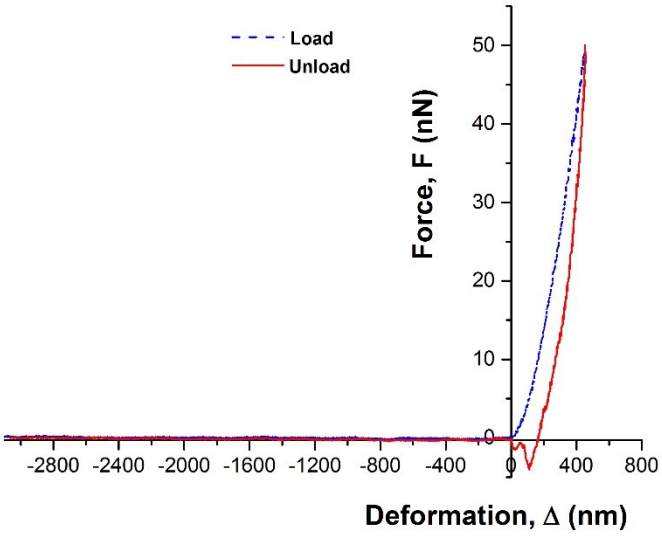

Figure 4-8: Illustrating force-deformation (F-Δ) curve for MB with D = 8.28 µm and stiffness (k_b) 0.158 N/m using a tipless cantilever with spring constant (k_c) 0.2839 N/m.

4.3.2.1 Stiffness

Many compression tests, more than 150 curves, were recorded in this study on 18 MBs with different diameters, with the intention to include a range of MBs, from one with a very large diameter (16.16 µm) compared to the mean to one much smaller (2.80 µm), to investigate the effect of the MB size on the mechanical properties. The MBs were compressed individually, gathering 8-10 curves for each MB. After obtaining the raw data and converting them to force-deformation (F-Δ) curves as explained in Chapter 3, the effective stiffness was calculated from the gradient of the initial linear part of the force-deformation (F-Δ) curve [15, 23], considering the third polynomial order fitting to make the calculation faster and make it easier to recognize

the linear part of the curve, especially for noisy curves, while maintaining high accuracy of the fitting where ($R^2 \geq 0.992$).

- **Instability**

After reviewing the F-Δ curves two regimes of behaviour were observed. The first one, represents most of the MBs (15 MBs), is a good, smooth curve while the second one, representing a minority of the MBs (3 MBs) is a curve or response appearing as unstable steps with either a sharp or gradual change. Figure 4-9 illustrates the two types of curves. Figure 4-9-(a) shows a good curve, clean of unstable areas, for a MB with D= 10.28 μm using a cantilever with spring constant K_C= 0.2839 N/m. The curve starts with a nonlinear region (representing the soft repulsive part) [25] followed by a linear curve from 125 nm to 400 nm; deformation then could become nonlinear again. These nonlinear parts of the curve were excluded from the analysis. It is noticeable that, for most of the MBs the linear region starts in the range of 100-200 nm deformation, depending on MB size, loading rate, cantilever geometry and MB and type of cantilever, where it is much smaller with tipped cantilevers and low speed. The gradient of the linear part of the curve (red line) is 0.09 N/m, which reflects the effective stiffness of the MB.

Figure 4-9-(b) represents the force-deformation (F-Δ) curve of a MB with diameter D= 4.68 μm, using a cantilever with spring constant K_C= 0.2655 N/m. This curve, as usual, starts with a nonlinear region, followed by a linear part at 25 nm deformation, reaching 200 nm deformation. An area of instability appears between 200-300 nm deformation, moving in a horizontal direction with low or almost zero slope. After this step the curve recovers and gains its uptrend again, with a higher gradient than the

previous, from 300 nm to 550 nm deformation. The second instability step then emerges at 550 nm to 650 nm deformation, with negative slope, followed by linear curve with the steepest gradient. The effective stiffness of the MB was calculated from gradient of the initial linear part (red line) and before any unstable step, at 0.075 N/m, as seen in the figure.

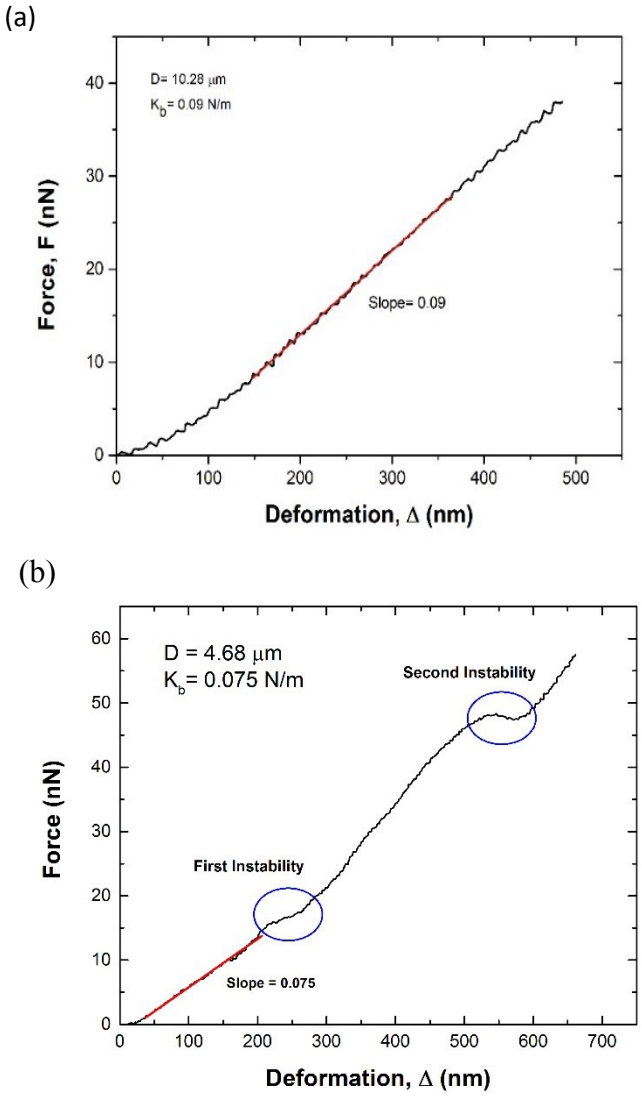

Figure 4-9: Illustrating two regimes of MB behaviour. (a) Shows a smooth curve clean of instability steps for a MB with D= 10.28 µm using a cantilever with spring constant K_C= 0.2839 N/m. (b) Curve with two instability areas for a MB with D=4.68 µm and using a cantilever with spring constant K_C= 0.2655 N/m.

When analysis was performed, it was recognized that the instability plays an important role in affecting the local stiffness of the MB, where the local stiffness increases noticeably after each unstable step, depending on the depth of the unstable area or depth of the buckling. This phenomenon appears in all the unstable curves, either showing sharp or gradual steps, and the local stiffness continues to increase unless the curve reaches the nonlinear region at the top of the curve.

Figure 4-10 shows a curve with three unstable regions (buckling steps) for a MB with diameter 3.20 μm and effective stiffness 0.058 N/m, using a cantilever with spring constant 0.2655 N/m. As usual, the curve starts with a small nonlinear region (indicating the soft repulsive part) of ~ 20 nm, followed by an initial linear curve with slope 0.058; after that, a sharp unstable step with 35 nm depth (5.7 % of deformation) appears and moves horizontally with zero slope at constant force ~ 8.5 nN, followed by another linear part with gradient 0.084, which is 45 % steeper than the initial slope. A second, sharp, unstable step occurs with depth 29 nm (4.7 % of deformation) at another constant force, ~ 13.5 nN, and later a linear curve with 0.10 slope, an increase of 19% above the previous one. A third instability emerges; however, this time it is a gradual step, with a greater depth of 85 nm (13.9 % of deformation), with a gradual increase in force from 32 nN to 39 nN. By the end of the curve the inclination is 0.18: 80% and 210% greater than the previous slope and the initial slope respectively. The slope (local stiffness) continues to increase after each unstable step until the curve becomes nonlinear again. It is worth noting that this phenomenon appeared in the behaviour of all MBs which have unstable steps.

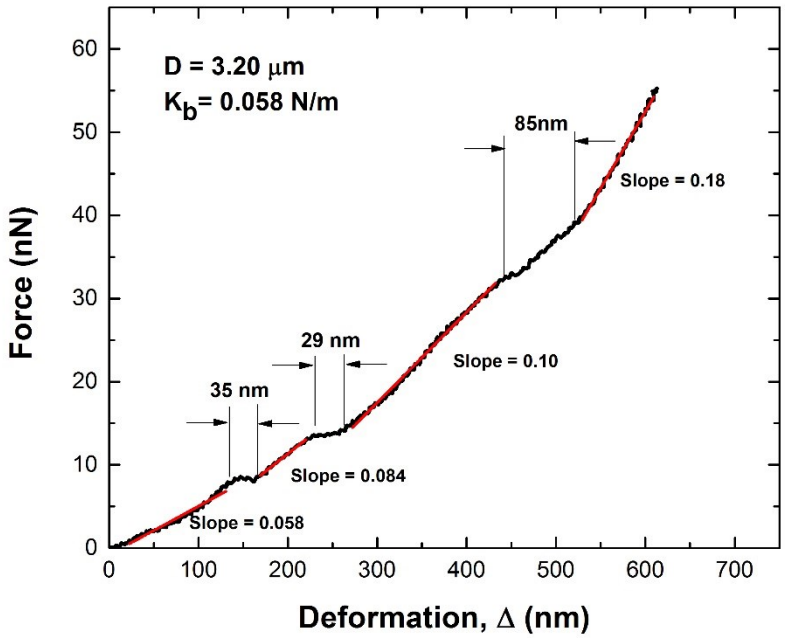

Figure 4-10: Representing a curve with three unstable steps, two of them sharp and one gradual, for a MB with size D= 3.20 μm and stiffness 0.058 N/m, where the local stiffness increases gradually after each step.

To predict the appearance of instability steps, or at which deformation depth the unstable steps will occur, according to relative deformation, a group of 4 MBs were studied which showed very clear and visible unstable steps. Figure 4-11 shows a set of 4 MBs with diameters in the range of 4.68 - 2.72 μm and average 3.73 μm. Each MB curve has two steps, where the first steps, solid black squares, appear in the range 0.024- 0.06 of relative deformation (ε), with mean 0.043 relative deformation (ε), and the second steps, hollow black squares, occur in the range 0.07- 0.16, with average 0.11 relative deformation (ε). It is clear that all the first steps begin at below 0.07 relative deformation ($\varepsilon < 0.07$) and the seconds steps occur at 0.07 onward ($\varepsilon \geq 0.07$).

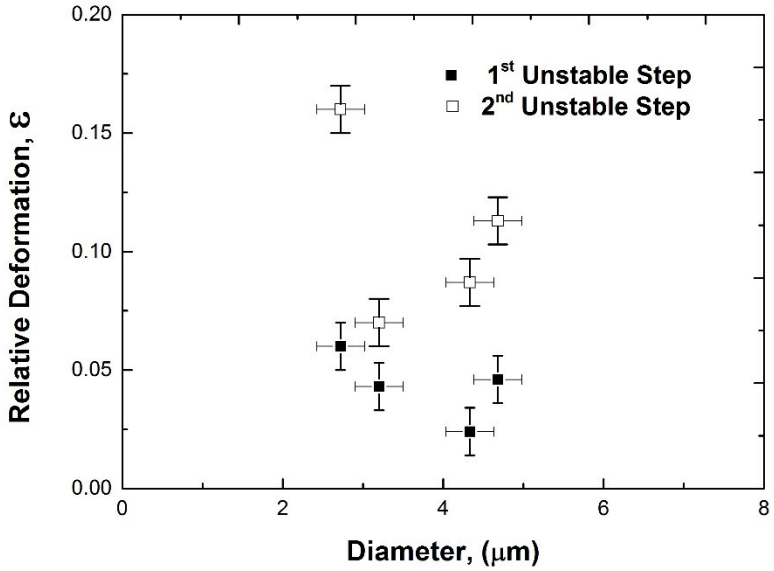

Figure 4-11: Representing a set of 4 MBs: each one has two unstable steps, where the first occurs at (ε < 0.07) while the second occurs at (ε ≥ 0.07).

- **Repeatability**

Each MB in this study was compressed to obtain 8-10 curves. The last 5 curves were adopted for each MB, to include any change which could occur in their behaviour at the end of the test, and also to give the machine plenty of curves to adjust itself, when shifting from MB to another, to reach the steady state, where the first curves could have an abnormal or odd curve shapes as a result of the adjustment of the machine itself according to the saved set point. After investigating the sets of curves, two types of repeatability were observed. The first one was a good repeatability where all the curves were moving in a very narrow path or completely identical, either with

unstable steps or without instability, which indicated that there was not any permanent plastic deformation. The second one also indicated a good repeatability, but at the end of the curves there were divergences, gaps between them, and change in the order of the curves, indicating that a small plastic deformation might have occurred.

Figure 4-12-(a) illustrates a good repeatability for the last 5 stable curves acquired from a MB with a diameter of 7.63 µm and average stiffness 0.185±0.008 N/m, using a cantilever with spring constant 0.284 N/m. All 5 curves are completely identical and there is no gap between them, indicating no permanent plastic deformation exists, nor is there any effect on the order of the curves, where curve No. 1 is the first acquired and curve No.5 is the last one. Figure 4-12-(b) shows a good repeatability for another set of 5 curves, however, this time with unstable steps, collected from a MB with a diameter 4.33 µm and average stiffness 0.075±0.001 N/m using a cantilever with spring constant 0.265 N/m. The five curves, even with unstable steps, are perfectly identical. Thus, no permanent plastic deformation has appeared.

The second case has a tiny divergence and a change in the position of the curves. Figure 4-13-(a) shows an acceptable repeatability for a set of 3 stable curves to be more visible than for all 5 curves. The curves were acquired from a MB with a diameter of 16.16 µm and average stiffness 0.076±0.009 N/m using a cantilever with spring constant 0.284N/m. The curves start from the origin point (0, 0) then go up, moving away from each other to end up with tiny gaps between the curves at the top of path. In addition, there is an order corresponding with the order of acquiring the curve, where the first represents the lowest stiffness and the last acquired represents the highest stiffness, which may indicate that there is some permanent plastic deformation.

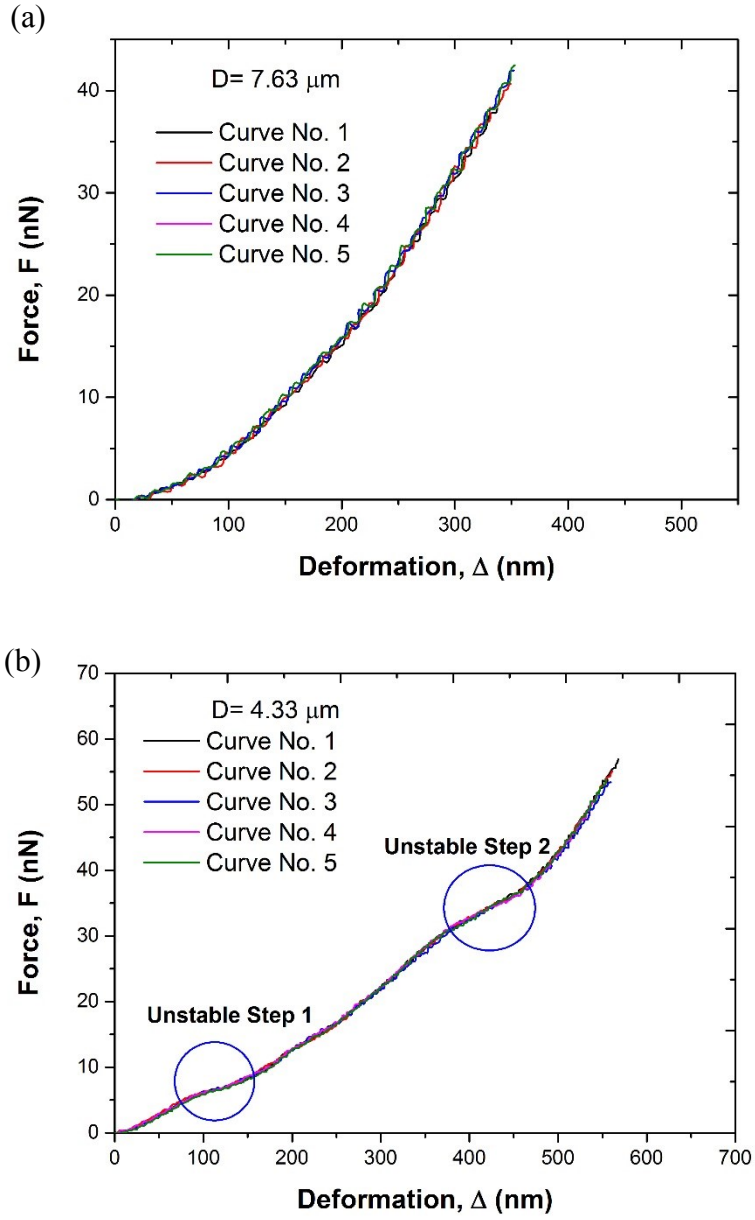

Figure 4-12: Showing two sets of 5 curves. (a) A set of five curves without instability are exactly identical. (b) Another five curves with two instabilities are identical too. Note that the first number is the first acquired.

The stiffnesses were 0.066, 0.068 and 0.075 N/m for the curve numbers 2, 3 and 4 respectively, where each curve shows a higher stiffness than the previous one. Figure 4-13-(b) represents a set of 3 unstable curves acquired from a MB with diameter 2.72 μm and average stiffness 0.054±0.004 N/m, using a cantilever with spring constant

0.266N/m. The curves start from point zero then go up, moving identically to each other, even after they have passed the first unstable step, and at the last unstable step, they end up with slight gaps between them but in an order consistent with their acquisition, which may indicate some plastic deformation. Because the first initial linear parts of the curves were considered in this analysis, before any unstable areas, their stiffnesses were almost the same.

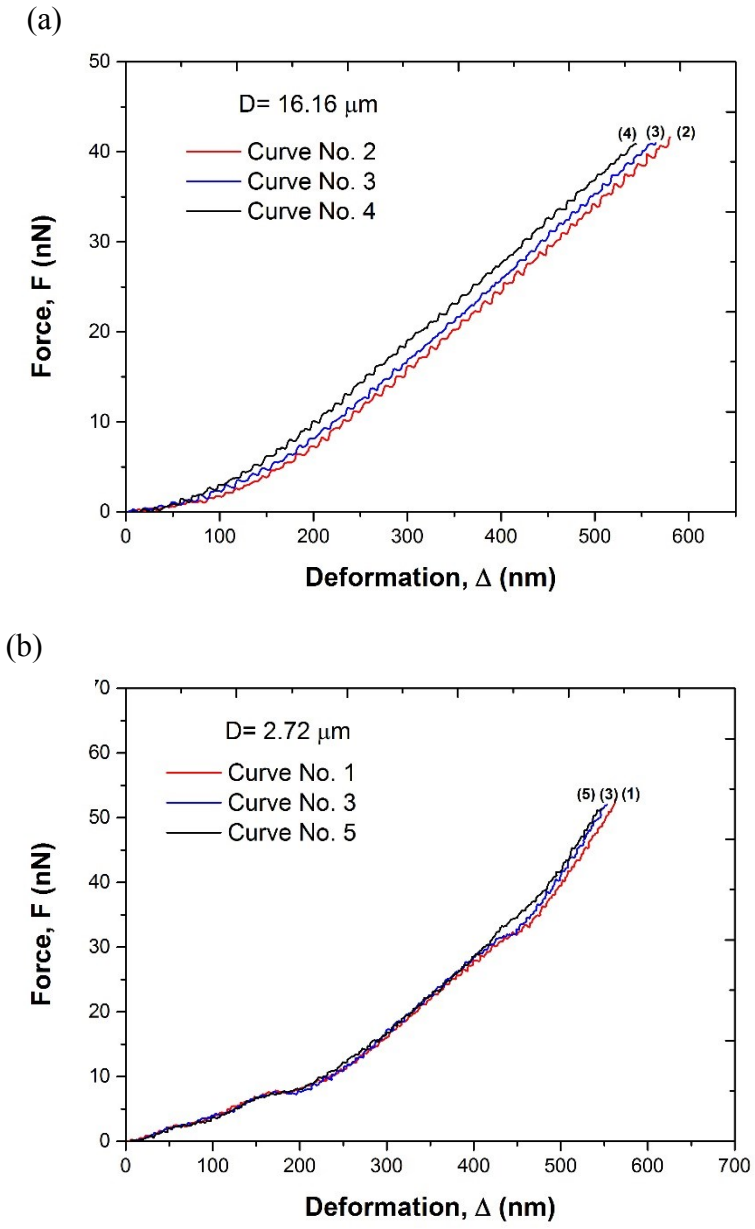

Figure 4-13: Illustrating the unrepeatability of both the stable and unstable curves. (a) A set of three curves without an unstable area shows little gaps. (b) Another three curves with two unstable areas have some divergence. Note that the first number is the first acquired.

- **Nonlinearity**

The curves for all the MBs (18 MBs) start with a nonlinear region. This nonlinearity depends on certain factors, such as MB size, cantilever speed (loading rate), cantilever geometry and characteristics both of the cantilever and the MB. The following figure focuses on some of these factors. Figure 4-14-(a) shows 3 curves for 3 MBs different in size, with diameters of 7.63, 10.28 and 13.46 μm and stiffnesses 0.158, 0.070 and 0.086 N/m, respectively. The speed of the cantilever was constant at 3 μm/s. The nonlinear region for the smallest MB (D=7.63 μm) was in the range 0-200 nm deformation (note that it has the highest stiffness) while the largest MB (D=13.46 μm) was in the range 0-50 nm deformation, with stiffness 0.086 N/m. It should be mentioned that the nonlinear region is occasionally tricky to determine. Figure 4-14-(b) shows the effect of the speed on the nonlinearity, where 3 curves are illustrated for a MB with diameter 13.46 μm and stiffness 0.086±0.010N/m. The speeds were varied at 12, 30 and 60 μm/s. The nonlinear region ends at 100, 250 and 350 nm deformation for the speeds 12, 30 and 60 μm/s, respectively.

Many experiments, producing 90 curves, were performed to investigate the correlation between the stiffness and MB size. All stiffnesses were calculated after the nonlinear region, which sometimes extended to and exceeded 200 nm deformation or more, reaching half of the maximum force. [23] The effective stiffnesses were calculated by the average of 5 curves for each MB. Figure 4-15 shows the effective stiffnesses of 18 MBs with diameters in the range of 2.72-16.16 μm and mean 8.17 μm giving stiffnesses in the range 0.048±0.010N/m (stable, unrepeatable) to

0.158±0.007N/m (stable, repeatable) and average 0.09±0.03N/m. It should be noted that, here, "stable, repeatable" means that the curves do not have any instability area and all the curves are identical during the whole tracing (loading) curve and vice versa for "unstable, unrepeatable".

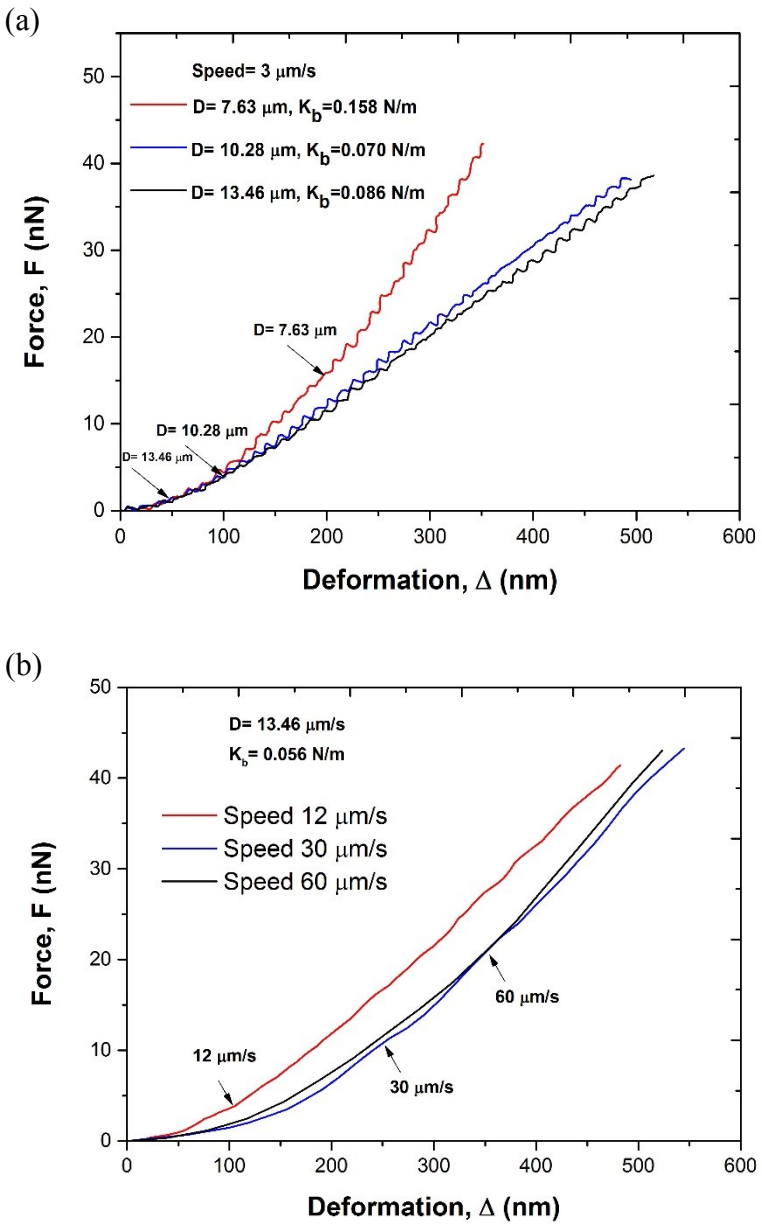

Figure 4-14: Showing the effect of some factors on the nonlinear region. (a) A set of three curves illustrating the effect of the MB size and stiffness on the nonlinear region. (b) Another three curves, illustrating the effect of speed on the nonlinear region.

It is clear that no correlation or trend can be observed between stiffness and MB size where the Pearson correlation coefficient, r = 0.3, and coefficient of determination (R-squared), $R^2 = 0.05$. As can be seen, the results are dispersed widely, forming a triangle shape where the highest stiffness values (stable, repeatable) are in the middle around the mean diameter (8-9 μm) and at the head of the triangle, while the lowest values (stable unrepeatable) are at the tips of the triangle base (at the smallest and largest diameters). In addition, the figure summarizes my previous results, in that most of the curves of the MBs (7 MBs, 38.89%) are stable and repeatable during whole of the test, (solid black squares) ranging in diameter from 6.55 μm to 13.87 μm and some of them (6 MBs, 33.33%) are stable but unrepeatable (hollow black square) distributed among all the diameters from the smallest to the largest. Other curves of MBs (2 MBs, 11.11% with diameters 4.33 μm and 7.89 μm) are unstable and repeatable (solid red triangle). The rest of the curves (3 MBs, 16.67%) are unstable and unrepeatable (hollow red triangle), with diameters in the range 2.72 - 4.68 μm, which is the lowest range of the diameters. It is clear that the unstable unrepeatable (red hollow triangle) curves are for the small and relatively soft (0.054-0.075 N/m) members of the population. No fracture behaviour or shell rupture was seen in any MB, although some of the MBs suffered a high degree of deformation ($\varepsilon = 0.75$), which means the initial diameter was compressed to 25% of its original value.

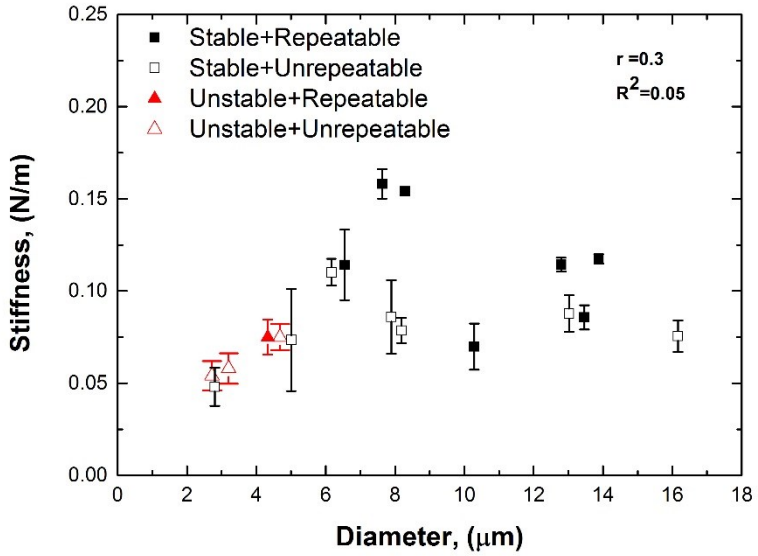

Figure 4-15: Showing the effective stiffness values for 18 MBs with diameters ranging from 2.72 μm to 16.16 μm and stiffnesses from 0.048 N/m to 0.158 N/m

4.3.2.2 Young's Modulus

In this section the acquired curves are used to investigate Young's Modulus, by applying three different models: Reissner's theory, the elastic membrane theory and Hertz theory. These models are used to calculate elasticity of the MBs: two of them, the Reissner and elastic membrane theories are used to estimate the elasticity of the MB shell, while the third one, Hertz Theory, is used to assess the elasticity of the whole MB body. After gathering the raw data and converting them to force-deformation (F-Δ) the deformation was divided by the initial diameter to give the relative deformation ($\varepsilon = \Delta/D_o$). The Young's Modulus was calculated from gradient of the force-relative deformation (F- ε) curve, where the relative deformation (ε) was raised to different

powers, according to the adopted model, and multiplied by an associated factor which was consistent with the model. The curves used were (F - ε), (F - ε^3) and (F - $\varepsilon^{3/2}$) for the Reissner, elastic membrane and Hertz theories respectively. In this study, the calculations were built on the assumptions that Poisson's ratio (ν) is 0.5, as MBs are compliant and compressible materials, and thickness (t) of the MB shell is 5 nm, consistently with previous similar studies in the field. As usually 5 curves were considered to calculate The Young's Modulus for each individual MB.

- **Reissner's Theory**

Figure 4-16-(a) shows a typical force-relative deformation (F- ε) curve for one of the 18 MBs, where the diameter 10.28 μm and the effective stiffness 0.09±0.01N/m. The curve starts with a nonlinear region followed by a linear part from ε = 0.015 to ε = 0.035 where the curve becomes nonlinear again. The gradient of the linear region, 934 nN, is multiplied by the associated factor, in this case 0.015 $(nm)^{-2}$, see equation 11 Chapter 3, producing a Young's modulus value of 14.0 GPa. Figure 4-16-(b) illustrates a set of 18 MBs with diameters in the range 2.72- 16.16 μm and effective stiffness 0.048- 0.18 N/m, to investigate the relation between the MBs size and the Young's modulus values. The Young's modulus values were in the range of 2.0-24.2 GPa and mean 12.8 GPa. It is clear that there is a correlation between Young's modulus and the MB's diameter, with an uptrend where the Young's modulus increases with increasing MB size where the Pearson correlation coefficient, r = 0.8, and coefficient of determination (R-squared), R^2 = 0.6. Figure 4-17 shows this relation using a

histogram graph where there is clearly an increasing trend between the Young's modulus and the MB's diameter.

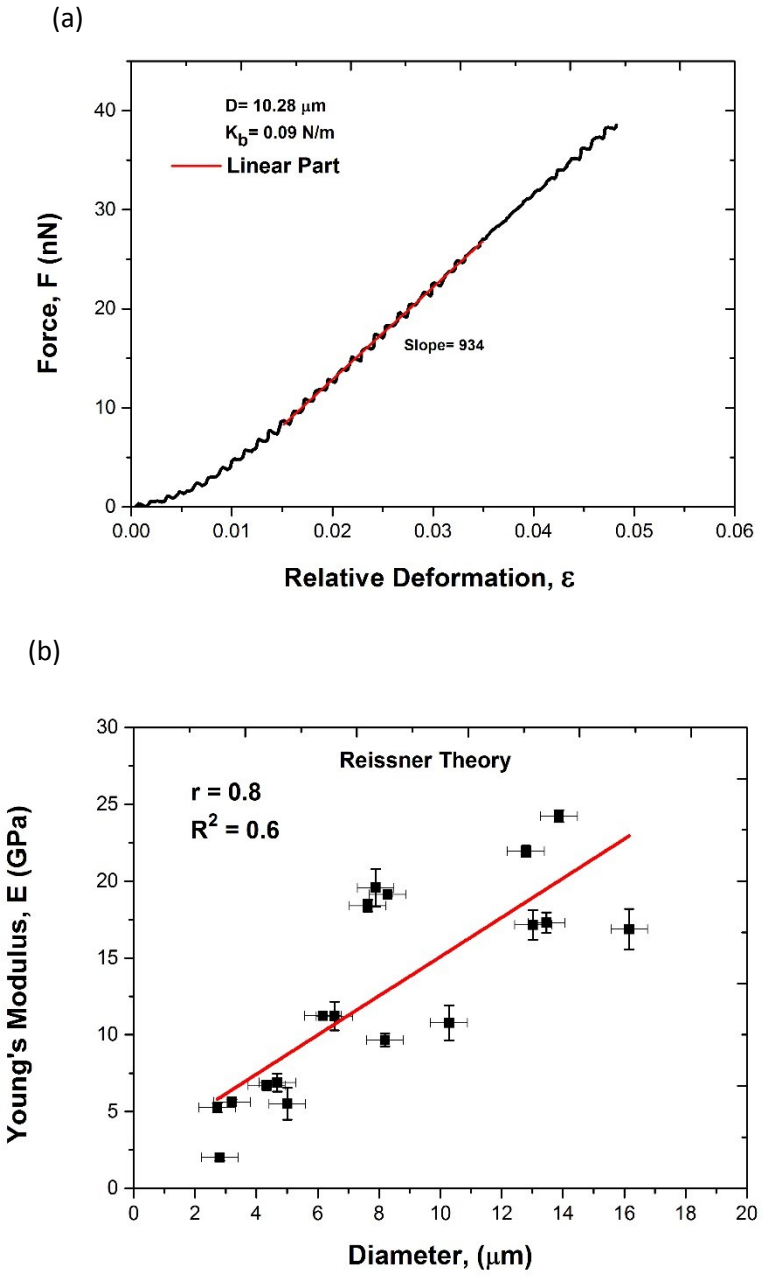

Figure 4-16: (a) A typical force-relative deformation (F- ε) curve for a MB with diameter 10.28μm and effective stiffness 0.09±0.01N/m. (b) Showing the relation between Young's modulus and the MBs size using Reissner theory.

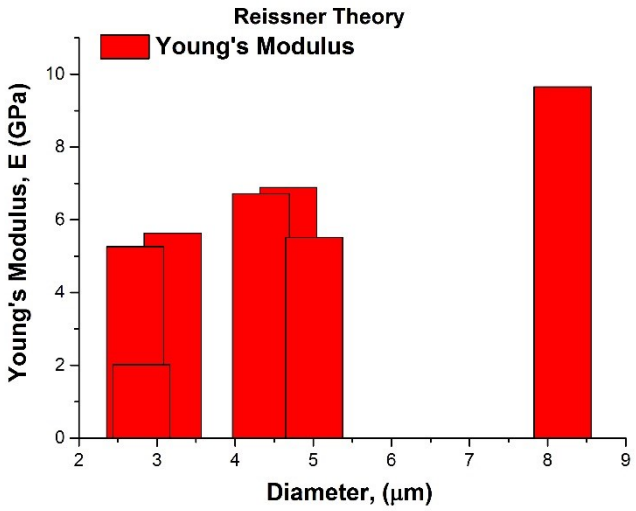

Figure 4-17: Showing the correlation between Young's modulus and the MBs' size using Reissner theory with histogram plot.

- **Elastic Membrane Theory**

This study investigates the elasticity of the MB shell by adapting the stretching component of elastic membrane theory and neglecting the bending component, where the thickness of the MB compared to its initial radius (R_0) is very small ($t << R_0$). [15] The relative deformation (ε) was large and the ratio between bending force and stretching force was small ($F_b/F_s \leq 0.08$), which indicates that the stretching component is the most dominant and there were no reasons to neglect the stretching term because the critical relative deformation values were so small ($\varepsilon_{cit} \leq 0.012$) and the relative deformation (ε) values were large ($\varepsilon \geq 0.04$), note that at ε_{cit} the ratio ($F_s/F_b = 0.05$). Figure 4-18-(a) shows a typical force-relative deformation to the power three

(F- ε^3) curve for one of the 18 MBs, where the diameter is 6.55 μm and the effective stiffness 0.11±0.02N/m. The curve starts with a nonlinear region, followed by a linear region at the end of the curve, from around ε^3= 0.0002 to almost the end of the curve. Note that the linear part of the F- ε^3 curve is not easy to define as most of the curve is nonlinear; however, it is usually at the end of the curve. The gradient of the linear region is 63090 nN multiplied by the associated factor, in this case 4.86×10^{-6} $(nm)^{-2}$, see equation 17 Chapter 3, producing a Young's modulus value of 0.3 GPa (300 MPa). Figure 4-18-(b) represents a set of 18 MBs with diameters in the range 2.72 - 16.16 μm and effective stiffness 0.048- 0.18 N/m, to investigate the relation between the MBs size and the Young's modulus values using elastic membrane theory. The Young's modulus values were in the range of 0.043-1.5 GPa and mean 0.46 GPa. It is possible that there is a slight suggestion of a correlation between Young's modulus and MB diameter, with an uptrend where the Pearson correlation coefficient, r = 0.7, and coefficient of determination (R-squared), R^2 = 0.5. Figure 4-19 displays the correlation between Young's modulus and MB size using the histogram plot however the relation does not appear clearly as in Figure 4-18-(b).

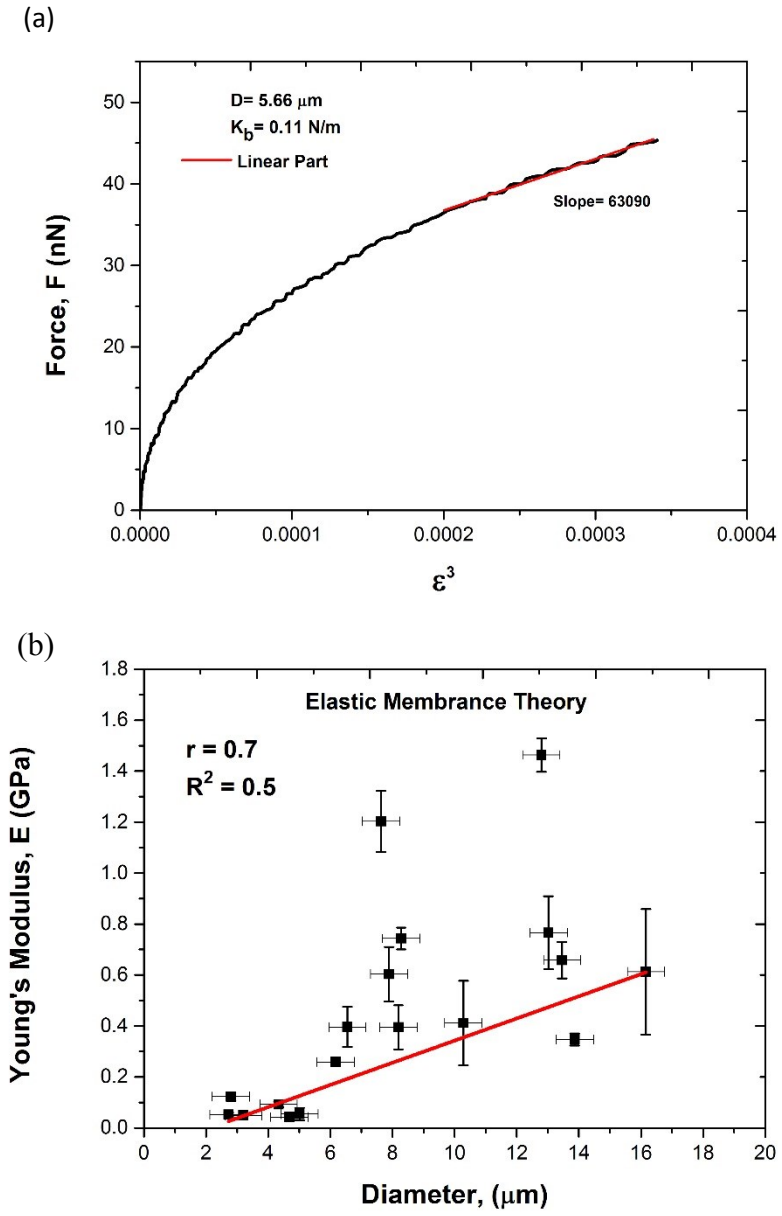

Figure 4-18: (a) Representing a typical F- ε^3 curve for a MB with diameter 6.55 μm and effective stiffness 0.11±0.02N/m. (b) Showing the relation between Young's modulus and the MBs' size using elastic membrane theory.

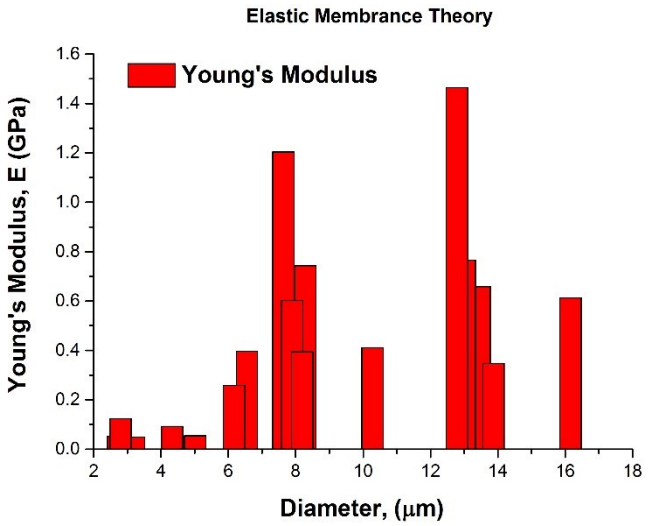

Figure 4-19: Showing the correlation between Young's modulus and the MBs' size using histogram plot.

- **Hertz Theory**

While the previous theories study the elasticity of the MB shell, Hertz theory studies the elasticity of the whole MB body as two spheres in contact with each other. The difference between the spheres is their diameter. One of them, the MB, has a specific diameter; however, the second, the cantilever, has an infinite diameter and is acting as a huge ball. Figure 4-20-(a) shows a typical force-relative deformation to the power one and half (F- $\varepsilon^{3/2}$) curve for one of the 18 MBs, where the diameter is 6.17 μm and the effective stiffness 0.11±0.001N/m. Unusually, the curve does not start with a nonlinear region and almost all of the curve is a linear curve. It is notable that most of the MBs have nonlinear regions at the beginning and end of the curve. The gradient of the linear region was 1883 nN, multiplied by the associated factor, in this case

$1.67x10^{-7}$ $(nm)^{-2}$, see equation 20 Chapter 3, producing a Young's modulus value of $3.10x10^{-4}$ GPa (310 kPa). Figure 4-20-(b) shows curves for a set of 18 MBs having diameters in the range 2.72- 16.16 μm and effective stiffness 0.048- 0.18 N/m, to estimate the relation between the MBs' size and the Young's modulus values using Hertz theory. The Young's modulus values were in the range of $1.44x10^{-4}$- $4.5x10^{-4}$ GPa and mean $2.96x10^{-4}$ GPa (296 kPa). It might be suggested that there is a link between Young's modulus (of the whole MB) and MB diameter, with a downtrend where the Pearson correlation coefficient, r = -0.7, and coefficient of determination (R-squared), $R^2 = 0.4$. Figure 4-21 shows the relation between the Young's modulus and the MBs' size using histogram plot and the correlation appears clearly; a decreasing trend connects them.

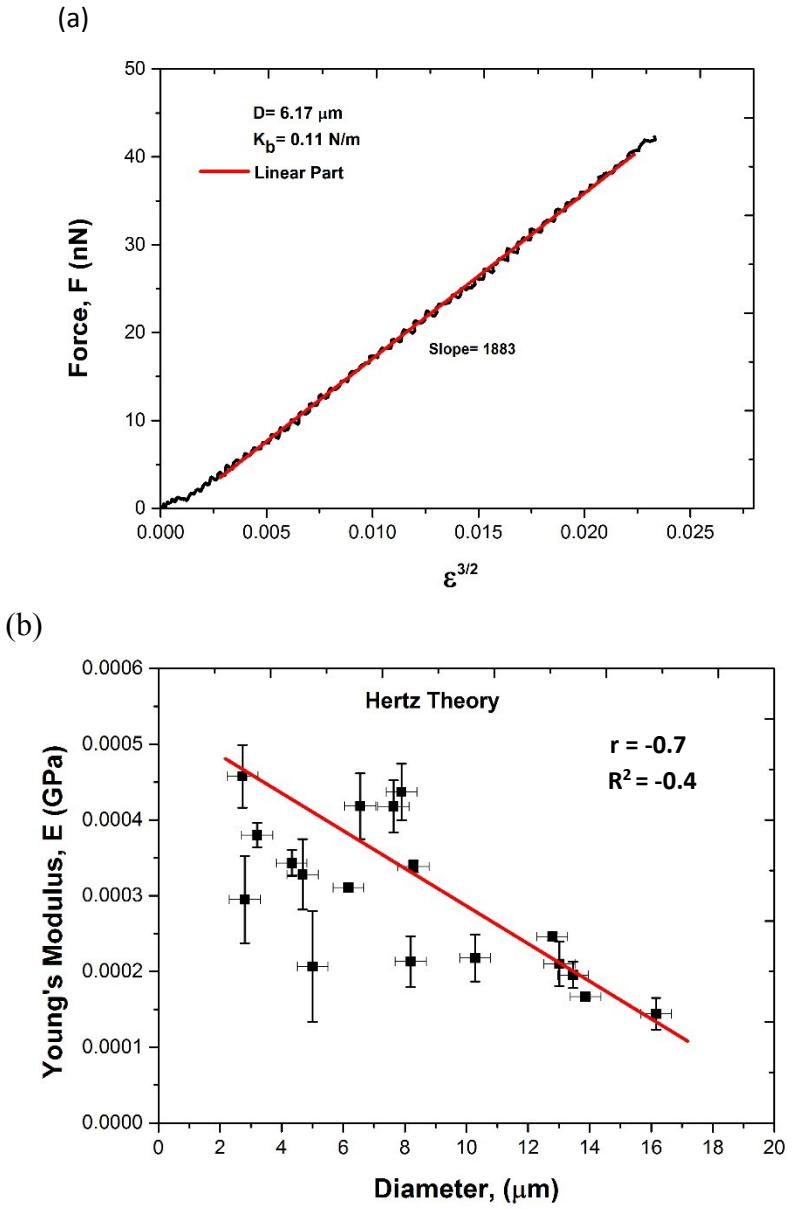

Figure 4-20: (a) A typical F- $\varepsilon^{3/2}$ curve for a MB with diameter 6.17 μm and effective stiffness 0.11±0.001N/m. (b) Showing the correlation between Young's modulus and the MBs' size using Hertz theory.

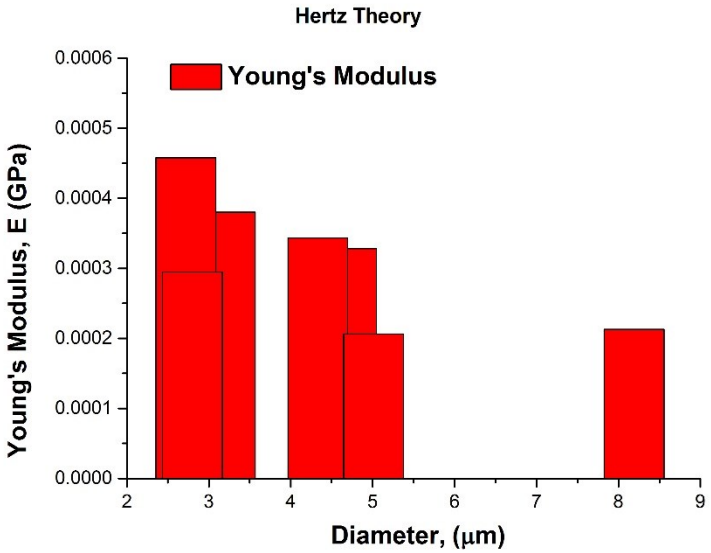

Figure 4-21: Showing the correlation between Young's modulus and the MBs' size using Hertz theory using histogram plot.

4.3.2.3 Hysteresis and Plasticity

- **Hysteresis**

Viscoelastic hysteresis is one of the hysteresis types that should be highlighted because of the energy loss that accompanies it. [31, 32] When a MB is exposed to a load (trace) and unload (retrace) cycle, the two curves produce an area, because of the divergence between them and this cycle is called a hysteresis loop. The area confined between the two curves expresses the energy dissipated during the compression processing cycle due to the materials' internal friction, which is possible to be observed in the form of a rise in temperature of the material. The MB is composed of soft materials that can exhibit a hysteresis area [33, 34] during the compression cycle, with a size depending on the nature of the MB and the experimental conditions. All MBs tested in the study showed either a small or significant hysteresis. Figure 4-22 shows two types of generated hysteresis. Figure 4-22-a displays a very small hysteresis for a

MB with diameter 12.79 μm and stiffness 0.11 N/m, using a cantilever with spring constant 0.2655 N/m, reaching to maximum force 46.6 nN, and producing 605 nN.nm hysteresis area. In contrast, Figure 4-22-b represents a large hysteresis for a MB with diameter 13.46 μm and effective stiffness 0.09 N/m, where the compression tool was a cantilever with spring constant 0.2839 N/m with maximum force 42.6 nN. This MB gives 3610 nN.nm hysteresis area. Even though both of the MBs were subjected to almost the same conditions, they produced different hysteresis areas. It should be noted that the hysteresis areas were estimated using a trapezoidal rule (see Chapter 3 for more detail).

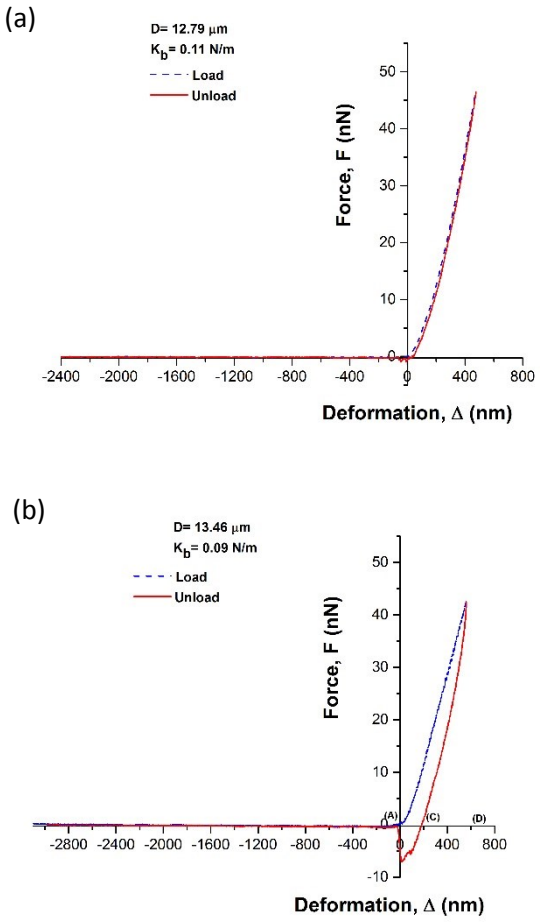

Figure 4-22: Showing two types of hysteresis, a small hysteresis area (a) and a comparatively large hysteresis area (b) at almost the same conditions.

To study the impact of other parameters on hysteresis, some of these factors are represented in figures to predict any correlation existing between them. Some parameters which could have an effect on the hysteresis area, such as MB size and effective stiffness, are reviewed here. Figure 4-23-a shows the link between MB size and hysteresis area for a set of 18 MBs with diameters from 2.72 μm to 16.16 μm and effective stiffness in the range 0.048- 0.18 N/m. The hysteresis areas were in the range of 469-12732 nN.nm and mean 4490 nN.nm. It is clear that no clear correlation was observed; the best coefficient of determination (R-squared), R^2 = 0.18, unless we neglect the two out of trend MBs with diameters 13.87 μm and 12.79 μm (red circle), in which case a good exponential decay fitting is obtained, where it is decreasing rapidly to a certain value then moves consistently. For the same group of MBs, Figure 4-23-b shows the relation of the hysteresis area to effective stiffness, where no specific correlation was observed; the best coefficient of determination (R-squared), R^2 = 0.16. Assuming that the MBs are completely spherical, having a homogenous diameter and homogenous thickness and, moreover, that the volume is constant, with incompressible gas, during the compression cycle, it is worth estimating the energy loss per cycle per unit volume. The hysteresis loss [35] per unit volume can be calculated by dividing the hysteresis area by the volume of the MB. The hysteresis loss per unit volume was in the range of 0.18 - 87.5 kJ/m^3 (kPa) and mean 14.1 kJ/m^3 (kPa). The 18 MBs were again assessed to predict the effect of MB size on hysteresis loss per cycle; Figure 4-24 represents this relationship.

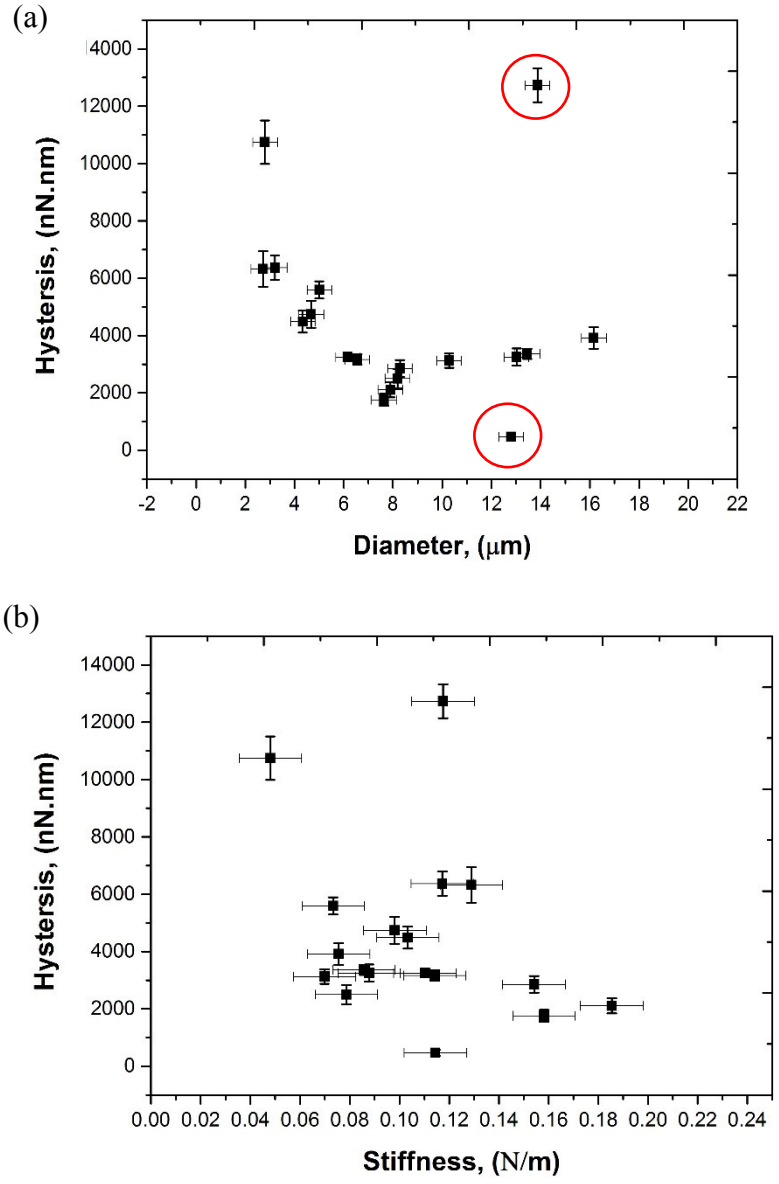

Figure 4-17 (a) The relation between hysteresis and diameter; the two circles indicate the two MBs which are out of the group; (b) The correlation between hysteresis and stiffness.

It is clear that the relationship is an exponential decay type (fitting curve) where; the coefficient of determination (R-squared), R^2 = 0.9 and there is a significant decrease in hysteresis loss when the MB size decreases, until around 6 μm diameter, when it then remains at almost a constant value, with average 2.4 kJ/m^3 (kPa), which means the large MB (D > 6 μm) undergoes less energy loss while the small MB (D ≤ 6 μm) will lose more energy. It is notable that even the two outlying MBs in Figure 4-23-a have vanished and become incorporated within the group.

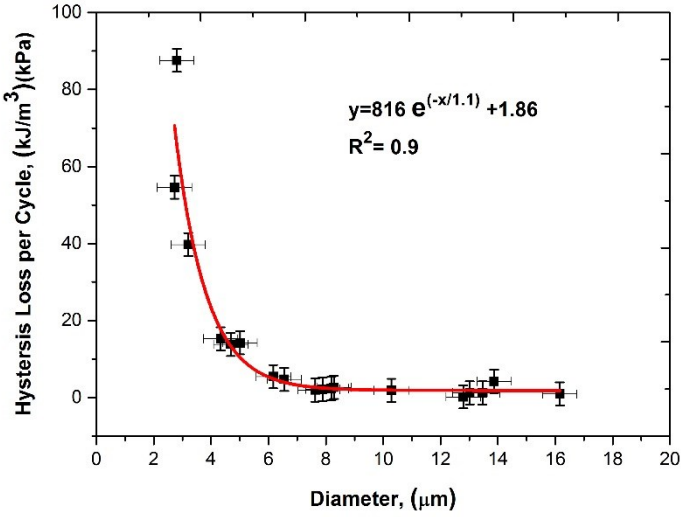

Figure 4-24: Showing the correlation between MB size and energy loss per cycle per unit volume.

- **Plasticity**

When compressing soft materials, e.g. phospholipid MBs, viscoelastic behaviour may take place. [23] Hysteresis between loading and unloading was observed for all MBs, as presented in the previous section. The data acquired from the unloading curve represent a reading for the elastic, viscoelastic and plastic behaviour. [36] Viscoelastic behaviour of the MBs can be estimated by calculating the plasticity index (η) by using the hysteresis area, which reflects the relative plastic/elastic behaviour of the material. Plasticity index (η) is equal to the ratio of the unloading area (A_u) to the loading area (A_l); thus ($\eta=1- A_u/ A_l$). [37] For a totally elastic sample $A_u = A_l$ and the unloading curve is identical to the loading curve, so η=0. On the other hand, for purely plastic samples $A_u = 0$: that is, the unloading curve is perpendicular to the x-axis (deformation axis) and η=1. [36-38]

All 18 MBs display a viscoelastic behaviour resulting in either a small hysteresis, as shown previously in Figure 4-20-a, in which case the sample behaves as a fully elastic material, where the plasticity index is too small (η=0.07), or a very large hysteresis, as appears in Figure 4-25, for a MB with diameter 2.8 μm and stiffness 0.05 N/m, which means that the MB has totally plastic behaviour, where (η=0.99). It can be seen that the unloading curve is approximately perpendicular to the x-axis (deformation axis) and the area under the unloading curve (A_u) is nearly zero. The index of plasticity (η) is in the range from 0.07 to 0.99 and its average is 0.47 ±0.2.

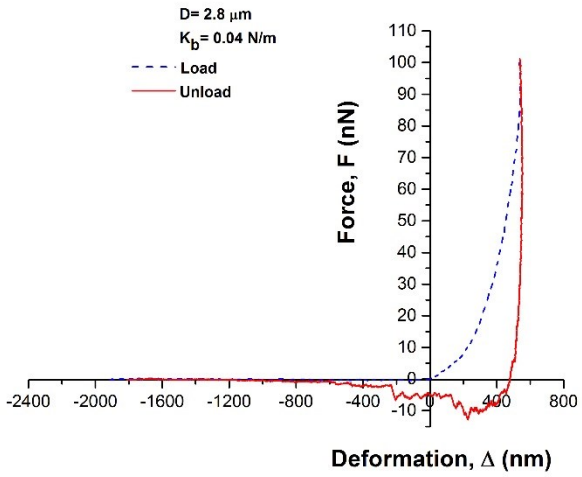

Figure 4-2518: Shows load and unload curves with large hysteresis, where the MB behaves as a fully plastic material (η=0.99).

To study the impact of some factors on the plasticity index (η) the reader is referred to Figure 4-26, showing the link between plasticity index (η) and MB size, in Figure 4-26-a. In general, we can say that there is a semi-correlation, where the coefficient of determination (R-squared), $R^2 = 0.65$, with an exponential decay fitting connecting the plasticity index (η) to the diameter of the MB, where the small MBs have a high plasticity index (η) and the large MBs have low plasticity index (η). The correlation between plasticity index (η) and effective stiffness is shown in Figure 4-26-b and there is no evidence of a connection between the stiffness to the index of plasticity where the best coefficient of determination (R-squared), $R^2 = 0.4$. In summary, the plasticity index reflects the hysteresis behaviour.

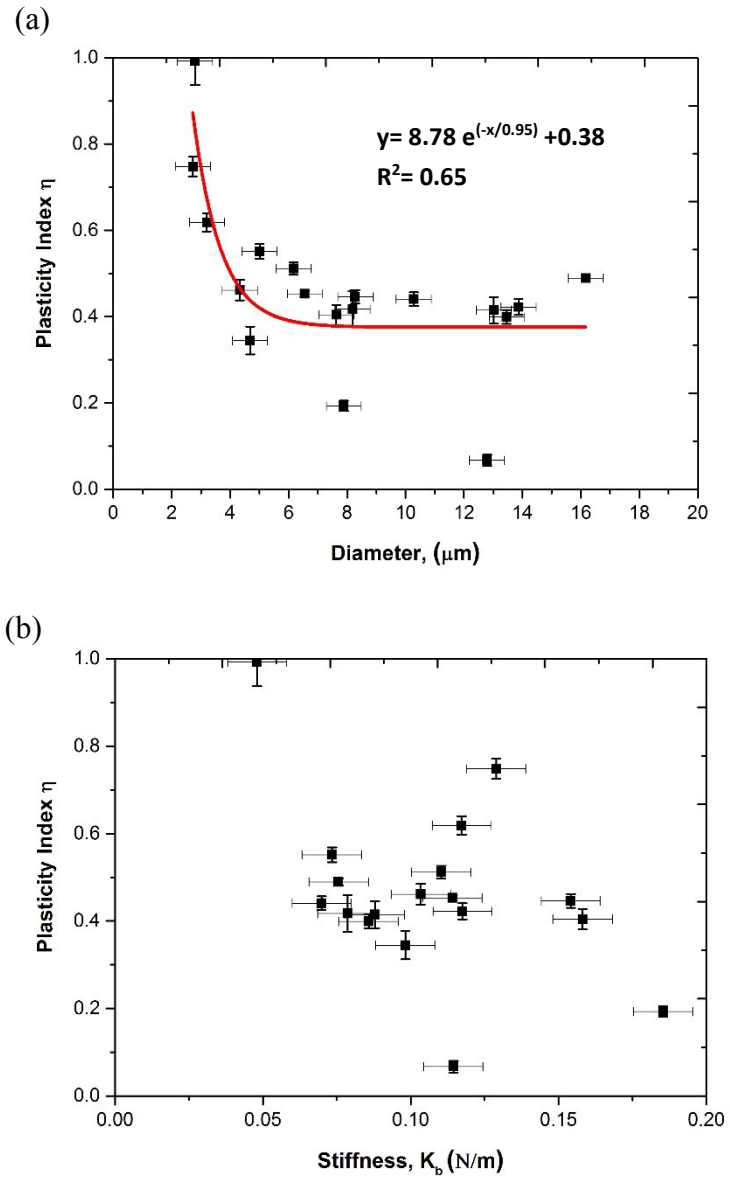

Figure 4-19: Showing the correlation between plasticity index (η) with MB size and effective stiffness, in (a) and (b) respectively.

4.3.2.4 Adhesion Forces

In the past, it has been found difficult to measure the interaction forces between particles directly because it is hard to work with such small bodies [39] (at micro/nano scales); therefore indirect methods were used, such as neutron scattering [40] and sedimentation. [41] The atomic force microscope (AFM) now allows us to perform direct measurements of interaction forces on an individual particle.[42] The interaction forces existing between any two particles depend on whether they are either semi-infinite solid [43, 44] or colloidal [39, 42] surfaces. These forces become more intensive and more effective if the particle is soft, such as phospholipid MBs, and so close to another surface. Interaction forces include both equilibrium forces, e.g. the electrostatic double layer, van der Waals, hydration, and hydrophobic forces and non-equilibrium forces, for example viscous forces, which are more important with small distances (nanometres).[42] The interaction forces were observed in the present experiments when the cantilever retracts away from the MB, where the MB keeps it in contact until the cantilever force overcomes the pull-off force, which is called the adhesion force ($F_{adh)}$. [37]. After reading the force-deformation (F-Δ) curves of a group of MBs (18 MBs), adhesion forces were observed in all retracing (unloading) curves, with different values from 1 nN to 12.35 nN and mean 6.17± 3.21 nN (in the negative direction). An adhesion force is displayed in the zoomed image in Figure 4-27, showing the value at (-7.13 nN) for a MB with size 13.46 μm diameter and stiffness 0.09 N/m, using a cantilever with spring constant 0.2839 N/m.

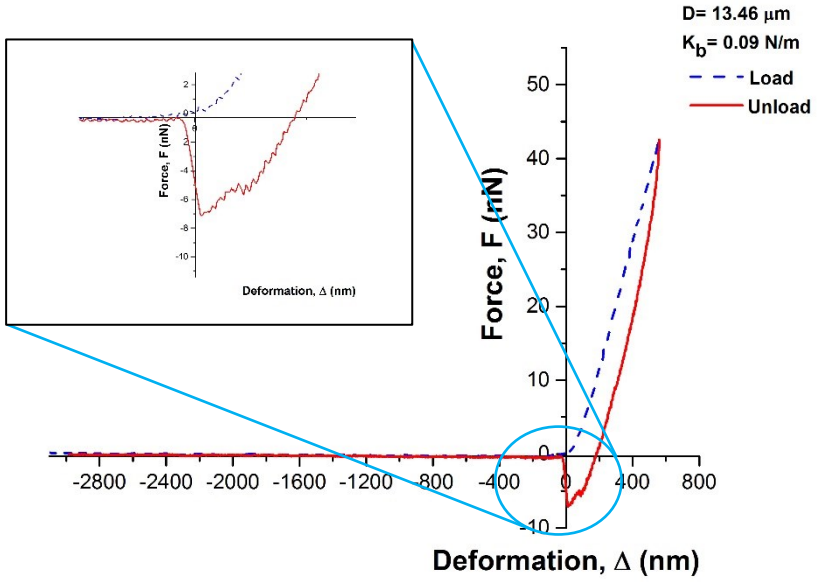

Figure 4-27: Showing an adhesion force (-7.13 nN) produced from a MB with 13.46 µm diameter and 0.09 N/m stiffness with 0.2839 N/m cantilever spring constant.

To track the adhesion force's relation with other factors, for instance the MB size and its stiffness, the 18 retracing curves were studied to reveal these correlations. It was concluded that no correlations exist between the adhesion force and MB size (Figure 4-28-a), where the values are widely spread and the best coefficient of determination (R-squared), R^2 = 0.4; however, there is some correlation between plasticity and adhesion force in an up trending linear relation, as represented in Figure 4-28-b where the Pearson correlation coefficient, r = 0.8 and coefficient of determination (R-squared), R^2 = 0.6.

To see all the results and the mechanical properties which are studied in this chapter for each MB individually, the reader is referred to Appendix A.

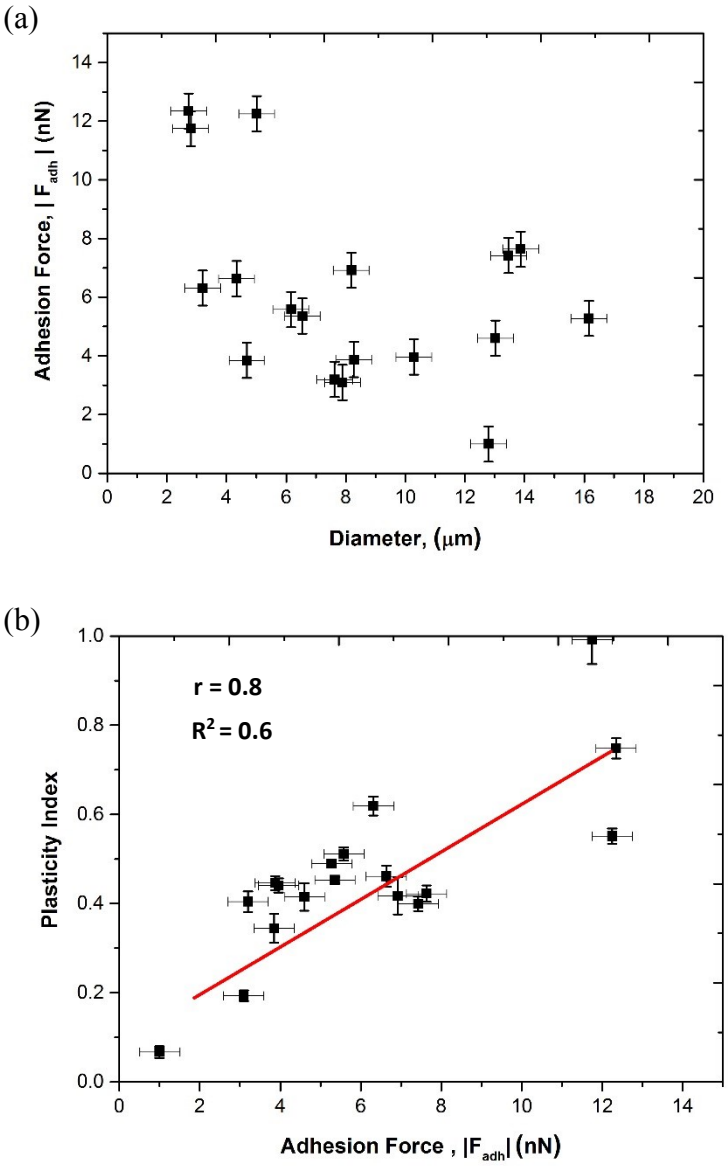

Figure 4-28: (a). Graph shows that there is no relation between adhesion force and MB size (b) A link appears between the plasticity index and adhesion force.

4.4 Discussion

In this study, the mechanical properties of SonoVue MBs were investigated by adopting the AFM technique and using tipless cantilevers. This technique is gaining in importance and accuracy because it is a real mechanical test and a direct measurement method. Many MBs were tested, of which 18 passed the experimental restrictions (as mentioned previously) to undergo further numerical analysis, to attempt to construct an adequate picture of phospholipid MBs mechanical properties. The effective stiffness of the MBs (k_b) was estimated to be in the range of 0.040 – 0.158 N/m and average 0.09 N/m, using cantilevers with spring constants 0.266 N/m and 0.284 N/m; this is near and in the same order of magnitude as Tu et al.'s [45] results. They found it to be 0.22 N/m for a MB with R_0 = 1.72 μm and using Marmottant's model. It should be noted that they used an indirect measurement method based on light scattering, which could involve some overstatement in the results. Another study [14] found values in the same range, 0.032 - 0.136 N/m, using hard cantilevers with spring constants 0.247 – 0.408 N/m; however, that study did not observe any instability steps or unrepeatability as were seen in the present study, which might have impacted on the values in the present experiments and raised the values by a small amount. No correlation or trend was found between stiffness and MB size and this observation is in agreement with [14]. Furthermore, no fracture or laceration of the MB shell occurred in cases when there was high deformation, where the diameter diminished to 25% of its initial value, which means the assumed Poisson's ratio was a logical value.

Some MBs showed good repeatability, with consistency with [46, 47] and some MBs produced unstable steps, mainly in the case of MBs with lower diameter and lower stiffness. As recorded, the local stiffness becomes higher after each unstable step and this phenomenon continues unless the curve becomes nonlinear at the top of the curve. This behaviour is related to the thickness of the MB shell, where the thickness in the local area could change because of the partial and local collapse/fold of the shell in this area; thus the thickness has been assumed to be constant and homogenous during the whole test which does not happen with the unstable steps because of the folding. Lulevich et al. [48] state that the elasticity of the shell increases when shell thickness rises. Our observations are consistent with previous studies in the same field [46, 48-50], where they observed some instability steps and damage to their particles, especially at high deformations. In addition, there was unrepeatability for some MBs, which could suggest some permanent deformation; this was observed in [46, 48, 49] as well. It seems there is a relation between the initial nonlinear part of the curve and the speed of the cantilever, as shown in Figure 4-14-b, where the initial nonlinear region becomes bigger when increasing the cantilever speed, and this might occur because the resistance of the liquid increases with the increased speed of the cantilever and hinders the cantilever movement before it is in contact with the specimen surface. Fluid mechanics [51] plays a role in the control forces affecting falling objects in a fluid. There are three forces which have an impact on the falling bodies: drag, buoyancy and gravity forces, where the drag and buoyancy force are pushing the body up while the gravity force is pulling it down. The drag force is proportional to the velocity of the body, as follows: $F_{drag} = -1/2\ C_d\ \rho A v^2$, it is notable that velocity has

significant effect on the drag force, where the velocity is raised to the power two. [52-54]

In this research three models were used to investigate the modulus of elasticity (Young's modulus) applying the Reissner theory, elastic membrane theory and Hertz theory. The results varied according to the adopted model where two of them, Reissner and membrane theory, were used to calculate the modulus of elasticity of the MB shell, whereas the third, Hertz theory, was used to estimate the Young's modulus of the whole MB.

Using Reissner's theory, the Young's modulus lies in the range of 2.0-24.2 GPa and mean 12.8 GPa. A previous study [14] using Reissner's theory found it to be in the range 1 to 4.5 GPa. These results are in the same order of magnitude, with slightly lower values because of the MBs' sizes, where the MBs used in the present study were bigger and there is a correlation between the Young's modulus and MB size, as illustrated in both studies. It also should be taken into account that the present study considered half of the MB deformation (as it is correct to do), since the deformation is assumed to be symmetrical on both of the MB poles, leading to higher values in this study than in the others. Abou-Saleh el at.[23] studied lipid MBs with and without coating and calculated the Young's Modulus to be 1 GPa and 2.9 GPa for no coating and coating, respectively: still in the same order but lower. It is notable that their stiffnesses were 0.01 and 0.03 N/m, lower than the stiffness in the present study as well. In general, Reissner's theory gives overestimated results for the Young's modulus. [15] Using the same theory, Dieluweit et al.[19] calculated the Young's modulus of phospholipid vesicles to be 0.1 GPa and stiffness 0.86×10^{-3} N/m. Note that the smallest Young's modulus is associated with the smallest stiffness.

The stretching component was considered in applying membrane theory but the bending term was neglected, because of the height of relative deformation (ε) values. The Young's modulus found by using this theory was in the range from 0.043 to 1.5 GPa and mean 0.46 GPa. This is again in harmony with and slightly higher than [14], who found it to be in the range 0.031-0.233 GPa. They observed an uptrend relation between MB size and the Young's modulus as observed in the present study. It is worth noting that the maximum size of their MBs was around 7.25 μm, whereas some of those used in the present study exceeded 13 μm. Moreover, the linear region of the (F-ε^3) curve is unclear, and tricky sometimes to determine, which means it may be a bit differently identified from person to another. A study investigated Young's modulus using membrane theory [15], for another type of phospholipid MBs. They assessed it to be in the range 0.008 GPa - 0.038 GPa, with a mean of 0.019 GPa, one order lower than in the present study; however, their stiffness was almost one order lower too, 0.01-.03 N/m.

The Young's modulus calculated using Hertz theory lies in the range from 1.44×10^{-4} GPa(144 kPa) to 4.5×10^{-4} GPa (450 kPa) and mean 2.96×10^{-4} GPa (296 kPa). This is in agreement with [14], where it was calculated at 30-220kPa, which is a reasonable value compared to stiffnesses in this study. A decreasing trend relation between the Young's modulus and MBs size was suggested in the present study, whereas they did not observe this link. It seems that the membrane theory is a good model to investigate the mechanical properties of MBs, where it gives reasonable results without over-estimation or extremely low values. [14, 15]

All the MBs throughout the compression cycle exhibited either a large or small hysteresis area, which is in consistency with Santos et al.'s [15] observations.

This hysteresis dissipates energy after each compression cycle. The appearance of the hysteresis area in each curve is related to several factors. In the liquids, one of the reasons is hydrodynamic drag or drag force on the cantilever[55]. Usually plasticity [37] or viscoelastic deformation [47] might cause hysteresis, so it is expected that an elastic deformation will not cause a hysteresis. However a study [56] mentioned that this could happen because of the friction due to slipping of the cantilever on the top of the sample surface at the contact point, resulting in a tilt of the cantilever(7-20^{o}). Lulevich et al. [49] point out that hysteresis could also be connected with the drainage of the water in and out of the capsule. In addition, the compressibility of the core gas, which is assumed as an incompressible gas, might be playing a role. The hysteresis did not show a relation with MBs, unless some MBs' results are neglected, as mentioned previously, and there was no correlation between hysteresis and stiffness of MBs either, which agrees with the findings of [47].. On the other hand, there is a good exponential decay relationship between hysteresis loss per cycle per unit volume and MB size, where the irregular MBs in Figure 4-20-a disappear because this relation is considering the unit volume instead of the whole MB size. It is notable that the largest MB has the lower energy loss and vice versa.

The plasticity of the MBs was also studied in this chapter, as it is related to the hysteresis area. By calculating the plasticity index (η), we can quantify the viscoelastic behaviour of the material. [15, 36, 38] The plasticity index (η) was estimated to be in the range of 0.07 - 0.99 and mean 0.47. This is in agreement with another study [23], which found the plasticity index for uncoated MBs at F_{max} = 20 nN to be 0.49 and 0.7-0.9, for 20-130 Nn, respectively, for coated MBs. At a wider range

we can say that there is a semi-exponential correlation between the plasticity index (η) and MB size. There is no association with stiffness and plasticity index (η).

The adhesion forces were highlighted in this study as well, to discover if there is any relation between the interaction forces and other factors or not. Interaction forces (adhesion forces) are mostly a combination of several forces such as the van der Waals force, the electrostatic forces, chemical bonds and the meniscus or capillary forces.[37] Adhesion forces may add more indentation to that caused by the spring force, where the total cantilever deflection appears to be due to the attractive surface forces, the adhesion forces and the deformability of the sample and the tip. [57] When a tip retracts away from the sample, the adhesion forces keep it in contact and pull it down; this happens with purely elastic materials, too.

All MBs appeared to exert adhesion forces at either a large or small amount. The smallest was 1 Nn, while the largest was 12.35 Nn, with mean 6.17± 3.21 nN (in the negative direction). No correlation appeared between adhesion force and MB size; however, it was found that there is a link between adhesion forces and the plasticity index in a positive uptrend relation, which is deduced to be the effect of the viscosity of the material on adhesion forces. Adhesion forces could also be affected by other factors e.g. the roughness of the contacting surfaces where the roughness has significant impact. [58, 59]

4.5 Conclusion

It has been possible to acquire insights about some of the influential factors and certain mechanical properties of SonoVue® microbubbles, such as stiffness, Young's modulus, Instability, Repeatability, Nonlinearity, Hysteresis, Plasticity and Adhesion

forces. The stiffnesses of the MBs were estimated using the gradient of the initial linear part of the force-deformation (F-Δ) curve and they lay in the range of 0.040 – 0.158 N/m and average 0.09 N/m. No correlation between stiffness and MB size was found; however, there is an increase in the stiffness after each instability step and it continues to increase unless the curve becomes nonlinear again. In this study, three models have been used: Reissner's theory, elastic membrane theory and Hertz theory, to investigate the modulus of elasticity where the average of the Young's modulus values were 12.8 GPa, 0.46 GPa and 2.96×10^{-4} GPa respectively. It seems that elastic membrane theory with stretching components at high deformations is a good model, giving reasonable results with no overestimation. The Reissner and membrane theories illustrated an uptrend relation, while Hertz theory showed a down-trend with MB size. The averages of the hysteresis and hysteresis loss were 4490 nN.nm and 14.1 kJ/m^3 respectively. A clear and visible exponential relation between hysteresis loss per unit volume and diameter of the MB was observed, meaning that the biggest MB has the lowest energy loss and vice versa. The viscoelastic behaviour of the MBs was studied as well, by calculating the plasticity index (η), which has a mean value equal to 0.47. One of the MBs responded with purely plastic behaviour, with a value of almost (η=0.99). A semi-exponential link was shown between the plasticity index (η) and MB size, corresponding to a hysteresis energy loss relationship. All the MBs appeared to have an adhesion force, with an average of 6.17 nN and a positive correlation up-trending with the plasticity index, according to the viscosity of the MBs. Note that the compression tool was a rectangular flat tipless cantilever, which will be replaced by a different form in the experiments reported in the next chapter.

4.6 References

1. Quaia, E., *Contrast media in ultrasonography basic principles and clinical applications*, ed. T.V. Bartolotta, E. Quaia, and SpringerLink. 2005, Berlin: Springer.

2. Ferrara, K., Pollard, R. and M. Borden, *Ultrasound microbubble contrast agents: Fundamentals and application to gene and drug delivery*, in *Annu. Rev. Biomed. Eng.* 2007. p. 415-447.

3. Goldberg, B.B., Liu, J. and F. Forsberg, *Ultrasound contrast agents: a review.* Ultrasound in medicine & biology, 1994. **20**(4): p. 319-333.

4. Ohlerth, S.a.R.T.O.B., *Contrast ultrasound: General principles and veterinary clinical applications.* The Veterinary Journal, 2007. **174**(3): p. 501-512.

5. Unger, E.C., Porter, T., Culp, W., Labell, R., Matsunaga, T. and R. Zutshi, *Therapeutic applications of lipid-coated microbubbles.* Advanced drug delivery reviews, 2004. **56**(9): p. 1291-1314.

6. Liu, Y., Miyoshi, H. and M. Nakamura, *Nanomedicine for drug delivery and imaging: a promising avenue for cancer therapy and diagnosis using targeted functional nanoparticles.* International journal of cancer, 2007. **120**(12): p. 2527-2537.

7. Sirsi, S.R.a.M.A.B., *Microbubble compositions, properties and biomedical applications.* Bubble Science, Engineering & Technology, 2009. **1**(1-2): p. 3-17.

8. Bracco, *Manufacturer's Leaflet Instructions*. 26/3/2001.

9. Petelska, A.D., Janica, J.R., Kotynska, J., Lebkowska, U. and Z.A. Figaszewski, *The Effect of Contrast Medium SonoVue(®) on the Electric Charge Density of Blood Cells.* The Journal of Membrane Biology, 2012. **245**(1): p. 15-22.

10. Westwood, M., Joore, M., Grutters, J., Redekop, K., Armstrong, N., Lee, K., Gloy, V., Raatz, H., Misso, K. and J. Severens, *Contrast-enhanced ultrasound using SonoVue®(sulphur hexafluoride microbubbles) compared*

with contrast-enhanced computed tomography and contrast-enhanced magnetic resonance imaging for the characterisation of focal liver lesions and detection of liver metastases: a systematic review and cost-effectiveness analysis. Health Technology Assessment, 2013. **17**(16): P. 1-268

11. Von Herbay, A., Westendorff, J., Gregor, M., Barreiros, A., Galle, P.R., Ignee, A. and C. Dietrich, *Contrast-enhanced ultrasonography with SonoVue: Differentiation between benign and malignant lesions of the spleen.* Journal of Ultrasound in Medicine, 2009. **28**(4): p. 421-434.

12. Schneider, M., *SonoVue, a new ultrasound contrast agent.* European Radiology, 1999. **9**(3): p. S347-S348.

13. Schneider, M., Arditi, M., Barrau, M.B., Brochot, J., Broillet, A., Ventrone, R. and F. Yan,, *BR1: a new ultrasonographic contrast agent based on sulfur hexafluoride-filled microbubbles.* Invest Radiol, 1995. **30**(8): p. 451-457.

14. Morris, J.K., *Mechanical properties of phospholipid coated microbubbles*. 2014, The University of Edinburgh, UK. PhD thesis. p. 157.

15. Buchner Santos, E., Morris, J.K., Glynos, E., Sboros, V. and V. Koutsos, *Nanomechanical properties of phospholipid microbubbles.* Langmuir : the ACS journal of surfaces and colloids, 2012. **28**(13): p. 5753-5760.

16. Domke, J. and M. Radmacher, *Measuring the elastic properties of thin polymer films with the atomic force microscope.* Langmuir, 1998. **14**(12): p. 3320-3325.

17. Fery, A., Dubreuil, F. and H. Möhwald, *Mechanics of artificial microcapsules.* New journal of Physics, 2004. **6**(1): p. 1634-1647

18. Chizhik, S., Huang, Z., Gorbunov, VV., Myshkin, N. and W. Tsukruk, *Micromechanical properties of elastic polymeric materials as probed by scanning force microscopy.* Langmuir, 1998. **14**(10): p. 2606-2609.

19. Dieluweit, S., Csiszar, A., Rubner, W., Fleischhauer, J., Houben, S. and R. Merkel, *Mechanical properties of bare and protein-coated giant unilamellar phospholipid vesicles. A comparative study of micropipet aspiration and atomic force microscopy.* Langmuir, 2010. **26**(13): p. 11041-11049.

20. European Fluorocarbons Technical Committee (EFCTC). *http://www.fluorocarbons.org/chemical-families/sf6/sf6-general-properties*. October, 2016.

21. Morel, D.R., Schwieger, I., Hohn, L., Terrettaz, J., Llull, J.B., Cornioley, Y.A. and M. Schneider,, *Human pharmacokinetics and safety evaluation of*

SonoVue, a new contrast agent for ultrasound imaging. Invest Radiol, 2000. **35**(1): p. 80-97.

22. Correas, J., Burns, P.N., Lai, X. and X. Qi, *Infusion versus bolus of an ultrasound contrast agent: In vivo dose- response measurements of BR1.* Investigative Radiology, 2000. **35**(1): p. 72-79.

23. Abou-Saleh, R.H., Peyman, S.A., Critchley, K., Evans, S.D. and N.H. Thomson, *Nanomechanics of lipid encapsulated microbubbles with functional coatings.* Langmuir : the ACS journal of surfaces and colloids, 2013. **29**(12): p. 4096-4103

24. Mikromash., *http://www.spmtips.com/afm-tips-and-accessories-search.afm* October, 2016.

25. Glynos, E., *Atomic force microscopy on self-assembled polymer structures*. 2007, The University of Edinburgh, UK. PhD thesis. p. 156.

26. Mahalingam, S., Raimi-Abraham, B.T., Craig, D.Q. M. and M. Edirisinghe, *Formation of Protein and Protein–Gold Nanoparticle Stabilized Microbubbles by Pressurized Gyration.* Langmuir, 2015. **31**(2): p. 659-666.

27. Evans, E.A., Waugh, R. and L. Melnik, *Elastic area compressibility modulus of red cell membrane.* Biophysical Journal, 1976. **16**(6): p. 585-595.

28. Ertel, A., Marangoni, A. G., Marsh, J., Hallett, F. R. and J.M. Wood, *Mechanical properties of vesicles. I. Coordinated analysis of osmotic swelling and lysis.* Biophysical Journal, 1993. **64**(2): p. 426-434.

29. Tu, J., Swalwell, J.E., Giraud, D., Cui, W., Chen, W. and T.J. Matula, *Microbubble sizing and shell characterization using flow cytometry.* Ultrasonics, Ferroelectrics and Frequency Control, IEEE Transactions on, 2011. **58**(5): p. 955-963.

30. Hutter, J.L. and J. Bechhoefer, *Calibration of atomic-force microscope tips.* Review of Scientific Instruments, 1993. **64**(7): p. 1868-1873.

31. Love, A.E.H., *A Treatise on the Mathematical Theory of Elasticity* Vol. 1. 2011: Dover Publications.

32. Dharan, C.K.H. and T.F. Tan, *A hysteresis-based damage parameter for notched composite laminates subjected to cyclic loading.* Journal of Materials Science, 2007. **42**(6): p. 2204-2207.

33. Chandran Suja, V., J.M. Frostad, and G.G. Fuller, *Impact of Compressibility on the Control of Bubble-Pressure Tensiometers.* Langmuir, 2016. **32**(46): p. 12031-12038.

34. Alvarez, N.J., L.M. Walker, and S.L. Anna, *A Microtensiometer To Probe the Effect of Radius of Curvature on Surfactant Transport to a Spherical Interface.* Langmuir, 2010. **26**(16): p. 13310-13319.

35. Parthasaradhy, P. and S. Ranganayakulu, *Hysteresis and eddy current losses of magnetic material by Epstein frame method-novel approach.* Int. J. Eng. Sci.(IJES), 2014: p. 85-93.

36. Briscoe, B., Fiori, L. and E. Pelillo, *Nano-indentation of polymeric surfaces.* Journal of Physics D: Applied Physics, 1998. **31**(19): p. 2395-2405.

37. Butt, H.J., B. Cappella, and M. Kappl, *Force measurements with the atomic force microscope: Technique, interpretation and applications.* Surface science reports, 2005. **59**(1): p. 1-152.

38. Klymenko, O., Wiltowska-Zuber, J., Lekka, M. and W.M. Kwiatek, *Energy dissipation in the AFM elasticity measurements.* Acta Physica Polonica-Series A General Physics, 2009. **115**(2): p. 548-551.

39. Ducker, W.A., Senden, T.J. and R.M. Pashley, *Direct measurement of colloidal forces using an atomic force microscope.* Nature, 1991. **353**(6341): p. 239-241.

40. Gray, A.D., Cram, L. E., Ekers, R. D. and W.M. Goss, *A filamentary radio source near the Galactic Centre.* Nature, 1991. **353**(6341): p. 237-239.

41. Reich, W. and E. Fuerst., *G357.7 + 0.3 and G359.1 - 0.5 - Two shell-type supernova remnants in the galactic centre region.* Astrophysics, 07/1984: p. 165-167.

42. Ducker, W.A., Xu, Z. and J.N. Israelachvili, *Measurements of Hydrophobic and DLVO Forces in Bubble-Surface Interactions in Aqueous Solutions.* Langmuir, 1994. **10**(9): p. 3279-3289.

43. Vinogradova, O.I. and F. Feuillebois, *Interaction of Elastic Bodies via Surface Forces. 1. Power-Law Attraction.* Langmuir, 2002. **18**(13): p. 5126-5132.

44. Vinogradova, O.I. and F. Feuillebois, *Interaction of elastic bodies via surface forces: 2. Exponential decay.* Journal of Colloid and Interface Science, 2003. **268**(2): p. 464-475.

45. Tu, J., Guan, J., Qiu, Y. and T.J. Matula, *Estimating the shell parameters of SonoVue microbubbles using light scattering.* J Acoust Soc Am, 2009. **126**(6): p. 2954-2962.

46. Glynos, E., Koutsos, V., McDicken, W.N., Moran, C.M., Pye, S.D., Ross, J.A. and V. Sboros, *Nanomechanics of Biocompatible Hollow Thin-Shell Polymer Microspheres.* Langmuir, 2009. **25**(13): p. 7514-7522.

47. Chen, C.C., Shih-Ying, J. D., Finan, B., Morrison, E.E. and E.E. Konofagou, *An experimental study on the stiffness of size-isolated microbubbles using atomic force microscopy.* Ultrasonics, Ferroelectrics and Frequency Control, IEEE Transactions on, 2013. **60**(3): p. 524-534.

48. Valentin, V., Lulevich, D.A. and O.I. Vinogradova, *Elasticity of polyelectrolyte multilayer microcapsules.* Journal of Chemical Physics, 2004. **120**: p. 3822-3826.

49. Lulevich, V., Radtchenko, I., Sukhorukov, G. and O.I. Vinogradova, *Deformation properties of nonadhesive polyelectrolyte microcapsules studied with the atomic force microscope.* The Journal of Physical Chemistry B, 2003. **107**(12): p. 2735-2740.

50. Byoung-sunk, K. and C. Jeong-woo, *Polyelectrolyte multilayer microcapsules: self-assembly and toward biomedical applications.* Biotechnology and Bioprocess Engineering, 2007. **12**: p. 323-332.

51. Frank M. White, *Fluid Mechanics*. Seventh Edition ed. Vol. 1. 2009: McGraw-Hill.

52. Abaid, N., Adalsteinsson, D., Agyapong, A., & McLaughlin, R. M., *An internal splash: Levitation of falling spheres in stratified fluids.* Physics of Fluids, 2004. **16**: p. 1567-1580.

53. Richardson, E.G., *The impact of a solid on a liquid surface.* Proc. of the Phys. Soc., 1948. **61**: p. 352-367.

54. Jenny, M. and J. Dušek, *Efficient numerical method for the direct numerical simulation of the flow past a single light moving spherical body in transitional regimes.* Journal of Computational Physics, 2004. **194**(1): p. 215-232.

55. Houston, J.E. and T.A. Michalske, *The interfacial-force microscope.* Nature, 1992. **356**(6366): p. 266-267.

56. Hoh, J.H. and A. Engel, *Friction effects on force measurements with an atomic force microscope.* Langmuir, 1993. **9**(11): p. 3310-3312.

57. Pethica, J.B., *On the stability of a tip and flat at very small separations.* Journal of Vacuum Science & Technology A: Vacuum, Surfaces, and Films, 1988. **6**(4): p. 2490-2495.

58. Schaefer , D.M., Carpenter , M., Gady , B., Reifenberger, R., Demejo, L.P. and D.S. Rimai, *Surface roughness and its influence on particle adhesion using atomic force techniques.* Adhesion Science and Technology 1995. **9**(8): p. 1049-1062.

59. Schaefer, D.M., Carpenter, M., Reifenberger, R., Demejo, L.P. and D.S. Rimai, *Surface force interactions between micrometer-size polystyrene spheres and silicon substrates using atomic force techniques.* Adhesion Science and Technology 1994. **8**: p. 197-210

CHAPTER 5

EVALUATION OF THE NANOMECHANICAL PROPERTIES OF SONOVUE® USING TIPPED CANTILEVER

CAPTER 5: EVALUATION OF THE NANOMECHANICAL PROPERTIES OF SONOVUE® USING TIPPED CANTILEVER

5.1 Introduction

The atomic force microscope (AFM) is a device to measure forces between surfaces which are either solid or soft. Several techniques and devices have been developed through the last decades to probe the nano/micromechanical properties of matter and one of them (probably the most significant) is AFM. [1] Many techniques or systems are difficult to use because of their complexity or because of limitation and restrictions on the type of materials that can be probed. On the other hand, AFM is an easy, direct and accurate technique and due to these advantages it has become commonly used for imaging topography. In fact, the key element of the AFM is the cantilever/tip assembly, since its performance is significantly controlled by its mechanical properties e.g. the cantilever spring constant and its resonance frequency. [2] At the same time the mechanical properties are affected by certain factors, such as geometry of the cantilever (tipless versus tipped cantilever), so it is worth focusing on the influence of the cantilever geometry on the mechanical properties of the test sample.

This chapter will focus on the effect of a rectangular cantilever with a conical tip on the mechanical properties of SonoVue® microbubbles. The mechanical properties and factors which are intended to be investigated here are the same as those investigated in the previous chapter; however, the compression tool here is a tipped

cantilever. Because the procedures are the same as those in Chapter 4, except for the compression probe used, a tipped cantilever, this chapter proceeds directly to the Apparatus and Tools section. Note that it was not possible to acquire as many MBs as in the experiment reported in Chapter 4, because in case of tipped cantilevers issues there is a higher probability of things to go wrong in the experimental work; results from 8 MBs were reliable and were analysed.

5.2 Apparatus and Tools

A molecular force probe (MFP 1-D) (Asylum Research, Santa Barbara, CA) was used, mounted on a Nikon TE2000U (Nikon UK Limited, Surrey, UK) inverted optical microscope, in order to allow the adjustment of the microbubble below the cantilever before the force measurements and the determination of the measured microbubble size. The tipped cantilevers used are CSC 12/ without Al/ 50 (Mikromasch, Tallinn, Estonia) without aluminium backside coating with tip. The tip is 20 μm in height with 10 nm radius of curvature and 20^{o} full tip cone angle, as shown in Figure 5-1. [3] The calibrated spring constant of the cantilever was 0.05±0.001 N/m, where the typical value in the data sheet was 0.03 N/m and the range was 0.01-0.08 N/m. For each experiment, the cantilevers were moved at a constant speed, 3 μm/s, and the same distance, 3 μm, away from the MB, including the contact and non-contact region.

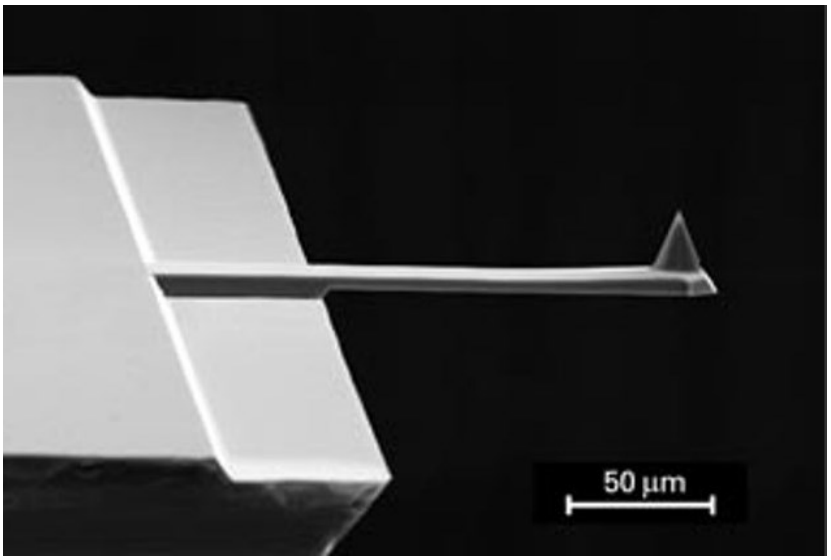

Figure 5-1: Cantilever with conical tip.

5.3 Results

5.3.1 Introduction

A good level of maturity has been reached in understanding the AFM technique and interaction forces between surfaces. In general, the AFM scans the sample using a tip mounted on a cantilever, however, in this study it is possible to use either a flat cantilever, as presented in the previous chapter, or a tipped cantilever as used in the investigations reported in this chapter. During scanning, the interaction forces between the sample and the tip of the cantilever can be measured by tracking the cantilever deflection. [2] Investigation of the effects of the tip, sample or the medium can be obtained by observing the interactions between them. These interactions and measurements are called ‘‘force measurements’’. In the AFM the tipped cantilever

moves toward the sample in the normal direction, where the cantilever deflection and position of the tip are registered then changed to force-distance curves: these data are referred to as ‘‘force curves’’. After gathering and analysing the force curves, some of the material properties can be investigated. The force curves can be obtained in a vacuum, air, different gases, or liquid as adopted environment in these experiments.

The experiments reported in this chapter used constant cantilever speed and cantilever deflection, which expresses the force, and the MB size was changed to investigate influence of the size of the MBs on the mechanical properties using a tipped cantilever.

5.3.2 Tipped Cantilever

In this section, the speed of the cantilever movement was fixed during approach and retraction at 3 μm/s as in Chapter 4 and cantilever deflection was fixed at ~ 170 nm (force ~ 10 nN), where this force is consistent with the spring constant of the cantilever to acquire an appropriate curve and to avoid damaging the MB’s shell with high forces exerted by the tip, while various diameters of MBs were used to investigate the effect of the MBs’ size on the mechanical properties. A tipped cantilever was used as a compression tool, with a spring constant value of 0.052±0.002 N/m, which is near to the typical value on the data sheet, and calibrated according to measurement of the intensity of the thermal noise method. This method was first introduced by Hutter and Bechhofer [4] and corrected later by other researchers. [5-7] It is widely used compared to other cantilever calibration methods because it involves no damage to the tip, is appropriate to most types of cantilevers and is easy to use. [8] The tipped

cantilever was adopted to record the raw position-deflection data which were subsequently converted to force-deformation (F-Δ), as introduced previously. It was possible to acquire data on 8 MBs with different sizes, ranging in diameter from 3.48 µm to 5.73 µm and mean 4.58 µm, these MBs produced reliable curves and presented a good experimental test to enable further analytical steps to highlight the effect of the MBs size on the mechanical properties using a tipped cantilever. All the experiments were performed in an aqueous environment. Compared to those of a tipless cantilever, tipped cantilever force curves are more wavy, according to tipped cantilever stiffness (the spring constant is smaller than for a tipless cantilever) and the size of the contact area between the tip and the sample surface is very small, which makes it more sensitive, so the need for the third order polynomial fitting is more important, as mentioned previously.

Figure 5-2 shows two typical force-deformation (F-Δ) curves: the first on a microbubble with diameter 3.63 µm and effective stiffness k_b= 0.030 N/m, (black curve) using a tipped cantilever with spring constant k_c= 0.052 N/m, while the second (red) curve is for a MB with diameter 13.45 µm and effective stiffness k_b= 0.086 N/m using a tipless cantilever with spring constant k_c= 0.284 N/m. It is clear that the tipped cantilever curve is more tortuous and not as smooth as the tipless cantilever curve; this is a result of the soft cantilever and small area of contact between the MB surface and the cantilever tip.

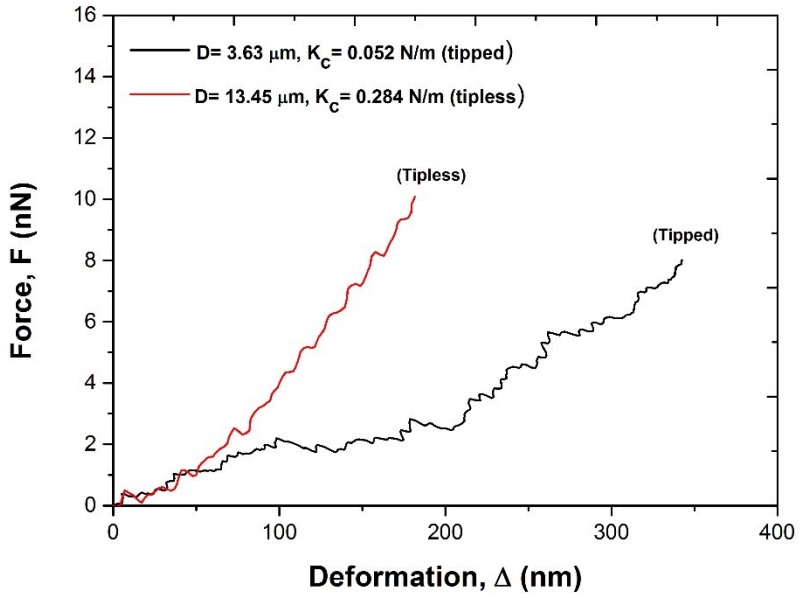

Figure 5-2: Two typical (F-Δ) curves: (in black) for a MB with D = 3.63 μm and stiffness (k_b) 0.030 N/m, using a tipped cantilever with spring constant (k_c) 0.052 N/m; (in red) for a MB with D = 13.45 μm and stiffness (k_b0.086 N/m, using a tipless cantilever with a spring constant (k_c) 0.284 N/m.

5.3.2.1 Stiffness

Each MB was tested individually, acquiring many force curves on a group of 8 MBs with different diameters in the range of 3.48 μm to 5.73 μm (average 4.58 μm) to investigate the impact of the MBs size on the mechanical properties using a tipped cantilever. After obtaining the raw data and converting them to force-deformation (F-Δ) curves, the effective stiffness was calculated from the gradient of the initial linear part of the force- deformation (F-Δ) curve [9, 10] and before any unstable step appeared, as the majority of the MBs (6 MBs) had unstable steps. The third polynomial order fitting was considered, as presented in Figure 5-3, to make the calculations easier and to recognize the linear part of the curve, when drawing the fitting curve on a

separated graph, especially for highly wavy curves, to maintain high accuracy of the fitting, where ($R^2 \geq 0.992$).

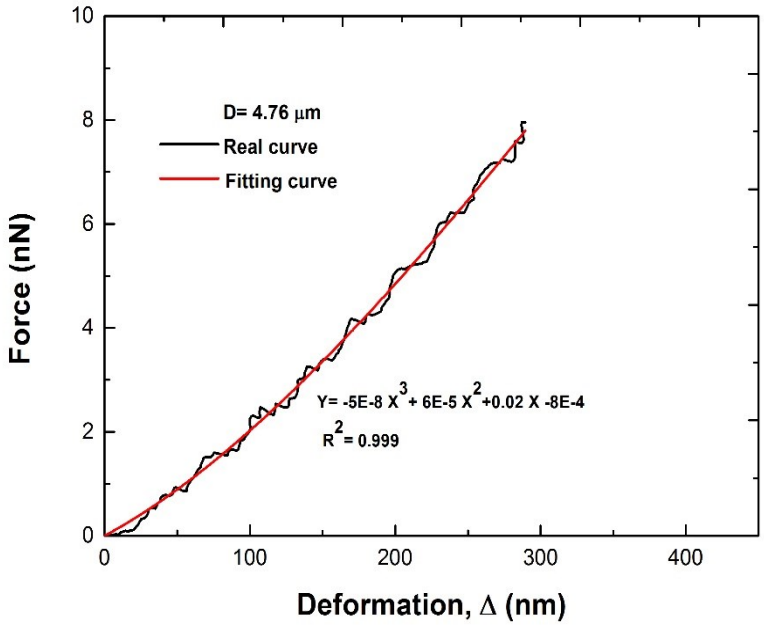

Figure 5-3: Represents the real data curve (black line) and the fitting data curve (red line) using third order polynomial.

- **Instability**

Two regimes of behaviours were observed. The first one, represented by a minority of the MBs (2 MBs), is a good and smooth curve, while the second one, shown by the majority of the MBs (6 MBs), is a curve or response appearing more frequently in unstable steps than those occurring in tipless cantilever force curves. Each MB here appeared to have from 3 to 8 unstable steps, despite of the low load used (~10 nN). Figure 5-4 illustrates the two types of the curves. Figure 5-4-(a) shows a smooth curve which is clean from unstable areas, for a MB with D= 5.73 µm, using

a tipped cantilever with spring constant K_C= 0.052 N/m. The gradient of the linear part of the curve (red line) is 0.036 N/m, which reflects the effective stiffness of the MB. Figure 5-4-(b) represents the force-deformation (F-Δ) curve of a MB with diameter D= 4.72 µm, using the same tipped cantilever. This curve starts with a linear part, then at 100 nm deformation, an instability area appears with deformation of depth 65 nm, moving in a horizontal direction with low or almost zero slope. After this step, the curve recovers and gains its uptrend again and continues at this pace until the end of the five unstable steps (blue circles). The effective stiffness of the MB is calculated from the gradient of the initial linear part (red line) and before any unstable steps, 0.021 N/m, as seen in Figure 5-4-(b).

In the same manner, the instability areas impact the local effective stiffness of the MB, as observed previously in Chapter 4. This phenomenon also appears here when using the tipped cantilever, where the local stiffness increases progressively after each unstable step, depending on the depth of the unstable area or the depth of the buckling. This phenomenon occurs in all unstable curves, either with sharp or gradual steps, and the local stiffness continues to increase unless the curve reaches the nonlinear region at the top of the curve.

Figure 5-5 shows a load (approach) curve with six unstable (in the blue circles) regions (buckling steps) for a MB with diameter 4.49 µm and effective stiffness 0.033 N/m, using a tipped cantilever with spring constant 0.052 N/m. The curve starts with an initial linear part with slope 0.033, then a sharp unstable step with 70 nm depth (20 % of deformation) appears and moves horizontally with zero slope at constant force ~

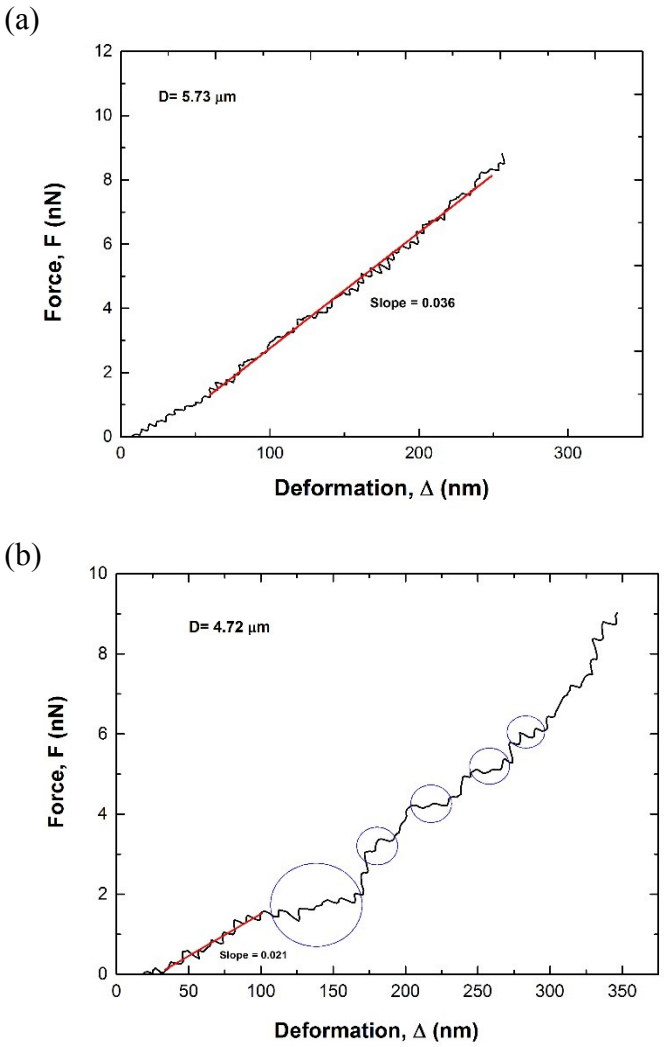

Figure 5-4: Two regimes of MB behaviours. (a) Shows a smooth curve, clean of instability steps, for a MB with D= 5.73 µm, using a tipped cantilever with spring constant K_C= 0.052 N/m. (b) Curve with five instability areas for a MB with D=4.72 µm and using same cantilever.

2.5 nN, followed by another linear part with gradient 0.058 N/m, which increases by 76 % more than the initial slope, and so on, until the fifth unstable step, where the effective stiffness becomes 0.090 N/m, rising by 36% and 173% above the previous and the initial slope respectively. The slope (local stiffness) continues to increase after each unstable step, unless the curve becomes nonlinear again, where it decreased here

to 0.086 N/m after the fifth and the sixth instability areas. The number of unstable steps with the tipped cantilever was greater and occurred at a faster rate than those that occurred with the tipless cantilever. It is worth mentioning that the unstable steps appeared in the unloading (retracing) curve as well, helping the MB to recover and to return to its initial shape. The reader is referred to Figure 5-11-(b) and Figure 5-17 to see some examples.

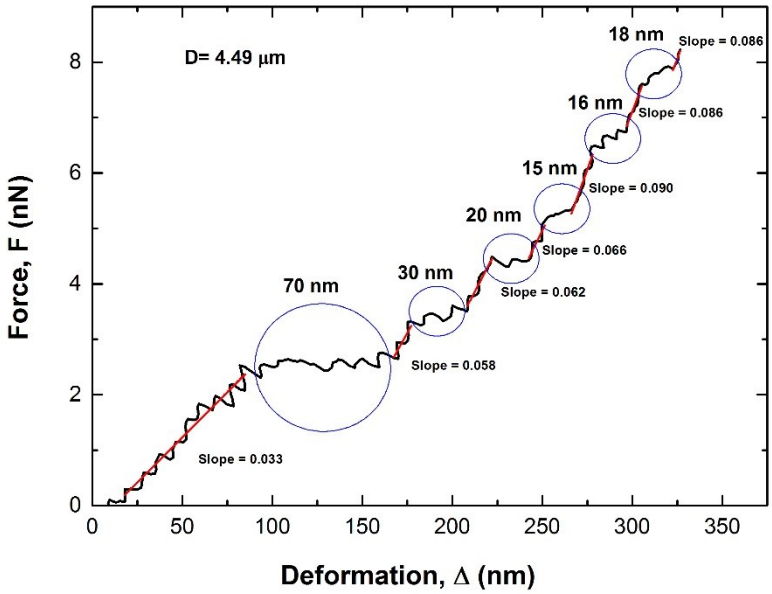

Figure 5-5: A curve with six unstable steps for a MB with size D= 4.49 µm and effective stiffness 0.033 N/m, where the local stiffness increases gradually after each step before reaching the non-linear region at the top of the curve.

In an attempt to predict the areas of instability, or where such unstable steps of relative deformation occurred, a group of 6 MBs were studied, which exhibited two or more very clear and visible unstable steps (which are 6 MBs here and 4 MBs in Chapter 4). Figure 5- 6 illustrates a set of 6 MBs with diameters in the range of 3.48 – 4.93 µm (average 4.35 µm) and from 3 to 8 unstable steps for each MB. However, only the

locations of the first three steps are being determined: the first step (solid black square) appears in the range 0.007-0.020 of relative deformation (ε), with mean relative deformation (ε) of 0.013 and the second (solid blue triangle) occurs in the range 0.01-0.04 and average relative deformation (ε) of 0.026 while the third (solid red circle) exists in the range of relative deformation (ε) 0.02- 0.05 and average 0.036. Thus, according to the mean values, the first step, the second step and the third step will appear at around 0.013, 0.026 and 0.036 relative deformation (ε) respectively, with some interference between the intervals. Compared to the results for the tipless cantilever the unstable steps, here with a tipped cantilever occurred, faster and in much greater numbers than the unstable steps occurred with a tipless cantilever even though the applied force is lower here. This is due to the fact that the overall contact pressure is higher as the force is concentrated in a much smaller area with a tipped cantilever.

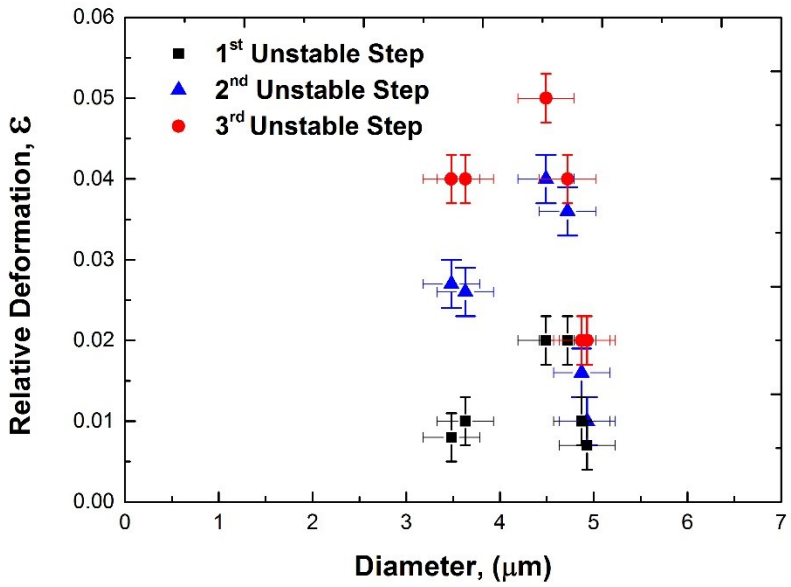

Figure 5-6: A set of 6 MBs, each with more than three unstable steps, where only the first three unstable steps are illustrated here. The mean values are 0.016, 0.026 and 0.036 relative deformation (ε) for the first, the second and the third unstable steps respectively.

- **Repeatability**

Many tests, producing more than 64 curves, were performed in this study: each MB was compressed producing 8-10 curves. The last 5 curves for each MB were adopted to include any change could occur in their behaviour in the end of the test, and also to give the machine some initial curves to adjust itself each time, after shifting from one MB to another, as mentioned previously. After investigations of all the MBs curves, it was observed that, in contrast with those for the tipless cantilever, there is no perfect repeatability in all the curves. This could be due to the sensitivity of the tipped cantilever and small area of contact between the tip and the sample. Figure 5-7-(a) illustrates a group of three stable curves acquired from a MB with a diameter of 4.76 μm and average stiffness 0.030±0.002 N/m, using a tipped cantilever with spring constant 0.052 N/m. They all start from the same point (0, 0) then move in divergence producing gaps between the curves, as seen in the figure, ending up with ordering the curves such that the first curve has the lowest stiffness and the last one acquired has the highest stiffness. The stiffnesses were 0.027, 0.029 and 0.033 N/m for the curve numbers 1, 3 and 5 respectively, which may indicate that there is some permanent plastic deformation occurring. However, it is notable that this ordering did not occur in all MBs, some of the MBs curves were organized randomly, where the first one was not the lowest stiffness and the last one was not the highest stiffness. Figure 5-7-(b) displays a group of three unstable curves obtained with a MB of diameter 4.72 μm and average stiffness 0.024±0.003 N/m, using the same tipped cantilever. No repeatability is noted in these curves; however, there is an ordering in the appearance of the unstable step, where the first curve obtained has the highest force that appear and the fifth curve

obtained has the lowest force that appear, as shown in the figure. The stiffnesses were 0.021, 0.021 and 0.027 N/m for the curve numbers 1, 3 and 5 respectively. Because the initial linear part of the curve was adopted, before the appearance of any unstable area, the stiffnesses are almost the same.

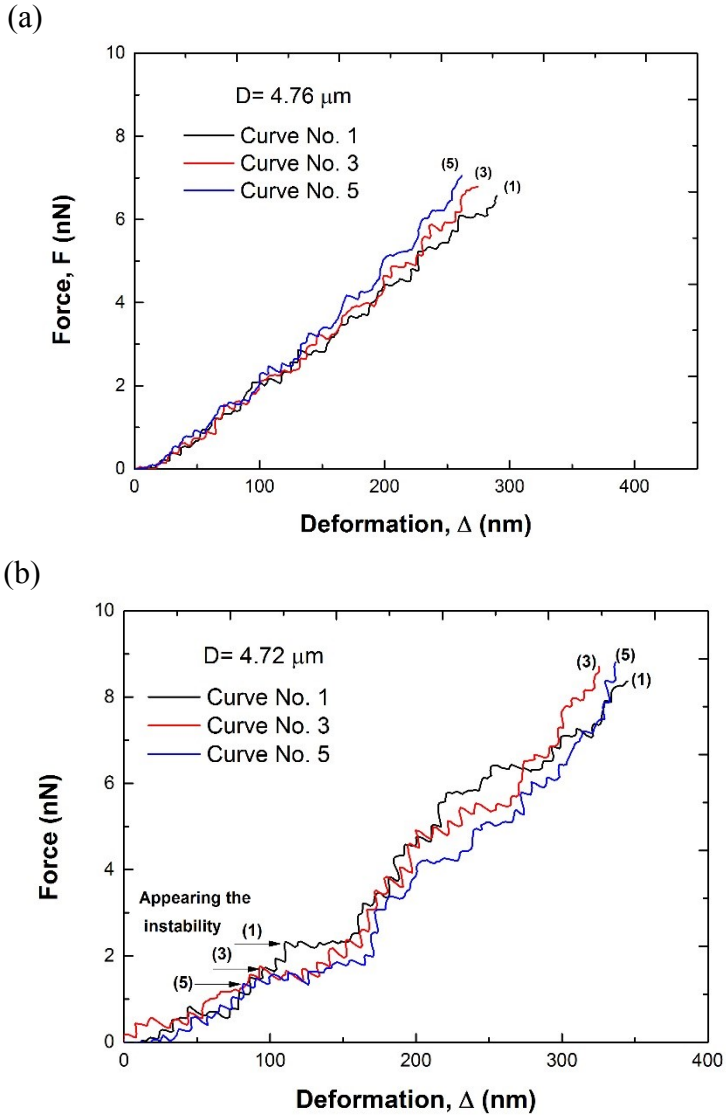

Figure 5-7: Illustrating the unrepeatability of both the stable and unstable curves. (a) A set of three curves without unstable areas, show small gaps. (b) Another three curves with unstable areas appearing in order. Note that the first number is the first acquired.

- **Nonlinearity**

In contrast with tipless cantilever, there is no nonlinear region in the beginning of the curve visible clearly with the tipped cantilever, unless we use third order polynomial fitting to make this area more visible. However, in similarity to the tipless cantilever, the tipped cantilever speed will affect the nonlinear region and there is a correlation between the nonlinear region and the speed, where the length of this region increases when the speed is increased. Figure 5-8-(a) shows curve for MBs with diameters 5.73 μm and average stiffnesses 0.035±0.008 N/m; depending on the third polynomial fitting curve, the nonlinear region ends at around 150 nm deformation, as shown in the figure. Looking at Figure 5-8-(b) gives us an image of the impact of the tipped cantilever speed on the nonlinearity; it displays 3 curves for a MB with diameters 4.76 μm and mean stiffnesses 0.030±0.002 N/m and various speeds: 12, 30 and 60 μm/s. The nonlinear region ends at 25, 50 and 175 nm deformation for the speeds 12, 30 and 60 μm/s respectively.

To investigate if there is any correlation between the size and stiffness of MBs when changing the compression tool to a tipped cantilever, 40 curves, acquired in the experimental work for 8 MBs were analysed. Figure 5-9-(a) illustrates a set of 3 curves for 3 MBs with various diameters: 5.73 (stable black line curve), 4.76 (relatively stable blue line curve) and 4.72 μm (unstable red line curve), and average stiffnesses of 0.035, 0.030 and 0.027 N/m respectively. The speed of the cantilever was constant at 3 μm/s. Considering an average of 5 curves for each MB, all stiffnesses were estimated after

the initial nonlinear region, for the stable curves, while they were calculated after the nonlinear region and before the first unstable step for the unstable curves.

(a)

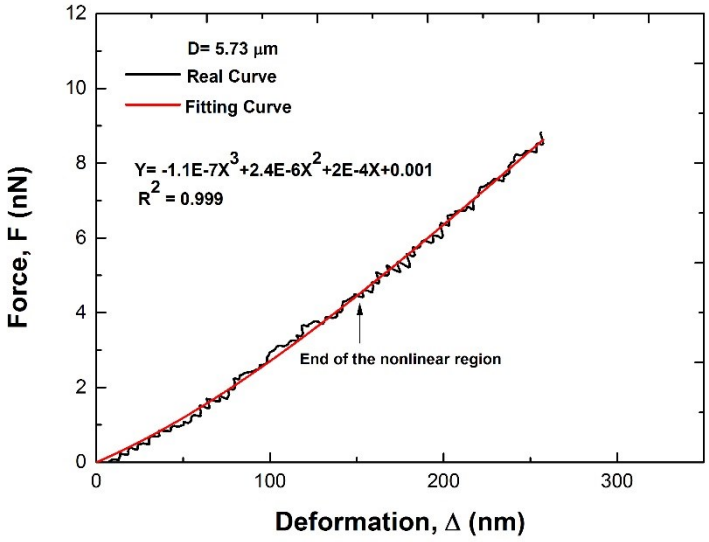

(b)

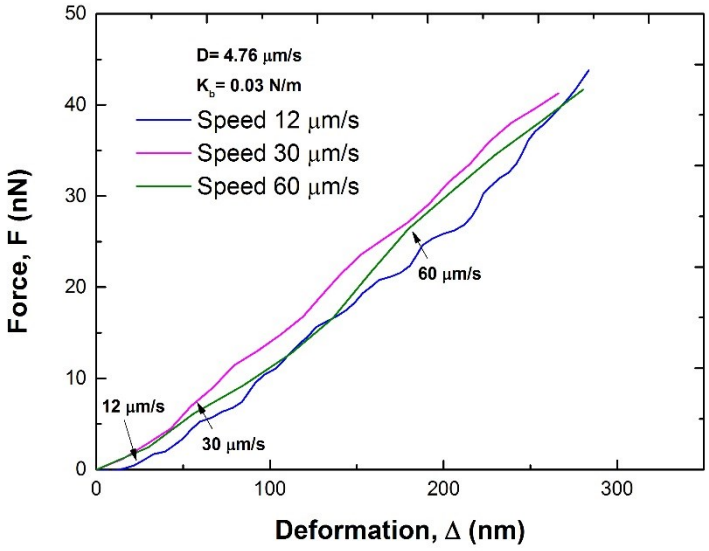

Figure 5-8: (a) Showing the end of nonlinear region for a MB, where it is around 150 nm deformation using a third order polynomial fitting curve. (b) A set of three curves illustrating effect of the speed on the nonlinear region.

Figure 5-9-(b) shows the effective stiffnesses of 8 MBs with diameters in the range of 3.48- 5.73 μm and mean 4.58 μm, while the stiffnesses were in the range 0.019±0.004 N/m (unstable) to 0.035±0.008 N/m (stable) and average 0.029±0.005 N/m. No

relation was seen between stiffnesses and the MBs size where the Pearson correlation coefficient, r = 0.2, and the best coefficient of determination (R-squared), R^2 = -0.11.

Most of the MBs (6 MBs, 75%) were observed to be unstable, while one of them (12.5 %) was completely stable, which is the largest MB, with D = 5.72 µm, and another one (12.5 %) was relatively stable with D = 4.76 µm. In the same manner as with the tipless cantilever, no fracture behaviour was observed.

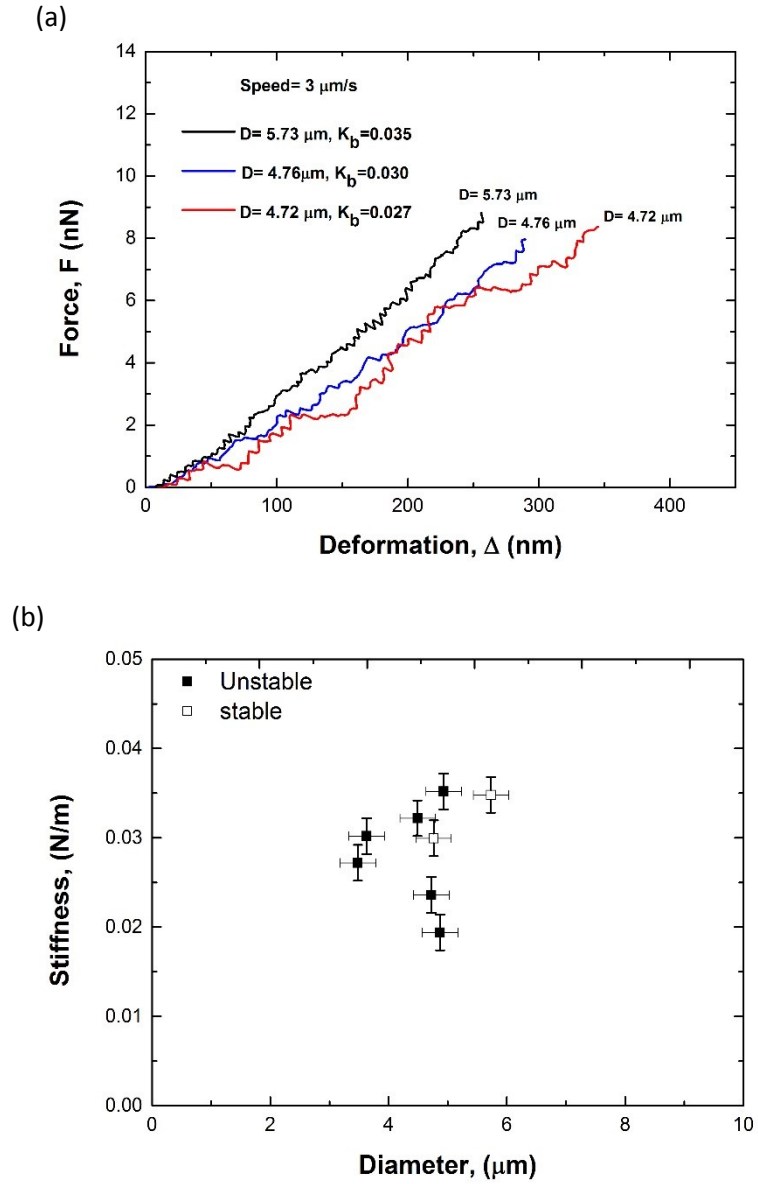

Figure 5-9: (a) A set of three curves with various diameters and various stiffnesses. One is completely stable, while the second relatively stable and the third is unstable. (b) Effective stiffness values for 8 MBs with diameters ranging from 3.43 µm to 5.73 µm.

5.3.2.2 Young's Modulus

In this section Young's Modulus is investigated, applying Hertz theory, using the acquired curves. This time Hertz theory will be used in the opposite situation, since the tip of the cantilever considered as a small ball, while the MB represents a huge ball with infinite diameter, and it becomes like a flat surface as explained in the theoretical section. Usually, 5 curves were considered to calculate Young's Modulus for each individual MB and the average was taken. Figure 5-10-(a) displays a typical force - relative deformation to the power one and half (F- $\varepsilon^{3/2}$) curve for one of the 8 MBs with diameter 4.87 μm and effective stiffness 0.019±0.004N/m. The gradient of the linear region was 645 nN multiplied by the associated factor, in this case 5.23×10^{-7} $(nm)^{-2}$ see equation 24 in Chapter 3, producing Young's modulus value 3.37×10^{-4} GPa (337 kPa). Figure 5-10-(b) illustrates a set of 8 MBs having diameters in the range 3.48- 5.73 μm and effective stiffness 0.019- 0.035 N/m, to predict the relation between the MB size and the Young's modulus values, using Hertz theory, with a tipped cantilever. The Young's modulus values were in the range of 1.19×10^{-4}- 6.72×10^{-4} GPa (119-672 kPa) and mean 3.28×10^{-4} GPa (328 kPa). No correlation was shown between Young's modulus and MB diameter where the Pearson correlation coefficient, r = 0.3, and the best coefficient of determination (R-squared), R^2 = -0.07. Figure 5-11 shows the relation between the MB size and the Young's modulus values using the histogram plot. It is clear that there is no correlation connecting them.

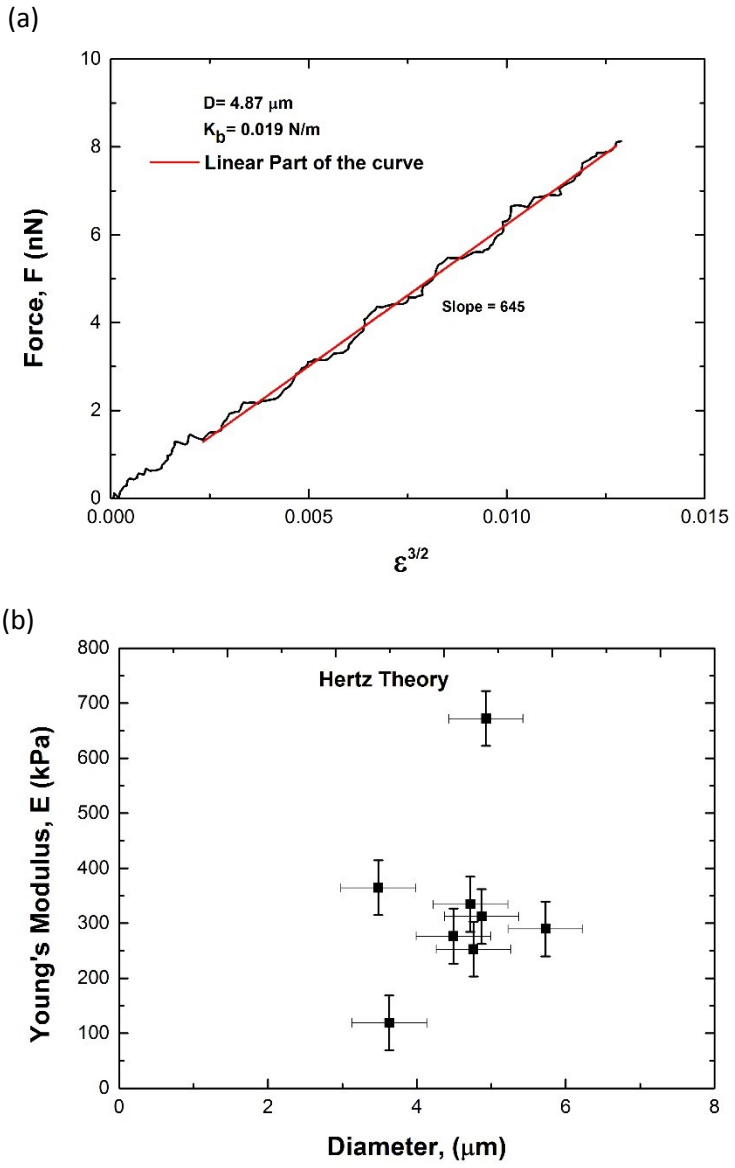

Figure 5-10: (a) Representing a typical F- $\varepsilon^{3/2}$ curve for a MB with diameter 4.87 μm and effective stiffness 0.19±0.004N/m. There is no correlation between Young's modulus and the MBs size, as shown in (b).

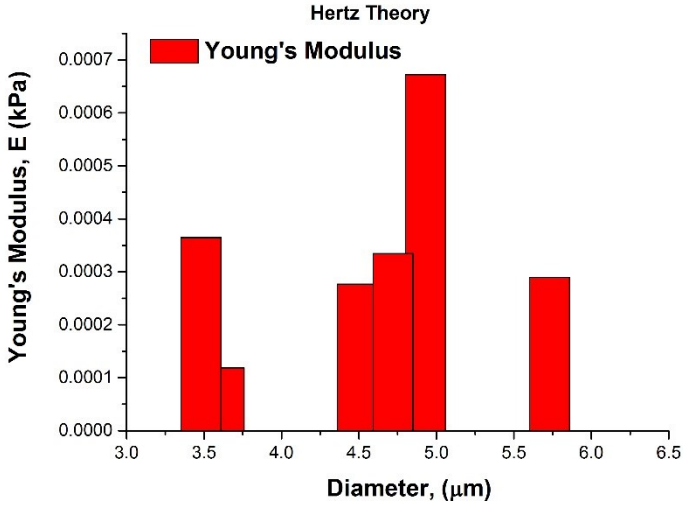

Figure 4-11: Showing the relation between Young's modulus and the MBs' size using histogram plot where no correlation was observed between them.

5.3.2.3 Hysteresis and Plasticity

- **Hysteresis**

It is important that we study the hysteresis of the material with different compression test tools, such as a tipped cantilever. [11, 12] When a MB is tested by a load (trace) and unload (retrace) cycle, the two curves limit an area between them, and this cycle is called a hysteresis loop. The energy dissipated during the compression processing cycle can be measured, depending on the hysteresis area. The lipid MB is one of the materials which produces a hysteresis area [13, 14] during the compression cycle, with a size depending on the nature of the MB and the experimental conditions. All 8 MBs, presented either a big or small hysteresis area, similarly to the tipless cantilever case. Figure 5-12 shows two MB curves, where Figure 4-12-(a) displays a very small hysteresis for a MB with diameter 5.73 μm and stiffness 0.035 N/m, using a cantilever with spring constant 0.052 N/m, reaching to maximum force 8.96 nN and

producing 147 nN.nm hysteresis area where the average over five curves was 177±48 nN.nm. In contrast, Figure 4-12-(b) represents a large hysteresis area for a MB with diameter 3.63 μm and effective stiffness 0.030 N/m, using the same cantilever with maximum force 8.01 nN. This MB gave hysteresis area of 732 nN.nm and the mean of five curves was 730±52 nN.nm. It is clear that the highest instability is associated with the highest hysteresis area and the lowest, or absence of, instability is associated with the lowest hysteresis area. The hysteresis areas were calculated using the trapezoidal rule.

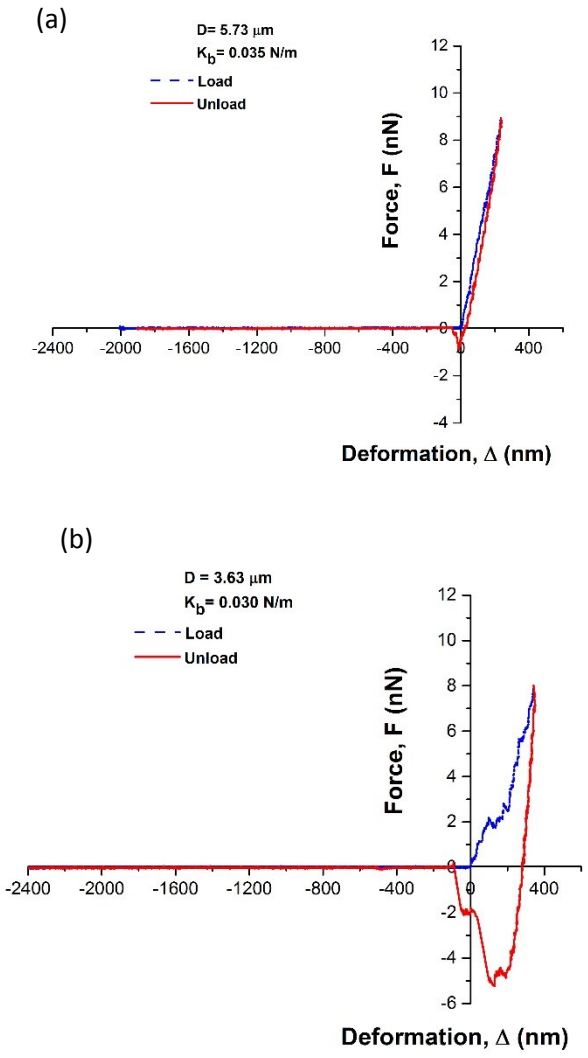

Figure 5-12: Two types of hysteresis, a small hysteresis area (a) and a large hysteresis area (b) using the same tipped cantilever with spring constant 0.052 N/m.

The parameters reviewed which could have an effect on the hysteresis area include MB size and effective stiffness. Figure 5-13-(a) displays the link between MB size and hysteresis area for a set of 8 MBs with diameters from 3.48 μm to 5.73 μm and effective stiffness in the range of 0.019- 0.035 N/m. The hysteresis areas were in the range of 177-767 nN.nm with mean of 556±240 nN.nm. A linear relation is suggested between the hysteresis area and MBs size, in a decreasing trend, where the Pearson correlation coefficient, r = -0.6, and coefficient of determination (R-squared), R^2 = 0.2. However, for the same group of MBs, there is no link between hysteresis area and the effective stiffness where the Pearson correlation coefficient, r = 0.01, and coefficient of determination (R-squared), R^2 = -0.17, as shown in Figure 5-13-(b).

(a)

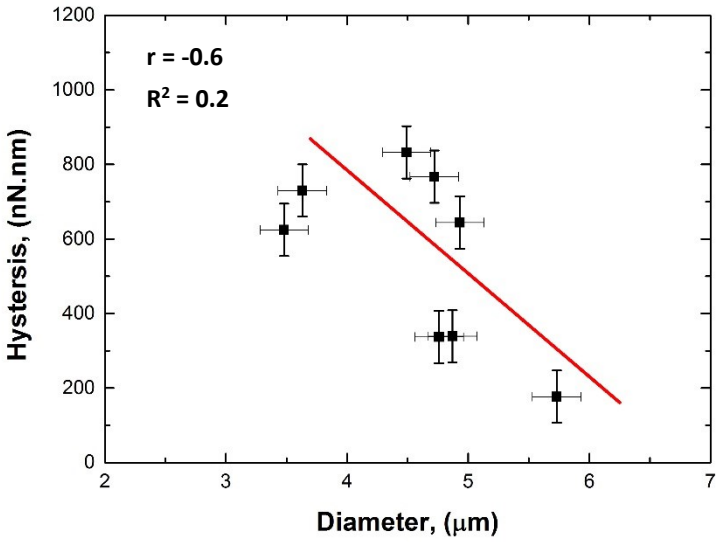

(b)

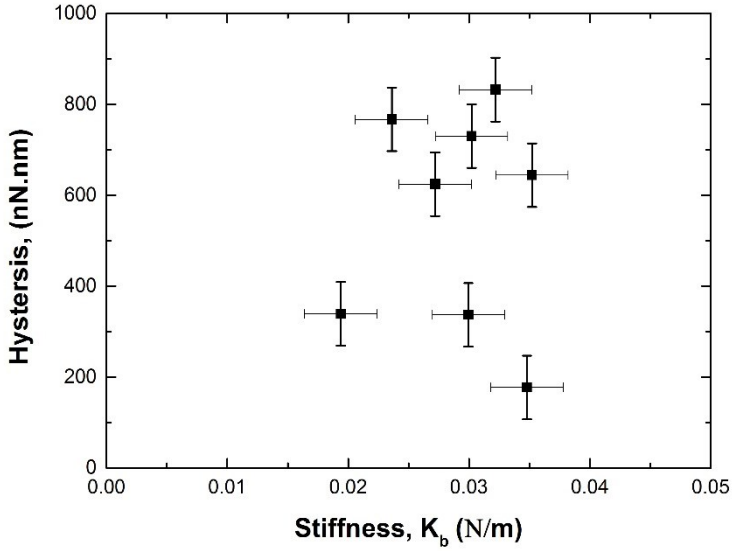

Figure 5-13: (a) The relation between hysteresis and diameters of the MBs; (b) effect of stiffness on hysteresis

The energy loss per cycle per unit volume was calculated by dividing the hysteresis area by the volume of the MB. [15] The hysteresis loss per unit volume was in the range of 0.344 – 3.54 kJ/m^3 (kPa) and the mean was 1.94 kJ/m^3 (kPa). The 8 MBs were again assessed to find the effect of MB size on hysteresis loss per cycle and Figure 5-14 displays this correlation. There is still, a relation; however, instead of an exponential curve (tipless cantilever case), in the case of tipped cantilevers it is a sharp decreasing trend; a linear fitting is a reasonable approximation where the Pearson correlation coefficient, r = -0.9, and coefficient of determination (R-squared), $R^2 = 0.8$. It has to be noted though that in the case of tipped cantilevers the range of microbubbles studied is smaller. It could be that the variation in diameters is small and insufficient to draw the whole picture of the relationship.

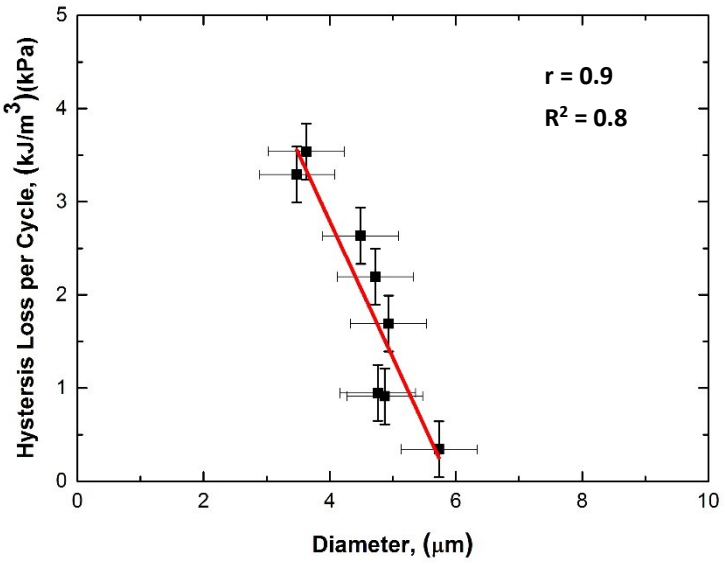

Figure 5-14: The correlation between MB size and energy loss per cycle per unit volume, where the largest MB has the least energy loss.

- **Plasticity**

Viscoelastic behaviour may appear when soft materials, such as phospholipid MBs, are under a load. [9] Hysteresis between loading and unloading was observed for all 8 MBs, as presented in the previous section. The data gathered from the unloading curve (retrace) provides a picture of the elastic, viscoelastic and plastic behaviour. [16] The viscoelastic behaviour of the MBs can be assessed by evaluating the plasticity index (η), by using the hysteresis area, which reflects the relative plastic/elastic behaviour of the material. Plasticity index (η) is equal to the ratio of the unloading area (A_u) to the loading area (A_l) thus ($\eta=1- A_u/ A_l$). [2] For a totally elastic sample, $A_u = A_l$ and the unloading curve is identical to the loading curve, so η=0. On the other hand, for purely plastic samples, $A_u = 0$: that is, the unloading curve is perpendicular to the x-axis (deformation axis) and η=1. [2, 16, 17]

All 8 MBs exhibit a viscoelastic behaviour, according to either a small or large hysteresis effect. Some of the MBs behave quite elastically, where η=0.20, as seen in Figure 5-12-(a), while others behave much more plastically (η=0.95), as shown in Figure 5-15. It is clear that the unloading curve (retrace) is almost perpendicular to the x-axis (deformation axis) and the area under the unloading curve (A_u) is almost zero. The index of plasticity (η) for all 8 MBs was in the range from 0.20 to 0.95 and the average was 0.67 ±0.26.

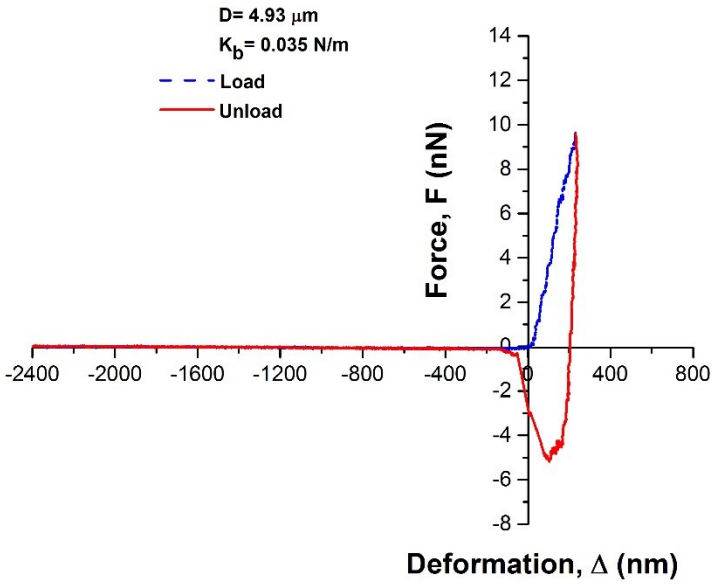

Figure 5-15: Load and unload curves with large hysteresis, where the MB behaves as a plastic material (η=0.95).

To see the influence of certain factors on the plasticity index (η), the reader is referred to Figure 5-16-(a), which shows the link between plasticity index (η) and MB size, where there is a weakrelationship between the plasticity index (η) and the diameter of the MB; we observe a decreasing trend where the Pearson correlation coefficient, r = -0.7, while the coefficient of determination (R-squared), R^2 = 0.3. In addition, no correlation between the plasticity index (η) and the effective stiffness was observed, as shown in Figure 5-16-(b) where the Pearson correlation coefficient, r = -0.004, while the coefficient of determination (R-squared), R^2 = -0.17. However, there is a connection between the plasticity index (η) and the hysteresis, which could be interpreted from Figure 5-17 as a linear relation, where the plasticity index (η)

rises with increased hysteresis and goes down when the hysteresis decreases here the Pearson correlation coefficient, r = 0.9, and coefficient of determination (R-squared), $R^2 = 0.8$.

.

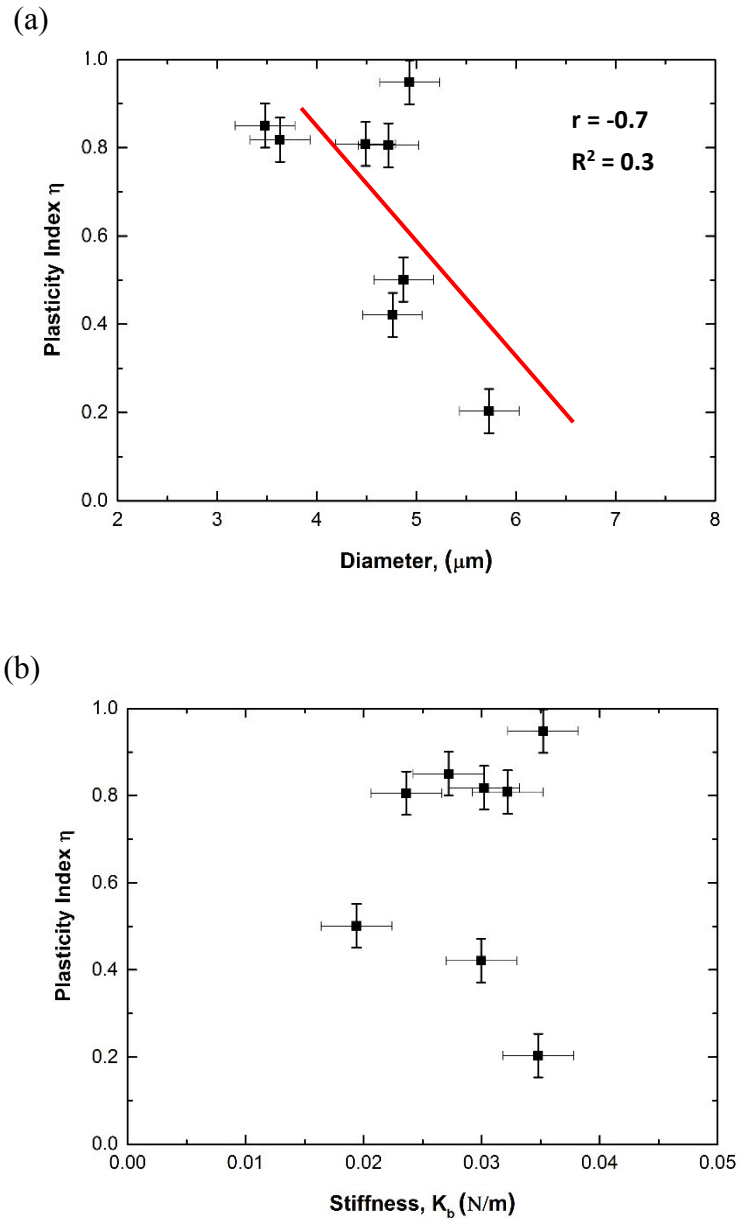

Figure 5-16: The correlation between plasticity index (η) and MB size (a) and effective stiffness (b)

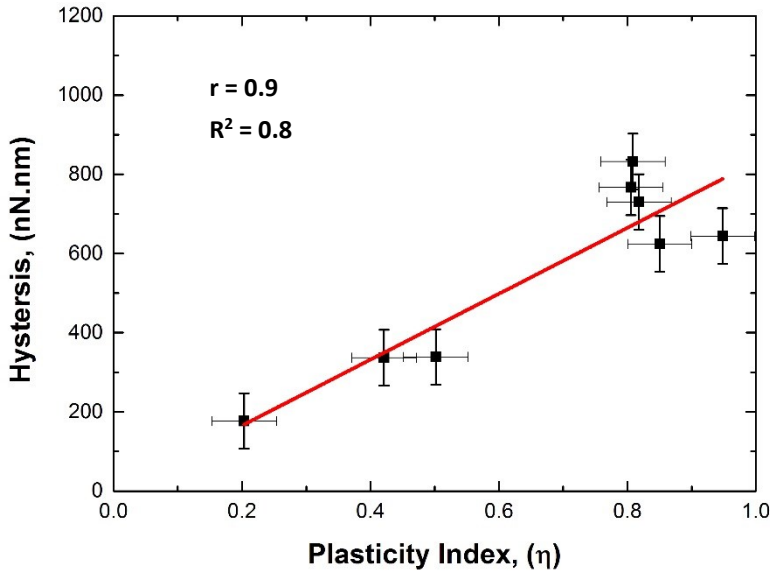

Figure 5-17: The relation between plasticity index (η) and hysteresis where the link is a linear up-trend.

5.3.2.4 Adhesion Forces

In the case of soft materials like phospholipid MBs, the interaction forces have significant impact on their behaviour, so it is essential that we highlight those forces, trying to understand them, and this is what the present section is intended to cover. The interaction forces were observed in the experiments in this study as adhesion forces (F_{adh}). When a cantilever retracts away from a MB, the MB is trying to hold it and pull it down, producing an adhesion force in the negative direction. Examining the force-deformation (F-Δ) curve of a group of MBs (8 MBs) adhesion forces were observed in all retracing (unloading) curves, with different values from 0.71 nN to 5.19 nN, with a mean of 3.13± 1.87 nN (in the negative direction). Figure 5-18 illustrates

an example of the load and unload curve with a significant adhesion force for a MB with size 4.72 μm (diameter) and stiffness 0.02 N/m, using a tipped cantilever with spring constant 0.052 N/m, where the adhesion force (F_{adh}) in this curve is 4.84 nN (in the negative direction).

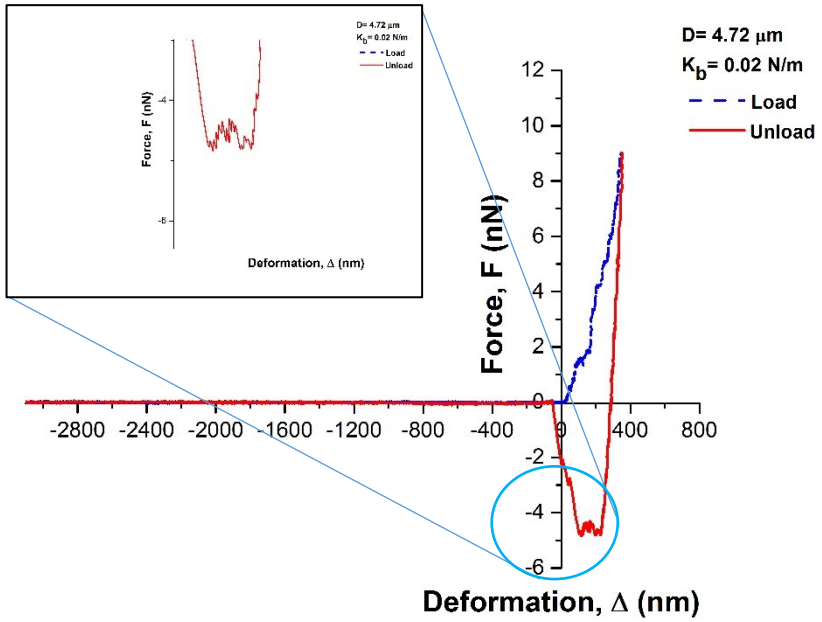

Figure 5-18: Representing an adhesion force at (-4.84 nN) for a MB with diameter 4.72 μm and stiffness 0.02 N/m, using tipped cantilever with spring constant 0.052 N/m.

To track the relation of adhesion force with other factors, for example the diameter of the MBs and their stiffness, the 8 retracing curves were studied to explore these correlations. It was found that there is a link between plasticity index (η) and adhesion force as an exponential relation, $R^2 = 0.92$, which is shown in Figure 5-19. However, no correlations exist between the adhesion force and MB size as seen in Figure 5-20-

a where the Pearson correlation coefficient, r = -0.45, and coefficient of determination (R-squared), $R^2 = 0.07$, or between adhesion force and MB stiffness where the Pearson correlation coefficient, r = 0.06, and coefficient of determination (R-squared), $R^2 = -0.17$, as shown in Figure 5-20-b, where the values are widespread and unorganized.

To see all the results and the mechanical properties which are studied in this chapter for each MB individually, the reader is referred to Appendix B.

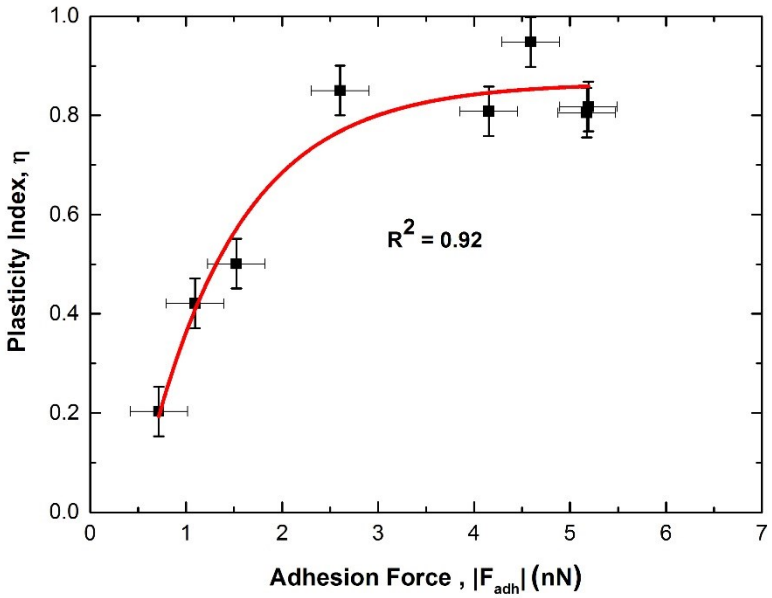

Figure 5-19: Illustrating the correlation between the plasticity index (η) and the absolute value of the adhesion force as an exponential relation.

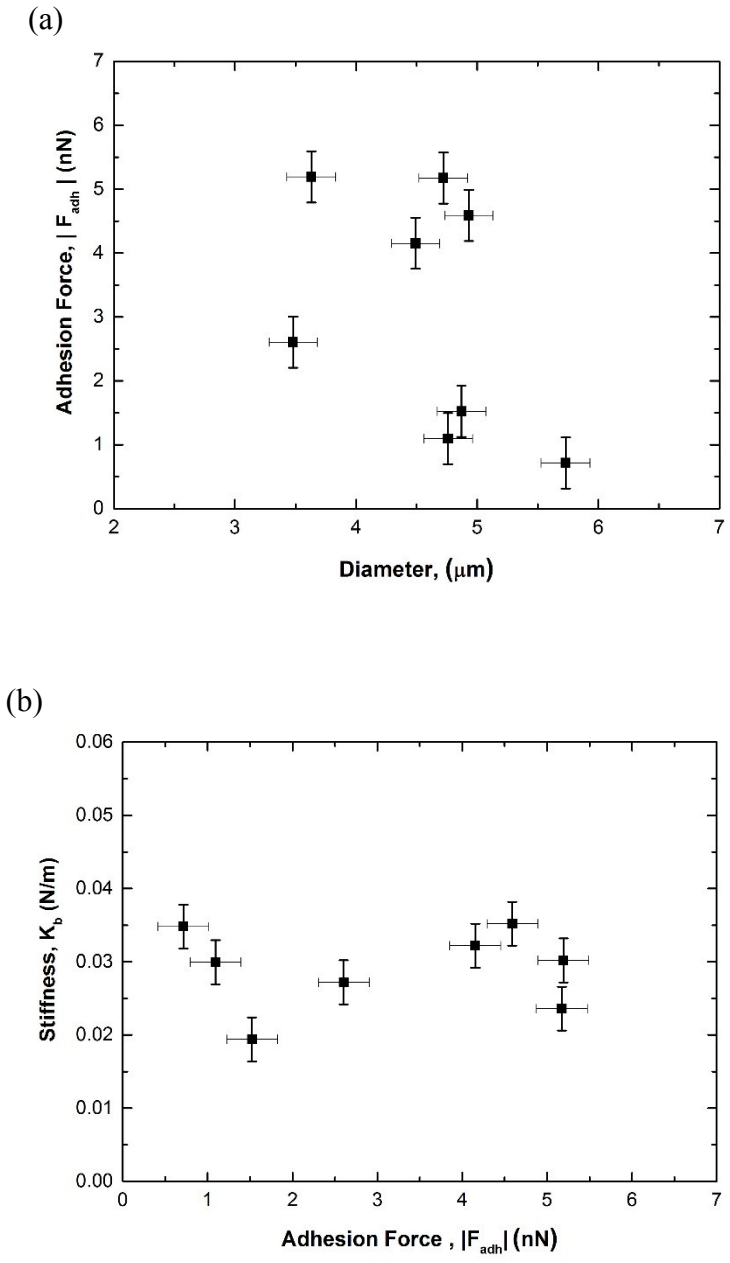

Figure 5-20: The relation between adhesion force and MBs size (a), and between adhesion force and stiffness (b). Clearly, there is no link between them.

5.4 Discussion

In this chapter the results were presented from an experimental study of the mechanical properties of SonoVue MBs by applying the AFM technique using a tipped cantilever. After the experimental work, eight MBs succeeded in passing the experimental conditions for further analytical steps. Some factors and parameters played different role when using the tipped cantilever.

The effective stiffness of the MBs (K_b) was calculated to lie in the range of 0.019– 0.035 N/m, with an average 0.029 N/m using a tipped cantilever with spring constant of 0.052 N/m; these values are only around one third of the values for the tipless cantilever, which are 0.048-0.158 N/m and 0.09 N/m for the range and the average stiffness respectively. It is notable that the spring constant of the tipless cantilever is 0.284 N/m but only 0.052 for the tipped cantilever. The results are identical to previous study results [18] that used a soft-tipped cantilever, which found the stiffness in the range 0.013-0.051 N/m, while another study [19] found it to be 0.025 N/m, using a soft, tipless cantilever. Abou-Saleh el at. [20] investigated similar lipid MBs with no PEG at the same applied force (10 nN), and they found the stiffness to be around 0.022 N/m, which indicates that there might be no influence of cantilever geometry on the stiffness values, if the cantilevers have the same spring constant and the same force is applied. Similarly to the tipless cantilever, no correlation was observed between the stiffness and MBs size. Moreover, no fracture or laceration of the MB shell occurred, even with the occurrence of many unstable steps. In contrast,

with the tipless cantilever, all the MBs exhibited unrepeatable force-deformation (F-Δ) curves. The evolution of curves with time could suggest some permanent deformation. Unstable steps appeared in abundance, compared to the curves from the tipless cantilever, even though the applied force was smaller with a tipped cantilever than with the tipless cantilever, because the force became more concentrated as the tip behaves like a point contact force.

As occurred with the tipless cantilever, the local stiffness becomes higher and higher after each unstable step and this phenomenon continues unless the curve reaches to nonlinear region at the top of the curve. The reason could be the thickness of the shell was larger after each unstable step. The effects of the thickness on stiffness were assessed in a study [21] which found that the elasticity of the shell increases with increasing shell thickness. It seems there is a relation between the initial nonlinear part of the curve and the speed of the tipped cantilever: as found previously with the tipless cantilever, the initial nonlinear region is bigger with increasing the cantilever speed, because of fluid mechanics and the drag force, which was discussed in the previous chapter.

Modulus of elasticity (Young's modulus) was estimated by applying Hertz theory, however, in the opposite situation this time, where the huge sphere (the flat part) is the MB and the small sphere is the tip of the cantilever. The results were in the range of 1.19×10^{-4}- 6.72×10^{-4} GPa, with a mean of 3.28×10^{-4} GPa (328 kPa), which are close to and in the same order of magnitude as the tipless cantilever results. In contrast with the tipless cantilever, no relation was observed between Young's modulus and the MBs' diameter. This is in agreement with the results and observation of Morris study, [18] where it was calculated to be in the range of 78 - 416 kPa.

All the compression cycles (load and unload curves) displayed a hysteresis area. The hysteresis areas were much smaller with the tipped cantilever than with the tipless cantilever: the means were 556 nN.nm and 4490 nN.nm for tipped and tipless cantilevers, respectively. The difference could be due to the adhesion forces in the tipped cantilever being smaller than those in the tipless cantilever because the contact area between the cantilever and the sample surface is much smaller in the tipped than the tipless cantilever. Moreover, the friction energy loss resulting from slipping is smaller in the tipped than in the tipless cantilever. The hysteresis did not display a relation with stiffness of MBs; however, there is a suggested linear relation with MBs size. A linear decreasing relationship between hysteresis loss per cycle per unit volume and MBs size was shown. The difference between the MBs sizes was small, and this can be the reason that the exponential relation (as appeared with the tipless cantilever) is missed. The hysteresis energy loss was in the range of 0.344 – 3.54 kJ/m^3 (kPa) and the mean was 1.94 kJ/m^3 (kPa), which is smaller than for the tipless cantilever case, where the average was 14.1 kJ/m^3 (kPa), because the hysteresis area was smaller with the tipped cantilever.

Plasticity index (η) was calculated and found to be in the range of 0.20 to 0.95 with an average of 0.67. There was no relation between plasticity index (η) and MB diameters or between plasticity index (η) and stiffness of the MBs but there was a correlation with hysteresis area: linear and increasing relationship.

The adhesion force was also studied, using a tipped cantilever, to discover if there is any link between the interaction forces and other factors or not. The adhesion forces were in the range from 0.71 nN to 5.19 nN with an average of 3.13 nN, which is smaller than the adhesion force incurred by the tipless cantilever, where the mean

was 6.17 nN, again resulting from a small contact area using the tipped cantilever. No correlation was found between adhesion force and either stiffness or MB size; however, there was a good exponential relation between adhesion force and plasticity index (η).

5.5 Conclusion

This chapter has reported how some factors and properties of SonoVue® microbubbles were studied in the same manner as in the studies reported in the previous chapter, however, by using a different compression tool, which was a tipped cantilever. The investigated factors were stiffness, Young's modulus, instability, repeatability, nonlinearity, hysteresis, plasticity index and adhesion forces. The MBs stiffnesses were calculated using the gradient of the initial linear part of the force-deformation (F-Δ) curve and before any unstable steps. The stiffness was in the range of 0.019 – 0.035 N/m and average 0.029 N/m. There is no relation between stiffness and MBs size. Unstable steps occurred frequently and the local effective stiffness increased after each step. Young's modulus was estimated by applying Hertz theory. The modulus of elasticity was in the range from 1.19×10^{-4} GPa to 6.72×10^{-4} GPa and mean 3.28×10^{-4} GPa (328 kPa) and no correlation was observed. The mean of the hysteresis and hysteresis energy loss were 556 nN.nm and 1.94 kJ/m^3 (kPa) respectively. A linear relation between hysteresis energy loss and MBs size was observed, where the energy loss decreases with decreasing MB diameters. The average of the plasticity index (η) was 0.67 and one of the MBs responded significantly as a plastic material, where (η=0.95). There was a correlation with hysteresis area as an uptrend line. The adhesion forces were also calculated to be in the mean 3.13 nN, and

an exponential relationship between adhesion forces and plasticity index (η) was found.

It can be concluded that the impact of the geometry of the cantilever is limited and has influence on some factors or parameters, such as adhesion forces and hysteresis, while the other properties are not affected significantly. If the same cantilever spring constant and the same applied forces are used, there might have not been any differences in stiffness and modulus of elasticity (Young's modulus) as calculated by Hertz theory.

5.6 References

1. Claesson, P.M., Ederth, T., Bergeron, V. and M.W. Rutland, *Techniques for measuring surface forces.* Advances in Colloid and Interface Science, 1996. **67**: p. 119-183.

2. Butt, H.J., Cappella, B. and M. Kappl, *Force measurements with the atomic force microscope: Technique, interpretation and applications.* Surface science reports, 2005. **59**(1): p. 1-152.

3. Schaefer Group, *http://www.schaefertec.com/osteuropa/produkte/ rastersondenmikroskopie/mikromasch.html.* November, 2016

4. Hutter, J.L. and J. Bechhoefer, *Calibration of atomic-force microscope tips.* Review of Scientific Instruments, 1993. **64**(7): p. 1868-1873.

5. Lévy, R. and M. Maaloum, *Measuring the spring constant of atomic force microscope cantilevers: thermal fluctuations and other methods.* Nanotechnology, 2002. **13**(1): p. 33-37.

6. Ohler, B., *Cantilever spring constant calibration using laser Doppler vibrometry.* Review of Scientific Instruments, 2007. **78**(6): p. 063701-063705.

7. Hutter, J.L., *Comment on Tilt of Atomic Force Microscope Cantilevers: Effect on Spring Constant and Adhesion Measurements.* Langmuir, 2005. **21**(6): p. 2630-2632.

8. Kim, M., Choi, J., Kim, J. and Y. Park, *Accurate determination of spring constant of atomic force microscope cantilevers and comparison with other methods.* Measurement, 2010. **43**(4): p. 520-526.

9. Abou-Saleh, R.H., Peyman, S.A., Critchley, K., Evans, S.D. and N.H. Thomson, *Nanomechanics of lipid encapsulated microbubbles with functional coatings.* Langmuir : the ACS journal of surfaces and colloids, 2013. **29**(12): p. 4096-4103.

10. Buchner Santos, E., Morris, J.K., Glynos, E., Sboros, V. and V. Koutsos, *Nanomechanical properties of phospholipid microbubbles.* Langmuir : the ACS journal of surfaces and colloids, 2012. **28**(13): p. 5753-5760.

11. Love, A.E.H., *A Treatise on the Mathematical Theory of Elasticity* Vol. 1. 2011: Dover Publications.

12. Dharan, C.K.H. and T.F. Tan, *A hysteresis-based damage parameter for notched composite laminates subjected to cyclic loading.* Journal of Materials Science, 2007. **42**(6): p. 2204-2207.

13. Chandran Suja, V., Frostad, J.M. and G.G. Fuller, *Impact of Compressibility on the Control of Bubble-Pressure Tensiometers.* Langmuir, 2016. **32**(46): p. 12031-12038.

14. Alvarez, N.J., Walker, L.M. and S.L. Anna, *A Microtensiometer To Probe the Effect of Radius of Curvature on Surfactant Transport to a Spherical Interface.* Langmuir, 2010. **26**(16): p. 13310-13319.

15. Parthasaradhy, P. and S. Ranganayakulu, *Hysteresis and eddy current losses of magnetic material by Epstein frame method-novel approach.* Int. J. Eng. Sci.(IJES), 2014: p. 85-93.

16. Briscoe, B., Fiori, L. and E. Pelillo, *Nano-indentation of polymeric surfaces.* Journal of Physics D: Applied Physics, 1998. **31**(19): p. 2395-2405.

17. Klymenko, O., Wiltowska-Zuber, J., Lekka, M. and W.M. Kwiatek, *Energy dissipation in the AFM elasticity measurements.* Acta Physica Polonica-Series A General Physics, 2009. **115**(2): p. 548-551.

18. Morris, J.K., *Mechanical properties of phospholipid coated microbubbles*. 2015, The University of Edinburgh: Edinburgh, UK. PhD thesis. p. 1-157.

19. McKendry, J., Grant, C., Johnson, B., Coletta, P., Evans, J. ans S. Evans, *Force spectroscopy of streptavidin conjugated lipid coated microbubbles.* Bubble Science, Engineering & Technology, 2010. **2**(2): p. 48-54.

20. Abou-Saleh, R.H., Swain, M., Evans, S.D. and N.H. Thomson, *Poly(ethylene glycol) Lipid-Shelled Microbubbles: Abundance, Stability, and Mechanical Properties.* Langmuir, 2014. **30**(19): p. 5557-5563.

21. Lulevich, V.V., Andrienko, D. and O.I. Vinogradova , *Elasticity of polyelectrolyte multilayer microcapsules.* JOURNAL OF CHEMICAL PHYSICS, 2004. **120**: p. 3822-3826.

CHAPTER 6

EVALUATION OF THE NANOMECHANICAL PROPERTIES OF HYDROGELS

CAPTER 6: EVALUATION OF THE NANOMECHANICAL PROPERTIES OF HYDROGELS

6.1 Introduction

The study of biological systems as structures began in the early part of the 20th century. [1] The first work published about structures of the biological systems was in 1917 by D'Arcy W. Thompson [2], which was a major work in this field. Although biological science is not a new field, the study of biological and biomedical materials and their applications is still nascent and evolving. [3] The field of tissue engineering is in its early stages and the structural relationships in many biological materials remain difficult to understand. The assessment of the mechanical properties of some soft tissues is limited by the complex nature of their structure and physiological environment. For instance, some of the soft tissues exhibit nonlinear and viscoelastic behaviour. [4-7] Thus, the nature of the tissue and developing the ability to probe specific properties in a controlled environment complicate the mechanical tests. Recently, nanoindentation has been adopted in the tissue engineering field as an applicable technique for investigating the local mechanical properties of tissue replacements, diseased tissues and healthy tissues. Many studies have used nanoindentation to assess the material behaviour of tooth enamel and dentin, bone and the mineralized matrix. [8-15] Nanoindentation techniques are easily used with stiff material where the material can be polished to acquire a flat surface. [11, 16, 17] However, the challenge appears when using the nanoindentation techniques with soft

materials, such as gels. Therefore, there is a genuine need to develop a new technique to probe the materials and evaluate their mechanical properties. To measure the mechanical properties of a soft material at the nanoscale, the nanoindentation technique can be used. The geometry of the indenter tip controls the resolution of this technique. Depth-sensing nanoindentation by AFM has been widely used to investigate the mechanical properties of materials, specifically for soft materials, where the reaction forces are measured upon applying a certain indentation depth using a rigid indenter in contact with the tested materials. [18, 19]

One group of those tissue engineering materials or biomaterials are the hydrogel products. The hydrogels comprise two groups: either they are natural or synthetic, based on their origin. [20-22] A hydrogel is defined as a water-swollen cross-linked polymeric network which is produced by one or more monomers by a simple reaction. Their hydrophilic structure helps them to hold a large amount of water in a three-dimensional network. [20, 21] They can be formed from either chains of natural polymers such as collagen, gelatine, agarose and alginate or synthetic polymers such as polyvinyl alcohol (PVA) and polyacrylic acid (PAA). This chapter will investigate the mechanical properties of a widely used soft biomedical material, which is the agarose hydrogel. In this research, the effect of the agarose gels' concentration on their mechanical properties is assessed and the correlations between the concentration of agarose gel and other factors, such as stiffness, adhesion forces and hardness will be identified.

6.2 Materials and Methods

6.2.1 Materials

A type of hydrogel called agarose hydrogel was investigated in this study. An agarose hydrogel consists of distilled and deionised water, 4X M9 Salts (Sigma-Aldrich Co., St. Louis, MO, USA), 1M $MgSO_4$ (Sigma-Aldrich Co., St. Louis, MO, USA), 20% glucose (Thermo Fisher Scientific, Waltham, MA, USA), 1M $CaCl_2$ (Sigma-Aldrich Co., St. Louis, MO, USA) and the agarose (Sigma-Aldrich Co., St. Louis, MO, USA), all these components with specific amounts. Three concentrations of agarose hydrogel were prepared 1wt% agarose gel, 2wt% agarose gel and 3wt% agarose gel which will be referred to GEL1, GEL2, and GEL3 respectively.

6.2.2 Sample Preparation

6.2.2.1 The protocol of the M9 agarose medium

Since the M9 growth medium is used in medical applications, sterilization is an important requirement in the samples' preparation. Thus, to prepare 100 ml M9 agarose media it was necessary to follow these procedures: [23]

71.79 ml of distilled and deionised water was poured into 250 ml sterile bottle.

4X M9 Salts (minimal salts) were added with amount 25 ml.

The agarose was added with the desired weight percent concentration (for example for 2wt% agarose 2 g agarose were added).

The sample was placed in the autoclave machine for 15 mins to a temperature greater than 100° C.

The sample was then placed in warm water bath for 15mins at 50° C.

200 µl of 1M $MgSO_4$ was added.

2 ml of 20% glucose was added.

10 µl of 1M $CaCl_2$ was added.

The bottle was shaken well to dissolve the $CaCl_2$ in the solution and to avoid deposition.

The agarose was poured in 2ml amounts in small bottles to be ready for the experiments.

Note: The agarose should be heated to just above the melting point when being used in the experiments.

6.2.2.2 The preparation of the M9 agarose medium for AFM

Preparing the agarose samples for the AFM test required equipment including a water bath (Grant Instruments Ltd, Station Road, Shepreth, Cambridgeshire, UK), 1000 µl pipette (Thermo Fisher Scientific, Waltham, MA, USA), 1000 µl pipette tips (Thermo Fisher Scientific, Waltham, MA, USA), petri dishes (60X15mm, Greiner Bio-OneGmbH, Frickenhausen, Germany), a hot plate (Cole-Parmer Ltd, Beacon Road, Stone, Staffordshire, UK) and tinfoil (see Figure 6-1).

After adding the glucose, $CaCl_2$ and $MgSO_4$, as mentioned previously, the agarose medium (the mixture) was reheated again up to 80° C in the water bath. The hot plate was switched on and heated to 90° C. A small piece of tinfoil was placed on the hot

plate; then a petri dish was placed on it (to be used for the agarose sample). 500 µl of M9 agarose was taken from the bulk store using the pipette then placed in the dish in the form of a large drop. The agarose drop was spread with a small roller to produce a very thin, less than 1 mm, and approximately homogenised layer of agarose.

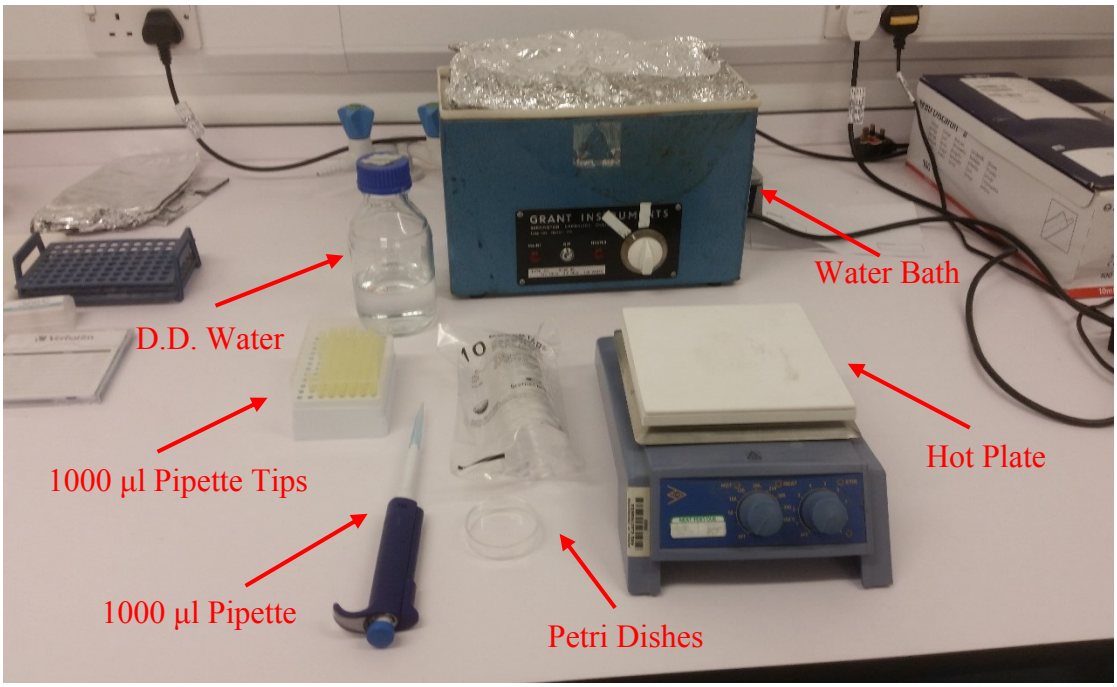

Figure 6-1: An image showing the equipment used to prepare the agarose hydrogels for AFM test.

The drop was positioned near the centre of the petri dish but not in the middle, to leave plenty of space to test the sensitivity of the cantilever on a hard surface (the petri dish surface) to compare the sensitivity of the cantilever before and after the test, as shown in Figure 6-2. The petri dish was removed and allowed to cool on the desk. When it became solid, the agarose gel was covered with distilled and deionised water (d. d. H_2O) in order to reduce the adhesion forces between the sample and the AFM tip. This also helped the sample to remain soft for longer time, by holding an amount of water

inside its structure, to finish the measurements. The sample was then taken to the AFM for the experiments.

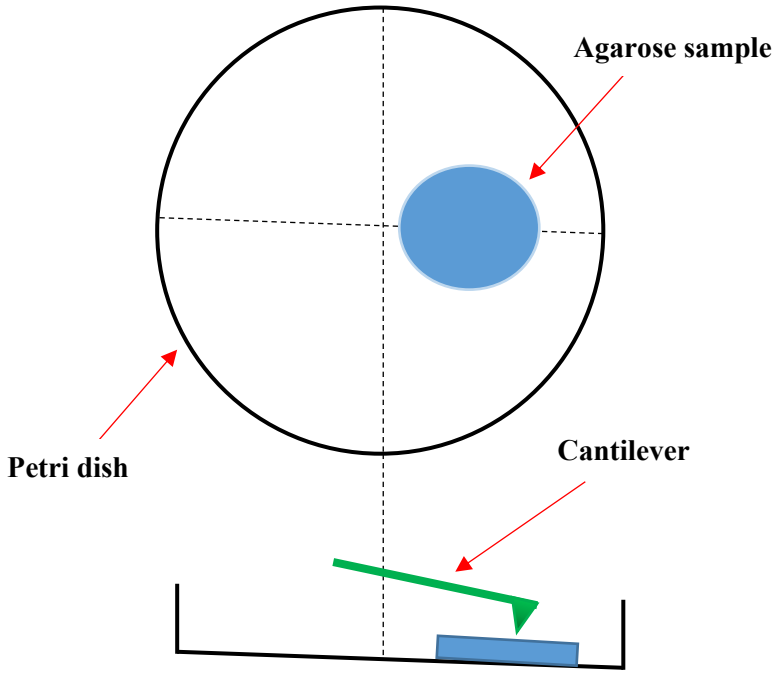

Figure 6-2: Schematic showing position of the agarose (the blue spot) on the petri dish. The agarose was positioned off the centre of the petri dish to provide plenty of space to test the sensitivity of the cantilever on the hard surface after finishing the sample test.

6.2.3 Experimental Approach

A large number of curves, 150 curves, were obtained in the gel experiments. The three different concentrations of gels were tested over three days using conical tipped cantilevers with spring constants of 0.050 N/m, 0.049 N/m and 0.040 N/m for GEL1, GEL2 and GEL3 respectively, according to their calibration, where the nominal typical value in the data sheet is 0.03 N/m and the range is 0.01– 0.08 N/m. Ten test points for each gel were chosen randomly and each test point was tested five times, which means

50 curves were acquired for each sample. The gels were transparent and invisible under the microscope which made performing the experiments very difficult. Performing the experiments with this disadvantage became a genuine challenge and the duration of the experiments was extended to many hours. Therefore, to avoid damage to the cantilever, starting from a high point away from the surface of the sample the cantilever was very gently moved down, step by step, to reach the contact point, which took more than an hour. Sometimes it would be discovered that the cantilever was already stuck, without any prior warning, in the gel surface (involving the whole of the cantilever holder), which required repeating the experiment again and again. Once proper contact occurred (without any undesirable sticking) the area around the first contact could be tested, which allowed 10 points to be tested around the first contact for each gel. Eventually, after multiple attempts, three gels in total were tested successfully. In order to acquire AFM force-distance curves, a continuous pull was adopted with constant speed (3 μm/s). The spring constants of the cantilevers were estimated by calibration procedures during the day preceding the experiment. After some initial exploratory curves, 5 curves were taken for each test point and 50 curves in total for each gel to investigate the gel's behaviour. All experiments were implemented at room temperature and in an aqueous environment (distilled and deionised water) to minimize adhesion forces and to avoid dehydration of the gel. During the specimen test, all vibration or heat sources, i.e. light, AC and camera, were turned off. The acquired raw data were passed through several stages to convert them from deflection-distance to force-indentation curves, as discussed in Chapter 3. The initial linear part of the force-indentation curve, before any yielding point, was taken into consideration to evaluate the gel stiffness.

6.3 Apparatus and Tools

As in previous experiments, the main instrument here is the molecular force probe (MFP 1-D) (Asylum Research, Santa Barbara, CA) which was mounted on a Nikon TE2000U (Nikon UK Limited, Surrey, UK) inverted optical microscope to help to view the cantilever from below. The conical tipped cantilevers, CSC 12/ without Al/ 50 (MikroMasch, Tallinn, Estonia), without aluminium backside coating were used. The tip was 20 μm in height with 10 nm radius of curvature and 20^{o} full tip cone angle. The calibrated spring constants of the cantilevers were 0.050±0.001 N/m (for GEL 1), 0.049±0.002 N/m (for GEL 2) and 0.040±0.001 N/m (for GEL 3), where the nominal typical value in the data sheet was 0.03 N/m and the range was 0.01-0.08 N/m. For each experiment, the cantilevers were moved at a constant speed, 3 μm/s, and from the same distance, 3 μm, away from the gel, including the contact and non-contact region.

6.4 Results

6.4.1 Introduction

In all experiments, the speed of the cantilever movement was fixed during approach and retraction at 3 μm/s and force was fixed at ~ 15 nN (which is consistent with the spring constant of the cantilever and led to acquisition of appropriate curves), while the concentrations of the agarose gel were varied to investigate the effect of the concentration on the mechanical properties of the gel. A conical-tipped cantilever was

used as an indenter tool. The cantilever was calibrated according to the measurement of the intensity of the thermal noise method. [24-27] This method is widely used as it is appropriate to most types of cantilevers, easy to use and involves no damage to the tip. [28] The raw position-deflection data were recorded which were subsequently converted to force-indentation (F-δ) data (as explained in Chapter 3). It was possible to acquire a significant number of curves for the three gels with different concentrations.

6.4.2 Stiffness

Each gel was tested individually, acquiring 50 force-indentation (F-δ) curves. After obtaining the raw data and converting them to force-indentation (F-δ) curves, the stiffness was calculated from the gradient of the initial linear part of the force-indentation (F-δ) curve [29, 30] and before any yielding point or penetration step appeared.

- **Instability**

Two types of behaviour were observed in the gels. In the first one, smooth curves were observed in some points of the gel, while the second was curves where a yielding point [6, 31] appeared. Figure 6-3 illustrates the two types of curves. Figure 6-3-(a) shows a smooth curve with no yielding point, for GEL 1 at test point 4, using a conical-tipped cantilever with spring constant k_c= 0.05 N/m. The gradient of the linear part of the curve (red line) is 0.06 N/m, which reflects the stiffness of the gel at this test point. Figure 6-3-(b) represents the force-indentation (F-δ) curve of GEL 1 at test point 9

using the same cantilever. This curve starts with a nonlinear part until around 100 nm indentation (δ), then becomes a linear curve, and at 250 nm indentation (δ) a yield point appears or penetration for the gel tissues occurs, which could indicate that the plastic behaviour region starts. The reader is referred to

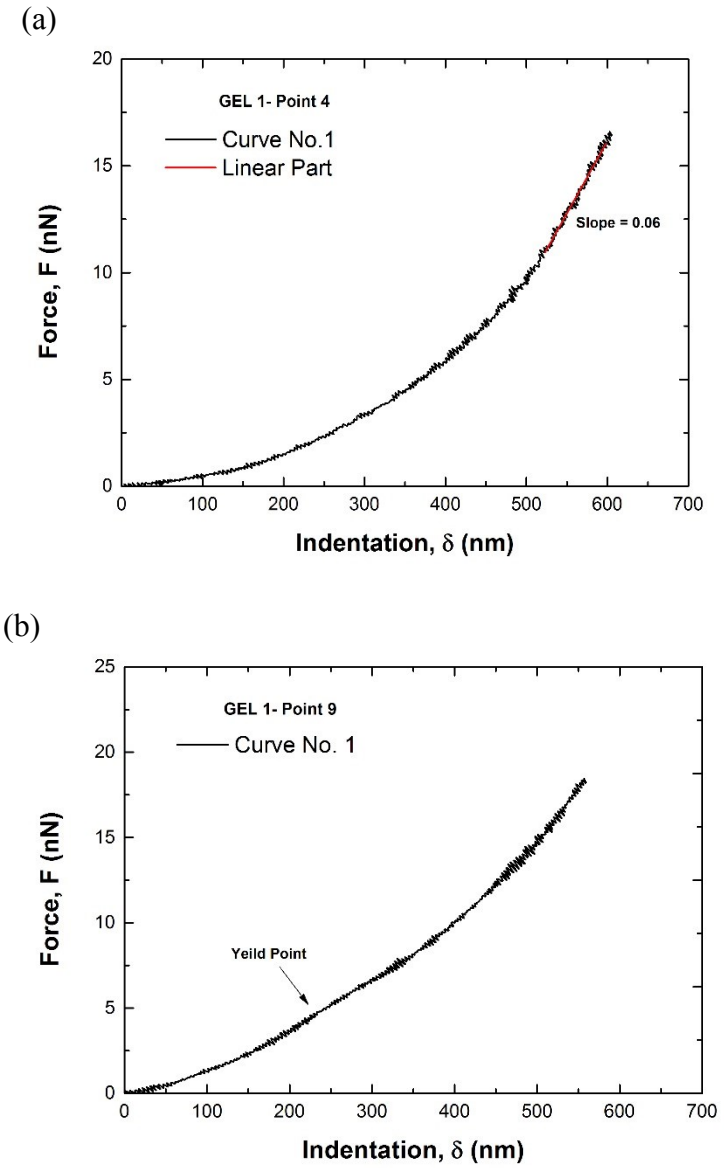

Figure 6-3: Two types of GEL 1 behaviours. (a) Showing a smooth curve, without yielding point, for test point 4 and curve No.1, using a conical tipped cantilever with spring constant K_c= 0.05 N/m. (b) Curve with yielding point or rupture for the gel tissues at test point 9 and curve No.1.

Figure 6-4 to distinguish the yielding point clearly. Sneddon model was used in this chapter where the curve starts with a nonlinear region until around $10x10^3$ $(nm)^2$, (δ^2), then moves linearly with slope $7.4x10^{-5}$ nN $(nm)^{-2}$ and at about $63x10^3$ $(nm)^2$, (δ^2), a yield point appears, with deviation in the curve from the elastic behaviour of the gel beyond this point. It can be seen that the slope of the curve changes before and after the yielding point, which indicates that a plastic deformation could be happening in the sample. It is noted that GEL1 and GEL3 exhibited yielding points in some places while GEL2 did not.

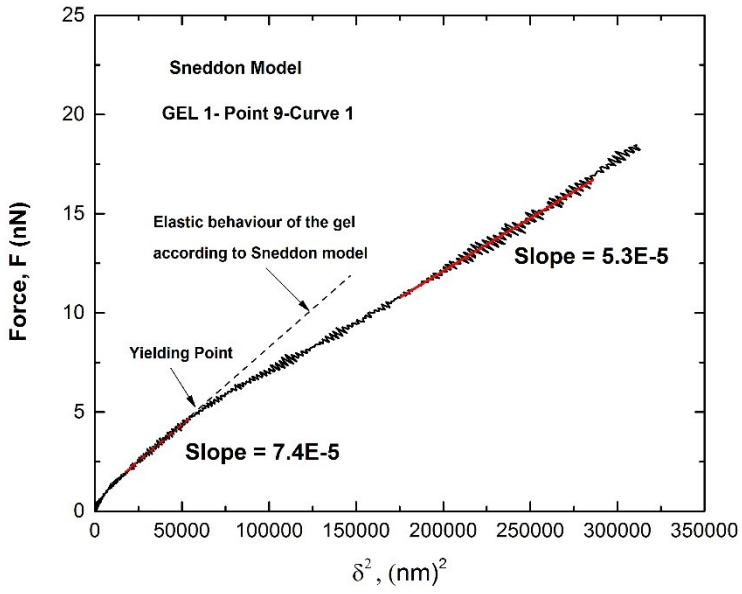

Figure 6-4: Showing the yield point on the (F-δ^2) curve using the Sneddon model where the slope varies before and after the yielding point, which indicates that plastic deformation might be occurring.

- **Repeatability**

After investigations of all the gels' curves, two types of repeatability behaviour were observed. The first one was a perfect repeatability where all the curves were completely identical either with or without a yielding point, which indicates that no permanent plastic deformation took place. The second one was also a good repeatability; however, there were little gaps between the curves, which were arranged either randomly or in the order in which they were acquired, which indicates that a small plastic deformation could have occurred where the slope changes from one curve to another. Figure 6-5-(a) illustrates a good repeatability for the last 5 stable curves acquired from GEL1 at test point 8, with average stiffness 0.052±0.008 N/m using a conical-tipped cantilever with spring constant 0.05 N/m. All 5 curves are almost identical indicating that no permanent plastic deformation exists. Figure 6-5-(b) shows a good repeatability for another set of 5 curves, however, this time with a yielding point obtained from GEL3 at test point 1 with average stiffness 0.114±0.006 N/m using a cantilever with spring constant 0.040 N/m. The five curves are essentially identical, even with a yielding point.

The second type of curves are those with gaps between them, and these are evolving one after another either in a organised manner (upwards or downwards) or are organised randomly. Figure 6-6-(a) shows a set of 4 curves acquired from GEL1 at test point 5, with average stiffness 0.050±0.005 N/m, using a tipped cantilever with spring constant 0.050 N/m. The curves start from the origin point (0, 0) then go up moving away from each other, ending up with gaps between them and they are organised in the order where the first number is the first acquired.

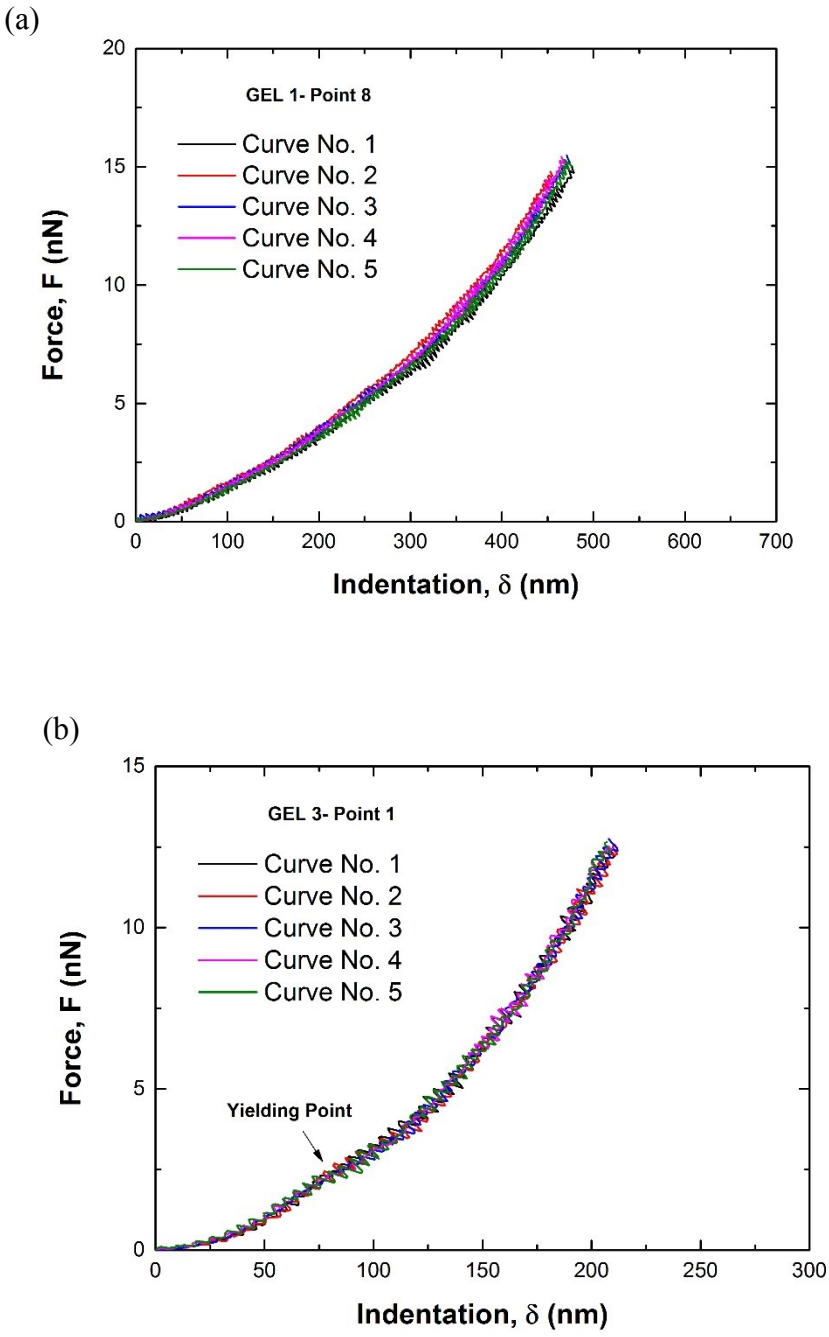

Figure 6-5: Showing two sets of 5 curves. (a) A set of five curves without yielding point are exactly identical for GEL 1at test point 8. (b) Another five curves with yielding point are also identical for GEL3 at test point 1. Note that the first number is the first acquired curve.

Figure 6-6-(b) represents another set of 4 unstable curves with yield points acquired from GEL3 at test point 3, with average stiffness 0.101±0.006 N/m, using a tipped

cantilever with spring constant 0.040 N/m. The curves start from point zero then go up, moving with a small gap between the curves, even after they have passed the unstable step (yielding point), finishing in an order consistent with the acquisition of the curves, which may involve the occurrence of some plastic deformation.

(a)

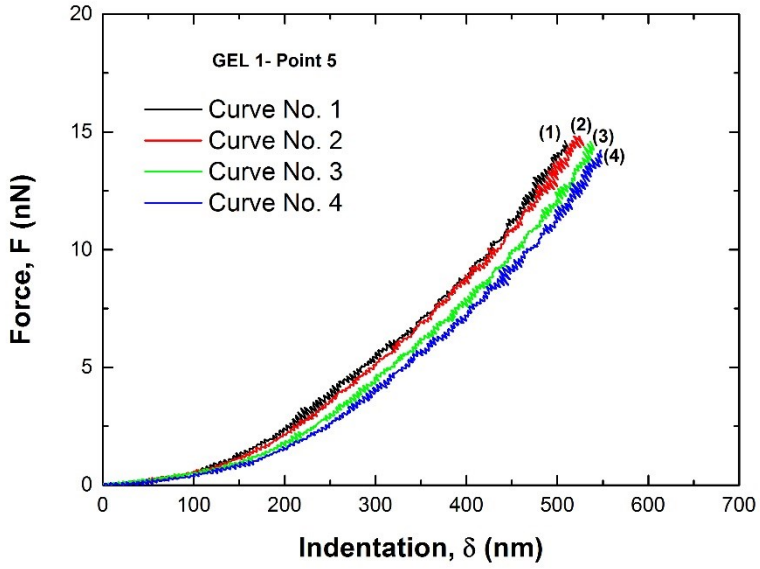

(b)

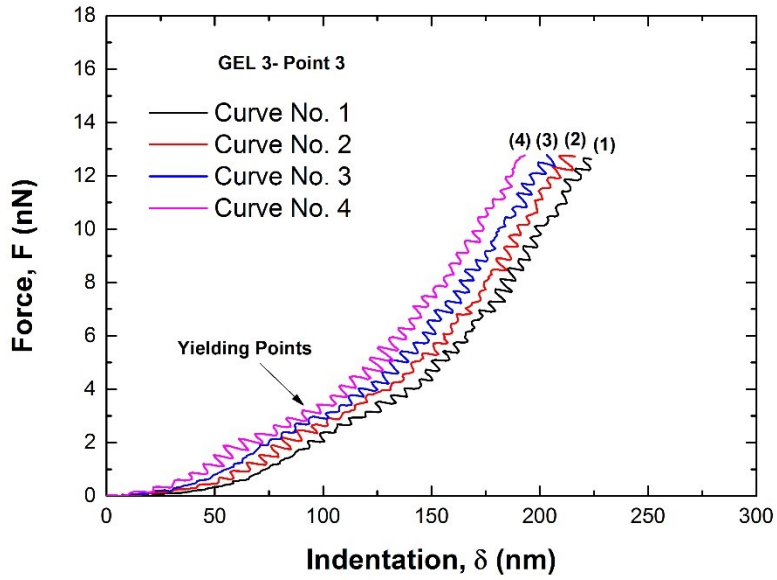

Figure 6-6: Illustrating the unrepeatability of both the stable (without yielding point) and unstable (with yielding point) curves. (a) A set of four curves without yielding point show small gaps between them. (b) Another set of four curves with yielding point.

Many curves, 50 curves for each gel and 150 curves for all the gels, were studied to investigate if there is any correlation between the concentration of the gels and their mechanical properties. Figure 6-7-(a) illustrates the stiffness of 29 test points. The raw data at test point 6 for GEL1 are unsaved, where each gel has 10 test points except GEL1, which has 9 test points; the results for each gel are similar for all the ten test points. Stiffness of the GEL1 is in the range of 0.043-0.063 N/m and average 0.054±0.007 N/m, while GEL2 is in the range from 0.104 to 0.138 N/m and mean 0.120±0.010 N/m and GEL3 is in the range 0.105-0.144 N/m and average 0.117±0.013 N/m. It is clear that the stiffnesses of GEL2 and GEL3 are close to each other, whereas GEL1's stiffness is much lower. Figure 6-7-(b) represents the correlation between concentration of the agarose gels and their stiffness. The relation seems logarithmic, coefficient of determination (R-squared), R^2 = 0.84, where the rate of change in stiffness value is high, 55%, between GEL1 and GEL2 however it is low, 2.5%, between GEL2 and GEL3.

(a)

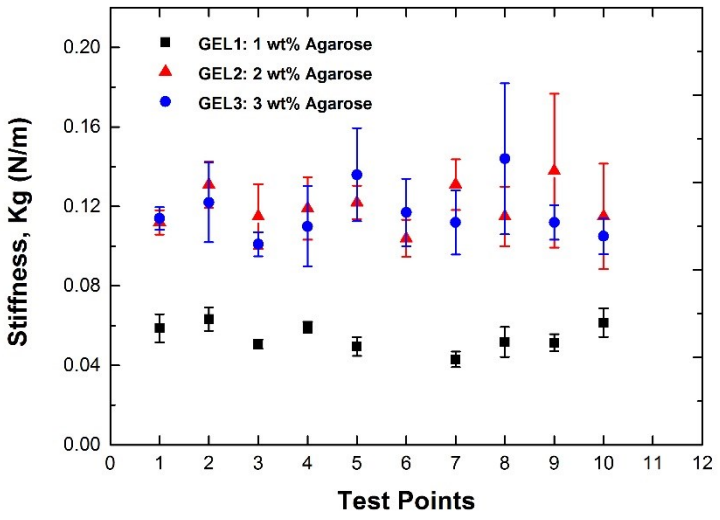

(b)

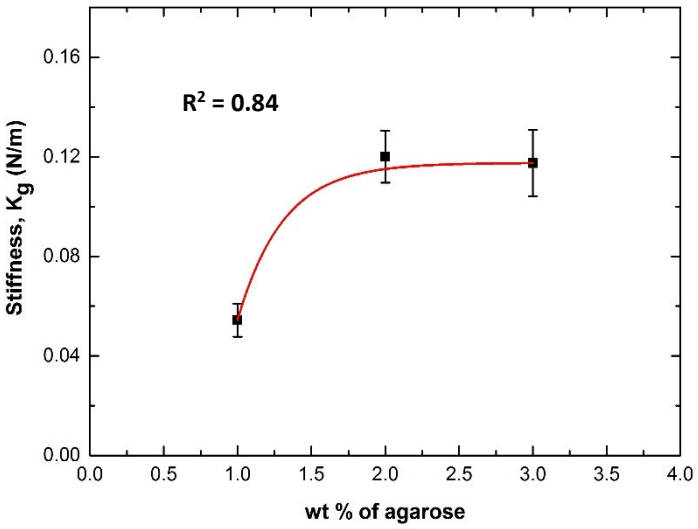

Figure 6-7: (a) Illustrating stiffness of ten test points for each gel. (b) The relation between agarose gel concentration and stiffness where the correlation is an exponential curve.

6.4.3 Young's Modulus

In this section Young's Modulus is investigated by applying Hertz theory, which was modified and expanded by Sneddon [32] to be applicable for other axisymmetric geometries, such as a conical tip. [33-35] After gathering the raw data and converting them to force-indentation (F-δ) curves, the Young's Modulus was calculated from the gradient of (F-δ^2) based on Sneddon's model as shown in equation 25 Chapter 3. The gradient was multiplied by a constant factor, in this case 6.68, see equation 28 Chapter 3, where Poisson's ratio (ν) was 0.5 and the full tip angle was 20^o, according to the data sheet provided by the manufacturing company. As mentioned previously, to predict the linear part of the curve, a third order polynomial fitting was used. Usually, 5 curves were considered to calculate Young's Modulus for each test point and ten test points for each gel were chosen, meaning that an average of 50 curves for each sample was estimated. Figure 6-8-(a) displays a typical (F-δ^2) curve for GEL2 at test point 1, where the Young's Modulus at this test point is in the range of 1.21-1.73 MPa and average 1.5300±0.0002 MPa. Figure 6-8-(b) illustrates the relation between concentration of the agarose gel and the Young's modulus values using Sneddon's solution with a conical-tipped cantilever. The Young's modulus values were in the range of 256-470 kPa and mean 331±78.9 kPa for GEL1 and ranged from 1.46 MPa to 2.27 MPa, with average 1.99±0.52 MPa, for GEL2, and from 1.68 MPa to 2.47 MPa and mean 2.14 ±0.28 MPa for GEL3.

A logarithmic correlation , coefficient of determination (R-squared), $R^2 = 1$, was found between Young's modulus and the concentration of the agarose gels, where the

Young's modulus increased rapidly, 500%, with increasing concentration between GEL1 and GEL2 and increased by a lower rate, 7.5%, between GEL2 and GEL3. In addition, The shear modulus can be estimated directly by applying the relation between Young's modulus and shear modulus, $E = 2G(1+\nu)$, [36] where G is the shear modulus. The average values of the shear modulus were 110 kPa, 663 kPa and 713 kPa for GEL1, GEL2 and GEL3 respectively. The correlation between the shear modulus and the concentration of the agarose gel is the same as the relation in Young's modulus since the Young's modulus was multiplied by a constant value. Figure 6-9 illustrates the relation between concentration of the agarose gel and the Young's modulus values using a histogram plot where the relationship is clearly increasing.

(a)

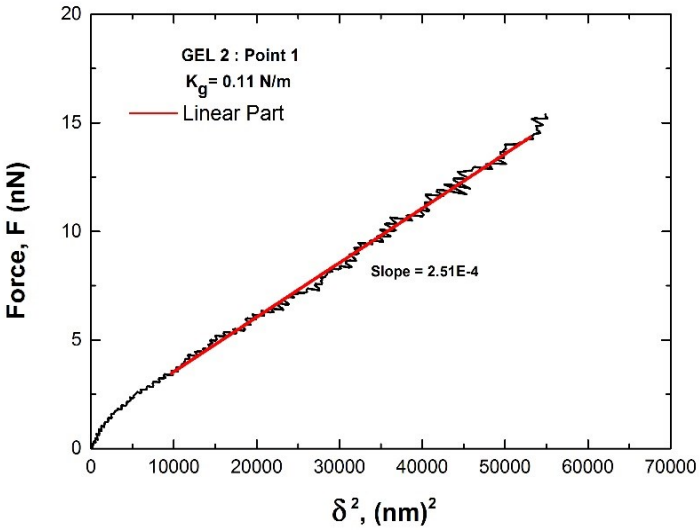

(b)

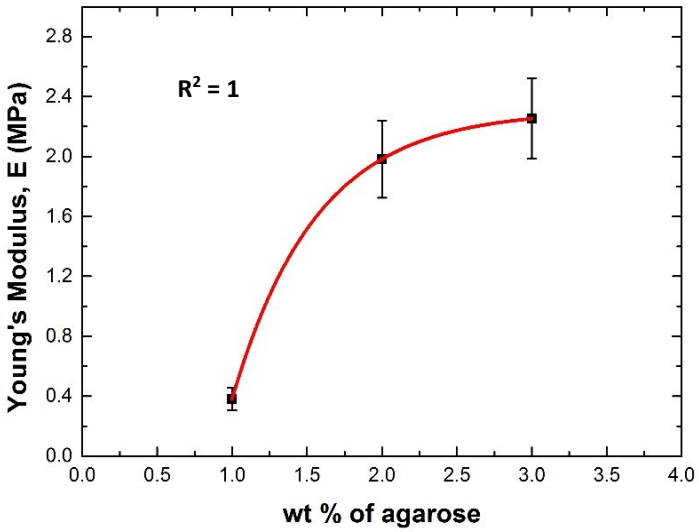

Figure 6-8: (a) A typical F-ε^2 curve for GEL2 at test point 1 with stiffness kg = 0.11N/m. A logarithmic correlation was observed between the Young's modulus and the concentration of the agarose gels, as shown in (b).

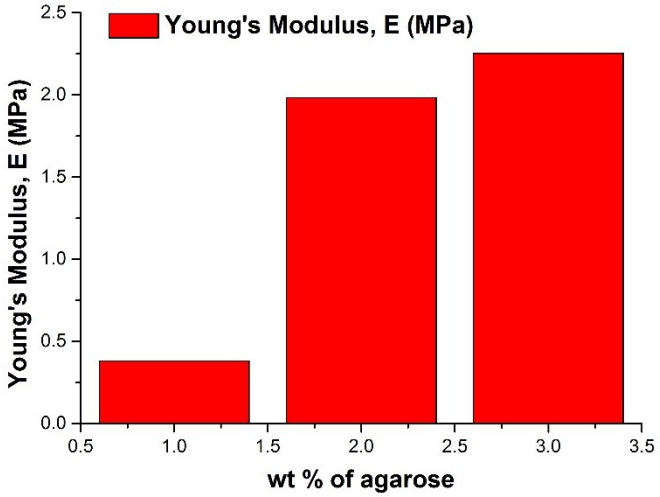

Figure 4-9: Showing the relation between Young's modulus and the MBs' size using histogram plot where no correlation was observed between them.

6.4.4 Hysteresis and Plasticity

- **Hysteresis**

All the gels presented a hysteresis with a variety of small and large values; however, compared to the results for lipid microbubbles, the hysteresis area here is smaller. Figure 6-10 shows two force-indentation (F-δ) curves, where Figure 6-10-(a) displays a very small hysteresis for GEL2 at test point 7, with stiffness 0.140 N/m, using a conical-tipped cantilever with spring constant 0.049 N/m, reaching maximum force of 15.7 nN and producing 231 nN.nm hysteresis area, where the average over five curves was 109±77 nN.nm. Figure 6-10-(b) represents a large hysteresis area for GEL1 at test point 9, with stiffness 0.050 N/m, using tipped cantilever with spring constant 0.050 N/m reaching maximum force of 18 nN. The gel at this point gave a hysteresis area of 674 nN.nm and the mean of the five curves was 656±177 nN.nm.

To investigate the effect of other parameters on hysteresis, 150 curves were assessed. Figure 6-11-(a) displays the link between concentration of the agarose gels and the hysteresis area. The average values of hysteresis areas were 542± 105 nN.nm, 217± 55 nN.nm and 153± 21 nN.nm for GEL1, GEL2 and GEL3, respectively. An exponential decay relation, coefficient of determination (R-squared), R^2 =1, connects the hysteresis area and the concentration of the agarose gels, where the hysteresis area decreases with the increase in the concentration of the agarose gels, with a high rate of decreasing, -150%, between GEL1 and GEL2 and with lower rate, -72%, between GEL2 and GEL3.Moreover, there is a correlation between hysteresis area and the stiffness of the gels, in a linear relation in a downward trend where the Pearson correlation coefficient, r = -0.92 and coefficient of determination (R-squared), R^2 = 0.70 as shown in Figure 6-11-(b).

(a)

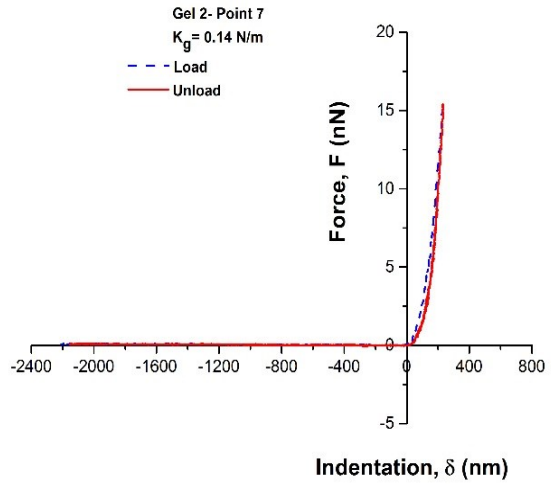

(b)

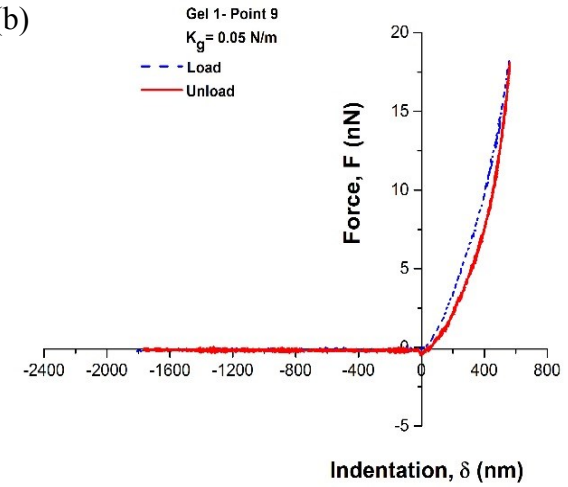

Figure 6-10: Two types of hysteresis: (a) a small hysteresis area for GEL2 at test point 7 with average hysteresis 109 nN.nm and (b) a large hysteresis area for GEL1 at test point 9 with average hysteresis 656 nN.nm.

By assuming that the deformed material of the gel equals to the immersed part of the conical tip at the maximum indentation (δ_{max}), the energy loss per cycle per unit volume was calculated by dividing the hysteresis area by the deformed volume of the gel. [37] The hysteresis loss per unit volume was in the range of 68.2 – 132 kJ/m^3 (kPa) and the mean was 101±23 kJ/m^3 (kPa) for GEL1 and range from 283 kJ/m^3 (kPa) to 731 kJ/m^3 (kPa) with average 526±136 kJ/m^3 (kPa) for GEL2 while GEL3 had a range of 431-652 kJ/m^3 (kPa) and average 555±69 kJ/m^3 (kPa).

Figure 6-12-(a) shows the relation between the hysteresis loss per unit volume and the concentration of the agarose gels, which is a logarithmic relation with coefficient of determination (R-squared), R^2 =1; it increases with increasing the concentration of the gel logarithmically. The link between the hysteresis loss per unit volume and the stiffness of the agarose gels is a linear relation with an increasing relationship where the Pearson correlation coefficient, r = 0.99 and coefficient of determination (R-squared), R^2 = 0.98; as shown in the linear fit in Figure 6-12-(b).

(a)

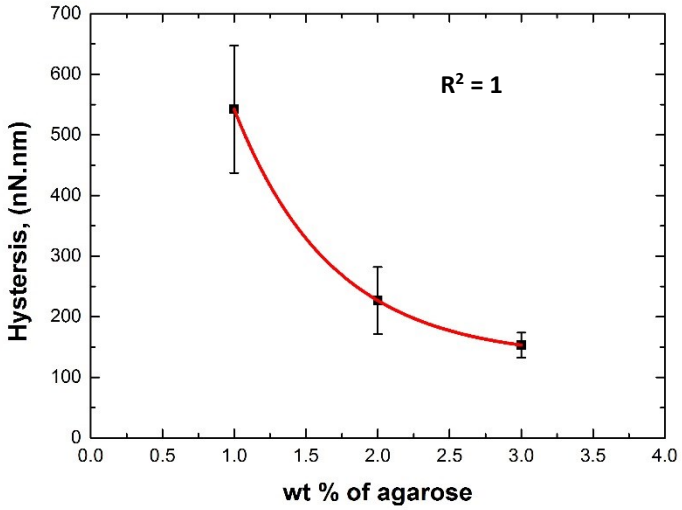

(b)

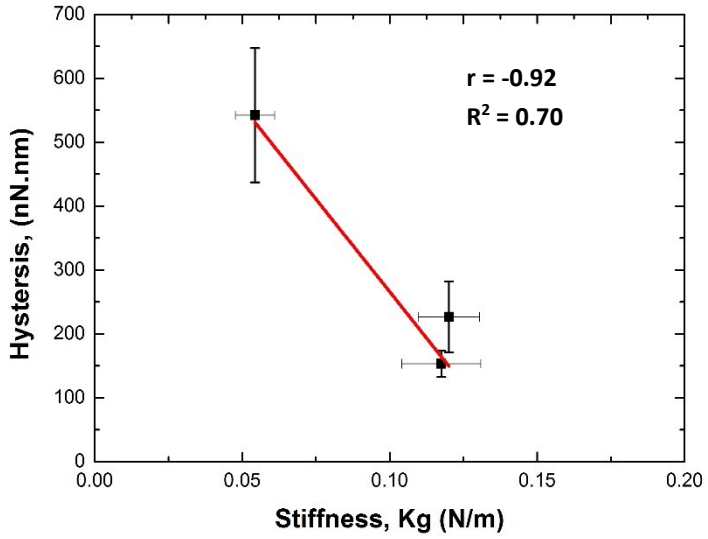

Figure 6-11: (a) The relation between hysteresis and concentration of the agarose gel; (b) the correlation between hysteresis and stiffness of the gels.

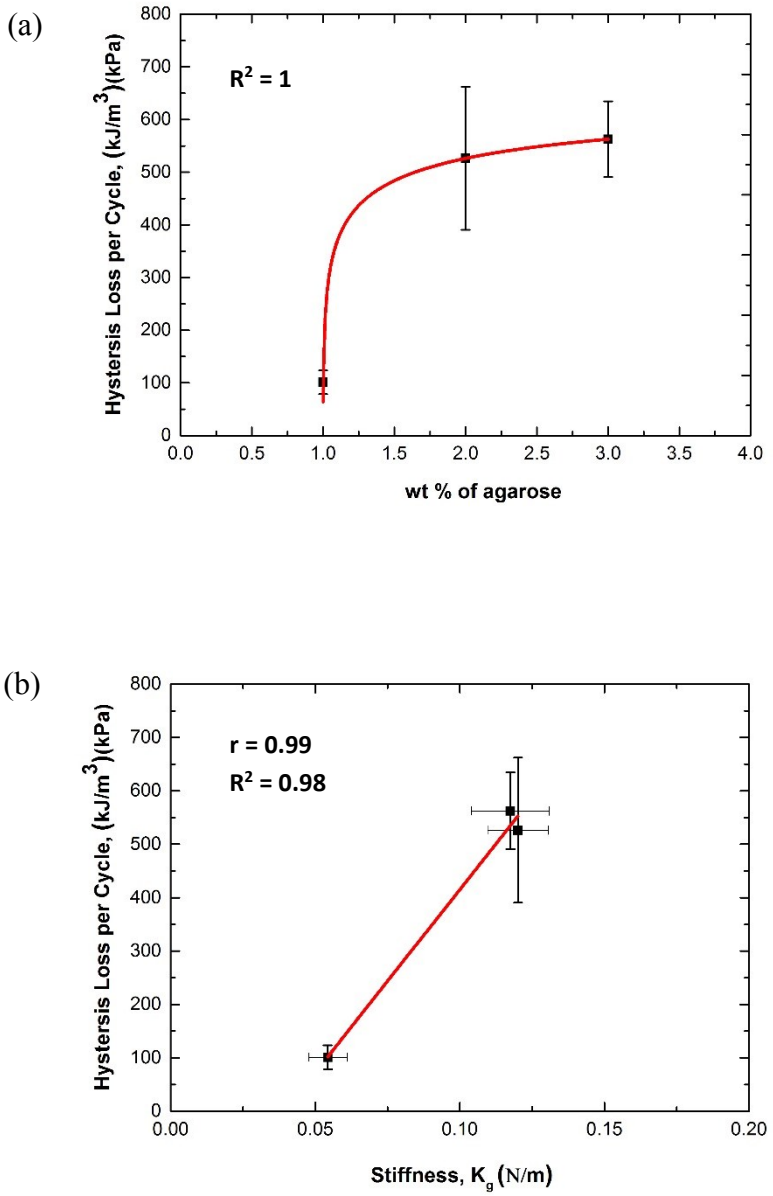

Figure 6-12: The correlation between the hysteresis loss per unit volume and the concentration of the agarose gels (a) and between the hysteresis loss per unit volume and stiffness (b).

- **Plasticity**

The gels were investigated to measure the plasticity of the material. The 150 curves were assessed to acquire the plasticity of the gels and its relation with other factors. It is clear that there was no big difference between the plasticity index (η) values of the

gels, where the average of plasticity indexes (η) of the gels were 0.223, 0.208 and 0.225 for GEL1, GEL2 and GEL3 respectively. In addition, there was no correlation observed between plasticity index (η) and the concentration of the agarose gels where the Pearson correlation coefficient, r = 0.19, and coefficient of determination (R-squared), R^2 = -0.93 and no correlation between plasticity index (η) and the stiffness, R^2= 0.21, as shown in Figure 6-13.

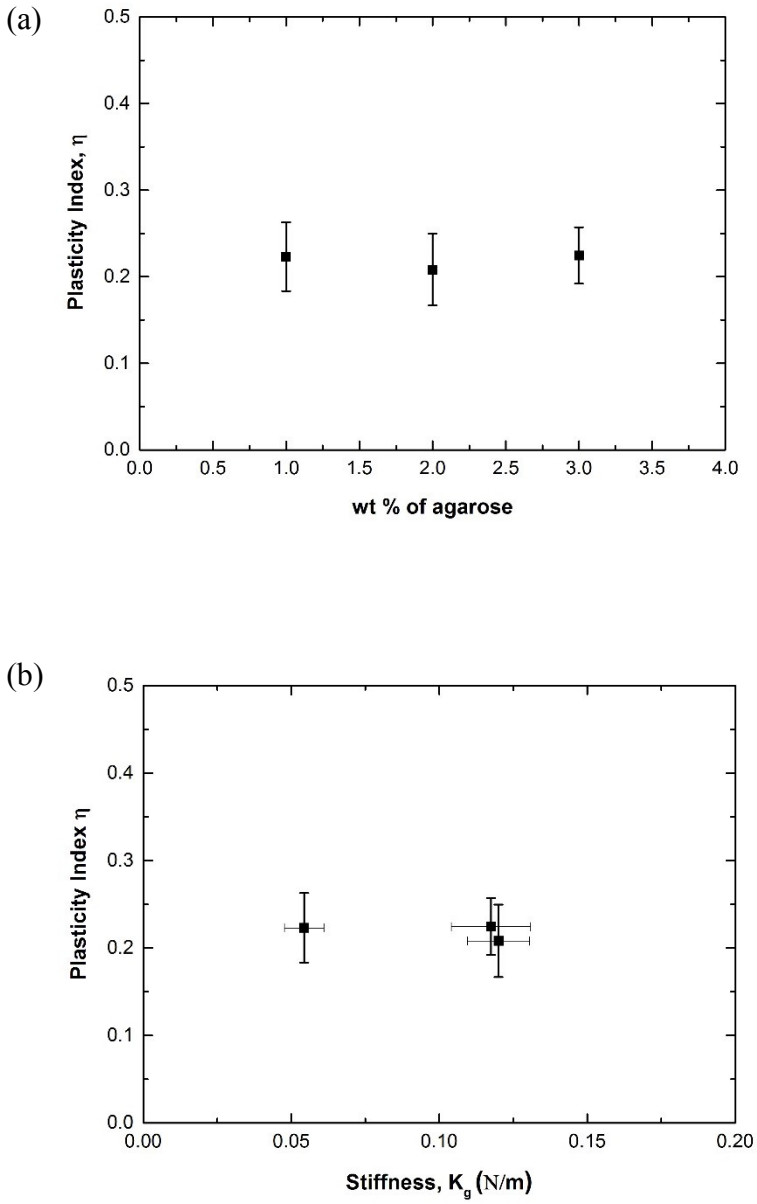

Figure 6-13: The relation between (a) plasticity index (η) and concentration of the agarose gels and (b) plasticity index (η) and stiffness.

6.4.5 Adhesion Forces

The adhesion forces were observed in the experiments. When a cantilever retracts away from the gel surface, the gel is trying to hold it and pull it down, which produce an adhesion force. However these adhesion forces are much smaller than those observed in the lipid MBs retracing curves which were studied in the previous chapters where they are lower here by 92% and 84% than those observed with tipless and tipped cantilevers respectively. After perusing 150 retracing curves for the force-indentation (F-δ) curves of the gels, the adhesion forces were found to be in the average 0.50±0.10 nN, 0.26±0.06 nN and 0.32±0.12 nN for GEL1, GEL2 and GEL3 respectively. Figure 6-14 gives an example of the load (dashed blue line) and unload (sold red line) curve for one of the strongest adhesion forces for GEL1 at test point 3, with stiffness 0.05 N/m, using a conical-tipped cantilever with spring constant 0.05 N/m, where the adhesion force (F_{adh}), as shown in the zoom-in graph is 0.95 nN (in the negative direction).

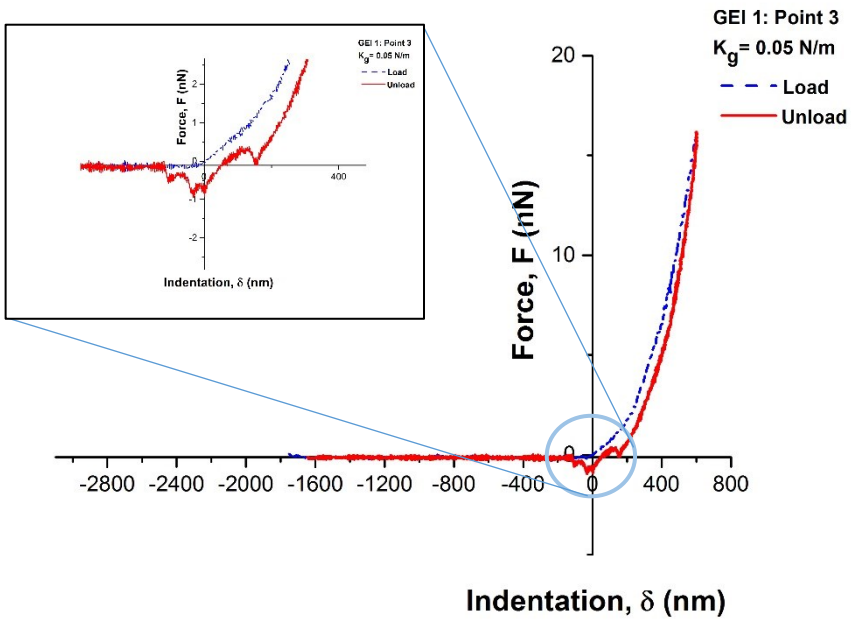

Figure 6-14: Illustrating one of the strongest adhesion forces, -0.95 nN, which appeared with GEL1 at test point 3.

To examine the relation of adhesion force with other factors, such as concentration and stiffness of the gel, the 150 curves were studied to explore these correlations where each point is the average of 50 curves. It was found that there is a link between adhesion force and the concentration, as shown in Figure 6-15-(a); there is a logarithmic relation between the adhesion force and concentration with coefficient

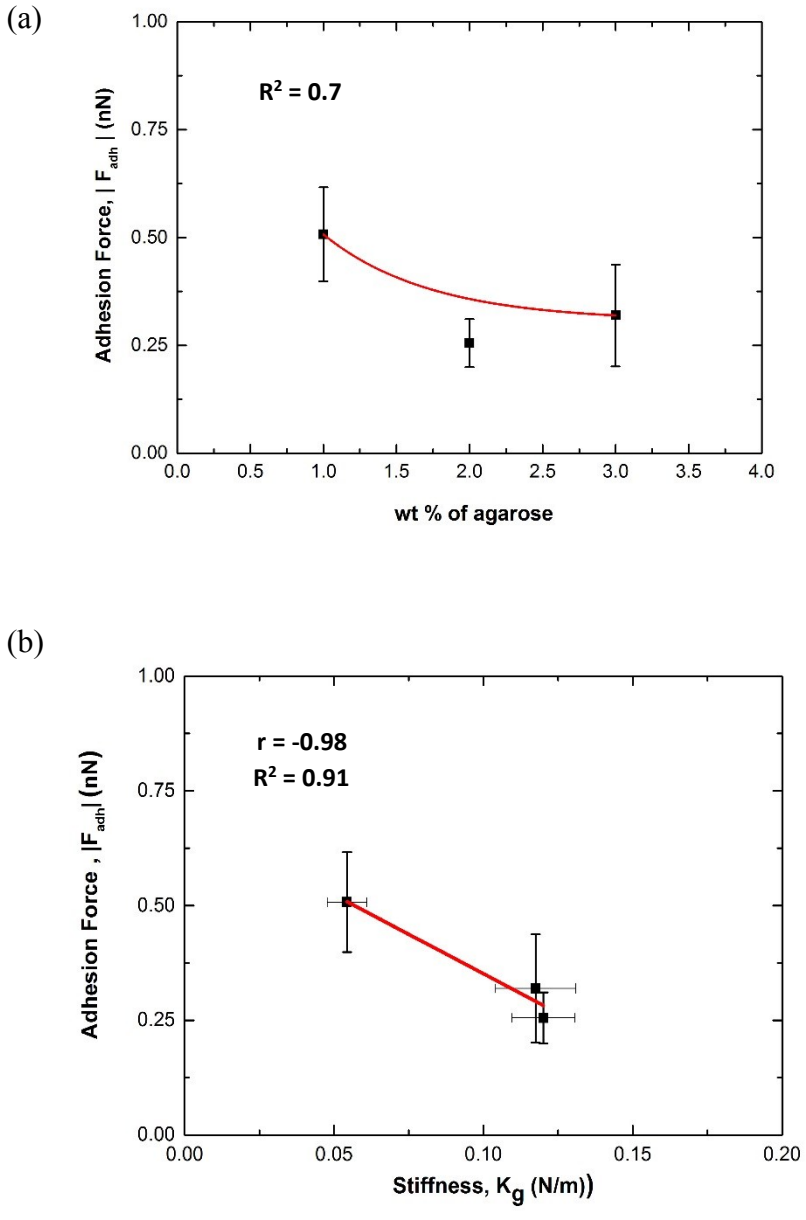

Figure 6-15: The relation between (a) the absolute value of the adhesion force and concentration of the gel and (b) the absolute value of the adhesion force and stiffness.

of determination (R-squared), $R^2 = 0.7$ while it is more linear between adhesion force and stiffness where the Pearson correlation coefficient, r = -0.98 and coefficient of determination (R-squared), $R^2 = 0.91$, as shown in Figure 6-15-(b).

6.4.6 Hardness

The indentation technique is commonly used to estimate the two most important mechanical properties, which are the elastic modulus (Young's modulus) (E), investigated in the previous sections, and the hardness (H), which will be studied in this section. [38] The data are gathered from a one-cycle loading and unloading, and subsequently the unloading data are analysed according to the used model for the deformation of the elastic half-space by a rigid axisymmetric indenter. [7, 18, 39-41] Hardness can be calculated using a known basic equation, H=F/A, where F is the maximum load at maximum indentation and A is the projected area of the elastic contact. The projected contact area, as explained in the theoretical background chapter, is related to experimentally measurable quantities such as indentation depth (h) and the indentation contact stiffness, S= dF/dh, slope of the upper portion of the unloading curve. Here one third [38] of the upper part of the unloading data was considered according to the suggestion and observation of Doerner and Nix [42] where part of the deformed material is in contact with the tip surface at the maximum load while the majority is not. Estimating the indentation contact stiffness (S) leads to determining the contact depth (h_c) then the contact radius (a), as shown in Figure 6-16, where the projected contact area is equal to πa^2, which was adopted in this study as Meyer's

(1908) definition for the projected contact area, and in many research studies subsequently [40, 43], to calculate the hardness.

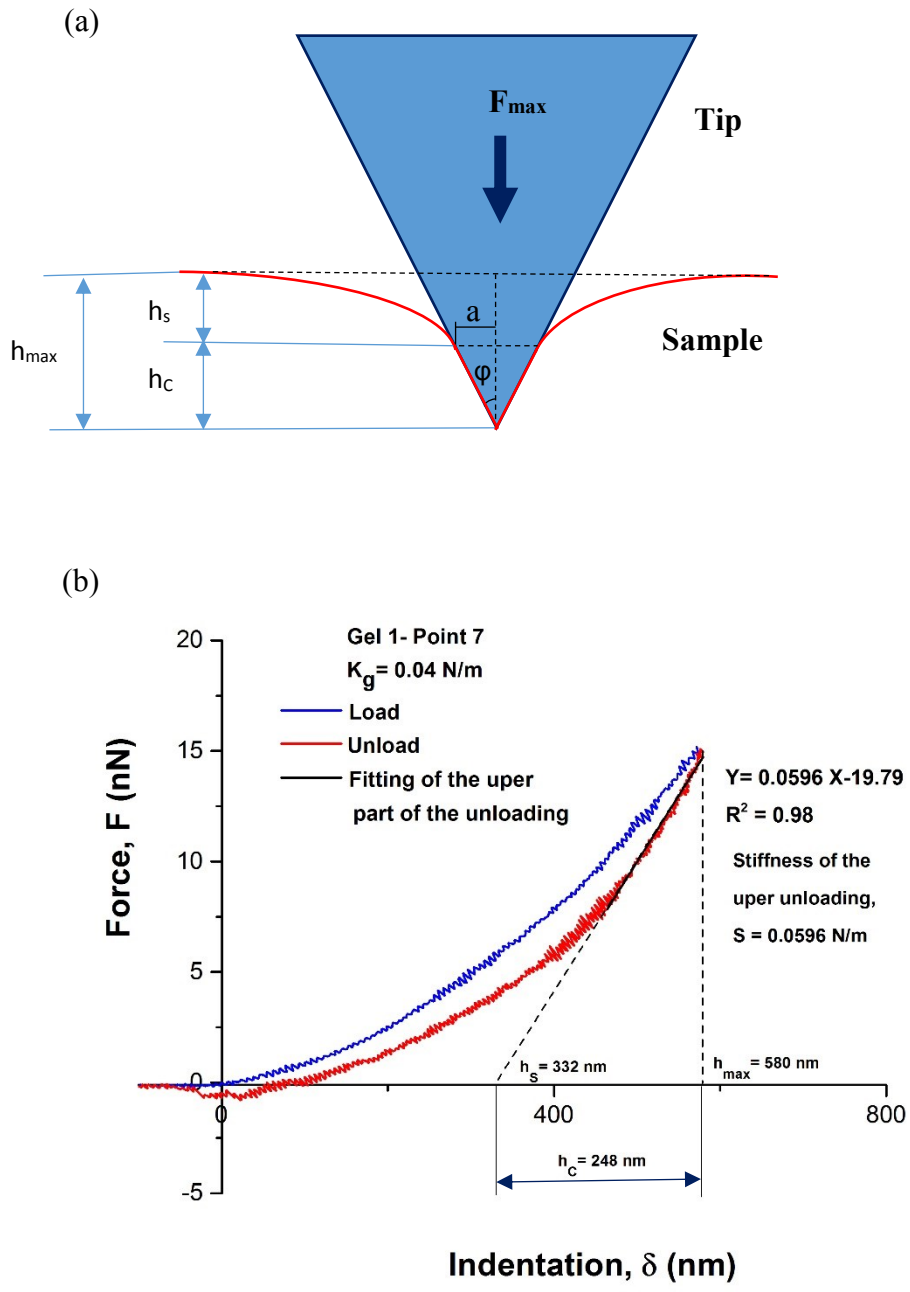

Figure 6-169: (a) Schematic drawing showing indentation form of the conical tip at maximum force, F_{max}. (b) The force-indentation (F-δ) curve for GEL1 at test point 7 with stiffness 0.04 N/m, where h_s, h_{max} and h_c are shown on the curve and the contact depth, h_c = 248 nm.

The hardness of the gels was studied with reference to 150 unloading curves and assuming that the indenter is a sharp cone, and it was found to be in the range of 2.40-5.30 MPa and average 4.00±0.76 MPa for GEL1, 11.5-20.70 MPa and mean 15.90 ±1.40 MPa for GEL2 and in the range from 10.40 MPa to 27.30 MPa with average 19.03±3.11 MPa for GEL3. To attempt to understand the correlation between hardness and the related factors such as the concentration of the agarose gel and the stiffness, Figure 6-16 shows these relationships and helps to illustrate the link between hardness and the concentration in Figure 6-17-(a). It can be observed, that the relation is a logarithmic type growth where the hardness increases with increasing, the concentration, coefficient of determination (R-squared), $R^2 = 1$, with a higher rate, 298%, between GEL1 and GEL2 than between GEL2 and GEL3, 20%. Figure 6-17-(b) represents the link between hardness and stiffness, where it is a linear increasing trend with the Pearson correlation coefficient, $r = 0.97$ and coefficient of determination (R-squared), $R^2 = 0.89$. There is a significant disagreement in the literature as to how to exactly define the hardness: is it the resistance of the material to the plastic deformation or to the total deformation when indented by a hard indenter? [44] Therefore another definition for hardness, called universal hardness, has been adopted in some research studies. Universal hardness, UH, is an idealized hardness defined as $UH=F_{max}/A$, where A is the surface area of indentation under working test force at the maximum indentation (h_{max}). This definition assumes that the indenter is in full contact with the surface to the maximum depth defined by the maximum indentation in the force-indentation (F-δ) curve, which is in contrast with the real situation as shown in Figure 6-16-(a). [19, 44] Universal hardness (UH), was on average 100 ±21 kPa, 506 ±56 kPa and 547 ±30 kPa for GEL1, GEL2 and GEL3 respectively. The correlation

between the universal hardness (UH), and concentration of the agarose gel and between the universal hardness (UH), and the stiffness are the same as those for concentrations with the hardness (H); however, the values are much smaller because the area is larger, as shown in Figure 6-18.

(a)

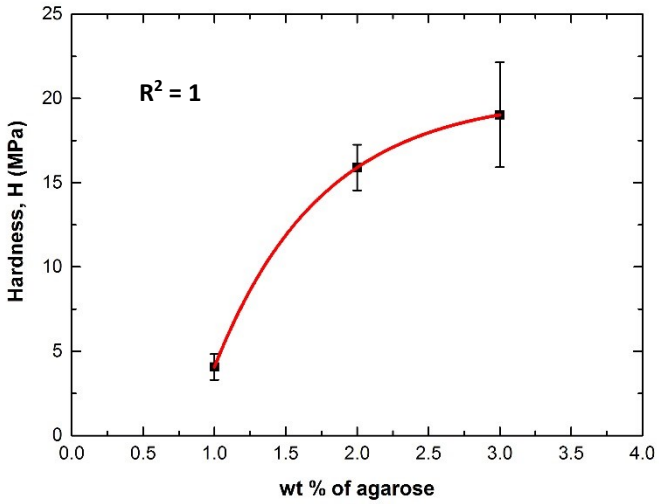

(b)

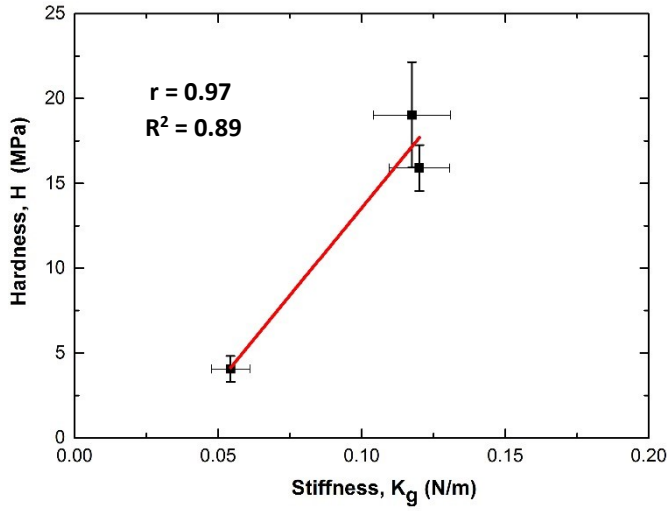

Figure 6-17: Representing the correlation between (a) the hardness, H and concentration of the agarose gel and (b) the hardness, H and the stiffness.

(a)

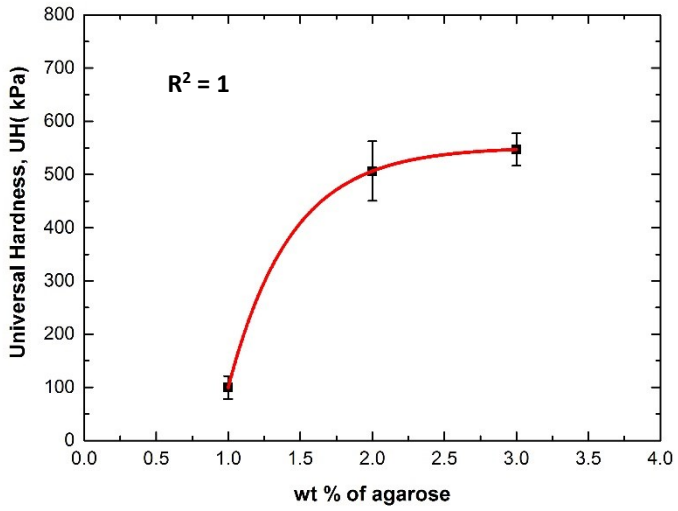

(b)

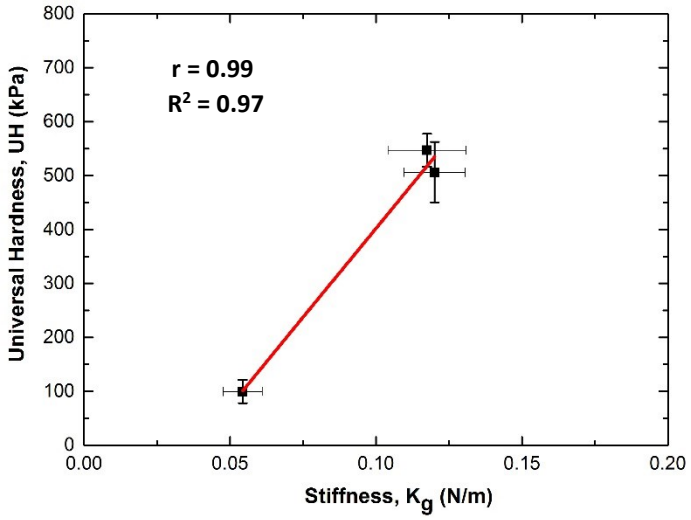

Figure 6-18: Representing the correlation between (a) the universal hardness, UH and concentration of the agarose gel and (b) the universal hardness, UH and the stiffness.

Pressure is an expression of a normal force applied on a unit surface. To estimate the pressure exerted on the gel surface by the conical tip, we need to divide the normal force by the contact area between the tip and the gel surface. After analysing all 150 curves, the pressure was calculated to be in the range of 79-158 kPa and average

110±44 kPa for GEL1 and between 345 kPa and 702 kPa with mean 480c41 kPa for GEL2 while GEL3 had ranged from 348 kPa to 823 kPa and average 574±94 kPa. Correlations of the pressure with concentration and stiffness of the gel are the same as those obs (a) llustrated in Figure

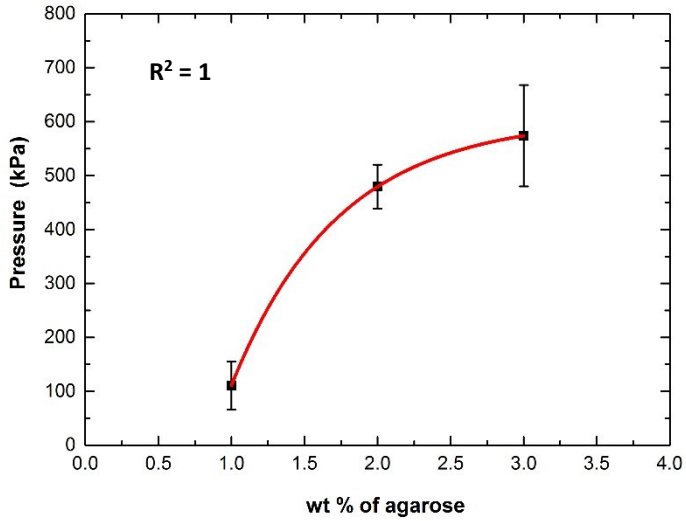

(b)

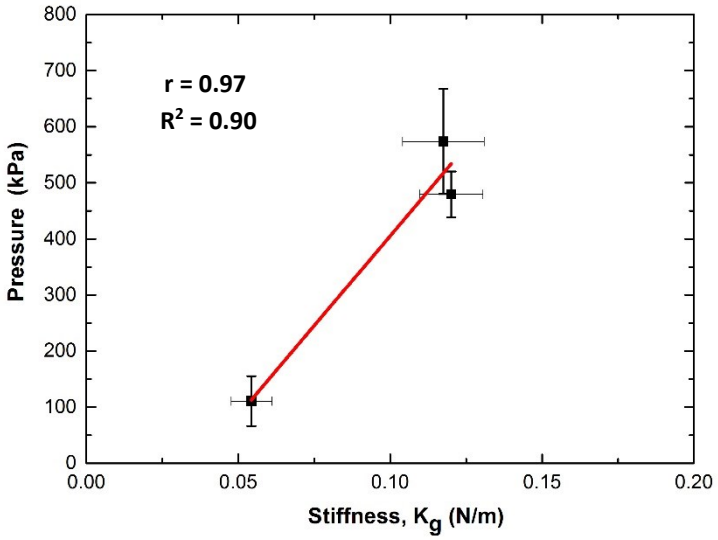

Figure 6-1910: Illustrating the relationship (a) between the pressure and concentration of the agarose gel and (b) between the pressure and the stiffness of the gel.

The strain rate, έ is linked to the displacement rate, as in these experiments, or the loading rate of the indenter over the softer surface. According to the displacement rate, the strain rate could be defined as $\acute{\varepsilon} = k(\dot{h}/h_{max})$, where $\dot{h}$ is the displacement rate here $\dot{h}$ =3000 nm/s, h_{max} is the maximum displacement, i.e. the maximum indentation depth, and k a constant usually equal to 1. After estimations, strain rate was in the range of 4.46-6.53 s^{-1} and average 5.48±0.54s^{-1} for GEL1 and in the range of 11.1-17.1 s^{-1} and mean 12.7±0.72 s^{-1} for GEL2 while it was in the range from 12.3 s^{-1} to 15.8 s^{-1} and average 14.8±0.54 s^{-1} for GEL3. The correlation with concentration and strain rate of the gel is same as those in pressure and hardness with concentration see Figure 6-20.

To see all the results and the mechanical properties which are studied in this chapter for each gel individually, the reader is referred to Appendix C.

(a)

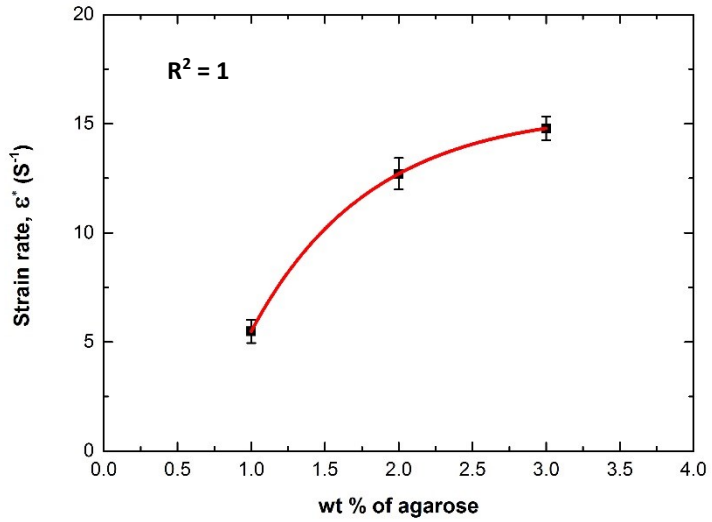

(b)

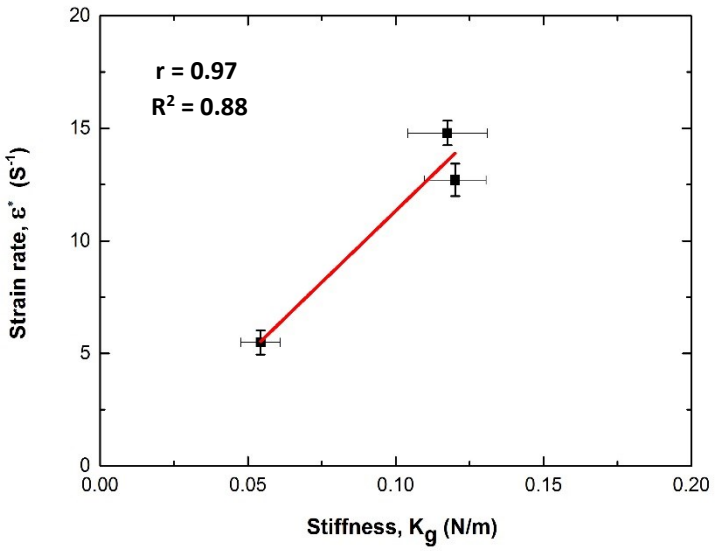

Figure 6-20: Representing the relationship between (a) the strain rate and concentration of the agarose gel and (b) the strain rate and the stiffness of the gel.

6.5 Discussion

The results in this study were deduced from a large number of experiments where three hydrogels differing in concentration were tested. Up to ten points were chosen randomly for every sample and each point was tested more than five times and five curves were considered, which means around 150 curves were implemented in total to extract the results of this study. There was a difficulty in completing the experimental work, since the hydrogels were transparent which hampered the examination of more than three samples.

Many mechanical properties were investigated in this chapter. The average stiffness of the gels was 0.054±0.007 N/m, 0.120±0.010 N/m and 0.117±0.013 N/m for GEL1, GEL2 and GEL3 respectively. Some points for the same gel represented a yielding point or rupture in the gel tissues while the others did not. This might have occurred because of weaknesses in the cross-links in the structure of the gel at those points. This is in agreement with Schuh's observation in his study [6] " Nanoindentation studies of materials". Butt et al. [31] also state that plastic deformation may take place when indenting soft samples such as polymers**.**

The averages of the modulus of elasticity, Young's modulus (E), were 0.33, 1.99 and 2.14 MPa for GEL1, GEL2 and GEL3 respectively. These values are in agreement and in the same range as the results of previous similar studies. [5, 44-48] Nayar et al. [46] found the averages of the reduced modulus, (E_r) to be 34 (E~ 25.5 kPa), 100 (E~ 75 kPa), 380 (E~ 285 kPa) and 785 (E~ 589 kPa) kPa for the agar concentrations 0.5%, 1%, 2% and 5% respectively; the value they found for the 1% agar concentration

is about one fourth of the values for 1% agarose gel in our investigation. In another study, Tripathy and Berger [47] studied the polymer PL-6 with 1% agarose gel and found the Young's modulus, (E) value of 1% agarose to be in the range of 0.9 MPa to 1.3 MPa, using three different approximation models, which are about three times higher than our results for 1% agarose gel. Tomkoria et al. [50] measured the Young's modulus, (E) of a rabbit articular cartilage, which contains collagen, which is a type of hydrogel. They found the modulus of elasticity, (E) at the collagen zone around 1.69 MPa, which is close to our results for 2% and 3% agar concentrations. in a study of rabbit cartilage, Ebenstein and Pruitt [5] found the reduced modulus (E_r) to be around 2.8 MPa (E~ 2.1 MPa) where this value is identical to the values in the present study for 2% and 3% agar concentrations. The difference in the values resulted from the effect of certain factors such as the geometry and size of the indenter used, [11, 23] loading rate (frequency), load [48] and indentation depth. [46] There was a correlation between Young's modulus and the concentration of the agarose gels, where the Young's modulus increases with increasing the concentration, which is in agreement with observations in previous studies. [18, 46]

The average hysteresis area was 542, 217, and 153 nN.nm for GEL1, GEL2 and GEL3 respectively. The values of the hysteresis area decreased with increasing the gel concentration while the hysteresis loss per unit volume increased with increasing the gel concentration, according to the volume of the deformed gel. These values are smaller than those which appeared in the MB experiments with or without tip. The averages of the hysteresis area in the MBs were 556 and 4490 nN.nm with tipped and tipless cantilever respectively. The rise in the values of the hysteresis area in MBs could be referred to compressibility of the core gas and the effect of the adhesion

forces, where these are stronger in MBs than those that appeared in gel experiments. The average adhesion forces were found to be 0.50, 0.26 and 0.32 nN for GEL1, GEL2 and GEL3 respectively. These values are smaller than those which appeared in the MB experiments, where they were 3.13 nN with tipped cantilever and 6.17 nN with tipless cantilever. This difference could be attributed to hydrophilic structure of the gels which helps them to contain a large volume of water, resulting in reducing the interaction forces (adhesion forces) between the tip and the gel surface. Drury and Mooney [21] reported that hydrogels are suitable materials to use as anti-adhesives.

Hardness, (*H*) averages were 4.00, 15.90 and 19.03 MPa, while the universal hardness (*UH*) averages were 100, 506 and 547 kPa for GEL1, GEL2 and GEL3 respectively. Jee and Lee [51] found the hardness for PVA polymer with similar Poisson ratio, (v) 0.49, to be 37.8 MPa, which is in the same order of magnitude as for 2% and 3% agarose gel concentrations. The difference in the results is attributed to the difference in the area definition used to calculate the hardness, where a major debate [44] exists as to how to define the contact area. Furthermore, Franke et al. [48] reported that the hardness might be an inappropriate mechanical property to characterize a soft biological tissue where the deformed material is not in contact with the whole of the tip which leads to differences in results between different studies; the contact region between the deformed material and the tip is estimated according to an assumption in each study; in this study is assumed to be one third of the unloading curve. There is an increasing relationship between hardness and concentration and between hardness and stiffness, which is in agreement with a similar previous study. [51]

6.6 Conclusion

In this chapter an experimental investigation has been presented of a widely used biological and biomedical material: an agar hydrogel. Hydrogels are used as tissue engineering materials. In the study, a systematic assessment was presented using a mechanical test on the agarose hydrogels to estimate their mechanical properties. The investigation was implemented by applying a nanoindentation technique using an atomic force microscope, (AFM). The indenter was a conical-tipped cantilever which helps to assess certain mechanical properties, including stiffness, Young's modulus, repeatability, hysteresis, plasticity, adhesion forces and hardness. Three different concentrations of agarose hydrogel, 1%, 2% and 3%wt, were prepared to estimate the mechanical properties. The stiffnesses of the agarose gels were calculated using the gradient of the initial linear part of the force-indentation (F-δ) curve and before any yielding point, the average values were found to be 0.054, 0.120 and 0.117 N/m for GEL1, GEL2 and GEL3 respectively. Yielding points (rupture) appeared at some points in GEL1 and GEL3, which could indicate that a plastic deformation had occurred. There was a logarithmic relation between the stiffness and concentration of the agarose gel, where the stiffness increased with increasing the concentration of the gel. The most two important properties in the nanoindentation test are the Young's modulus (E) and the hardness (H). Young's moduli, (E) were on average 0.33, 1.99 and 2.14 MPa for GEL1, GEL2 and GEL3 respectively, and the average of the hardness was 4.00, 15.90 and 19.03 MPa, while the universal hardness (UH) averages were 100, 506 and 547 kPa for GEL1, GEL2 and GEL3 respectively. A logarithmic correlation between the Young's modulus and concentration of the agarose gel was

observed, where Young's modulus increased with raising the gel concentration and the same relation was noted between the hardness and concentration of the agarose gel. The means of the hysteresis were 542, 217, and 153 nN.nm for GEL1, GEL2 and GEL3 respectively and averages of hysteresis energy loss were 101, 526 and 555 kJ/m^3 (kPa) for GEL1, GEL2 and GEL3 respectively. The plasticity indices (η) of the gels were almost constant with average 0.22 for all the gels. The adhesion forces averaged 0.50, 0.26 and 0.32 nN for GEL1, GEL2 and GEL3 respectively, where a downward trend relationship was observed between adhesion force and concentration of the gel and between adhesion force and stiffness.

6.7 References

1. Meyers, M.A., Chen, P., Lin, A.Y. and Y. Seki,, *Biological materials: structure and mechanical properties.* Progress in Materials Science, 2008. **53**(1): p. 1-206.

2. López, M.I., *The growth of Nacre in Abalone: seasonal and feeding effects on the process of mineral formation*. 2011, University of California, San Diego: University of California San Diego, CA, USA. Master thesis. p. 90

3. Bruck, H., *Implantable biomedical devices and biologically inspired materials*, in *Springer Handbook of Experimental Solid Mechanics*. 2008, Springer. p. 891-928.

4. Franke, O., Göken, M. and A.M. Hodge, *The nanoindentation of soft tissue: current and developing approaches.* JOM Journal of the Minerals, Metals and Materials Society, 2008. **60**(6): p. 49-53.

5. Ebenstein, D.M. and L.A. Pruitt, *Nanoindentation of biological materials.* Nano Today, 2006. **1**(3): p. 26-33.

6. Schuh, C.A., *Nanoindentation studies of materials.* Materials today, 2006. **9**(5): p. 32-40.

7. VanLandingham, M.R., *Review of instrumented indentation.* Journal of Research of the National Institute of Standards and Technology, 2003. **108**(4): p. 249-265.

8. Lee, F.Y., Rho, J.Y., Harten Jr, R., Parsons, J.R. and F.F. Behrens, *Micromechanical properties of epiphyseal trabecular bone and primary spongiosa around the physis: an in situ nanoindentation study.* Journal of Pediatric Orthopaedics, 1998. **18**(5): p. 582-585.

9. Zysset, P.K., Guo, X.E., Hoffler, C.E., Moore, K.E. and S.A. Goldstein , *Elastic modulus and hardness of cortical and trabecular bone lamellae measured by nanoindentation in the human femur.* Journal of biomechanics, 1999. **32**(10): p. 1005-1012.

10. Lundkvist, A., Lilleodden, E., Siekhaus, W., Kinney, J., Pruitt, L. and M. Balooch, *Viscoelastic properties of healthy human artery measured in saline*

solution by AFM-based indentation technique. in *MRS Proceedings*. 1996. Cambridge Univ Press.

11. Ebenstein, D. and L. Pruitt, *Nanoindentation of soft hydrated materials for application to vascular tissues.* Journal of Biomedical Materials Research Part A, 2004. **69**(2): p. 222-232.

12. Ebenstein, D.M., Chapman, J.M., Li, C., Saloner, D., Rapp, J. and L.A. Pruitt, *Assessing Structure-Property Relations of Diseased Tissues Using Nanoindentation and FTIR*. in *MRS Proceedings*. 2001. Cambridge Univ Press.

13. Balooch, M., Wu-Magidi, I.C., Balazs, A., Lundkvist, A.S., Marshall, S.J., Marshall, G.W., Siekhaus, W.J. and J.H. Kinney, *Viscoelastic properties of demineralized human dentin measured in water with atomic force microscope (AFM)-based indentation.* Journal of biomedical materials research, 1998. **40**(4): p. 539-544.

14. Kinney, J., Et Al., *Atomic Force Microscope Measurements Of The Hardness And Elasticity Of Peritubular And Intertubular Human Dentin.* Transactions-American Society of Mechanical Engineers Journal of Biomechanical Engineering, 1996. **118**: P. 133-135.

15. Nauman, E.A., Ebenstein, D.M., Hughes, K.F., Pruitt, L., Halloran, B.P., Bikle, D.D. and T.M. Keaveny, *Mechanical and chemical characteristics of mineral produced by basic fibroblast growth factor-treated bone marrow stromal cells in vitro.* Tissue engineering, 2002. **8**(6): p. 931-939.

16. Rho, J.Y., Zioupos, P., Currey, J.D . and G.M. Pharr, *Variations in the individual thick lamellar properties within osteons by nanoindentation.* Bone, 1999. **25**(3): p. 295-300.

17. Marshall, G., et al., *Mechanical properties of the dentinoenamel junction: AFM studies of nanohardness, elastic modulus, and fracture.* Journal of biomedical materials research, 2001. **54**(1): p. 87-95.

18. Yang, Y., Bagnaninchi, P.O., Ahearne, M., Wang, R.K. and K. Liu, *A novel optical coherence tomography-based micro-indentation technique for mechanical characterization of hydrogels.* Journal of The Royal Society Interface, 2007. **4**(17): p. 1169-1173.

19. Briscoe, B.,Fiori, L. and E. Pelillo, *Nano-indentation of polymeric surfaces.* Journal of Physics D: Applied Physics, 1998. **31**(19): p. 2395-2405.

20. Ahmed, E.M., *Hydrogel: Preparation, characterization, and applications: A review.* Journal of Advanced Research, 2015. **6**(2): p. 105-121.

21. Drury, J.L. and D.J. Mooney, *Hydrogels for tissue engineering: scaffold design variables and applications.* Biomaterials, 2003. **24**(24): p. 4337-4351.

22. Zhao, W., Jin, X., Cong, Y., Liu, Y. and J. Fu , *Degradable natural polymer hydrogels for articular cartilage tissue engineering.* Journal of Chemical Technology and Biotechnology, 2013. **88**(3): p. 327-339.

23. McVey, A.F., *Three-dimensional imaging of bacterial microcolonies*, in *Physics Department* 2015, The University of Edinburgh: Edinburgh, UK. PhD thesis. p. 158.

24. Hutter, J.L. and J. Bechhoefer, *Calibration of atomic-force microscope tips.* Review of Scientific Instruments, 1993. **64**(7): p. 1868-1873.

25. Lévy, R. and M. Maaloum, *Measuring the spring constant of atomic force microscope cantilevers: thermal fluctuations and other methods.* Nanotechnology, 2002. **13**(1): p. 33-37.

26. Ohler, B., *Cantilever spring constant calibration using laser Doppler vibrometry.* Review of Scientific Instruments, 2007. **78**(6): p. 063701-063705.

27. Hutter, J.L., *Comment on Tilt of Atomic Force Microscope Cantilevers: Effect on Spring Constant and Adhesion Measurements.* Langmuir, 2005. **21**(6): p. 2630-2632.

28. Kim, M., Choi, J., Kim, J. and Y. Park, *Accurate determination of spring constant of atomic force microscope cantilevers and comparison with other methods.* Measurement, 2010. **43**(4): p. 520-526.

29. Abou-Saleh, R.H., Peyman, S.A., Critchley, K., Evans, S.D. and N.H. Thomson, *Nanomechanics of lipid encapsulated microbubbles with functional coatings.* Langmuir : the ACS journal of surfaces and colloids, 2013. **29**(12): p. 4096-4103.

30. Buchner Santos, E., Morris, J.K., Glynos, E., Sboros, V. and V. Koutsos, *Nanomechanical properties of phospholipid microbubbles.* Langmuir : the ACS journal of surfaces and colloids, 2012. **28**(13): p. 5753-5760.

31. Butt, H.J., Cappella, B. and M. Kappl, *Force measurements with the atomic force microscope: Technique, interpretation and applications.* Surface science reports, 2005. **59**(1): p. 1-152.

32. Sneddon, I.N., *The relation between load and penetration in the axisymmetric Boussinesq problem for a punch of arbitrary profile.* International journal of engineering science, 1965. **3**(1): p. 47-57.

33. Rico, F., Roca-Cusachs, P., Gavara, N., Farré, R., Rotger, M. and D. Navajas, *Probing mechanical properties of living cells by atomic force microscopy with blunted pyramidal cantilever tips.* Physical Review E, 2005. **72**(2): p. 021914-021924.

34. Costa, K. and F. Yin, *Analysis of indentation: implications for measuring mechanical properties with atomic force microscopy.* Transactions-American Society of Mechanical Engineers Journal of Biomechanical Engineering, 1999. **121**: P. 462-471.

35. Donno, R., *Nanomechanical characterisation of cells and biocompatible substrates*, in *Medical and Human Sciences*. 2014, University of Manchester: Manchester. UK. PhD thesis. p. 258.

36. Chen, J., *Nanobiomechanics of living cells: a review.* Interface focus, 2014. **4**(2): p. 1-16.

37. Parthasaradhy, P. and S. Ranganayakulu, *Hysteresis and eddy current losses of magnetic material by Epstein frame method-novel approach.* Int. J. Eng. Sci.(IJES), 2014: p. 85-93.

38. Oliver, W.C. and G.M. Pharr, *An improved technique for determining hardness and elastic modulus using load and displacement sensing indentation experiments.* Journal of materials research, 1992. **7**(06): p. 1564-1583.

39. Hay, J.C., Bolshakov, A. and G. Pharr, *A critical examination of the fundamental relations used in the analysis of nanoindentation data.* Journal of materials Research, 1999. **14**(06): p. 2296-2305.

40. Borodich, F.M. and L.M. Keer, *Contact problems and depth-sensing nanoindentation for frictionless and frictional boundary conditions.* International Journal of Solids and Structures, 2004. **41**(9): p. 2479-2499.

41. Costa, K.D., Ho, M.M. and C.T. Hung. *Multi-scale measurement of mechanical properties of soft samples with atomic force microscopy*. in *2003 Summer Bioengineering Conference*. June 25-29, 2003. Sonesta Beach Resort in Key Biscayne, Florida. p. 285-286.

42. Doerner, M.F. and W.D. Nix, *A method for interpreting the data from depth-sensing indentation instruments.* Journal of Materials research, 1986. **1**(4): p. 601-609.

43. Tabor, D., *The hardness of metals.* 1951, Clarendon Press: Oxford.

44. Turnbull, A. and D. White, *Nanoindentation and microindentation of weathered unplasticised poly-vinyl chloride (UPVC).* Journal of materials science, 1996. **31**(16): p. 4189-4198.

45. Franke, O., Göken, M., Meyers, M.A., Durst, K. and A.M. Hodge, *Dynamic nanoindentation of articular porcine cartilage.* Materials Science and Engineering: C, 2011. **31**(4): p. 789-795.

46. Nayar, V.T., Weiland, J.D., Nelson, C.S. and A.M. Hodge, *Elastic and viscoelastic characterization of agar.* Journal of the mechanical behavior of biomedical materials, 2012. **7**: p. 60-68.

47. Tripathy, S. and E. Berger, *Measuring viscoelasticity of soft samples using atomic force microscopy.* Journal of biomechanical engineering, 2009. **131**(9): p. 094507-094512.

48. Franke, O., Durst, K., Maier, V., Göken, M., Birkholz, T., Schneider, H., Hennig, F. and K. Gelse, *Mechanical properties of hyaline and repair cartilage studied by nanoindentation.* Acta Biomaterialia, 2007. **3**(6): p. 873-881.

49. Hagiwara, T., Kumagai, H. and T. Matsunaga, *Fractal analysis of the elasticity of BSA and β-lactoglobulin gels.* Journal of Agricultural and Food Chemistry, 1997. **45**(10): p. 3807-3812.

50. Tomkoria, S., Patel, R.V. and J.J. Mao, *Heterogeneous nanomechanical properties of superficial and zonal regions of articular cartilage of the rabbit proximal radius condyle by atomic force microscopy.* Medical engineering & physics, 2004. **26**(10): p. 815-822.

51. Jee, A.Y. and M. Lee, *Comparative analysis on the nanoindentation of polymers using atomic force microscopy.* Polymer Testing, 2010. **29**(1): p. 95-99.

CHAPTER 7

GENERAL CONCLUSIONS AND FUTURE WORK

CAPTER 7: GENERAL CONCLUSIONS AND FUTURE WORK

7.1 General Conclusion

The aim of this study was to investigate and to calculate the nanomechanical properties of soft biomaterials, in particular phospholipid microbubbles (MBs) and agarose hydrogels, using the atomic force microscopy (AFM) technique with force spectroscopy mode. This is the first study that provides a comprehensive assessment of a large set of nanomechanical properties of phospholipid-shelled microbubbles and agarose hydrogels. In the present study the stiffness and Young's modulus were investigated for both microbubbles and agarose hydrogels and the hardness was studied for agarose hydrogels. In addition, several nanomechanical properties were studied for the first time to the best of my knowledge for these materials such as hysteresis, hysteresis loss, plasticity index, instability and adhesion forces. Studying these materials widely as presented in this study could be of help to other researchers and developers, improve their manufacturing for ultrasound applications or drug/gene carriers; it could be useful for the rational design and fabrication of lipid-based MBs for new therapeutic applications.

Because of their importance in medical applications as ultrasound contrast agents (UCAs) and drug/gene deliveries, SonoVue® phospholipid microbubbles (with average diameter 8.17 μm and range 2.80-16.16 μm) were studied in the experiments

reported in Chapter 4 by exerting a direct, genuinely mechanical test using an AFM at constant speed and constant force with a flat (tipless) cantilever, to investigate their nanomechanical properties. Values for several properties were determined in this chapter, including stiffness (with average 0.9 N/m) , Young's modulus (with average 12.8, 0.46, and 2.9×10^{-4} GPa for Reissner, membrane and Hertz theory, respectively), hysteresis (with average 4490 nN.nm), hysteresis loss (with average 14.1 kJ/m^3), plasticity (with mean value 0.47), adhesion forces (with mean value 6.17 nN), nonlinearity and instability. The results obtained were comparable to those reported in the literature review and similar studies in the field. The Young's modulus was calculated by applying three different models, where two (Reissner and Membrane theory) were to estimate the elasticity of the MB shell, while the third (Hertz Theory) was used to evaluate the elasticity of the whole MB. Among the three models, the best prediction was found with the stretching component of the membrane theory. A new interesting phenomenon was observed, which was an increase in the local stiffness of the MB after each instability during the linear region of the curve. The plasticity index was studied as well for first time in such systems and it was shown that in some cases a phospholipid MB can exhibit a strong plastic behaviour.

In Chapter 5, the same properties were studied for the same MBs; however, the compression tool was different: a conical tipped cantilever was used to investigate and assess the impact of the tip geometry on the nanomechanical properties of the MBs, where their average diameter was 4.58 μm and range was 3.48-5.73 μm. In this geometry the local properties of the shells were probed and the interest was to examine if the properties are different at the more local level; where the properties investigated were stiffness (with average 0.029 N/m), Young's modulus (with average 3.28×10^{-4}),

hysteresis (with average 556 nN.nm), hysteresis loss (with average 1.49 kJ/m^3), plasticity (with mean value 0.67), adhesion forces (with mean value 3.13 nN). It was concluded that there is no significant effect of the tip geometry on the elastic properties values. However, there is an effect on the adhesion forces and the hysteresis due to the tip geometry. The phenomenon of an increase in local stiffness after each unstable step was also observed, however, occurring at a higher rate. It is the first time that a direct comparison between tipless and tipped cantilevers is explored for the phospholipid MBs system.

Chapter 6 reported the investigation of the effect of the agarose hydrogels' concentration on their nanomechanical properties, where gel concentrations, 1%, 2% and 3% agarose hydrogel for GEL1, GEL2 and GEL3 respectively, were investigated and found to have an impact on the nanomechanical properties.). The nanoindentation technique was applied using AFM, where the indenter was a conical tipped cantilever, and was used to measure the nanomechanical properties of the hydrogels. In addition to the previous properties studied in Chapters 4 and 5, further properties were investigated, which included the hardness (with average 4.00, 15.90 and 19.03 MPa for GEL1, GEL2 and GEL3 respectively), the universal hardness (with average 100, 506, and 547 kPa for GEL1, GEL2 and GEL3 respectively), and the pressure (with average 110, 480, and 574 kPa for GEL1, GEL2 and GEL3 respectivelyThe instability was monitored as well, and unstable steps were observed, which indicated that there was a yielding point or ruptures occurring in the gel tissues at some points. There is a contrast to the results in the literature, where some of the reviewed studies reported higher or lower values than those found in the present study, while others were in the same range. This difference in the results could be attributed to several factors, such

as indenter geometry, applied force and the load rate, indicating that those materials need to be studied more extensively and deeply.

7.2 Future Work

This study consisted of a systematic investigation of soft biomaterials based on certain factors such as the size of the MBs' and the concentration of the gels. However, there are some other factors that could affect or play a role in the mechanical properties of those materials, since they are soft and exhibit viscoelastic behaviour. These factors are worthy of consideration and are applicable for both the MBs and the gels. These factors are presented and explained in the following paragraphs.

- **Time Dependence**

The study investigated the mechanical properties of the biomaterials with no time dependence; however, it is important to take into account the time effect, especially with those materials that have viscoelastic behaviour. It would be useful to exert the load and hold it on the material for a period of time, to observe the impact of the time duration on the material's response and to monitor the relaxation and the creep behaviour. According to the time-dependence, the material relaxes toward equilibrium. [1] The viscoelasticity and time-dependent plasticity can be investigated and controlled by several loading-unloading cycles, while the maximum load is held for a period of time. [2] Some of the properties might be affected by association with the time-dependent load, such as the elasticity modulus [2] and the hardness. [3]

- **Temperature Dependence**

The soft materials are affected by temperature fluctuation; therefore, the influence of the temperature on the mechanical properties of those materials should be investigated. Most of the force spectroscopy experiments were implemented at room temperature, which does not reflect the real expected behaviour *in vivo*. [4]

Viscoelastic materials are not only sensitive to time-dependent behaviour but also sensitive to temperature-dependent behaviour. [5] Therefore, determining the mechanical properties of the viscoelastic materials based on temperature-dependence is required, as it represents their behaviour in the real environment in which they will be used.

- **Water Absorption (for Gels)**

Hydrogels are defined as water-swollen materials, due to their hydrophilic structure. From this perspective, it is important to take into account this characteristic, the water absorption, when the hydrogels' mechanical properties are being assessed. The mechanical properties of the gels might change resulting from the water absorption and holding a large amount of liquid inside the gel structure network. Useful results could be obtained if the hydrogels are investigated after soaking them for different periods of time in water to reveal the influence of water absorption on the mechanical properties of the gels. Some of the gels' properties, such as the stiffness, are very sensitive to the trapping of water in the network.

7.3 References

1. Frieberg, B., Glynos, E. and P.F. Green, *Structural relaxations of thin polymer films.* Physical review letters, 2012. **108**(26): p. 268304-268308.

2. Fan, Z. and J.Y. Rho, *Effects of viscoelasticity and time-dependent plasticity on nanoindentation measurements of human cortical bone.* Journal of Biomedical Materials Research Part A, 2003. **67**(1): p. 208-214.

3. Flores, A., Bayer, R.K., Krawietz, K. and CF.J. Baltá Calleja, *Elastoplastic properties of starch-based materials as revealed by microindentation measurements.* Journal of Macromolecular Science, Part B, 2000. **39**(5-6): p. 749-759.

4. Grant, C.A., McKendry, J.E. and S.D. Evans, *Temperature dependent stiffness and visco-elastic behaviour of lipid coated microbubbles using atomic force microscopy.* Soft Matter, 2012. **8**(5): p. 1321-1326.

5. Tranchida, D.A., Kiflie, Z.B., Acierno, S.C. and S.B. Piccarolo, *Nanoscale mechanical characterization of polymers by atomic force microscopy (AFM) nanoindentations: viscoelastic characterization of a model material.* Measurement Science and Technology, 2009. **20**(9): p. 095702-095710.

APPENDICES

APPENDICES

Appendix A: Chapter 4 Results

The mechanical properties that are studied in Chapter 4 which are stiffness, the Young's modulus, hysteresis, hysteresis loss, plasticity index and adhesion force for each MB individually.

	(Stiffness) N/m								
	MBs	SN01	SN02	SN03	SN04	SN05	SN06	SN07	SN08	SN09
	Dim (µm)	12.79	7.89	4.68	3.2	4.33	2.72	5.01	2.8	8.19
		1.13E-01	1.86E-01	8.54E-02	1.28E-01	1.08E-01	1.24E-01	6.43E-02	3.93E-02	7.93E-02
		1.19E-01	1.85E-01	8.83E-02	1.13E-01	9.42E-02	1.23E-01	6.53E-02	3.91E-02	8.46E-02
		1.17E-01	2.05E-01	8.47E-02	1.18E-01	9.28E-02	1.20E-01	4.98E-02	4.46E-02	8.54E-02
		1.12E-01	1.52E-01	1.12E-01	1.11E-01	1.08E-01	1.55E-01	6.60E-02	6.31E-02	6.97E-02
		1.10E-01	1.99E-01	1.20E-01	1.16E-01	1.15E-01	1.21E-01	1.21E-01	5.42E-02	7.40E-02
AVRG.	1.05E-01	1.14E-01	1.85E-01	9.81E-02	1.17E-01	1.03E-01	1.29E-01	7.34E-02	4.80E-02	7.86E-02
STA.	3.91E-02	3.70E-03	2.07E-02	1.67E-02	6.71E-03	9.50E-03	1.48E-02	2.76E-02	1.04E-02	6.76E-03
	MBs	SN10	SN11	SN12	SN13	SN14	SN15	SN16	SN17	SN18
	Dim (µm)	10.28	13.46	13.02	6.55	8.28	7.63	13.87	6.17	16.16
		6.19E-02	9.07E-02	8.69E-02	1.21E-01	1.58E-01	1.50E-01	1.13E-01	1.11E-01	8.49E-02
		9.13E-02	7.56E-02	7.09E-02	1.29E-01	1.53E-01	1.50E-01	1.18E-01	1.11E-01	7.54E-02
		6.77E-02	9.11E-02	9.40E-02	8.25E-02	1.53E-01	1.68E-01	1.18E-01	1.10E-01	6.82E-02
		5.98E-02	8.27E-02	9.38E-02	1.11E-01	1.53E-01	1.63E-01	1.18E-01	1.10E-01	6.61E-02
		6.84E-02	8.86E-02	9.35E-02	1.27E-01	1.54E-01	1.60E-01	1.20E-01	1.09E-01	8.33E-02
AVRG.	1.08E-01	6.98E-02	8.57E-02	8.78E-02	1.14E-01	1.54E-01	1.58E-01	1.17E-01	1.10E-01	7.56E-02
STA.	3.20E-02	1.26E-02	6.60E-03	9.90E-03	1.91E-02	1.98E-03	7.97E-03	2.56E-03	7.29E-04	8.54E-03

	(Young's Modulus, Reissner) Gpa								
	MBs	SN01	SN02	SN03	SN04	SN05	SN06	SN07	SN08	SN09
	Dim (µm)	12.79	7.89	4.68	3.2	4.33	2.72	5.01	2.8	8.19
		2.18E+01	2.20E+01	6.00E+00	6.15E+00	6.99E+00	5.07E+00	4.83E+00	1.65E+00	9.74E+00
		2.29E+01	2.18E+01	6.20E+00	5.44E+00	6.12E+00	5.04E+00	4.91E+00	1.64E+00	1.04E+01
		2.24E+01	2.43E+01	5.95E+00	5.66E+00	6.03E+00	4.89E+00	3.75E+00	1.87E+00	1.05E+01
		2.15E+01	1.80E+01	7.86E+00	5.32E+00	6.99E+00	6.33E+00	4.96E+00	2.65E+00	8.56E+00
		2.11E+01	1.18E+01	8.43E+00	5.56E+00	7.45E+00	4.96E+00	9.12E+00	2.28E+00	9.10E+00
AVRG.	9.24E+00	2.19E+01	1.96E+01	6.89E+00	5.63E+00	6.71E+00	5.26E+00	5.51E+00	2.02E+00	9.66E+00
STA.	6.85E+00	7.10E-01	4.90E+00	1.17E+00	3.22E-01	6.17E-01	6.05E-01	2.08E+00	4.36E-01	8.30E-01
	MBs	SN10	SN11	SN12	SN13	SN14	SN15	SN16	SN17	SN18
	Dim (µm)	10.28	13.46	13.02	6.55	8.28	7.63	13.87	6.17	16.16
		9.56E+00	1.83E+01	1.70E+01	1.19E+01	1.96E+01	1.87E+01	2.30E+01	1.13E+01	2.01E+01
		1.40E+01	1.52E+01	1.39E+01	1.27E+01	1.90E+01	1.72E+01	2.42E+01	1.13E+01	1.69E+01
		1.05E+01	1.84E+01	1.84E+01	8.10E+00	1.90E+01	1.92E+01	2.43E+01	1.13E+01	1.49E+01
		9.24E+00	1.67E+01	1.83E+01	1.09E+01	1.90E+01	1.87E+01	2.46E+01	1.12E+01	1.37E+01
		1.06E+01	1.79E+01	1.83E+01	1.25E+01	1.91E+01	1.83E+01	2.50E+01	1.11E+01	1.88E+01
AVRG.	1.63E+01	1.08E+01	1.73E+01	1.72E+01	1.12E+01	1.91E+01	1.84E+01	2.42E+01	1.12E+01	1.69E+01
STA.	4.47E+00	1.89E+00	1.33E+00	1.93E+00	1.88E+00	2.46E-01	7.69E-01	7.74E-01	7.40E-02	2.65E+00

	(Young's Modulus, Hertz) GPa									
	MBs	SN01	SN02	SN03	SN04	SN05	SN06	SN07	SN08	SN09
	Dim (µm)	12.79	7.89	4.68	3.2	4.33	2.72	5.01	2.8	8.19
		2.41E-04	4.38E-04	2.92E-04	4.08E-04	3.58E-04	4.58E-04	1.74E-04	2.49E-04	2.50E-04
		2.53E-04	4.42E-04	3.01E-04	3.69E-04	3.33E-04	4.51E-04	1.89E-04	2.54E-04	2.30E-04
		2.50E-04	4.74E-04	2.91E-04	3.73E-04	3.19E-04	4.27E-04	1.46E-04	2.74E-04	2.29E-04
		2.43E-04	3.75E-04	3.89E-04	3.73E-04	3.47E-04	5.27E-04	1.89E-04	3.89E-04	1.69E-04
		2.44E-04	4.56E-04	3.68E-04	3.78E-04	3.59E-04	4.25E-04	3.33E-04	3.09E-04	1.87E-04
AVRG.	3.23E-04	2.46E-04	4.37E-04	3.28E-04	3.80E-04	3.43E-04	4.58E-04	2.06E-04	2.95E-04	2.13E-04
STA.	9.17E-05	4.97E-06	3.71E-05	4.65E-05	1.61E-05	1.71E-05	4.15E-05	7.31E-05	5.77E-05	3.37E-05
	MBs	SN10	SN11	SN12	SN13	SN14	SN15	SN16	SN17	SN18
	Dim (µm)	10.28	13.46	13.02	6.55	8.28	7.63	13.87	6.17	16.16
		1.97E-04	2.08E-04	2.05E-04	4.23E-04	3.50E-04	3.59E-04	1.63E-04	3.12E-04	1.71E-04
		2.69E-04	1.69E-04	1.61E-04	4.63E-04	3.31E-04	4.27E-04	1.66E-04	3.15E-04	1.44E-04
		2.15E-04	2.10E-04	2.30E-04	3.62E-04	3.42E-04	4.49E-04	1.66E-04	3.15E-04	1.27E-04
		1.90E-04	1.87E-04	2.26E-04	3.89E-04	3.34E-04	4.33E-04	1.68E-04	3.05E-04	1.21E-04
		2.17E-04	2.02E-04	2.27E-04	4.55E-04	3.38E-04	4.21E-04	1.70E-04	3.08E-04	1.57E-04
AVRG.	2.69E-04	2.18E-04	1.95E-04	2.10E-04	4.18E-04	3.39E-04	4.18E-04	1.67E-04	3.11E-04	1.44E-04
STA.	1.05E-04	3.10E-05	1.73E-05	2.94E-05	4.33E-05	7.56E-06	3.45E-05	2.84E-06	4.40E-06	2.08E-05

	(Young's Modulus, Elastic Membrane) GPa									
	MBs	SN01	SN02	SN03	SN04	SN05	SN06	SN07	SN08	SN09
	Dim (µm)	12.79	7.89	4.68	3.2	4.33	2.72	5.01	2.8	8.19
		1.41E+00	6.67E-01	3.99E-02	5.26E-02	9.76E-02	5.23E-02	4.64E-02	1.29E-01	4.72E-01
		1.41E+00	6.90E-01	4.24E-02	4.59E-02	8.29E-02	5.11E-02	4.99E-02	1.28E-01	4.41E-01
		1.44E+00	6.30E-01	3.90E-02	5.00E-02	7.75E-02	4.76E-02	3.12E-02	1.31E-01	4.57E-01
		1.50E+00	4.20E-01	5.34E-02	4.85E-02	9.94E-02	6.44E-02	4.78E-02	1.32E-01	2.84E-01
		1.56E+00	6.09E-01	4.00E-02	4.71E-02	1.03E-01	4.46E-02	9.62E-02	9.29E-02	3.19E-01
AVRG.	3.19E-01	1.46E+00	6.03E-01	4.30E-02	4.88E-02	9.22E-02	5.20E-02	5.43E-02	1.23E-01	3.95E-01
STA.	4.71E-01	6.56E-02	1.07E-01	6.00E-03	2.58E-03	1.13E-02	7.56E-03	2.46E-02	1.67E-02	8.64E-02
	MBs	SN10	SN11	SN12	SN13	SN14	SN15	SN16	SN17	SN18
	Dim (µm)	10.28	13.46	13.02	6.55	8.28	7.63	13.87	6.17	16.16
		2.64E-01	7.15E-01	7.06E-01	4.13E-01	6.86E-01	1.07E+00	3.18E-01	2.58E-01	9.90E-01
		6.94E-01	5.57E-01	5.44E-01	4.45E-01	7.35E-01	1.07E+00	3.34E-01	2.66E-01	6.23E-01
		3.78E-01	7.35E-01	9.00E-01	2.60E-01	8.06E-01	1.26E+00	3.41E-01	2.71E-01	4.75E-01
		3.24E-01	6.21E-01	8.32E-01	4.12E-01	7.50E-01	1.27E+00	3.69E-01	2.41E-01	3.31E-01
		3.96E-01	6.63E-01	8.49E-01	4.51E-01	7.40E-01	1.33E+00	3.74E-01	2.59E-01	6.43E-01
AVRG.	6.00E-01	4.11E-01	6.58E-01	7.66E-01	3.96E-01	7.43E-01	1.20E+00	3.47E-01	2.59E-01	6.13E-01
STA.	2.90E-01	1.66E-01	7.19E-02	1.43E-01	7.81E-02	4.29E-02	1.20E-01	2.37E-02	1.15E-02	2.46E-01

	(Hysteresis) nN.nm								
	MBs	SN01	SN02	SN03	SN04	SN05	SN06	SN07	SN08	SN09
	Dim (µm)	12.79	7.89	4.68	3.2	4.33	2.72	5.01	2.8	8.19
		6.05E+02	1.89E+03	4.55E+03	6.46E+03	4.15E+03	5.69E+03	5.38E+03	1.04E+04	2.15E+03
		5.00E+02	1.85E+03	4.34E+03	6.05E+03	4.02E+03	5.71E+03	5.61E+03	1.05E+04	2.43E+03
		4.92E+02	2.38E+03	4.33E+03	6.91E+03	4.57E+03	6.39E+03	6.03E+03	9.85E+03	2.31E+03
		3.16E+02	2.02E+03	5.34E+03	5.86E+03	4.92E+03	6.77E+03	5.70E+03	1.12E+04	2.56E+03
		4.32E+02	2.40E+03	5.12E+03	6.59E+03	4.76E+03	7.07E+03	5.26E+03	1.18E+04	3.03E+03
AVRG.	4.81E+03	4.69E+02	2.11E+03	4.74E+03	6.37E+03	4.48E+03	6.32E+03	5.59E+03	1.07E+04	2.50E+03
STA.	3.00E+03	1.06E+02	2.66E+02	4.68E+02	4.20E+02	3.87E+02	6.21E+02	2.98E+02	7.56E+02	3.33E+02
	MBs	SN10	SN11	SN12	SN13	SN14	SN15	SN16	SN17	SN18
	Dim (µm)	10.28	13.46	13.02	6.55	8.28	7.63	13.87	6.17	16.16
		3.01E+03	3.61E+03	3.25E+03	3.32E+03	3.31E+03	1.97E+03	1.37E+04	3.31E+03	3.43E+03
		3.00E+03	3.16E+03	2.78E+03	3.36E+03	2.77E+03	1.97E+03	1.24E+04	3.29E+03	3.77E+03
		3.18E+03	3.28E+03	3.35E+03	2.93E+03	2.51E+03	1.64E+03	1.22E+04	3.29E+03	3.79E+03
		3.54E+03	3.30E+03	3.23E+03	3.02E+03	2.83E+03	1.74E+03	1.26E+04	3.06E+03	4.25E+03
		2.90E+03	3.47E+03	3.61E+03	3.21E+03	2.86E+03	1.50E+03	1.28E+04	3.28E+03	4.32E+03
AVRG.	4.16E+03	3.13E+03	3.36E+03	3.25E+03	3.17E+03	2.86E+03	1.76E+03	1.27E+04	3.25E+03	3.91E+03
STA.	3.27E+03	2.51E+02	1.77E+02	2.99E+02	1.88E+02	2.89E+02	2.04E+02	5.88E+02	1.05E+02	3.72E+02

	(Hysteresis) /Volume nN.nm/(nm)^3 (kJ/m^3) (kPa)								
	MBs	SN01	SN02	SN03	SN04	SN05	SN06	SN07	SN08	SN09
	Dim (µm)	12.79	7.89	4.68	3.2	4.33	2.72	5.01	2.8	8.19
		0.235765	1.930723	13.24834	40.27181	14.13222	49.10438	13.66532	85.06306	2.046389
		0.194557	1.896091	12.64495	37.71481	13.67564	49.28686	14.26073	85.18525	2.30948
		0.191743	2.438857	12.60138	43.08723	15.56636	55.14785	15.31318	80.27263	2.194112
		0.123223	2.064631	15.55938	36.55432	16.747	58.44835	14.47716	91.2712	2.432098
		0.168081	2.457892	14.92648	41.06825	16.19068	61.02934	13.36552	96.09784	2.876439
AVRG.	25.54528	0.182674	2.157639	13.7961	39.73928	15.26238	54.60336	14.21638	87.57799	2.371703
STA.	2.264242	0.041199	0.272848	1.363766	2.622067	1.318448	5.359049	0.758379	6.157232	0.316088
	MBs	SN10	SN11	SN12	SN13	SN14	SN15	SN16	SN17	SN18
	Dim (µm)	10.28	13.46	13.02	6.55	8.28	7.63	13.87	6.17	16.16
		1.813114	1.268249	1.221826	4.940482	3.081026	2.152531	4.533816	5.544144	0.836128
		1.807427	1.110291	1.046414	4.988007	2.57845	2.152531	4.096385	5.518333	0.919343
		1.920532	1.1537	1.260165	4.349424	2.33613	1.792651	4.036638	5.517945	0.924292
		2.132212	1.16013	1.214371	4.487475	2.630316	1.906313	4.161012	5.129468	1.037317
		1.75019	1.221814	1.357083	4.772509	2.659684	1.643666	4.253143	5.500565	1.054471
AVRG.	2.68826	1.884695	1.182837	1.219972	4.707579	2.657121	1.929538	4.216199	5.442091	0.95431
STA.	0.076605	0.151439	0.062133	0.112441	0.280098	0.269093	0.223859	0.194864	0.175452	0.090848

	Plasticity Index									
	MBs	SN01	SN02	SN03	SN04	SN05	SN06	SN07	SN08	SN09
	Dim (µm)	12.79	7.89	4.68	3.2	4.33	2.72	5.01	2.8	8.19
		0.08451	0.195635	0.329958	0.617214	0.439635	0.722747	0.548841	1.082639	0.390991
		0.066929	0.194925	0.317924	0.59582	0.441401	0.729445	0.5581	0.991849	0.409819
		0.067649	0.198235	0.32313	0.652987	0.471642	0.746156	0.577143	0.989097	0.385957
		0.047337	0.172525	0.396036	0.609824	0.496566	0.770284	0.536962	0.942543	0.410915
		0.069099	0.204013	0.3567	0.617918	0.458875	0.772293	0.536282	0.954816	0.489055
AVRG.	0.488276	0.067105	0.193067	0.344749	0.618753	0.461624	0.748185	0.551465	0.992189	0.417347
STA.	0.281374	0.01321	0.012027	0.032322	0.021099	0.023566	0.02276	0.016964	0.054892	0.041593
	MBs	SN10	SN11	SN12	SN13	SN14	SN15	SN16	SN17	SN18
	Dim (µm)	10.28	13.46	13.02	6.55	8.28	7.63	13.87	6.17	16.16
		0.44271	0.422662	0.425987	0.459622	0.467936	0.424935	0.451421	0.516965	0.491899
		0.435826	0.384679	0.363618	0.448603	0.429648	0.424935	0.40601	0.50585	0.484412
		0.453937	0.386423	0.439624	0.452752	0.449026	0.3679	0.407003	0.533791	0.490854
		0.456034	0.393888	0.409936	0.459624	0.452788	0.401674	0.42075	0.494695	0.501498
		0.416919	0.408876	0.435229	0.444694	0.432186	0.40138	0.426082	0.506498	0.479958
AVRG.	0.442483	0.441085	0.399305	0.414879	0.453059	0.446317	0.404165	0.422253	0.51156	0.489724
STA.	0.038137	0.015835	0.016174	0.03083	0.006635	0.015765	0.023409	0.018467	0.014715	0.008189

	Adhesion Force (F_{adh}) nN									
	MBs	SN01	SN02	SN03	SN04	SN05	SN06	SN07	SN08	SN09
	Dim (µm)	12.79	7.89	4.68	3.2	4.33	2.72	5.01	2.8	8.19
		-9.13E-01	-3.12E+00	-4.02E+00	-5.05E+00	-5.72E+00	-1.06E+01	-1.42E+01	-1.28E+01	-8.80E+00
		-1.18E+00	-3.80E+00	-3.05E+00	-5.74E+00	-7.35E+00	-1.21E+01	-9.83E+00	-1.41E+01	-7.91E+00
		-1.14E+00	-3.49E+00	-4.21E+00	-6.03E+00	-6.34E+00	-1.34E+01	-1.46E+01	-9.09E+00	-5.69E+00
		-7.88E-01	-2.09E+00	-3.44E+00	-7.90E+00	-7.23E+00	-1.31E+01	-1.08E+01	-1.03E+01	-4.86E+00
		-9.60E-01	-2.97E+00	-4.52E+00	-6.85E+00	-6.52E+00	-1.24E+01	-1.18E+01	-1.25E+01	-7.34E+00
AVRG.	-7.13E+00	-9.97E-01	-3.09E+00	-3.85E+00	-6.31E+00	-6.63E+00	-1.23E+01	-1.23E+01	-1.17E+01	-6.92E+00
STA.	4.19E+00	1.64E-01	6.49E-01	5.92E-01	1.10E+00	6.71E-01	1.09E+00	2.10E+00	2.01E+00	1.61E+00
	MBs	SN10	SN11	SN12	SN13	SN14	SN15	SN16	SN17	SN18
	Dim (µm)	10.28	13.46	13.02	6.55	8.28	7.63	13.87	6.17	16.16
		-4.12E+00	-7.13E+00	-5.06E+00	-5.46E+00	-4.03E+00	-3.49E+00	-7.65E+00	-5.82E+00	-5.65E+00
		-4.40E+00	-7.66E+00	-5.01E+00	-5.20E+00	-3.98E+00	-3.49E+00	-7.31E+00	-5.57E+00	-5.76E+00
		-3.93E+00	-8.19E+00	-4.26E+00	-5.55E+00	-4.02E+00	-3.56E+00	-7.71E+00	-5.39E+00	-5.31E+00
		-3.91E+00	-6.96E+00	-4.26E+00	-5.11E+00	-3.38E+00	-3.34E+00	-8.19E+00	-5.82E+00	-3.80E+00
		-3.43E+00	-7.18E+00	-4.41E+00	-5.46E+00	-3.96E+00	-2.11E+00	-7.31E+00	-5.30E+00	-5.86E+00
AVRG.	-5.21E+00	-3.96E+00	-7.42E+00	-4.60E+00	-5.36E+00	-3.87E+00	-3.20E+00	-7.64E+00	-5.58E+00	-5.28E+00
STA.	1.53E+00	3.55E-01	5.02E-01	4.01E-01	1.89E-01	2.75E-01	6.12E-01	3.62E-01	2.39E-01	8.51E-01

Summary of the Results									
Samples		Stiffness N/m		Reissner GPa		Membrane GPa		Hertz GPa	
MB	Dim(µm)	AVRG.	STA.	AVRG.	STA.	AVRG.	STA.	AVRG.	STA.
SN01	12.79	0.114	0.004	2.2E+01	7.1E-01	1.46E+00	6.56E-02	2.46E-04	4.97E-06
SN02	7.89	0.185	0.021	2.0E+01	4.9E+00	6.03E-01	1.07E-01	4.37E-04	3.71E-05
SN03	4.68	0.098	0.017	6.9E+00	1.2E+00	4.30E-02	6.00E-03	3.28E-04	4.65E-05
SN04	3.20	0.117	0.007	5.6E+00	3.2E-01	4.88E-02	2.58E-03	3.80E-04	1.61E-05
SN05	4.33	0.103	0.009	6.7E+00	6.2E-01	9.22E-02	1.13E-02	3.43E-04	1.71E-05
SN06	2.72	0.129	0.015	5.3E+00	6.1E-01	5.20E-02	7.56E-03	4.58E-04	4.15E-05
SN07	5.01	0.073	0.028	5.5E+00	2.1E+00	5.43E-02	2.46E-02	2.06E-04	7.31E-05
SN08	2.80	0.048	0.010	2.0E+00	4.4E-01	1.23E-01	1.67E-02	2.95E-04	5.77E-05
SN09	8.19	0.079	0.007	9.7E+00	8.3E-01	3.95E-01	8.64E-02	2.13E-04	3.37E-05
SN10	10.28	0.070	0.013	1.1E+01	1.9E+00	4.11E-01	1.66E-01	2.18E-04	3.10E-05
SN11	13.46	0.086	0.007	1.7E+01	1.3E+00	6.58E-01	7.19E-02	1.95E-04	1.73E-05
SN12	13.02	0.088	0.010	1.7E+01	1.9E+00	7.66E-01	1.43E-01	2.10E-04	2.94E-05
SN13	6.55	0.114	0.019	1.1E+01	1.9E+00	3.96E-01	7.81E-02	4.18E-04	4.33E-05
SN14	8.28	0.154	0.002	1.9E+01	2.5E-01	7.43E-01	4.29E-02	3.39E-04	7.56E-06
SN15	7.63	0.158	0.008	1.8E+01	7.7E-01	1.20E+00	1.20E-01	4.18E-04	3.45E-05
SN16	13.87	0.117	0.003	2.4E+01	7.7E-01	3.47E-01	2.37E-02	1.67E-04	2.84E-06
SN17	6.17	0.110	0.001	1.1E+01	7.4E-02	2.59E-01	1.15E-02	3.11E-04	4.40E-06
SN18	16.16	0.076	0.009	1.7E+01	2.6E+00	6.13E-01	2.46E-01	1.44E-04	2.08E-05
AVRG.	8.17	0.11	0.01	1.28E+01	1.29E+00	4.60E-01	6.84E-02	2.96E-04	2.88E-05
STA.	4.21	0.03	0.01	6.67E+00	1.16E+00	4.06E-01	6.73E-02	9.98E-05	1.94E-05

Summary of the Results									
Samples		Hysteresis nN.nm		Hy/Vol (kPa)		Plasticity Index		Adh. F. (nN)	
MB	Dim(µm)	AVRG.	STA.	AVRG.	STA.	AVRG.	STA.	AVRG.	STA.
SN01	12.79	469.03	105.78	1.83E-01	4.12E-02	6.71E-02	1.32E-02	-9.97E-01	1.64E-01
SN02	7.89	2107.18	266.47	2.16E+00	2.73E-01	1.93E-01	1.20E-02	-3.09E+00	6.49E-01
SN03	4.68	4736.31	468.19	1.38E+01	1.36E+00	3.45E-01	3.23E-02	-3.85E+00	5.92E-01
SN04	3.20	6372.09	420.44	3.97E+01	2.62E+00	6.19E-01	2.11E-02	-6.31E+00	1.10E+00
SN05	4.33	4484.51	387.40	1.53E+01	1.32E+00	4.62E-01	2.36E-02	-6.63E+00	6.71E-01
SN06	2.72	6322.36	620.51	5.46E+01	5.36E+00	7.48E-01	2.28E-02	-1.23E+01	1.09E+00
SN07	5.01	5593.93	298.41	1.42E+01	7.58E-01	5.51E-01	1.70E-02	-1.23E+01	2.10E+00
SN08	2.80	10746.79	755.56	8.76E+01	6.16E+00	9.92E-01	5.49E-02	-1.17E+01	2.01E+00
SN09	8.19	2495.85	332.63	2.37E+00	3.16E-01	4.17E-01	4.16E-02	-6.92E+00	1.61E+00
SN10	10.28	3125.54	251.14	1.88E+00	1.51E-01	4.41E-01	1.58E-02	-3.96E+00	3.55E-01
SN11	13.46	3363.66	176.69	1.18E+00	6.21E-02	3.99E-01	1.62E-02	-7.42E+00	5.02E-01
SN12	13.02	3246.07	299.18	1.22E+00	1.12E-01	4.15E-01	3.08E-02	-4.60E+00	4.01E-01
SN13	6.55	3167.65	188.47	4.71E+00	2.80E-01	4.53E-01	6.64E-03	-5.36E+00	1.89E-01
SN14	8.28	2858.03	289.44	2.66E+00	2.69E-01	4.46E-01	1.58E-02	-3.87E+00	2.75E-01
SN15	7.63	1762.19	204.44	1.93E+00	2.24E-01	4.04E-01	2.34E-02	-3.20E+00	6.12E-01
SN16	13.87	12731.53	588.43	4.22E+00	1.95E-01	4.22E-01	1.85E-02	-7.64E+00	3.62E-01
SN17	6.17	3249.02	104.75	5.44E+00	1.75E-01	5.12E-01	1.47E-02	-5.58E+00	2.39E-01
SN18	16.16	3912.22	372.43	9.54E-01	9.08E-02	4.90E-01	8.19E-03	-5.28E+00	8.51E-01
AVRG.	8.17	4485.78	340.58	14.12	1.10	0.47	0.02	-6.17	0.77
STA.	4.21	3062.84	177.70	23.47	1.82	0.20	0.01	3.21	0.60

Appendix B: Chapter 5 Results

The mechanical properties that are studied in Chapter 5 which are stiffness, the Young's modulus, hysteresis, hysteresis loss, plasticity index and adhesion force for each MB individually.

	(Stiffness) N/m								
	MBs	SN01	SN02	SN03	SN04	SN05	SN06	SN07	SN08
	Dim (µm)	4.76	3.63	4.87	4.93	4.49	4.72	3.48	5.73
		3.27E-02	3.40E-02	2.20E-02	4.50E-02	3.30E-02	2.10E-02	2.70E-02	3.87E-02
		3.20E-02	5.20E-02	2.10E-02	4.60E-02	2.40E-02	2.40E-02	2.00E-02	4.31E-02
		2.85E-02	2.40E-02	1.50E-02	2.80E-02	4.90E-02	2.10E-02	3.90E-02	2.72E-02
		2.92E-02	2.00E-02	2.40E-02	1.10E-02	2.30E-02	2.50E-02	2.40E-02	2.55E-02
		2.73E-02	2.10E-02	1.50E-02	4.60E-02	3.20E-02	2.70E-02	2.60E-02	3.95E-02
AVRG.	2.91E-02	3.00E-02	3.02E-02	1.94E-02	3.52E-02	3.22E-02	2.36E-02	2.72E-02	3.48E-02
STA.	5.47E-03	2.30E-03	1.34E-02	4.16E-03	1.55E-02	1.04E-02	2.61E-03	7.12E-03	7.91E-03

	(Young's Modulus, Hertz) GPa								
	MBs	SN01	SN02	SN03	SN04	SN05	SN06	SN07	SN08
	Dim (µm)	4.76	3.63	4.87	4.93	4.49	4.72	3.48	5.73
		2.63E-04	1.62E-04	3.25E-04	6.51E-04	2.74E-04	6.00E-04	3.00E-04	3.27E-04
		2.58E-04	1.17E-04	3.21E-04	5.70E-04	3.64E-04	1.69E-04	5.05E-04	3.51E-04
		3.07E-04	1.59E-04	3.15E-04	5.98E-04	4.10E-04	2.59E-04	3.28E-04	2.20E-04
		2.24E-04	1.36E-04	2.95E-04	7.59E-04	1.74E-04	2.64E-04	3.38E-04	2.09E-04
		2.12E-04	1.91E-05	3.05E-04	7.85E-04	1.62E-04	3.79E-04	3.52E-04	3.42E-04
AVRG.	3.28E-04	2.53E-04	1.19E-04	3.12E-04	6.72E-04	2.77E-04	3.34E-04	3.65E-04	2.90E-04
STA.	1.58E-04	3.74E-05	5.85E-05	1.23E-05	9.57E-05	1.11E-04	1.66E-04	8.08E-05	6.94E-05

	(Hysteresis) nN.nm								
	MBs	SN01	SN02	SN03	SN04	SN05	SN06	SN07	SN08
	Dim (µm)	4.76	3.63	4.87	4.93	4.49	4.72	3.48	5.73
		3.66E+02	7.32E+02	3.33E+02	7.71E+02	6.94E+02	7.20E+02	5.31E+02	1.47E+02
		3.06E+02	6.91E+02	2.95E+02	6.04E+02	8.57E+02	7.61E+02	6.71E+02	2.21E+02
		2.84E+02	8.19E+02	3.05E+02	5.67E+02	8.94E+02	7.19E+02	6.64E+02	2.36E+02
		3.66E+02	7.05E+02	3.49E+02	6.03E+02	8.95E+02	7.80E+02	6.64E+02	1.28E+02
		3.63E+02	7.05E+02	4.11E+02	6.76E+02	8.22E+02	8.56E+02	5.92E+02	1.53E+02
AVRG.	5.56E+02	3.37E+02	7.30E+02	3.39E+02	6.44E+02	8.32E+02	7.67E+02	6.25E+02	1.77E+02
STA.	2.40E+02	3.91E+01	5.17E+01	4.57E+01	8.10E+01	8.29E+01	5.63E+01	6.15E+01	4.81E+01

	(Hysteresis) /Volume nN.nm/(nm)^3 (kJ/m^3) (kPa)								
	MBs	SN01	SN02	SN03	SN04	SN05	SN06	SN07	SN08
	Dim (µm)	4.76	3.63	4.87	4.93	4.49	4.72	3.48	5.73
		1.030173	3.547826	0.89656	2.022961	2.1978	2.060536	2.799357	0.285125
		0.860743	3.346201	0.79431	1.585519	2.71244	2.178184	3.540046	0.429173
		0.800289	3.96609	0.82161	1.488442	2.830378	2.059048	3.4989	0.457869
		1.031075	3.413098	0.938989	1.583472	2.831958	2.235018	3.503095	0.24853
		1.021153	3.415679	1.105851	1.775161	2.600538	2.450992	3.12117	0.298103
AVRG.	1.94E+00	9.49E-01	3.54E+00	9.11E-01	1.69E+00	2.63E+00	2.20E+00	3.29E+00	3.44E-01
STA.	1.17E+00	0.11004	0.250354	0.12305	0.21272	0.262342	0.161217	0.324336	0.093418

	Plasticity Index (η)								
	MBs	SN01	SN02	SN03	SN04	SN05	SN06	SN07	SN08
	Dim (µm)	4.76	3.63	4.87	4.93	4.49	4.72	3.48	5.73
		0.43593	0.841488	0.456483	0.940243	0.778443	0.759999	0.826593	0.179658
		0.411511	0.779454	0.511669	0.906292	0.764782	0.851532	0.923246	0.256276
		0.392666	0.830873	0.521966	1.003252	0.796826	0.820127	0.852886	0.248148
		0.426511	0.831876	0.485375	0.868356	0.816841	0.763902	0.825741	0.145743
		0.438688	0.806368	0.531747	1.023111	0.885591	0.831879	0.82277	0.186684
AVRG.	6.70E-01	0.421061	0.818012	0.501448	0.948251	0.808496	0.805488	0.850247	0.203302
STA.	2.61E-01	0.019098	0.025155	0.030511	0.064879	0.047338	0.041321	0.042576	0.047344

	Adhesion Force (F_{adh}) nN								
	MBs	SN01	SN02	SN03	SN04	SN05	SN06	SN07	SN08
	Dim (µm)	4.76	3.63	4.87	4.93	4.49	4.72	3.48	5.73
		-8.98E-01	-5.22E+00	-1.67E+00	-5.19E+00	-4.11E+00	-4.84E+00	-2.76E+00	-9.05E-01
		-9.90E-01	-4.66E+00	-1.32E+00	-4.46E+00	-3.82E+00	-5.14E+00	-2.54E+00	-6.87E-01
		-1.04E+00	-5.30E+00	-1.04E+00	-4.07E+00	-4.78E+00	-4.95E+00	-2.57E+00	-7.44E-01
		-1.37E+00	-5.83E+00	-1.47E+00	-4.59E+00	-4.21E+00	-5.46E+00	-2.57E+00	-6.30E-01
		-1.16E+00	-4.95E+00	-2.11E+00	-4.64E+00	-3.86E+00	-5.48E+00	-2.59E+00	-6.06E-01
AVRG.	-3.13E+00	-1.09E+00	-5.19E+00	-1.52E+00	-4.59E+00	-4.15E+00	-5.17E+00	-2.60E+00	-7.15E-01
STA.	1.87E+00	1.84E-01	4.34E-01	3.99E-01	4.01E-01	3.86E-01	2.90E-01	8.65E-02	1.19E-01

Summary of the Results							
Samples		Stiffness N/m		Hertz GPa		Hysteresis nN.nm	
MB	Dim(µm)	AVRG.	STA.	AVRG.	STA.	AVRG.	STA.
SN01	4.76	0.0300	2.30E-03	2.53E-04	3.74E-05	336.93	39.08
SN02	3.63	0.0302	1.34E-02	1.19E-04	5.85E-05	730.24	51.68
SN03	4.87	0.0194	4.16E-03	3.12E-04	1.23E-05	338.86	45.75
SN04	4.93	0.0352	1.55E-02	6.72E-04	9.57E-05	644.32	81.05
SN05	4.49	0.0322	1.04E-02	2.77E-04	1.11E-04	832.46	82.89
SN06	4.72	0.0236	2.61E-03	3.34E-04	1.66E-04	767.12	56.30
SN07	3.48	0.0272	7.12E-03	3.65E-04	8.08E-05	624.54	61.52
SN08	5.73	0.0348	7.91E-03	2.90E-04	6.94E-05	176.98	48.10
AVRG.	4.58	0.03	0.01	3.28E-04	7.89E-05	556.43	58.29
STA.	0.73	0.01	0.00	1.58E-04	4.72E-05	239.84	16.09

Summary of the Results							
Samples		Hy/Vol (kPa)		Plasticity Index(η)		Adh. F. (nN)	
MB	Dim(µm)	AVRG.	STA.	AVRG.	STA.	AVRG.	STA.
SN01	4.76	0.95	0.11	0.42	0.02	-1.09	0.18
SN02	3.63	3.54	0.25	0.82	0.03	-5.19	0.43
SN03	4.87	0.91	0.12	0.50	0.03	-1.52	0.40
SN04	4.93	1.69	0.21	0.95	0.06	-4.59	0.40
SN05	4.49	2.63	0.26	0.81	0.05	-4.15	0.39
SN06	4.72	2.20	0.16	0.81	0.04	-5.17	0.29
SN07	3.48	3.29	0.32	0.85	0.04	-2.60	0.09
SN08	5.73	0.34	0.09	0.20	0.05	-0.71	0.12
AVRG.	4.58	1.94	0.19	0.67	0.04	-3.13	0.29
STA.	0.73	1.17	0.08	0.26	0.01	1.87	0.14

Appendix C: Chapter 6 Results

The mechanical properties that are studied in Chapter 6 which are stiffness, the Young's modulus, hysteresis, hysteresis loss, plasticity index, adhesion force, hardness, universal hardness, pressure and strain rate for each gel individually.

	GEL 1% (Stiffness) N/m										
	Points	1	2	3	4	5	6	7	8	9	10
		6.69E-02	5.91E-02	4.92E-02	5.48E-02	5.70E-02	Unsaved	4.33E-02	5.32E-02	5.50E-02	6.47E-02
		5.55E-02	5.64E-02	5.20E-02	6.12E-02	4.67E-02	Unsaved	4.00E-02	5.32E-02	5.33E-02	6.46E-02
		6.41E-02	6.99E-02	5.40E-02	5.86E-02	4.99E-02	Unsaved	4.38E-02	6.30E-02	4.55E-02	6.72E-02
		4.90E-02	6.90E-02	4.81E-02	5.98E-02	4.46E-02	Unsaved	3.90E-02	4.39E-02	5.49E-02	6.19E-02
		5.80E-02	6.24E-02	5.04E-02	6.15E-02	4.96E-02	Unsaved	4.90E-02	4.56E-02	4.82E-02	4.91E-02
AVRG.	5.44E-02	5.87E-02	6.33E-02	5.07E-02	5.92E-02	4.95E-02		4.30E-02	5.18E-02	5.14E-02	6.15E-02
STA.	6.65E-03	7.10E-03	5.93E-03	2.32E-03	2.69E-03	4.72E-03		3.91E-03	7.57E-03	4.33E-03	7.17E-03

	GEL 2% (Stiffness) N/m										
	Points	1	2	3	4	5	6	7	8	9	10
		1.04E-01	1.33E-01	1.29E-01	1.32E-01	1.32E-01	8.97E-02	1.22E-01	1.08E-01	1.30E-01	1.22E-01
		1.09E-01	1.23E-01	1.07E-01	9.40E-02	1.16E-01	9.95E-02	1.35E-01	1.14E-01	1.31E-01	6.87E-02
		1.14E-01	1.44E-01	9.88E-02	1.33E-01	1.21E-01	1.09E-01	1.45E-01	1.23E-01	1.21E-01	1.25E-01
		1.20E-01	1.38E-01	1.35E-01	1.16E-01	1.29E-01	1.07E-01	1.41E-01	9.44E-02	1.03E-01	1.38E-01
		1.12E-01	1.15E-01	1.04E-01	1.20E-01	1.12E-01	1.14E-01	1.15E-01	1.34E-01	2.04E-01	1.19E-01
AVRG.	1.20E-01	1.12E-01	1.31E-01	1.15E-01	1.19E-01	1.22E-01	1.04E-01	1.31E-01	1.15E-01	1.38E-01	1.15E-01
STA.	1.05E-02	6.07E-03	1.16E-02	1.63E-02	1.57E-02	8.41E-03	9.33E-03	1.27E-02	1.50E-02	3.87E-02	2.66E-02

	GEL 3% (Stiffness) N/m										
	Points	1	2	3	4	5	6	7	8	9	10
		1.15E-01	1.22E-01	9.81E-02	1.06E-01	1.43E-01	9.96E-02	1.12E-01	1.04E-01	1.09E-01	1.15E-01
		1.12E-01	1.46E-01	9.60E-02	1.20E-01	1.13E-01	1.20E-01	1.33E-01	1.02E-01	1.16E-01	1.13E-01
		1.23E-01	1.01E-01	1.11E-01	1.36E-01	1.21E-01	1.01E-01	1.19E-01	1.70E-01	1.01E-01	1.05E-01
		1.07E-01	1.38E-01	9.96E-02	8.10E-02	1.72E-01	1.27E-01	1.10E-01	1.79E-01	1.09E-01	9.32E-02
		1.15E-01	1.04E-01	9.98E-02	1.07E-01	1.29E-01	1.40E-01	8.84E-02	1.66E-01	1.24E-01	1.00E-01
AVRG.	1.17E-01	1.14E-01	1.22E-01	1.01E-01	1.10E-01	1.36E-01	1.17E-01	1.12E-01	1.44E-01	1.12E-01	1.05E-01
STA.	1.34E-02	5.71E-03	2.00E-02	6.03E-03	2.03E-02	2.34E-02	1.70E-02	1.62E-02	3.80E-02	8.70E-03	9.03E-03

	GEL 1% (Young's Modulus, Hertz, Sneddon) Gpa										
	Points	1	2	3	4	5	6	7	8	9	10
		3.39E-04	3.26E-04	2.59E-04	1.73E-04	3.22E-04	Unsaved	3.46E-04	3.87E-04	3.68E-04	4.94E-04
		2.73E-04	4.08E-04	2.58E-04	2.04E-04	2.91E-04	Unsaved	3.46E-04	3.97E-04	3.73E-04	4.65E-04
		3.57E-04	3.24E-04	2.48E-04	1.86E-04	3.24E-04	Unsaved	2.82E-04	4.08E-04	3.18E-04	4.98E-04
		2.51E-04	2.98E-04	2.57E-04	1.76E-04	3.88E-04	Unsaved	2.87E-04	4.31E-04	3.66E-04	4.96E-04
		3.13E-04	3.50E-04	2.60E-04	2.28E-04	4.08E-04	Unsaved	3.43E-04	3.72E-04	3.20E-04	3.98E-04
AVRG.	3.31E-04	3.07E-04	3.41E-04	2.56E-04	1.93E-04	3.46E-04		3.21E-04	3.99E-04	3.49E-04	4.70E-04
STA.	7.89E-05	4.41E-05	4.17E-05	4.80E-06	2.26E-05	4.92E-05		3.33E-05	2.25E-05	2.77E-05	4.23E-05

	GEL 2% (Young's Modulus, Hertz, Sneddon) Gpa										
	Points	1	2	3	4	5	6	7	8	9	10
		1.46E-03	2.22E-03	3.32E-03	2.04E-03	1.51E-03	2.24E-03	1.73E-03	1.58E-03	1.58E-03	1.48E-03
		1.21E-03	1.77E-03	2.65E-03	1.61E-03	1.43E-03	2.79E-03	1.92E-03	1.41E-03	1.49E-03	8.29E-04
		1.69E-03	2.76E-03	2.28E-03	2.11E-03	1.52E-03	2.48E-03	2.12E-03	1.87E-03	1.47E-03	1.66E-03
		1.58E-03	2.21E-03	4.18E-03	2.20E-03	1.48E-03	2.57E-03	2.35E-03	1.48E-03	1.39E-03	1.67E-03
		1.73E-03	2.41E-03	3.05E-03	2.24E-03	1.67E-03	2.47E-03	1.80E-03	1.98E-03	3.24E-03	1.65E-03
AVRG.	1.99E-03	1.53E-03	2.27E-03	3.10E-03	2.04E-03	1.52E-03	2.51E-03	1.98E-03	1.66E-03	1.84E-03	1.46E-03
STA.	5.19E-04	2.10E-04	3.58E-04	7.21E-04	2.55E-04	9.04E-05	1.95E-04	2.56E-04	2.50E-04	7.87E-04	3.60E-04

	GEL 3% (Young's Modulus, Hertz, Sneddon) Gpa										
	Points	1	2	3	4	5	6	7	8	9	10
		1.66E-03	2.04E-03	1.73E-03	2.53E-03	1.90E-03	2.09E-03	1.98E-03	1.66E-03	1.93E-03	2.69E-03
		1.65E-03	2.53E-03	1.85E-03	2.47E-03	1.72E-03	2.28E-03	2.36E-03	1.61E-03	2.54E-03	2.80E-03
		1.71E-03	2.47E-03	2.00E-03	2.53E-03	1.79E-03	2.35E-03	2.12E-03	2.59E-03	1.97E-03	2.36E-03
		1.62E-03	3.25E-03	1.59E-03	1.90E-03	2.55E-03	2.32E-03	2.04E-03	2.63E-03	2.29E-03	1.67E-03
		1.75E-03	2.08E-03	1.47E-03	2.40E-03	1.66E-03	2.83E-03	2.09E-03	2.55E-03	2.41E-03	2.16E-03
AVRG.	2.14E-03	1.68E-03	2.47E-03	1.73E-03	2.37E-03	1.92E-03	2.37E-03	2.12E-03	2.21E-03	2.23E-03	2.34E-03
STA.	2.78E-04	4.89E-05	4.87E-04	2.12E-04	2.68E-04	3.60E-04	2.75E-04	1.46E-04	5.24E-04	2.68E-04	4.51E-04

	GEL 1% (Hysteresis) nN.nm										
	Points	1	2	3	4	5	6	7	8	9	10
		4.20E+02	4.57E+02	1.62E+02	6.57E+02	3.39E+02	Unsaved	6.65E+02	4.80E+02	4.52E+02	4.71E+02
		3.63E+02	6.83E+02	7.78E+02	3.75E+02	4.40E+02	Unsaved	5.88E+02	3.71E+02	6.74E+02	5.19E+02
		6.28E+02	5.80E+02	5.37E+02	8.23E+02	5.95E+02	Unsaved	7.17E+02	5.09E+02	7.06E+02	4.16E+02
		7.58E+02	5.00E+02	5.53E+02	5.86E+02	5.69E+02	Unsaved	8.76E+02	4.99E+02	9.14E+02	6.00E+01
		4.94E+02	5.46E+02	5.28E+02	5.10E+02	7.28E+02	Unsaved	6.63E+02	4.15E+02	5.34E+02	2.65E+02
AVRG.	5.42E+02	5.33E+02	5.53E+02	5.12E+02	5.90E+02	5.34E+02		7.02E+02	4.55E+02	6.56E+02	3.46E+02
STA.	1.05E+02	1.61E+02	8.61E+01	2.21E+02	1.67E+02	1.49E+02		1.08E+02	5.95E+01	1.77E+02	1.86E+02

	GEL 2% (Hysteresis) nN.nm										
	Points	1	2	3	4	5	6	7	8	9	10
		2.79E+02	2.48E+02	2.53E+02	2.38E+02	3.00E+02	1.01E+02	7.72E+01	1.86E+02	1.23E+02	1.33E+02
		2.85E+02	1.59E+02	2.41E+02	2.10E+02	3.68E+02	2.27E+02	3.07E+01	1.62E+02	1.41E+02	2.71E+02
		6.75E+02	3.20E+02	2.18E+02	2.82E+02	2.99E+02	3.03E+02	1.28E+02	1.39E+02	2.59E+02	2.42E+02
		2.46E+02	2.77E+02	3.65E+02	2.36E+02	3.08E+02	2.62E+02	2.31E+02	2.54E+02	4.31E+02	2.06E+02
		3.38E+01	2.87E+02	1.37E+02	2.95E+02	1.55E+02	1.24E+02	7.51E+01	2.50E+02	1.01E+02	1.58E+02
AVRG.	2.27E+02	3.04E+02	2.58E+02	2.43E+02	2.52E+02	2.86E+02	2.03E+02	1.09E+02	1.98E+02	2.11E+02	2.02E+02
STA.	5.53E+01	2.32E+02	6.13E+01	8.20E+01	3.55E+01	7.86E+01	8.75E+01	7.69E+01	5.20E+01	1.38E+02	5.73E+01

	GEL 3% (Hysteresis) nN.nm										
	Points	1	2	3	4	5	6	7	8	9	10
		2.08E+02	7.61E+01	2.22E+02	1.06E+02	1.47E+02	1.54E+02	2.47E+02	1.97E+02	1.54E+02	1.37E+02
		1.64E+02	8.27E+01	1.42E+02	2.19E+02	1.26E+02	1.80E+02	6.14E+01	1.80E+01	1.21E+02	1.79E+02
		1.50E+02	6.02E+01	1.65E+02	1.31E+02	1.24E+02	9.58E+01	2.25E+02	1.81E+02	1.41E+02	1.48E+02
		6.75E+01	1.81E+02	2.67E+02	1.64E+02	1.94E+02	1.77E+02	1.45E+02	1.98E+02	7.51E+01	5.47E+01
		1.43E+02	2.26E+02	1.76E+02	1.95E+02	1.95E+02	2.69E+02	8.33E+01	9.48E+01	1.68E+02	2.18E+02
AVRG.	1.53E+02	1.46E+02	1.25E+02	1.94E+02	1.63E+02	1.57E+02	1.75E+02	1.52E+02	1.38E+02	1.32E+02	1.47E+02
STA.	2.07E+01	5.07E+01	7.36E+01	4.99E+01	4.58E+01	3.53E+01	6.23E+01	8.27E+01	7.94E+01	3.61E+01	6.04E+01

	GEL 1% (Hysteresis)/Volume nN.nm/(nm)^3 (GPa)									
	Points	1	2	3	4	5	6	7	8	9	10
		6.87E-05	1.15E-04	2.27E-05	8.77E-05	5.38E-05	Unsaved	1.22E-04	1.11E-04	8.19E-05	1.39E-04
		5.69E-05	1.94E-04	1.02E-04	5.17E-05	8.04E-05	Unsaved	1.11E-04	9.49E-05	1.30E-04	1.43E-04
		1.16E-04	1.24E-04	6.55E-05	8.28E-05	9.97E-05	Unsaved	1.06E-04	1.11E-04	1.38E-04	1.16E-04
		1.12E-04	1.02E-04	7.81E-05	6.04E-05	1.14E-04	Unsaved	1.38E-04	1.58E-04	1.58E-04	1.73E-05
		7.62E-05	1.27E-04	7.31E-05	7.05E-05	1.50E-04	Unsaved	9.95E-05	1.14E-04	9.28E-05	8.26E-05
AVRG.	1.01E-04	8.60E-05	1.32E-04	6.82E-05	7.06E-05	9.95E-05		1.15E-04	1.18E-04	1.20E-04	9.95E-05
STA.	2.25E-05	2.66E-05	3.59E-05	2.88E-05	1.50E-05	3.62E-05		1.51E-05	2.36E-05	3.18E-05	5.19E-05

	GEL 2% (Hysteresis) /Volume nN.nm/(nm)^3 (GPa)									
	Points	1	2	3	4	5	6	7	8	9	10
		5.45E-04	6.44E-04	6.52E-04	5.66E-04	5.80E-04	3.29E-04	1.80E-04	4.14E-04	2.69E-04	2.07E-04
		5.03E-04	3.99E-04	6.69E-04	4.35E-04	6.33E-04	7.84E-04	7.37E-05	2.84E-04	2.57E-04	5.92E-04
		1.50E-03	8.36E-04	4.96E-04	6.43E-04	5.24E-04	8.18E-04	3.13E-04	3.49E-04	4.59E-04	6.13E-04
		4.96E-04	5.89E-04	1.07E-03	5.84E-04	5.14E-04	7.56E-04	6.68E-04	4.93E-04	8.14E-04	4.72E-04
		6.75E-05	7.70E-04	7.75E-04	6.47E-04	4.00E-04	3.20E-04	1.81E-04	4.87E-04	2.75E-04	3.68E-04
AVRG.	5.26E-04	6.23E-04	6.48E-04	7.31E-04	5.75E-04	5.30E-04	6.01E-04	2.83E-04	4.05E-04	4.15E-04	4.51E-04
STA.	1.36E-04	5.29E-04	1.70E-04	2.12E-04	8.62E-05	8.70E-05	2.54E-04	2.31E-04	8.99E-05	2.38E-04	1.68E-04

	GEL 3% (Hysteresis) /Volume nN.nm/(nm)^3 (GPa)										
	Points	1	2	3	4	5	6	7	8	9	10
		6.72E-04	3.15E-04	7.30E-04	4.78E-04	4.58E-04	6.02E-04	8.70E-04	7.85E-04	6.13E-04	5.99E-04
		5.41E-04	1.73E-04	5.56E-04	8.99E-04	4.63E-04	5.83E-04	2.16E-04	7.11E-05	5.53E-04	8.12E-04
		4.53E-04	2.70E-04	5.54E-04	5.29E-04	3.85E-04	3.86E-04	Hyst. Loss=	7.40E-04	4.53E-04	6.41E-04
		2.02E-04	5.77E-04	7.71E-04	6.18E-04	8.60E-04	4.84E-04	6.41E-04	7.99E-04	3.05E-04	1.90E-04
		4.40E-04	8.18E-04	4.35E-04	7.36E-04	7.25E-04	8.31E-04	4.27E-04	3.91E-04	6.88E-04	8.66E-04
AVRG.	5.55E-04	4.62E-04	4.31E-04	6.09E-04	6.52E-04	5.78E-04	5.77E-04	5.39E-04	5.57E-04	5.22E-04	6.22E-04
STA.	6.94E-05	1.72E-04	2.63E-04	1.39E-04	1.69E-04	2.04E-04	1.66E-04	2.81E-04	3.19E-04	1.49E-04	2.66E-04

	GEL 1% Plasticity Index (η)										
	Points	1	2	3	4	5	6	7	8	9	10
		1.64E-01	2.41E-01	7.20E-02	3.17E-01	1.51E-01	Unsaved	2.65E-01	1.96E-01	1.52E-01	2.22E-01
		1.45E-01	3.17E-01	2.82E-01	1.84E-01	2.23E-01	Unsaved	2.62E-01	1.57E-01	2.41E-01	2.17E-01
		2.40E-01	2.64E-01	1.88E-01	3.23E-01	2.65E-01	Unsaved	2.74E-01	1.90E-01	2.44E-01	1.67E-01
		2.76E-01	2.24E-01	2.29E-01	2.40E-01	2.54E-01	Unsaved	3.34E-01	2.49E-01	2.97E-01	2.87E-02
		1.85E-01	2.59E-01	2.06E-01	2.34E-01	3.32E-01	Unsaved	2.29E-01	2.02E-01	1.75E-01	1.22E-01
AVRG.	2.23E-01	2.02E-01	2.61E-01	1.95E-01	2.60E-01	2.45E-01		2.73E-01	1.99E-01	2.22E-01	1.51E-01
STA.	3.98E-02	5.47E-02	3.47E-02	7.75E-02	5.95E-02	6.62E-02		3.83E-02	3.28E-02	5.81E-02	7.97E-02

	GEL 2% Plasticity Index (η)										
	Points	1	2	3	4	5	6	7	8	9	10
		2.63E-01	2.21E-01	2.48E-01	2.29E-01	2.30E-01	1.16E-01	8.46E-02	1.87E-01	1.20E-01	1.20E-01
		2.07E-01	1.53E-01	2.31E-01	1.81E-01	3.25E-01	2.71E-01	3.54E-02	1.53E-01	1.38E-01	2.63E-01
		5.44E-01	2.48E-01	1.89E-01	2.42E-01	2.27E-01	2.69E-01	1.26E-01	1.39E-01	2.29E-01	2.71E-01
		2.57E-01	2.16E-01	3.25E-01	2.02E-01	2.46E-01	2.24E-01	2.19E-01	2.44E-01	3.68E-01	2.29E-01
		3.17E-02	2.35E-01	2.33E-01	2.34E-01	1.69E-01	1.19E-01	8.36E-02	2.35E-01	1.09E-01	1.65E-01
AVRG.	2.08E-01	2.61E-01	2.15E-01	2.45E-01	2.18E-01	2.39E-01	2.00E-01	1.10E-01	1.92E-01	1.93E-01	2.10E-01
STA.	4.15E-02	1.84E-01	3.65E-02	4.98E-02	2.55E-02	5.59E-02	7.74E-02	6.90E-02	4.72E-02	1.09E-01	6.51E-02

	GEL 3% Plasticity Index (η)										
	Points	1	2	3	4	5	6	7	8	9	10
		2.66E-01	1.14E-01	3.06E-01	1.59E-01	2.27E-01	2.38E-01	2.89E-01	3.32E-01	2.27E-01	2.29E-01
		2.40E-01	1.37E-01	2.04E-01	3.14E-01	1.83E-01	2.42E-01	8.10E-02	2.64E-02	1.69E-01	3.28E-01
		2.01E-01	9.49E-02	2.33E-01	2.33E-01	2.13E-01	1.44E-01	2.97E-01	2.54E-01	1.71E-01	2.35E-01
		9.11E-02	2.28E-01	3.37E-01	2.36E-01	3.02E-01	2.50E-01	2.62E-01	3.05E-01	1.12E-01	1.07E-01
		1.96E-01	2.70E-01	2.67E-01	2.58E-01	3.62E-01	2.77E-01	1.69E-01	1.77E-01	2.51E-01	3.80E-01
AVRG.	2.25E-01	1.99E-01	1.69E-01	2.69E-01	2.40E-01	2.58E-01	2.30E-01	2.20E-01	2.19E-01	1.86E-01	2.56E-01
STA.	3.27E-02	6.69E-02	7.64E-02	5.35E-02	5.57E-02	7.30E-02	5.06E-02	9.28E-02	1.23E-01	5.47E-02	1.05E-01

	GEL 1% Adhesion Force (Fmin) nN									
	Points	1	2	3	4	5	6	7	8	9	10
		-2.79E-01	-2.83E-01	-9.50E-01	-7.49E-01	-5.41E-01	Unsaved	-5.65E-01	-3.82E-01	-5.13E-01	-4.87E-01
		-2.39E-01	-1.02E+00	-5.60E-01	-6.60E-01	-4.76E-01	Unsaved	-3.06E-01	-5.89E-01	-3.64E-01	-4.11E-01
		-3.51E-01	-2.48E-01	-9.37E-01	-4.89E-01	-3.68E-01	Unsaved	-4.83E-01	-4.53E-01	-4.53E-01	-1.23E-01
		-6.48E-01	-2.89E-01	-5.14E-01	-4.08E-01	-4.52E-01	Unsaved	-7.84E-01	-5.05E-01	-5.05E-01	-3.29E-01
		-6.25E-01	-4.56E-01	-5.55E-01	-4.81E-01	-9.17E-01	Unsaved	-9.28E-01	-4.02E-01	-4.02E-01	-3.58E-01
AVRG.	-5.08E-01	-4.29E-01	-4.60E-01	-7.03E-01	-5.58E-01	-5.51E-01		-6.13E-01	-4.66E-01	-4.47E-01	-3.42E-01
STA.	1.09E-01	1.94E-01	3.24E-01	2.20E-01	1.41E-01	2.14E-01		2.46E-01	8.39E-02	6.47E-02	1.36E-01

	GEL 2% Adhesion Force (Fmin) nN									
	Points	1	2	3	4	5	6	7	8	9	10
		-1.53E-01	-1.14E-01	-5.43E-01	-2.46E-01	-2.07E-01	-1.95E-01	-2.04E-01	-4.28E-01	-2.19E-01	-1.71E-01
		-2.62E-01	-2.26E-01	-1.77E-01	-1.76E-01	-1.22E-01	-4.33E-01	-5.96E-02	-5.79E-01	-2.92E-01	-1.68E-01
		-1.41E-01	-1.81E-01	-1.84E-01	-2.39E-01	-1.31E-01	-2.22E-01	-4.52E-01	-3.27E-01	-1.80E-01	-2.05E-01
		-3.32E-01	-3.60E-01	-2.69E-01	-2.07E-01	-3.55E-01	-2.22E-01	-1.54E-01	-2.46E-01	-2.23E-01	-1.89E-01
		-1.58E-01	-2.61E-01	-1.54E-01	-3.82E-01	-2.20E-01	-1.69E-01	-3.57E-01	-3.77E-01	-5.62E-01	-3.17E-01
AVRG.	-2.55E-01	-2.09E-01	-2.28E-01	-2.65E-01	-2.50E-01	-2.07E-01	-2.48E-01	-2.45E-01	-3.91E-01	-2.95E-01	-2.10E-01
STA.	5.54E-02	8.42E-02	9.15E-02	1.61E-01	7.88E-02	9.36E-02	1.06E-01	1.58E-01	1.25E-01	1.55E-01	6.17E-02

	GEL 3% Adhesion Force (Fmin) nN									
	Points	1	2	3	4	5	6	7	8	9	10
		-1.61E-01	-4.62E-01	-2.08E-01	-5.32E-01	-5.32E-01	-2.64E-01	-2.77E-01	-1.52E-01	-1.32E-01	-2.19E-01
		-2.83E-01	-2.66E-01	-2.90E-01	-1.61E-01	-1.61E-01	-2.74E-01	-3.04E-01	-3.19E-01	-2.27E-01	-1.89E-01
		-4.98E-01	-2.03E-01	-4.63E-01	-7.83E-01	-7.83E-01	-3.29E-01	-1.72E-01	-1.80E-01	-4.74E-01	-1.48E-01
		-3.08E-01	-1.80E-01	-9.30E-01	-2.65E-01	-2.65E-01	-7.40E-02	-1.86E-01	-1.61E-01	-3.09E-01	-1.68E-01
		-2.75E-01	-1.77E-01	-1.23E-01	-8.34E-01	-8.34E-01	-1.52E-01	-3.38E-01	-6.05E-01	-1.45E-01	-1.96E-01
AVRG.	-3.19E-01	-3.05E-01	-2.58E-01	-4.03E-01	-5.15E-01	-5.15E-01	-2.19E-01	-2.55E-01	-2.83E-01	-2.57E-01	-1.84E-01
STA.	1.18E-01	1.22E-01	1.20E-01	3.20E-01	3.01E-01	3.01E-01	1.03E-01	7.30E-02	1.92E-01	1.40E-01	2.70E-02

	GEL 1% (Hardness) (GPa)										
	Points	1	2	3	4	5	6	7	8	9	10
		4.68E-04	8.59E-04	4.52E-04	6.72E-04	6.70E-04	Unsaved	5.82E-04	7.30E-04	7.34E-04	9.16E-04
		6.78E-04	9.10E-04	4.73E-04	9.22E-04	6.87E-04	Unsaved	5.48E-04	7.78E-04	7.45E-04	8.05E-04
		6.05E-04	8.87E-04	4.14E-04	7.77E-04	6.44E-04	Unsaved	5.61E-04	6.98E-04	7.16E-04	7.77E-04
		8.45E-04	8.53E-04	5.36E-04	7.88E-04	7.66E-04	Unsaved	5.50E-04	7.45E-04	7.07E-04	8.04E-04
		7.00E-04	8.10E-04	4.79E-04	9.14E-04	6.98E-04	Unsaved	4.92E-04	7.72E-04	7.07E-04	8.80E-04
AVRG.	7.06E-04	6.59E-04	8.64E-04	4.71E-04	8.14E-04	6.93E-04		5.47E-04	7.45E-04	7.22E-04	8.37E-04
STA.	1.32E-04	1.38E-04	3.76E-05	4.46E-05	1.05E-04	4.55E-05		3.34E-05	3.29E-05	1.71E-05	5.89E-05

	GEL 2% (Hardness) (GPa)										
	Points	1	2	3	4	5	6	7	8	9	10
		3.36E-03	2.48E-03	3.15E-03	2.33E-03	4.04E-03	2.60E-03	2.57E-03	2.69E-03	2.88E-03	2.30E-03
		2.92E-03	2.54E-03	2.23E-03	2.39E-03	3.60E-03	2.66E-03	2.60E-03	2.57E-03	3.32E-03	2.25E-03
		3.04E-03	2.37E-03	2.26E-03	2.70E-03	2.70E-03	2.65E-03	2.67E-03	3.07E-03	2.33E-03	3.71E-03
		3.10E-03	2.11E-03	2.78E-03	2.76E-03	2.43E-03	2.86E-03	3.13E-03	2.63E-03	2.88E-03	2.68E-03
		2.79E-03	1.99E-03	3.75E-03	2.69E-03	2.88E-03	2.66E-03	2.78E-03	2.50E-03	2.90E-03	2.79E-03
AVRG.	2.76E-03	3.04E-03	2.30E-03	2.84E-03	2.57E-03	3.13E-03	2.69E-03	2.75E-03	2.69E-03	2.86E-03	2.75E-03
STA.	2.34E-04	2.12E-04	2.38E-04	6.39E-04	1.99E-04	6.69E-04	1.02E-04	2.26E-04	2.24E-04	3.50E-04	5.88E-04

	GEL 3% (Hardness) (GPa)										
	Points	1	2	3	4	5	6	7	8	9	10
		3.52E-03	3.03E-03	3.28E-03	3.00E-03	3.52E-03	2.75E-03	2.66E-03	4.04E-03	2.87E-03	3.57E-03
		3.61E-03	3.04E-03	3.84E-03	3.75E-03	3.45E-03	2.37E-03	2.55E-03	3.84E-03	2.01E-03	3.56E-03
		3.21E-03	3.40E-03	4.16E-03	3.45E-03	4.03E-03	2.76E-03	3.46E-03	3.27E-03	2.21E-03	3.66E-03
		3.10E-03	2.85E-03	3.45E-03	3.53E-03	3.78E-03	2.24E-03	3.40E-03	3.92E-03	2.83E-03	3.50E-03
		3.46E-03	2.94E-03	3.90E-03	3.07E-03	4.67E-03	1.81E-03	3.72E-03	4.74E-03	2.61E-03	3.79E-03
AVRG.	3.30E-03	3.38E-03	3.05E-03	3.73E-03	3.36E-03	3.89E-03	2.39E-03	3.16E-03	3.97E-03	2.51E-03	3.61E-03
STA.	5.40E-04	2.14E-04	2.11E-04	3.56E-04	3.19E-04	4.92E-04	3.95E-04	5.20E-04	5.25E-04	3.82E-04	1.13E-04

	GEL 1% Universal Hardness (GPa)										
	Points	1	2	3	4	5	6	7	8	9	10
		9.78E-05	1.11E-04	7.94E-05	7.05E-05	8.68E-05	Unsaved	8.89E-05	1.18E-04	1.06E-04	1.35E-04
		9.55E-05	1.25E-04	7.90E-05	7.63E-05	8.30E-05	Unsaved	8.49E-05	1.22E-04	1.09E-04	1.36E-04
		1.01E-04	1.13E-04	7.74E-05	7.16E-05	8.72E-05	Unsaved	7.78E-05	1.19E-04	1.08E-04	1.40E-04
		8.88E-05	1.09E-04	7.27E-05	6.93E-05	9.58E-05	Unsaved	8.03E-05	1.25E-04	1.02E-04	1.38E-04
		9.43E-05	1.13E-04	7.61E-05	8.05E-05	9.85E-05	Unsaved	8.53E-05	1.15E-04	1.04E-04	1.40E-04
AVRG.	9.97E-05	9.55E-05	1.14E-04	7.69E-05	7.36E-05	9.03E-05		8.34E-05	1.20E-04	1.06E-04	1.38E-04
STA.	2.14E-05	4.57E-06	6.19E-06	2.72E-06	4.68E-06	6.57E-06		4.40E-06	3.67E-06	2.51E-06	2.01E-06

	GEL 2% Universal Hardness (GPa)										
	Points	1	2	3	4	5	6	7	8	9	10
		4.58E-04	5.84E-04	5.21E-04	5.24E-04	4.59E-04	5.82E-04	5.09E-04	5.02E-04	4.74E-04	3.91E-04
		4.36E-04	5.77E-04	5.48E-04	5.05E-04	4.29E-04	6.01E-04	5.01E-04	4.33E-04	4.24E-04	4.83E-04
		4.76E-04	6.03E-04	4.97E-04	5.25E-04	4.44E-04	5.64E-04	4.99E-04	5.23E-04	4.23E-04	4.85E-04
		4.59E-04	5.38E-04	5.69E-04	5.51E-04	4.26E-04	5.95E-04	5.76E-04	4.42E-04	4.04E-04	4.53E-04
		4.88E-04	6.00E-04	7.03E-04	5.17E-04	4.90E-04	5.80E-04	5.18E-04	4.51E-04	5.05E-04	4.76E-04
AVRG.	5.06E-04	4.63E-04	5.80E-04	5.68E-04	5.24E-04	4.50E-04	5.84E-04	5.21E-04	4.70E-04	4.46E-04	4.58E-04
STA.	5.60E-05	1.97E-05	2.61E-05	8.04E-05	1.70E-05	2.61E-05	1.47E-05	3.16E-05	3.98E-05	4.18E-05	3.93E-05

	GEL 3% Universal Hardness (GPa)										
	Points	1	2	3	4	5	6	7	8	9	10
		5.09E-04	5.86E-04	5.56E-04	6.34E-04	5.26E-04	5.38E-04	5.93E-04	5.34E-04	5.58E-04	5.78E-04
		5.11E-04	3.94E-04	5.79E-04	6.06E-04	5.76E-04	5.08E-04	5.71E-04	5.72E-04	6.40E-04	5.60E-04
		4.84E-04	6.56E-04	5.27E-04	5.88E-04	4.83E-04	5.82E-04	5.97E-04	5.86E-04	5.53E-04	5.38E-04
		4.78E-04	5.30E-04	4.80E-04	5.67E-04	5.92E-04	4.63E-04	5.62E-04	5.42E-04	5.73E-04	4.72E-04
		4.86E-04	6.13E-04	4.35E-04	5.63E-04	5.33E-04	5.53E-04	5.60E-04	5.40E-04	5.64E-04	5.24E-04
AVRG.	5.47E-04	4.94E-04	5.56E-04	5.15E-04	5.92E-04	5.42E-04	5.29E-04	5.76E-04	5.55E-04	5.78E-04	5.34E-04
STA.	3.04E-05	1.52E-05	1.01E-04	5.81E-05	2.94E-05	4.32E-05	4.56E-05	1.73E-05	2.31E-05	3.57E-05	4.05E-05

	GEL 1% Pressure (GPa)										
	Points	1	2	3	4	5	6	7	8	9	10
		8.13E-05	1.49E-04	7.85E-05	1.17E-04	1.16E-04		1.01E-04	1.27E-04	1.28E-04	1.59E-04
		1.18E-04	1.58E-04	8.21E-05	1.60E-04	1.19E-04		9.52E-05	1.35E-04	1.29E-04	1.40E-04
		1.05E-04	1.54E-04	7.19E-05	1.35E-04	1.12E-04		9.75E-05	1.21E-04	1.24E-04	1.35E-04
		1.47E-04	1.48E-04	9.31E-05	1.37E-04	1.33E-04		9.55E-05	1.29E-04	1.23E-04	1.40E-04
		1.22E-04	1.41E-04	8.32E-05	1.59E-04	1.21E-04		8.55E-05	1.34E-04	1.23E-04	1.53E-04
AVRG.	1.23E-04	1.14E-04	1.50E-04	8.18E-05	1.41E-04	1.20E-04		9.49E-05	1.29E-04	1.25E-04	1.45E-04
STA.	2.28E-05	2.39E-05	6.54E-06	7.74E-06	1.82E-05	7.90E-06		5.81E-06	5.71E-06	2.97E-06	1.02E-05

	GEL 2% Pressure (GPa)										
	Points	1	2	3	4	5	6	7	8	9	10
		5.83E-04	4.30E-04	5.48E-04	4.05E-04	7.02E-04	4.52E-04	4.46E-04	4.67E-04	5.01E-04	4.00E-04
		5.08E-04	4.40E-04	3.87E-04	4.14E-04	6.25E-04	4.63E-04	4.52E-04	4.46E-04	5.76E-04	3.91E-04
		5.28E-04	4.12E-04	3.93E-04	4.69E-04	4.69E-04	4.60E-04	4.63E-04	5.34E-04	4.05E-04	6.45E-04
		5.38E-04	3.66E-04	4.83E-04	4.79E-04	4.22E-04	4.97E-04	5.43E-04	4.56E-04	5.01E-04	4.65E-04
		4.85E-04	3.45E-04	6.51E-04	4.67E-04	5.00E-04	4.61E-04	4.82E-04	4.35E-04	5.04E-04	4.84E-04
AVRG.	4.80E-04	5.28E-04	3.99E-04	4.92E-04	4.47E-04	5.44E-04	4.66E-04	4.77E-04	4.68E-04	4.97E-04	4.77E-04
STA.	4.07E-05	3.69E-05	4.13E-05	1.11E-04	3.46E-05	1.16E-04	1.77E-05	3.92E-05	3.88E-05	6.08E-05	1.02E-04

	GEL 3% Pressure (GPa)										
	Points	1	2	3	4	5	6	7	8	9	10
		6.12E-04	5.26E-04	5.69E-04	5.20E-04	6.12E-04	4.78E-04	4.62E-04	7.02E-04	4.98E-04	6.20E-04
		6.26E-04	5.28E-04	6.67E-04	6.52E-04	5.99E-04	4.12E-04	4.44E-04	6.67E-04	3.48E-04	6.17E-04
		5.58E-04	5.91E-04	7.23E-04	6.00E-04	7.00E-04	4.79E-04	6.01E-04	5.68E-04	3.84E-04	6.36E-04
		5.39E-04	4.95E-04	6.00E-04	6.13E-04	6.57E-04	3.89E-04	5.90E-04	6.81E-04	4.91E-04	6.08E-04
		6.01E-04	5.11E-04	6.77E-04	5.34E-04	8.11E-04	3.15E-04	6.46E-04	8.23E-04	4.54E-04	6.58E-04
AVRG.	5.74E-04	5.87E-04	5.30E-04	6.47E-04	5.84E-04	6.76E-04	4.15E-04	5.49E-04	6.89E-04	4.35E-04	6.28E-04
STA.	9.38E-05	3.71E-05	3.66E-05	6.19E-05	5.54E-05	8.55E-05	6.85E-05	9.02E-05	9.12E-05	6.63E-05	1.96E-05

	GEL 1% (Strain Rate) S-1 at Speed 3 µm / S									
	Points	1	2	3	4	5	6	7	8	9	10
		5.24E+00	6.04E+00	4.97E+00	4.90E+00	5.19E+00	Unsaved	5.44E+00	5.88E+00	5.42E+00	6.38E+00
		5.17E+00	6.30E+00	4.86E+00	4.95E+00	5.43E+00	Unsaved	5.49E+00	6.08E+00	5.53E+00	6.23E+00
		5.46E+00	5.73E+00	4.75E+00	4.46E+00	5.28E+00	Unsaved	5.07E+00	5.76E+00	5.56E+00	6.26E+00
		5.06E+00	5.64E+00	4.99E+00	4.49E+00	5.60E+00	Unsaved	5.17E+00	6.53E+00	5.34E+00	6.32E+00
		5.14E+00	5.90E+00	4.96E+00	4.95E+00	5.66E+00	Unsaved	5.09E+00	6.23E+00	5.35E+00	6.49E+00
AVRG.	5.48E+00	5.21E+00	5.92E+00	4.91E+00	4.75E+00	5.43E+00		5.25E+00	6.09E+00	5.44E+00	6.34E+00
STA.	5.36E-01	1.53E-01	2.62E-01	1.00E-01	2.53E-01	2.02E-01		1.98E-01	3.00E-01	1.02E-01	1.07E-01

	GEL 2% (Strain Rate) S-1 at Speed 3 µm / S									
	Points	1	2	3	4	5	6	7	8	9	10
		1.20E+01	1.32E+01	1.31E+01	1.28E+01	1.19E+01	1.42E+01	1.27E+01	1.25E+01	1.24E+01	1.11E+01
		1.16E+01	1.30E+01	1.35E+01	1.22E+01	1.15E+01	1.45E+01	1.28E+01	1.16E+01	1.17E+01	1.24E+01
		1.25E+01	1.32E+01	1.26E+01	1.26E+01	1.15E+01	1.33E+01	1.29E+01	1.30E+01	1.16E+01	1.31E+01
		1.21E+01	1.23E+01	1.37E+01	1.30E+01	1.14E+01	1.36E+01	1.36E+01	1.20E+01	1.18E+01	1.26E+01
		1.21E+01	1.33E+01	1.71E+01	1.24E+01	1.31E+01	1.31E+01	1.29E+01	1.20E+01	1.34E+01	1.27E+01
AVRG.	1.27E+01	1.21E+01	1.30E+01	1.40E+01	1.26E+01	1.19E+01	1.38E+01	1.30E+01	1.22E+01	1.22E+01	1.24E+01
STA.	7.19E-01	3.31E-01	3.94E-01	1.77E+00	2.92E-01	7.28E-01	5.66E-01	3.73E-01	5.69E-01	7.44E-01	7.47E-01

	GEL 3% (Strain Rate) S-1 at Speed 3 µm / S									
	Points	1	2	3	4	5	6	7	8	9	10
		1.42E+01	1.54E+01	1.43E+01	1.58E+01	1.40E+01	1.51E+01	1.46E+01	1.52E+01	1.52E+01	1.57E+01
		1.43E+01	1.23E+01	1.51E+01	1.54E+01	1.48E+01	1.42E+01	1.46E+01	1.51E+01	1.59E+01	1.59E+01
		1.39E+01	1.58E+01	1.44E+01	1.52E+01	1.40E+01	1.52E+01	1.54E+01	1.53E+01	1.41E+01	1.56E+01
		1.38E+01	1.41E+01	1.36E+01	1.49E+01	1.57E+01	1.34E+01	1.57E+01	1.52E+01	1.53E+01	1.45E+01
		1.39E+01	1.47E+01	1.29E+01	1.49E+01	1.48E+01	1.40E+01	1.65E+01	1.54E+01	1.53E+01	1.52E+01
AVRG.	1.48E+01	1.40E+01	1.44E+01	1.41E+01	1.52E+01	1.47E+01	1.44E+01	1.53E+01	1.53E+01	1.52E+01	1.54E+01
STA.	5.44E-01	2.05E-01	1.38E+00	8.09E-01	3.75E-01	7.24E-01	7.87E-01	8.26E-01	9.28E-02	6.38E-01	5.46E-01

Summary of the Results									
Samples		Stiffness N/m		Reissner GPa		Strain Rate (s^{-1})		Pressure (kPa)	
Gel	wt%	AVRG.	STA.	AVRG.	STA.	AVRG.	STA.	AVRG.	STA.
GEL 1	1.00	0.0544	6.65E-03	1.10E+01	3.55E-01	5.48E+00	5.36E-01	1.10E+02	4.43E+01
GEL2	2.00	0.1201	1.05E-02	1.10E+01	1.22E+00	1.27E+01	7.19E-01	4.80E+02	4.07E+01
GEL3	3.00	0.1175	1.34E-02	3.44E+00	5.86E-01	1.48E+01	5.44E-01	5.74E+02	9.38E+01
AVRG.		0.10	0.01	8.46E+00	7.21E-01	10.99	0.60	387.88	59.62
STA.		0.04	0.00	4.35E+00	4.49E-01	4.89	0.10	244.99	29.70

Summary of the Results									
Samples		Hysteresis nN.nm		Hy/Vol (kPa)		Plasticity Index		Adh. F. (nN)	
Gel	wt%	AVRG.	STA.	AVRG.	STA.	AVRG.	STA.	AVRG.	STA.
GEL 1	1.00	469.03	105.78	1.83E-01	4.12E-02	6.71E-02	1.32E-02	-9.97E-01	1.64E-01
GEL2	2.00	2107.18	266.47	2.16E+00	2.73E-01	1.93E-01	1.20E-02	-3.09E+00	6.49E-01
GEL3	3.00	4736.31	468.19	1.38E+01	1.36E+00	3.45E-01	3.23E-02	-3.85E+00	5.92E-01
AVRG.		2437.50	280.15	5.38	0.56	0.20	0.02	-2.65	0.47
STA.		2152.73	181.59	7.36	0.71	0.14	0.01	1.48	0.27

Summary of the Results									
Samples		Hardness (MPa)		Uni. Hardness(kPa)					
Gel	wt%	AVRG.	STA.	AVRG.	STA.				
GEL 1	1.00	4.06	0.76	9.97E+01	2.14E+01				
GEL2	2.00	15.90	1.35	5.06E+02	5.60E+01				
GEL3	3.00	19.03	3.11	5.47E+02	3.04E+01				
AVRG.		13.00	1.74	384.41	35.94				
STA.		7.89	1.23	247.38	17.95				

Appendix D: Related Publications

- "Nanomechanical Properties of phospholipid- Based Microbubbles", Ibrahim Albaijan, Julia Morris, Vassilis Sboros and Vasileios Koutsos. The 23th International Materials Research Congress, 17-21 August, 2014, Cancun, Mexico.

- "Nanomechanical Properties of SonoVue Microbubbles and Hysteresis Behaviour", Ibrahim Albaijan, Vassilis Sboros and Vasileios Koutsos. The 24th International Materials Research Congress, 16-20 August, 2015, Cancun, Mexico.

- "Investigating the Mechanical Properties of Soft Biomaterials Using the Atomic Force Microscopy (AFM)", Ibrahim Albaijan, Vassilis Sboros and Vasileios Koutsos. Nanotech France 2017, 28 - 30 June, 2017, Paris, France.

- "Investigating the Mechanical Properties of the Hydrogels Using the Atomic Force Microscopy (AFM)", Ibrahim Albaijan, Vassilis Sboros and Vasileios Koutsos. Nanotech France 2017, 28 - 30 June, 2017, Paris, France.